

Flow Separation  
on Wind Turbine Blades

Gustave P. Corten



# Flow Separation on Wind Turbine Blades

Het Loslaten van Stroming over Windturbinebladen



# Flow Separation on Wind Turbine Blades

## Het Loslaten van Stroming over Windturbinebladen

(met een samenvatting in het Nederlands)

Proefschrift

ter verkrijging van de graad van doctor aan de Universiteit Utrecht,  
op gezag van de Rector Magnificus, Prof. Dr. H.O. Voorma,  
ingevolge het besluit van het College voor Promoties  
in het openbaar te verdedigen op maandag 8 januari 2001 des middags te 16:15 uur

door

Gustave Paul Corten

geboren op 8 september 1968, te Rotterdam

promotor: Prof. dr. ir. C.D. Andriessse  
verbonden aan de Faculteit Natuur- en Sterrenkunde  
van de Universiteit Utrecht

leescommissie:  
Prof. W.C. Sinke  
Ir. H. Snel  
Prof. dr. ir. G.A.M. van Kuik  
Prof. dr. W.F. van der Weg

examencommissie:  
voorzitter: Prof. dr. H.J.G.L.M. Lamers  
gasten: Ir. H.J.M. Beurskens  
Prof. dr. ir. G.A.M. van Kuik  
Ing. O. de Vries  
hoogleraren: Prof. dr. ir. W. Lourens  
Prof. dr. F. W. Saris  
Prof. dr. W. C. Sinke  
Prof. dr. P. van de Straten  
Prof. dr. W.F. van der Weg

dit proefschrift werd mede mogelijk gemaakt met financiële steun van Energieonderzoek  
Centrum Nederland

on januari 16, 2001 some corrections were made

ISBN 90-393-2582-0 , NUGI 837

*'What is needed now is a new era of economic growth - growth that is forceful and at the same time socially and environmentally sustainable.'*

*'Sustainable development is development that meets the needs of the present without compromising the ability of future generations to meet their own needs.'*

Brundtland, G.H., Our Common Future, 1987





# Summary

In the year 2000, 15GW of wind power was installed throughout the world, producing 100PJ of energy annually. This contributes to the total electricity demand by only 0.2%. Both the installed power and the generated energy are increasing by 30% per year world-wide. If the airflow over wind turbine blades could be controlled fully, the generation efficiency and thus the energy production would increase by 9%.

## **Power Control**

To avoid damage to wind turbines, they are cut out above 10 Beaufort (25 m/s) on the wind speed scale. A turbine could be designed in such a way that it converts as much power as possible in all wind speeds, but then it would have to be too heavy. The high costs of such a design would not be compensated by the extra production in high winds, since such winds are rare. Therefore turbines usually reach maximum power at a much lower wind speed: the rated wind speed, which occurs at about 6 Beaufort (12.5 m/s). Above this rated speed, the power intake is kept constant by a control mechanism. Two different mechanisms are commonly used. Active pitch control, where the blades pitch to vane if the turbine maximum is exceeded or, passive stall control, where the power control is an implicit property of the rotor.

## Stall Control

The flow over airfoils is called 'attached' when it flows over the surface from the leading edge to the trailing edge. However, when the angle of attack of the flow exceeds a certain critical angle, the flow does not reach the trailing edge, but leaves the surface at the separation line. Beyond this line the flow direction is reversed, i.e. it flows from the trailing edge backward to the separation line. A blade section extracts much less energy from the flow when it separates. This property is used for stall control.

Stall controlled rotors always operate at a constant rotation speed. The angle of attack of the flow incident to the blades is determined by the blade speed and the wind speed. Since the latter is variable, it determines the angle of attack. The art of designing stall rotors is to make the separated area on the blades extend in such a way, that the extracted power remains precisely constant, independent of the wind speed, while the power in the wind at cut-out exceeds the maximum power of the turbine by a factor of 8. Since the stall behaviour is influenced by many parameters, this demand cannot be easily met. However, if it can be met, the advantage of stall control is its passive operation, which is reliable and cheap.

## **Problem Definition**

In practical application, stall control is not very accurate and many stall-controlled turbines do not meet their specifications. Deviations of the design-power in the order of tens of percent are regular. In the nineties, the aerodynamic research on these deviations focussed on: profile aerodynamics, computational fluid dynamics, rotational effects on separation and pressure measurements on test turbines. However, this did not adequately solve the actual problems with stall turbines.

In this thesis, we therefore formulated the following as the essential question:

*'Does the separated blade area really extend with the wind speed, as we predict?'*

To find the answer a measurement technique was required, which 1) was applicable on large commercial wind turbines, 2) could follow the dynamic changes of the stall pattern, 3) was not influenced by the centrifugal force and 4) did not disturb the flow. Such a technique was not available, therefore we decided to develop it.

## **Stall Flag Method**

For this method, a few hundred indicators are fixed to the rotor blades in a special pattern. These indicators, called 'stall flags' are patented by the Netherlands Energy Research Foundation (ECN). They have a retro-reflective area which, depending on the flow direction, is or is not covered. A powerful light source in the field up to 500m behind the turbine illuminates the swept rotor area. The uncovered reflectors reflect the light to the source, where a digital video camera records the dynamic stall patterns. The images are analysed by image processing software that we developed. The program extracts the stall pattern, the blade azimuth angles and the rotor speed from the stall flags. It also measures the yaw error and the wind speed from the optical signals of other sensors, which are recorded simultaneously. We subsequently characterise the statistical stall behaviour from the sequences of thousands of analysed images. For example, the delay in the stall angle by vortex generators can be measured within 1° of accuracy from the stall flag signals.

### Properties of the Stall Flag

The new indicators are compared to the classic tufts. Stall flags are pressure driven while tufts are driven by frictional drag, which means that they have more drag. The self-excited motion of tufts, due to the Kelvin-Helmholtz instability, complicates the interpretation and gives more drag. We designed stall flags in such a way that this instability is avoided. An experiment with a 65cm diameter propeller confirms the independence of stall flags from the centrifugal force and that stall flags respond quickly to changes in the flow.

We developed an optical model of the method to find an optimum set-up. With the present system, we can take measurements on turbines of all actual diameters. The stall flag responds to separated flow with an optical signal. The contrast of this signal exceeds that of tuft-signals by a factor of at least 1000. To detect the stall flag signal we need a factor of 25 fewer pixels of the CCD chip than is necessary for tufts. Stall flags applied on fast moving objects may show light tracks due to motion blur, which in fact yields even more information. In the case of tuft visualisations, even a slight motion blur is fatal.

## Principal Results

In dealing with the fundamental theory of wind turbines, we found a new aspect of the conversion efficiency of a wind turbine, which also concerns the stall behaviour. Another new aspect concerns the effects of rotation on stall. By using the stall flag method, we were able to clear up two practical problems that seriously threatened the performance of stall turbines. These topics will be described briefly.

### 1. Inherent Heat Generation

The classic result for an actuator disk representing a wind turbine is that the power extracted equals the kinetic power transferred. This is a consequence of disregarding the flow around the disk. When this flow is included, we need to introduce a heat generation term in the energy balance. This has the practical consequence that an actuator disk at the Lanchester-Betz limit transfers 50% more kinetic energy than it extracts. This surplus is dissipated in heat.

Using this new argument, together with a classic argument on induction, we see no reason to introduce the concept of edge-forces on the tips of the rotor blades (Van Kuik, 1991). We rather recommend following the ideas of Lanchester (1915) on the edge of the actuator disk and on the wind speed at the disc. We analyse the concept induction, and show that correcting for the aspect ratio, for induced drag and application of Blade Element Momentum Theory all have the same significance for a wind turbine. Such corrections are sometimes made twice (Viterna & Corrigan, 1981).

### 2. Rotational Effects on Flow Separation

In designing wind turbine rotors, one uses the aerodynamic characteristics measured in the wind tunnel on fixed aerodynamic profiles. These characteristics are corrected for the effects of rotation and subsequently used for wind turbine rotors. Such a correction was developed by Snel (1990-1999). This correction is based on boundary layer theory, the validity of which we question in regard to separated flow.

We estimated the effects of rotation on flow separation by arguing that the separation layer is thick so the velocity gradients are small and viscosity can be neglected. We add the argument that the chord-wise speed and its derivative normal to the wall is zero at the separation line, which causes the terms with the chord-wise speed or accelerations to disappear. The conclusion is that the chord-wise pressure gradient balances the Coriolis force. By doing so we obtain a simple set of equations that can be solved analytically. Subsequently, our model predicts that the convective term with the radial velocity ( $v_r \partial v_r / \partial r$ ) is dominant in the equation for the  $r$ -direction, precisely the term that was neglected in Snel's analysis.

### 3. Multiple Power Levels

Several large commercial wind turbines demonstrate drops in maximum power levels up to 45%, under apparently equal conditions. Earlier studies attempting to explain this effect by technical malfunctioning, aerodynamic instabilities and blade contamination effects estimated with computational fluid dynamics, have not yet yielded a plausible result.

We formulated many hypotheses, three of which were useful. By taking stall flag measurements and making two other crucial experiments, we could confirm one of those three hypotheses: the insect hypothesis. Insects only fly in low wind, impacting upon the blades at specific locations. In these conditions, the insectal remains are located at positions where roughness has little influence on the profile performance, so that the power is not affected. In high winds however, the flow around the blades has changed. As a result, the positions at

which the insects have impacted at low winds are very sensitive to contamination. So the contamination level changes at low wind when insects fly and this level determines the power in high winds when insects do not fly. As a consequence we get discrete power levels in high winds.

The other two hypotheses, which did not cause the multiple power levels for the case we studied, gave rise to two new insights. First, we expect the power to depend on the wind direction at sites where the shape of the terrain concentrates the wind. In this case the power level of all turbine types, including pitch regulated ones, will be affected. Second, we infer heuristically that the stalled area on wind turbine blades will adapt continuously to wind variations. Therefore, the occurrence of strong bi-stable stall-hysteresis, which most blade sections demonstrate in the wind tunnel, is lost. This has been confirmed by taking special stall flag measurements.

#### 4. Deviation of Specifications

The maximum power of stall controlled wind turbines often shows large systematic deviations from the design. We took stall flag measurements on a rotor, the maximum power of which was 30% too high, so that the turbine had to be cut out far below the designed cut-out wind speed. We immediately observed the blade areas with deviating stall behaviour. Some areas that should have stalled did not and caused the excessive power. We adapted those areas by shifting the vortex generators. In this way we obtained a power curve that met the design much more closely and we realised a production increase of 8%.

# Contents

<b>Summary</b>	vii
<b>Contents</b>	xi
<b>1. Introduction</b>	1
<b>2. Energy Extraction</b>	5
List of Symbols	7
2.1 Maximum Energy Transfer	9
2.1.1 The Lanchester-Betz Limit	9
2.1.2 Heat Generation	11
2.2 Induction	17
2.2.1 Prandtl Finite Airfoil Induction	18
2.2.2 Induction for a Wind Turbine	19
2.2.3 Blade Element Momentum Theory	20
2.3 Tip Correction	22
2.3.1 Prandtl Tip Correction	22
2.3.2 Tip Correction for an Actuator Disk	23
2.4 Blade Aerodynamics	25
2.4.1 The Angle of Attack	25
2.4.2 Lift and Drag	26
2.4.3 Stall	27
2.5 Rotational Effects	30
2.5.1 Fundamental Equations in a Rotating Frame of Reference	30
2.5.2 Boundary Layer Assumptions	31
2.5.3 Attached Flow on a Rotating Blade	32
2.5.4 Rotational Effects on Flow Separation; Snel's Analysis	34
2.5.5 Rotational Effects on Flow Separation; Our Analysis	38
2.5.6 Extension of the Heuristics with $\theta$ -z Rotation	41

<b>3. The Stall Flag Method</b>	45
List of Symbols	46
3.1 The Stall Flag	48
3.1.1 Controlled Evolutionary Development	48
3.1.2 List of Recommendations.	52
3.2 Interpretation of Signals	53
3.2.1 Aerodynamic Forces on the Stall Flag	53
3.2.2 External Forces	55
3.2.3 Sensitivity	56
3.2.4 Response Time	56
3.2.5 Hysteresis and the $h/2h$ -Model	57
3.2.6 Kelvin-Helmholtz Instability	60
3.2.7 Observations	62
3.3 Flow Disturbance	64
3.3.1 Transition	64
3.3.2 Drag Increase	65
3.3.3 Influence to Pressure Distributions	66
3.4 Tufts and Stall Flags Compared	68
<b>4. Optical Aspects of Stall Flags</b>	69
List of symbols	70
4.1 Principles of Detection	72
4.1.1 Detectable or Visible	72
4.1.2 Active or Passive	72
4.1.3 Stall Flag Positioning	73
4.1.4 Type and Locus of Contrasting Area	73
4.1.5 Retro-reflection	74
4.1.6 Differential Detection	75
4.2 Quantifying Stall Flag Signals	77
4.2.1 Sources of Radiation	77
4.2.2 Intensity of Stall Flag Signals	77
4.2.3 Stall Flag Image Size.	79
4.2.4 Image Spectral Irradiance.	79
4.2.5 Image Spectral Exposure	80
4.2.6 The Absolute Demand	81
4.2.7 The Relative Demand	82
4.2.8 Visibility	82
4.3 Optimisation	84
4.3.1 Diffuse Reflection	84
4.3.2 Retro-reflection	85
4.3.3. Summary	86
4.4 Application on a Wind Turbine	87
4.5 Tufts Signals	90

<b>5. Stall Flag Experiments</b>	93
5.1 The Standard Procedure	94
5.1.1 Instrumentation of the Turbine	94
5.1.2 The Stall Flag Pattern	95
5.1.3 The Measurements	97
5.1.4 Image Analysis	98
5.1.5 Experimental Data	99
5.2 Proof of Concept Using a 25mHAT	101
5.3 Multiple Power Levels	105
5.3.1 The Tip Commands Hypothesis	105
5.3.2 The Insect Hypothesis	107
5.3.3 Experience with a 44m HAT	108
5.3.4 Validation of the Tip Commands Hypothesis	109
5.3.5 Validation of the Insect Hypothesis	110
5.3.6 The Terrain Concentration Hypothesis.	112
5.3.7 Conclusion on Multiple Power Levels	114
5.4 Comparison with Theory	115
<b>6. Conclusions.</b>	117
<b>References</b>	121
<b>A: The Aerpac 43m Rotor</b>	125
A.1 First Stall Flag Measurement	125
A.2 Second Stall Flag Measurement	129
A.3 Vortex Generator Modelling	130
<b>B: Propeller Experiment</b>	133
<b>C: Stall Flag Patent</b>	135
<b>Samenvatting</b>	145
<b>Curriculum Vitae</b>	149
<b>Dankwoord.</b>	151





# 1. Introduction

This thesis deals with flow separation on wind turbine blades. When air flows over an airfoil it may not follow the surface from the leading edge towards the trailing edge, but may turn away and break loose from that surface. This phenomenon is called flow separation. It spoils the performance of the blades. When separation occurs, the lift, which normally is rapidly increasing with the angle of attack, stops rising and the drag, which normally is very small, becomes comparable to the lift.

An aircraft that suddenly stalls slows down due to the large drag and loses lift, due to both stalling and due to the decrease in speed. Therefore, flow separation is to be avoided in aviation, unless braking firmly is intended.

A wind turbine should not always extract the highest possible power from the wind. Very high wind speeds are rare and do not add much to the energy production during the year. To withstand such speeds in normal operation the turbine would have to be heavy and expensive. Therefore, wind turbines are designed with a maximum power level that will be reached dozens of times per year. A control mechanism is required in order to not exceed this so-called rated power level, which is just reached at the rated wind speed (figure 1.1).

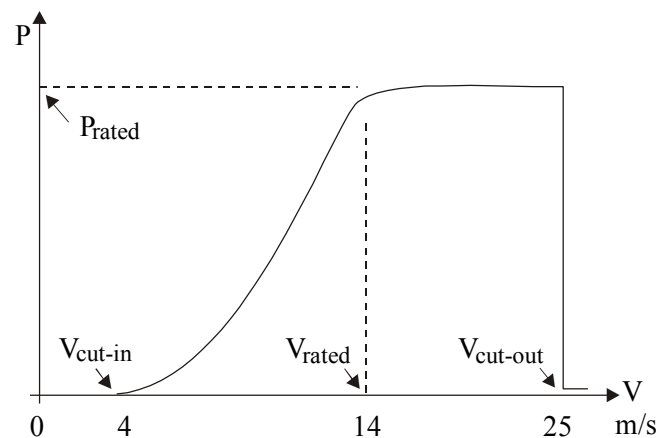


**figure 1.1** A power curve of a wind turbine, with indicative numerical values.

About half of all wind turbines use flow separation to control the power. With increasing wind speed the separated flow, which is less efficient in transferring energy from the wind to the blades, extends over the blade surfaces in such a way that the power in excess of the rated-value is zero. These turbines rotate at constant speed, so that the angles of attack increase with the wind speed. Flow separation depends first of all on the angles of attack. It is initiated above a certain critical angle and progresses with the angle of attack. By using the relations between the angle of attack and the wind and between the flow separation and the angle of attack, the rotor can be designed in

such a way that the maximum power captured is limited by the rotor geometry. The constant rotation speed and the passive power control lead to a simple but efficient design of the turbine, which is therefore relatively cheap.

The other half of the wind turbines turn their blades actively to vane position at high wind speeds, so that the smaller angles of attack limit the transfer of energy. This principle is more expensive since it requires a mechanism to turn the blades. Here one needs to understand less of the physics of flow separation, however. The angles of attack approach the conditions of flow separation only around rated wind speed.

Flow separation depends in a complex way on many parameters. When the inflow approaches the separation angle, any parameter, no matter how small, can have a decisive role. Therefore, the separation behaviour cannot be predicted. In practice one relies on empirical studies of airfoil sections in a wind tunnel. However, the same airfoils in different wind tunnels often demonstrate different stall properties. When the airfoils characterised in a tunnel are used as part of a wind turbine blade and rotate in the field one observes further deviations. The phenomenon of separation is very sensitive to surface roughness, turbulence level and imperfections of the airfoil contour.

Turbine power control based on passive stall is often inaccurate up to  $\pm 15\%$ , but in the worst case it can deviate as much as 45%. Overpower leads to overheating of the generator of the turbine, so that the latter has to be stopped and an economic loss is suffered. Large deviations become unacceptable for the increasing investments in wind energy generation. Pitch-controlled turbines may produce about 15% less power near the rated wind speed due to premature separation, but they are more predictable.

Poor control of flow separation leads to economic losses of 15% for stall-regulated turbines and 2.5% for pitch-regulated turbines. Every GW wind power installed loses 22GWh per percent annually due to flow separation. Presently, in August 2000, the wind power installed world-wide is 15GW, so that for an average separation loss of 9%, the present losses are 3GWh or 10 PJ per year. This corresponds to about 3% of the electricity consumption in the Netherlands.

In chapter 2 of this thesis the process of energy extraction by a rotor is described. We first reproduce the classic result for the maximum power that a wind turbine can extract from a flow. We stress - and this is not new but often overlooked - that energy extraction by a wind turbine is inherently coupled to turbulent mixing and viscous shear behind the turbine, which causes that a large amount of kinetic energy dissipates in heat. The amount is about  $1/3$  of the total decrease of the kinetic energy in the flow. This clarifies the peculiar situation that the power required to drive a force  $D$  with speed  $U$  in air is  $-D \cdot U$ , while the same force at standstill in a wind of speed  $U$  can extract maximally  $2/3 D \cdot U$ . Then we deal with induction. We discuss the corrections for angles of attack, for induced drag and for the finite aspect ratios. These three corrections address the same physical effect, however. This is not well known so that sometimes more than one of these corrections is applied.

The remainder of chapter 2 is devoted to the effects of rotation on flow separation. The discussion is focused on relevant approximations of the Navier-Stokes equation. We estimate the radial component of the flow in the separated area to be the largest, precisely the one that has been neglected so far. In our physical model of the separated flow, the chord-wise

pressure gradient just balances the Coriolis force. Furthermore, in separated flow viscous forces will be so small that they can be neglected. Thus, we arrive at Euler equations, which can be solved analytically.

In chapters 3 and 4 we present a flow visualisation technique, based on a new detector, the so-called stall flag. This stall flag has been patented in European Countries and in the United States. The uncertainties associated with flow separation were an incentive for measuring the properties of stall in practice, but there appeared to be no good method of doing so. We have developed a method with which the separated area on any wind turbine can be visualised from half a kilometre distance. By this method, the fast dynamic variations in the separated flow can be followed. The very thin and very light wireless stall flags, that only need to be pasted on the surface of the airfoil, have a negligible influence on the flow. Chapter 3 deals with the aerodynamic aspects of the stall flag, and addresses the influence of external forces. The signals of the stall flags are optical. The development and modelling of the stall flag observation system are described in chapter 4.

Chapter 5 describes the actual stall flag experiments. It first gives an impression of the field work and continues with proofs of the value of stall flag measurements (The application of stall flags to improve the power curve of an 43m diameter rotor and a proof with a rotating propeller of 65cm diameter are described in appendices). Chapter 6 presents the conclusions.



## 2. Energy Extraction

This chapter describes the fundamentals of energy transfer by a wind turbine. In section 1 the maximum power that can be extracted from a fluid flow is discussed. The classic result for an actuator disk is that the power extracted equals the kinetic power transferred. This is a consequence of disregarding the flow around it. When we include this flow we get the balance below, having the practical consequence that an actuator disk representing a wind turbine in optimum operation transfers 50% more kinetic energy than it extracts and that this amount is dissipated into heat.

$- U \cdot D$	=	$- (U+U_i) \cdot D$	+	$U_i \cdot D$
<i>kinetic power transferred</i>		<i>power extracted</i>		<i>rate of heat production</i>

Lanchester [46] proved that the velocity at an actuator disk should be the average of that far upwind and that far downwind, but adds to this that in practice the tips of a rotor emit vortices that also represent kinetic energy. If these flows of energy are included, the energy per second increases so that the speed at the force should be higher than average.

We see no reason to doubt this plausible explanation and to introduce another, based on the concept of edge-forces on the tips of the rotor blades [45]. We question the concept wherein the edge-forces transfer momentum but no energy. First of all, from the above energy balance it follows that any axial force appears in the energy balance, and second, the axial force at the tips will accelerate the flow in the direction of the force and inevitably have induced drag or will transfer energy. The experiment with a rotor [45] in hover, to confirm the edge-force concept, was not reliable. The heat production referred to above was neglected, re-circulation may have been significant and the velocity changes used for the momentum transfer estimate were not measured in the far wake, so that the momentum exchange was not completed.

Section 2 deals with induction by presenting models of the phenomenon and by showing that correcting for the aspect ratio, for induced drag and application of Blade Element Momentum

Theory all have the same significance for a wind turbine. This is not generally known, and may lead to double corrections as proposed in [26] or to the idea that the aspect ratio correction includes the tip correction [45].

Section 3 deals with tip corrections. Prandtl's tip correction addresses the azimuthal non-uniformity of disk loading, but does not correct for the flow around the tips or for the flow around the edges of an actuator disk. Lanchester [46] stated '*At the disk edge, it is manifestly impossible to maintain any finite pressure difference between the front and the rear faces.*' So in fact a concept for a second tip correction is proposed that affects even an actuator disk.

Section 4 briefly reviews airfoil aerodynamics. They are basic for the detailed treatment of the aerodynamics on rotating blades given in section 5.

Here we estimated the effects of rotation on flow separation by arguing that the separation layer is thick, therefore the velocity gradients are small and viscosity can be neglected. With the argument that the chord-wise speed and its derivative normal to the wall is 0 at the separation line, the terms with the chord-wise speed or accelerations disappear and we must conclude that the chord-wise pressure gradient balances the Coriolis force. By doing so we get a simple set of equations that can be solved analytically. We oppose the classic model of Snel [52,53]. He uses boundary layer theory, which is invalid in separated flow [51,64]. As a consequence he neglects precisely those terms which we estimate to be dominant.

## List of Symbols

$a$	[-]	axial induction factor
$a'$	[-]	tangential induction factor
$A$	[m <sup>2</sup> ]	surface of the actuator disk
$b$	[m]	half of the span of the airfoil
$c$	[m]	chord
$C_D$	[-]	axial force coefficient
$C_H$	[-]	total pressure head coefficient
$C_{heat}$	[-]	dissipated heat coefficient
$c_{sep}$	[m]	separated length of the chord
$c_{di}$	[-]	induced drag coefficient
$c_l$	[-]	lift coefficient $L/(\frac{1}{2}\rho v^2 c)$
$C_P$	[-]	power coefficient
$c_p$	[-]	pressure coefficient $p/(\frac{1}{2}\rho v^2)$
$D$	[N/m]	drag force per unit span
$D_{ax}$	[N]	axial force exerted by the actuator disk
$D_i$	[N/m]	induced drag force per unit span
$D_N$	[N]	normalisation for axial force $\frac{1}{2}\rho A U^2$
$f$	[-]	stalled fraction of the chord $c_{sep}/c$
$d\tau$	[m <sup>3</sup> ]	infinitely small element of volume
$F$	[N/kg]	external force per unit of mass
$F_r$	[N/kg]	external force per unit of mass in the $r$ -direction
$F_\theta$	[N/kg]	external force per unit of mass in the $\theta$ -direction
$F_z$	[N/kg]	external force per unit of mass in the $z$ -direction
$i$	[rad]	induced angle of attack
$L$	[N/m]	lift force per unit span
$\dot{m}$	[kg/s]	mass flow of the wind, in section 2.2.2 it is the mass flow per unit span in kg/ms to which the momentum transfer per unit span is confined.
$P$	[W]	power
$P_{flow}$	[W/m]	kinetic power extracted from the flow per unit airfoil span
$P_N$	[W]	normalisation power $\frac{1}{2}\rho A U^3$
$p$	[N/m <sup>2</sup> ]	pressure
$p_0$	[N/m <sup>2</sup> ]	atmospheric pressure
$p^+$	[N/m <sup>2</sup> ]	pressure on upwind site of the actuator disk
$p^-$	[N/m <sup>2</sup> ]	pressure on downwind side of the actuator disk
$p_d$	[N/m <sup>2</sup> ]	dynamic pressure $\frac{1}{2}\rho U^2$
$r$	[m]	radial position
$R$	[m]	radius of the turbine rotor
$s$	[-]	location of the separation point
$t$	[s]	time
$U$	[m/s]	wind speed
$U_D$	[m/s]	wind speed at the disk
$U_i$	[m/s]	induced velocity

$U_W$	[m/s]	wind speed in the far wake
$V$	[m/s]	wind speed in the very far wake
$v$	[m/s]	velocity of the airfoil
$v_r$	[m/s]	flow velocity in the $r$ -direction in the rotating frame of reference
$v_\theta$	[m/s]	flow velocity in the $\theta$ -direction in the rotating frame of reference
$v_z$	[m/s]	flow velocity in the $z$ -direction in the rotating frame of reference
$W$	[m/s]	resultant inflow velocity
$x$	[m]	position in the direction of the chord
$y$	[m]	position in the direction of the span
$z$	[m]	position normal to the blade surface
$\alpha$	[rad]	angle of attack
$\alpha_0$	[rad]	zero lift angle of attack
$\beta$	[rad]	local pitch angle including twist
$\Gamma$	[m <sup>2</sup> /s]	circulation
$\delta$	[m]	boundary layer thickness
$\Delta U$	[m/s]	velocity change in very far wake due to actuator disk.
$\Delta P_s$	[W]	kinetic power extracted from the flow through the stream tube.
$\Delta P$	[W]	kinetic power extracted from the total flow.
$\varepsilon$	[-]	fraction of the total mass flow $\dot{m}$ through the actuator disk
$\nabla$	[m <sup>-1</sup> ]	nabla-operator ( $\partial/\partial x, \partial/\partial y, \partial/\partial z$ )
$\rho$	[kg/m <sup>3</sup> ]	air density $\approx 1.25$ kg/m <sup>3</sup>
$\mu$	[Ns/m <sup>2</sup> ]	dynamic viscosity of air $\approx 17.1 \cdot 10^{-6}$ Ns/m <sup>2</sup>
$\tau$	[N/m <sup>2</sup> ]	shear stress
$\eta$	[-]	efficiency of kinetic energy transfer
$\varphi$	[rad]	geometric angle of attack
$\theta$	[rad]	position in chord-wise direction
$\lambda$	[-]	tip speed ratio $\Omega R/U$
$\lambda$	[-]	aspect ratio $(2b^2)/bc$
$\lambda_r$	[-]	local speed ratio $\Omega r/U$
$\Sigma$	[m]	cross section of inflow per unit span to which momentum change is confined
$\omega$	[s <sup>-1</sup> ]	vorticity
$\Omega$	[rad/s]	rotor angular frequency



## 2.1 Maximum Energy Transfer

The theory predicting the maximum useful power that can be extracted from a fluid flow was first published by F.W. Lanchester [46] in 1915. In most cases however, this theory is attributed to A. Betz, who published the same argument in 1920 [7]. To do justice to the first author, we will speak of the 'Lanchester-Betz' limit. The first subsection briefly describes the model, in which Lanchester analyses the actuator disk introduced by Froude in 1889 [32]. The second subsection adds a new aspect to the classic model: the inherent viscous losses of an actuator disk. It will be shown that an actuator disk operating in wind turbine mode extracts more energy from the fluid than can be transferred into useful energy. At the Lanchester-Betz limit the decrease of the kinetic energy in the wind is converted by  $\frac{2}{3}$  into useful power and by  $\frac{1}{3}$  into heat. The heat is produced by the viscous force of the outer flow on the stream tube that just encloses the flow through the actuator disk. The analysis shows that there is no necessity to add edge-forces to the actuator disk model [45].

### 2.1.1 The Lanchester-Betz Limit

This section summarises a text written by Glauert [34], to which physical arguments are added. First the actual wind turbine will be replaced by a so-called actuator disk which was introduced by Froude (see figure 2.1). This actuator disk is an abstract theoretical analogue of a wind turbine being used in momentum theory. The disk has a surface  $A$ , equal to the swept area of the wind turbine, and it is oriented perpendicular to the wind. The disk does not consist of several rotor blades but has a homogeneous structure. The undisturbed wind speed is  $U$ , at the actuator disk it is  $U_D=(1-a)U$  and in the far wake it is  $(1-2a)U$ . The parameter  $a$  is called the induction factor which takes into account the decrease of the wind speed when it passes through the permeable actuator disk. The mass flow through this disk is  $\rho A(1-a)U$  and it is driven by the difference in pressure  $p^+$  on the upwind side of the disk and  $p^-$  on the downwind side. So the pressure at the disk is discontinuous and the disk is subject to a net axial force  $D_{ax} = A(p^+ - p^-)$ . This force is also exerted on the fluid and thus it should be equal to the change of the flow of momentum. From conservation of mass it follows that the stream tube just enclosing the flow through the actuator disk has a constant

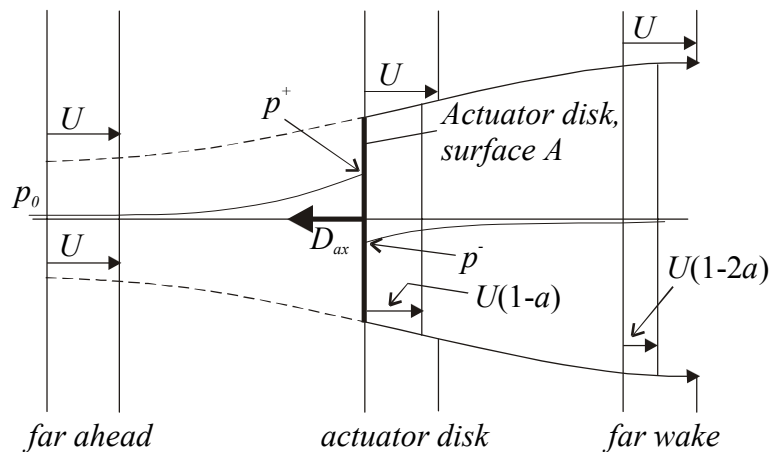


**figure 2.1** Froude's actuator model. The stream tube consists of a slipstream behind the disk, but has no velocity discontinuity in front of the disk.

mass flow  $\rho A(1-a)U$  at all cross sections from far upstream to far downstream. The figure shows this stream tube and its expansion. Behind the actuator we have a clear slipstream, but in front of it such a boundary does not exist, therefore we dashed the slip stream contour here. As this mass flow is constant, the change of momentum should be attributed to a velocity difference between the flow in the far wake and the undisturbed wind speed far upstream:

$$p^+ - p^- = \rho(1-a)U(U - U_w). \quad (2.1)$$

Upwind and downwind of the actuator disk, the kinetic energy in the flow is transferred into 'pressure' energy. So the actuator disk does not directly extract kinetic energy. The disk slows down the flow which causes a pressure difference over the disk. The extracted energy comes from the product of the pressure difference and the volume flow through the disk. Application of Bernoulli's relation that  $p + \frac{1}{2}\rho U^2 = \text{constant}$  along a streamline (when no power is extracted), yields for the flow upwind and downwind respectively:

$$\frac{1}{2}\rho U^2 + p_o = \frac{1}{2}\rho(1-a)^2 U^2 + p^+, \quad (2.2)$$

$$\frac{1}{2}\rho U_w^2 + p_o = \frac{1}{2}\rho(1-a)^2 U^2 + p^-, \quad (2.3)$$

where  $p_o$  is the undisturbed atmospheric pressure. By subtracting equations 2.2 and 2.3 it follows that:

$$p^+ - p^- = \frac{1}{2}\rho(U^2 - U_w^2). \quad (2.4)$$

The combination of equations 2.1 and 2.4 demonstrates that the velocity decrease in front of the disk equals that behind the disk:

$$U_w = (1-2a)U, \quad U_D = (1-a)U. \quad (2.5)$$

The remarkable fact that half the acceleration must take place in front of the disk and half behind it will be discussed in sections 2.1.2 and 2.2. The absolute values for  $p^+$  and  $p^-$  are found to be:

$$p^+ = p_o + \frac{1}{2}\rho U^2(2a - a^2) = p_o + p_{dyn}(2a - a^2), \quad (2.6)$$

$$p^- = p_o - \frac{1}{2}\rho U^2(2a - 3a^2) = p_o - p_{dyn}(2a - 3a^2), \quad (2.7)$$

where the free stream dynamic pressure  $p_d = \frac{1}{2}\rho U^2$  is used. It should be noted that the increase of the pressure on the upwind side is larger than the decrease of the pressure on the downwind side. This suggests that the pressure field far from the turbine can be modelled as the sum of a dipole and a monopole or source.

The extracted power is equal to the difference of the kinetic energy in the flow far upstream, minus the kinetic energy in the flow far downstream, multiplied by the mass flow  $\rho A(1-a)U$ . Far upstream the velocity is  $U$  and far downstream it is  $(1-2a)U$ . Thus we find for the power:

$$P = 4a(1-a)^2 \frac{1}{2}\rho A U^3 = 4a(1-a)^2 P_N, \quad (2.8)$$

in which  $P_N$  ( $\frac{1}{2}\rho AU^3$ ) is the flow of kinetic energy through a cross section of size  $A$  perpendicular to the undisturbed wind. It follows that only the axial induction factor  $a$  determines the fraction of the power extracted by the wind turbine. From  $dP/da = 0$  we find that the maximum fraction extracted is  $\frac{16}{27}$ , which corresponds to  $a = \frac{1}{3}$ . This maximum was derived by Lanchester in 1915. If both the maximum power and the corresponding axial force are normalised with  $P_N$  and  $D_N = \frac{1}{2}\rho AU^2$  respectively, then it follows that:

$$C_p = 4a(1-a)^2 = \frac{16}{27}, \quad (2.9)$$

$$C_D = 4a(1-a) = \frac{8}{9}, \quad (2.10)$$

for the power and the axial force coefficients respectively.

Equation 2.9 only gives the fraction of  $P_N$  that can be converted into useful power. It should not be confused with the efficiency of the turbine. When we read the literature of almost a century ago we find the following text on efficiency written by Betz, 1920 [7]: '*Eine Fläche welche dem Winde einen gewissen Widerstand entgegensetzt, dadurch seine Geschwindigkeit, also seine kinetische Energie, vermindert und diese ihm entzogene kinetische Energie verlustlos in nutzbare Form überführt.*' But in the same paper Betz states that a turbine on an airplane translating with velocity  $U$  and axial force  $D_{ax}$  has efficiency  $P/(U \cdot D_{ax})$ , which is  $1-a$ . However Betz says about this: '*Diese Definition befriedigt nun zwar das theoretische Bedürfnis, da die Axialkraft eine Größe ist, die für die wirtschaftliche Beurteilung eines Windmotors nur untergeordnete Bedeutung hat.*' Glauert 1934 [34] confirms this by stating that it is necessary to distinguish between a windmill driven by the speed of an airplane and a windmill on the ground driven by the wind. In the first case the efficiency is meaningful, but for the latter only the extracted energy is relevant. So, in classic theory the efficiency of a wind turbine ( $1-a$ ) is considered unimportant, which probably was one reason for not paying attention to the physical effect which caused the loss.

In recent literature we find that the decrease of the flow of kinetic energy equals the useful power produced by the actuator disk. Spera 1994 [57], Hunt 1981 [42] and Wilson and Lissaman 1974 [65] normalise the power produced by  $(1-a)P_N$  instead of  $P_N$  since the mass flow *through* the actuator is  $(1-a)UA$  and not  $UA$ . So they hold that the power in the flow is converted with an *efficiency* (defined as power output/power input) =  $C_p/(1-a) = 4a(1-a)$ , which is  $\frac{8}{9}$  at the Lanchester-Betz limit. This means that they limit themselves to the wind that flows through the actuator disk. They find that  $\frac{1}{9}$  of the kinetic energy remained in the flow and thus  $\frac{8}{9}$  was converted into useful power, where the conversion is assumed to have an efficiency of 100%.

In the next section the power transfer by an actuator disk will be calculated for the case in which the outer flow is included.

### 2.1.2 Heat Generation

In the actuator disk model, the power extracted by the axial force is  $-(1-a)U \cdot D_{ax}$ . However, if the same actuator disk, exerting a force  $D_{ax}$ , is fixed on an airplane moving with speed  $U$ , the power required to move the disk would be  $-U \cdot D_{ax}$ . So it takes more power to drive the disk

than the maximum power that can be generated by the disk. This difference is understood when the flow around the actuator is also included in the analysis. It then follows that the energy conversion by an actuator disk has an inherent dissipation of kinetic energy into heat.

Kinetic Power Transfer by an Axial Force

Let  $\dot{m}$  be the indefinite but large mass flow in the wind, in which an actuator disk is placed perpendicular to the flow direction (see figure 2.2). Only a fraction  $\epsilon$  of  $\dot{m}$  flows through the stream tube that just encloses the actuator disk, which exerts a finite axial force  $D_{ax}$  on the flow against the flow direction. In the far wake, the momentum and the energy relations will be:

$$D_{ax} = -\dot{m}2aU, \tag{2.11}$$

$$\Delta P_s = \frac{1}{2}\epsilon\dot{m}(U^2 - (1-2a)^2U^2) = -(1-a)U \cdot D_{ax}. \tag{2.12}$$

Where  $\Delta P_s$  refers to the change of the kinetic power in the flow in the stream tube when it crosses the actuator disk. We now provide the actuator disk model with a *very far wake*, defined as the location beyond the far wake, where the velocity distribution has become uniform again. The definition of the far wake remains classic, namely the location where the axial force has stopped transferring momentum to the flow, or in other words, where the stream tube is no longer expanding. The velocity is  $(1-2a)U$  in the far wake and  $U$  outside the wake. The smoothing of the velocity profile behind the far wake is due to turbulent mixing and viscous shear, which will eventually make all velocities equal to a common speed  $V$  in the *very far wake*. During this process no external force acts on the flow, so momentum is conserved and the flow does not expand further.

Comparing the flow far upwind  $\dot{m} U$  with that in the very far wake  $\dot{m} V$ , the difference in the flow of momentum should be equal to the axial force.

$$D_{ax} = \dot{m}(U - V). \tag{2.13}$$

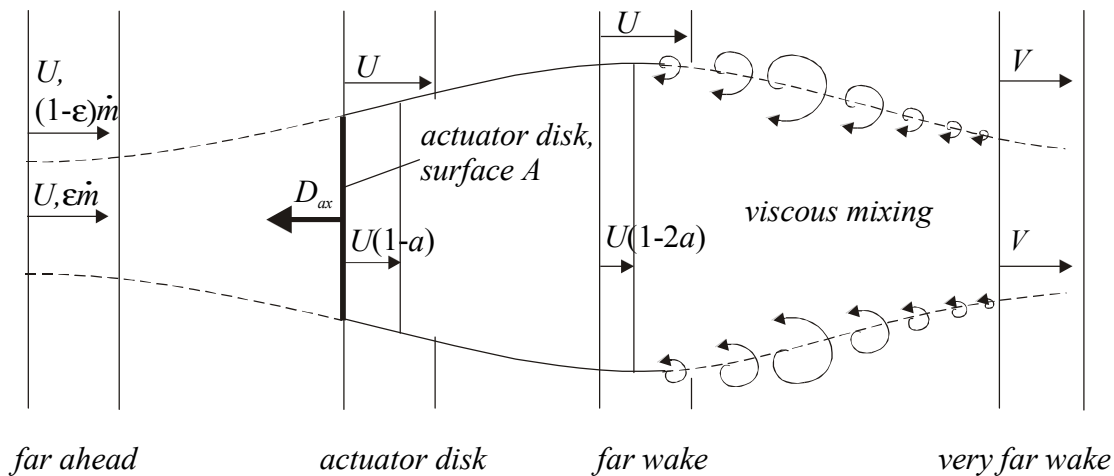


**figure 2.2** Introduction of the very far wake and viscous dissipation. When the outer flow and that inside the stream tube mix, heat is generated and the slipstream vanishes while it contracts.

We can express  $V$  in  $U$ ,  $a$  and  $\varepsilon$  by using the momentum balance between the far wake and the very far wake. The momentum in the outer flow of the far wake is  $(1-\varepsilon)\dot{m}U$ , and in the stream tube it is  $\varepsilon\dot{m}(1-2a)U$ , which together should be equal to  $\dot{m}V$  to conserve momentum, or

$$V = (1 - \varepsilon)U + \varepsilon(1 - 2a)U = (1 - 2a\varepsilon)U. \quad (2.14)$$

The velocity change obtained from the momentum relation 2.13 is connected to the change of the kinetic power in the wind, by

$$\Delta P = \frac{1}{2}\dot{m}(U^2 - V^2) = -(1 - a\varepsilon)U \cdot D_{ax}. \quad (2.15)$$

To clarify: this is the change of the kinetic power in the flow due to the axial force when the outer flow is included, whereas equation 2.12 expresses that change when the outer flow is excluded. In practice the mass flow  $\dot{m}$  is large but finite, so that the fraction of  $\dot{m}$  going through the disk,  $\varepsilon$ , is much smaller than 1 and  $\Delta P$  is close to  $-D_{ax}U$ . So, the decrease of flow of kinetic energy by a force  $D_{ax}$  approaches the scalar product of the undisturbed wind speed  $-U$  and  $D_{ax}$  and *not* the often used product of the local velocity  $-(1-a)U$  and the force  $D_{ax}$ . The latter corresponds to the power extracted from the flow.

#### Dissipation into Heat

In the process of mixing between the far wake and the very far wake, the kinetic power in the flow will not be conserved, but it will be partially converted into heat. This heat is generated by the viscous force that accelerates the flow in the stream tube to the velocity  $V$  in the very far wake. In this process the flow inside the stream tube gains less kinetic energy than the outer flow loses. In the far wake the kinetic power inside the stream tube is  $\frac{1}{2}\varepsilon\dot{m}(1-2a)^2U^2$  and in the outer flow it is  $\frac{1}{2}(1-\varepsilon)\dot{m}U^2$ . In the very far wake the kinetic power is  $\frac{1}{2}\dot{m}V^2$ . The difference has to be the heat generated;

$$P_{heat} = \frac{1}{2}\dot{m}\{[\varepsilon(1 - 2a)^2U^2 + (1 - \varepsilon)U^2] - V^2\} = -(1 - \varepsilon)aU \cdot D_{ax}. \quad (2.16)$$

Of course, this is also equal to  $\Delta P - \Delta P_s$ .

If we want to normalise to  $P_N = \frac{1}{2}\rho AU^3$ , as in the previous section, the mass flow through the actuator disk  $(1-a)\rho AU$  has to be replaced by  $\varepsilon\dot{m}$ . So we use  $P_N = \frac{1}{2}\varepsilon\dot{m}U^2/(1-a) = -D_{ax}U/(4a(1-a))$ . Since the mass flow through the actuator disk is much smaller than the flow outside the wake, we take the limit  $\varepsilon \rightarrow 0$ , and find the following power coefficients,

$$C_H = \frac{\Delta P}{P_N} \approx 4a(1 - a), \quad (2.17)$$

$$C_P = \frac{\Delta P_s}{P_N} = 4a(1 - a)^2, \quad (2.18)$$

$$C_{heat} = \frac{P_{heat}}{P_N} \approx 4a^2(1-a). \quad (2.19)$$

Here  $C_H$  refers to the transferred kinetic power,  $C_P$  to the kinetic power actually extracted and  $C_{heat}$  to the power in the viscous heating.  $C_P$  is the commonly used (classic) power coefficient.

It follows that the maximum efficiency for the process of transfer of kinetic energy into useful power by an actuator disk  $\eta$  is:

$$\eta = \frac{C_P}{C_H} \approx 1-a, \quad (2.20)$$

which is in agreement with Betz's result [7]. Our calculation makes clear that an actuator disk does not convert all transferred kinetic energy into useful energy. The energy balance reads:

$$C_H = C_P + C_{heat}. \quad (2.21)$$

As mentioned before, the maximum extractable useful power from the flow is obtained for  $a = 1/3$ . In that case a fraction  $C_H = 24/27$  of the flow of kinetic energy  $P_N$  is transferred. From this,  $2/3$  is extracted as useful power, and  $1/3$  is dissipated as heat. Figure 2.3 shows schematically the power transfer by an actuator disk representing a wind turbine. We introduced  $U_i = -aU$  for the induction velocity in order to make the model more general, so that the situation for an actuator disk representing a propeller is also included.

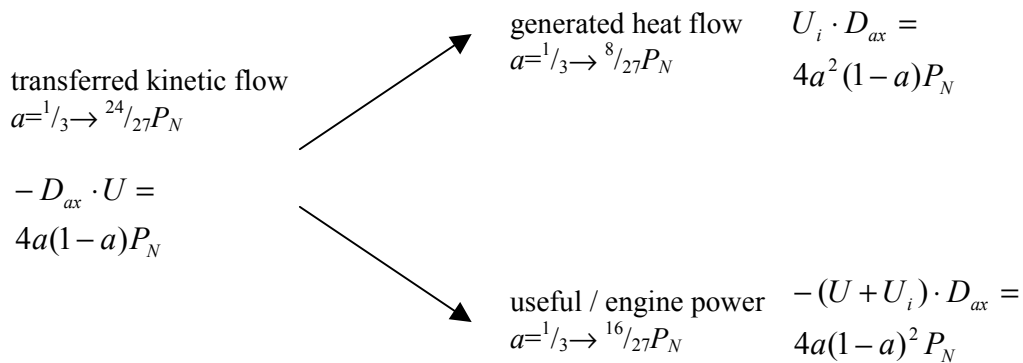


**figure 2.3** Schematic view of the kinetic energy transfer by an actuator disk.

For an actuator disk representing a rotor in hover ( $U=0$ ) it follows from equations 2.17 to 2.19 and from figure 2.3 that the power required to yield  $D_{ax}$  is  $U_i \cdot D_{ax}$  and that this power is entirely converted into heat. It first turns up as kinetic energy, which is eventually dissipated via turbulent mixing and viscous shear as heat. For an actuator in propeller state ( $U \geq 0$  and  $U_i \geq 0$ ), the engine power is  $(U+U_i) \cdot D_{ax}$  and the heat produced is  $U_i \cdot D_{ax}$  and the kinetic energy of the flow is increased by  $U \cdot D_{ax}$ . (The co-ordinate system is still attached to the actuator).

We conclude that the inherent limitation to the efficiency of energy extraction by an actuator disk is determined by dissipation as heat. This dissipation is  $a/(1-a)$  times the extracted useful energy. The heat capacity of the mass flow through a wind turbine is so large that the heat generated will hardly affect the temperature. To give an example: a wind turbine operating at 10 m/s at the Lanchester-Betz limit will transfer 44.4J of kinetic energy per unit of air mass into 29.6J of useful work and 14.8J of heat. This heat raises the temperature by only 0.015°C. In practice it will be even less since the heat generated is not limited to the flow inside the stream tube.

### Edge-Forces

Adding forces to the edges of the actuator disk has been proposed by Van Kuik [45]. These forces would transfer momentum without having an effect on the energy relations. In this way he explains a 10-15% increase of the velocity through the disk and at the same time a 1 degree increase of the angle of attack along the span of actual wind turbine blades. This proposal is therefore relevant to the present thesis.

Our heat-analysis implies that any measurement of the extracted, or fed, power based on the decrease of the total pressure (represented by the transferred kinetic power in the scheme) in the wake of a wind turbine depends on the position of measurement. If we measure the velocities induced by a rotor in hover, the sensors should be close to the rotor, otherwise the velocity pattern will be affected by dissipation or turbulent mixing. But, the closer to the rotor, the more the total pressure depends on the dynamics of the blade passages. This sets high demands on the sensors. On the other hand, if we want to know the total change of momentum from velocity measurements, the sensors should be far behind the rotor, in the far wake, since only there has the momentum exchange taken place fully. This difficulty can be illustrated by Van Kuik's interesting measurement on a rotor in hover [45]. Here the velocity sensors (hot-wires) were at  $0.5R$  behind the rotor, where the velocity discontinuity at the boundary of the slip stream is already vanishing or, in Van Kuik's words: '*Figure 4.10 (in his thesis) shows that the vortex cores are not visible any more as the vortex structure has desintegrated.*' We propose that the disappearance is due to turbulent mixing and viscous dissipation. If we estimate how much kinetic power was lost (by calculating the kinetic power by assuming that the velocity does not decrease up to the stream tube boundary and using Van Kuik's figure 4.8), we find this to be approximately 16%. So this is approximately the loss of total pressure flow at this position and it is as much as the effect to be validated. Besides to this we have uncertainty in the estimated momentum change Van Kuik tries to validate regarding the position of measurement and possible re-circulation.

We have shown however that any axial force, doing useful work or not, does transfer energy (for  $U \neq 0$ ) if the outer flow is included. This is not in contradiction with Van Kuik's proposed edge-forces *for an actuator disk*, which is in fact an extension of the proven theory on cylinder symmetric concentrators. However in practice, for a wind turbine without a cylinder

symmetric concentrator or tip-vanes [41], when we have a select number of blades, possible axial edge-forces at the blade tips acting on a certain span-wise flow would bend this flow in the direction of the forces according to state of the art induction theory (next section). So the flow aligns with the forces to some extent and subsequently the forces transfer energy, which is in contradiction with Van Kuik's concept. For this reason we used classic momentum theory (without edge-forces) in our simulations of rotor behaviour.

#### The $\frac{1}{2}$ Factor

The velocity at the actuator disk is assumed to be half the sum of that far upwind and far downwind (eq. 2.5). Only then were both the momentum and energy balance met. But in this energy balance only the kinetic energy was considered, while in fact all types of energy should be included. In the classic stream tube theory we assumed a uniform disk, which may not be true in practice. Near the centre of rotation, and near the tips, the velocity distribution immediately downwind of the rotor will not be uniform. Velocity differences will surely lead to viscous dissipation, in this case also between the rotor and the far wake. This heat should be included in the energy balance, otherwise the velocity at the location of the force, when calculated from the relation - force times local speed equals change of kinetic energy - will be too low. Lanchester [46] analysed the situation of a real rotor, where the tips are emitting vortices that contain kinetic energy, which will not remain in the fluid far downstream. But this energy had to be produced, so the transfer of kinetic energy is larger than eq. 2.12 for an actuator disk without tips. When the speed at the disk is calculated so that it includes the energy emitted by the vortices it should be higher than  $\frac{1}{2}$  of the sum of the velocity far upwind and far downwind. We did not include this argument in our further analysis, because it was not yet available in a quantitative form.

#### Practice

The above analysis does not put the Lanchester-Betz limit in a different light, since the maximum extractable useful energy of a wind turbine remains unchanged. But for a wind turbine park as a whole (present park optimisation studies are based on momentum balances and thus deal correctly with the dissipated heat), our model clarifies what determines the loss. And we conclude that the maximum extractable useful energy shall not occur when all turbines operate individually at maximum output. By choosing the induction factor 10% below the optimum, the power coefficient decreases less than 1%, while the efficiency rises more than 3%. In the turbulent wake state in particular, when  $a$  is approximately 0.4-0.5, the efficiency  $(1-a)$  becomes rather low, thus other wind turbines in the wake get a lower power input. This could be reason to operate turbines at the upwind side of a park below the optimum for  $a$ , and certainly not in the turbulent wake state, so that the production of the park as a whole increases.



## 2.2 Induction

In this section the concept 'induction' will be discussed. Induction takes the differences between a three-dimensional steady or unsteady situation of practice and the two-dimensional test situation in a wind tunnel into account. The concept is also used to derive the potential theoretical contribution to the drag force, which is the induced drag. It is useful therefore to start with definitions concerning induction in aerodynamics. Section 1 then deals with the induced velocities which were proposed by Prandtl for a finite airfoil. Section 2 discusses induction related to a wind turbine. Section 3 involves the classic blade element momentum theory.

### Induced velocities and vorticity

The velocity field around an aerodynamic object, which experiences forces perpendicular to the flow direction (lift forces), can be described mathematically by a vorticity distribution. But, vorticity is only a way to describe a velocity field, it is not the cause of the velocity field. Vortices do not induce velocities; they are equivalent to certain velocity patterns.

### Pressure distribution and velocity field

In inviscid flow, the flow field is determined by the Euler equation which describes the interaction between pressure distribution, external forces and velocity field and assumes that no internal friction (viscosity) exists. When an aerodynamic object is placed in a fluid in motion a pressure distribution over the surface of the object comes into being. This pressure distribution is in agreement with the velocity field around the object. The words 'in agreement with' were used to emphasise the *mutual interaction* between pressure distribution on the object and velocity field around the object instead of a *causal connection*. In summary: an object in combination with a flow causes a combination of a velocity field and a pressure distribution. The resulting velocity field can be described as the sum of the undisturbed fluid motion and the motion described by a vorticity distribution.

### Induced velocities in 'Prandtl-terms'

Vortices describe induced velocities, but only a specific portion of them are 'induction velocities' in Prandtl-terms. This portion accounts for the difference between the three-dimensional steady or unsteady practical situations and the 'two-dimensional steady' wind tunnel situation. The difference consists in general of three types of vortices, shown in figure 2.4. The first is the trailing vorticity of the tips of a finite airfoil (what BT induces at BB); the second the vorticity shed from the airfoil when the bound circulation changes over time (what PP induces at BB); and the third is the absence of the (shed) vorticity outside the span of the airfoil (what

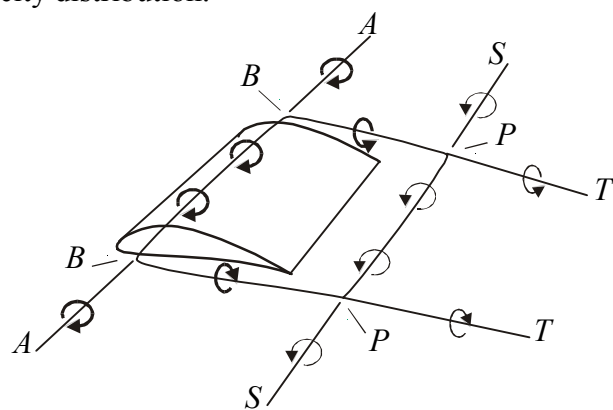


**figure 2.4** Prandtl's induction velocities.

SP, which is the shed vorticity of AB, induces at BB. This contribution does not exist in the 3d-situation, but is present in the 2d-situation. So the difference has to be corrected). For a precise definition of the third contribution we refer to Van Holten [41]. It is especially important for helicopter rotors with their strong variations in circulation with azimuth. In the case of a wind turbine it is normally sufficient to account for the tip vortices only. It should be noted that the velocity pattern described by the bound vorticity that was present in the wind tunnel is excluded from the induction velocities in 'Prandtl terms'.

### 2.2.1 Prandtl Finite Airfoil Induction

This section gives a summary of Prandtl's reasoning for obtaining a general expression for the induced drag of finite airfoils. The fact that lift is necessarily accompanied by induced drag was first pointed out by Lanchester; later Prandtl developed a rigorous system of mathematical equations which will be explained below. The text is based on the contribution of von Karmán and Burgers in [44].

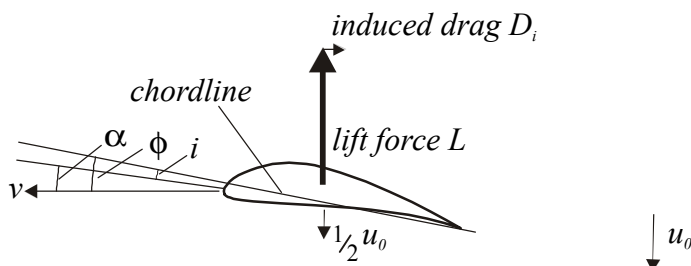


figure 2.5 Prandtl's finite airfoil.

When a finite airfoil of span  $2b$  exerts a lift force per unit span  $L$  on the flow, this force is balanced by an equal momentum change. If this change of momentum is confined to a certain area  $\Sigma$  per unit span perpendicular to the flow direction then it results in a downward velocity  $u_0$  which equals  $L/\rho v \Sigma$  (see figure 2.5). The downward motion is associated with a flow of kinetic energy per unit span.

$$P_{flow} = \frac{1}{2} \rho v \Sigma u_0^2 = \frac{L^2}{2 \rho v \Sigma} = D_i v. \quad (2.22)$$

This power per unit span is produced by the so-called induced resistance of the airfoil  $D_i$  per unit span. The power loss due to the motion of the airfoil times  $D_i$  equals the flow of kinetic energy of the downward flow per unit span, as was shown in equation 2.22. (We know that we should in fact account for the total power loss, thus also static pressure changes, kinetic energy changes in any direction and possibly heat produced.) It can be derived (see [44]) that  $\Sigma$  has the maximum value  $\pi b$ , when  $2b$  is the span of the airfoil. It follows that:

$$u_0 = \frac{L}{\rho v \pi b}. \quad (2.23)$$

This maximum corresponds to a minimum induced drag. The minimum drag and minimum drag coefficient read respectively:

$$D_i = \frac{L^2}{2 \rho v^2 \pi b}, \quad c_{di} = \frac{c_l^2}{\pi \lambda}, \quad (2.24)$$

in which  $c_l = L/(\frac{1}{2}\rho v^2 c)$  is the lift coefficient,  $c$  is the chord of the airfoil and  $\lambda = (2b)^2/bc$  is the aspect ratio. It is assumed that half of the downward velocity is imparted to the air before it reaches the airfoil and half is imparted after it has passed the airfoil. The same relation was found for the entire rotor (see equation 2.5). Lanchester explains this using the following argument for a fluid which is initially at rest:

*'Let  $m$  = the mass of fluid per second, and  $V$  its ultimate velocity; then  $mV^2/2$  is the energy or work done per second. And the momentum per second of the stream =  $mV$ , which is also the force by which the flow is impelled. And this force must (to comply with the energy condition) move through a distance per second, in other words act with a velocity  $U$  such that:'*

$$UmV = \frac{mV^2}{2}, \quad \text{or} \quad U = \frac{V}{2}, \tag{2.25}$$

Lanchester also proves the validity for any nonzero initial velocity; the change of the velocity where the force acts is given by half of the total change. It follows that the downward velocity at the airfoil  $u = \frac{1}{2}u_0$ . If we combine this velocity with the undisturbed velocity  $v$  we obtain the resultant velocity  $\sqrt{(v^2+u^2)}$  which is inclined under an angle  $\tan(i) = v/u$ . In practice  $u$  is much smaller than  $v$ , therefore the approximation  $i=v/u$  is acceptable. The conclusion is that the effective angle of incidence  $\alpha$  differs from the geometric angle of attack  $\phi$  by the angle  $i$ :

$$\alpha = \phi - i . \tag{2.26}$$

In summary: the inflow direction is inclined by an angle  $i$  compared to the geometrical inflow direction and thus the lift force has a component in the backward direction. This component equals the induced drag. The induced drag times the velocity of the airfoil equals the flow of kinetic energy in the downstream.

### 2.2.2 Induction for a Wind Turbine

This section deals with the induction of a wind turbine rotor and relates it to the above for a finite airfoil. It will be shown that the induced drag of wind turbine blades is implicitly taken into account in momentum theory.

#### Induced Drag

We will follow Prandtl's analysis for a finite airfoil to derive the induced drag for a wind turbine blade section. The situation is slightly more complicated due to the speed of flow itself starting with  $U$  instead of 0. Figure 2.6 gives an overview. Assume that the blade section has its own speed  $v$  and that the wind speed is  $U$ . The blade exerts a lift force per unit span  $L$  on the flow. The lift force is tilted forward under an angle  $\phi = \arctan(U/v) \approx U/v$ , if  $U \ll v$ .

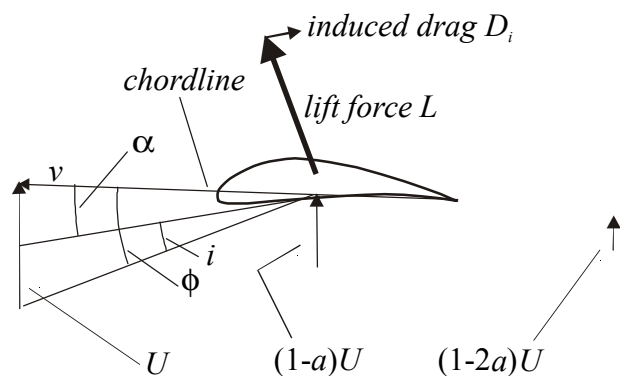


**figure 2.6** Induction for a wind turbine blade.

Thus the power extracted from the flow in this initial situation is  $L \cdot U$ , which has to be compared with 0 for Prandtl's finite airfoil. The lift force will be balanced by the change of momentum of the mass flow per unit span. This mass flow  $\dot{m}$  refers to the mass flow through the cross section  $\Sigma$  (and not to the indefinite flow referred to in 2.1.2). The resulting velocity change will be  $\Delta U = L / \dot{m}$ . The kinetic power of the inflow was  $\frac{1}{2} \dot{m} U^2$  and decreased to  $\frac{1}{2} \dot{m} (U - \Delta U)^2$  when passing the airfoil. Thus the kinetic power extracted from the flow per unit span  $P_{flow}$  is:

$$P_{flow} = \dot{m} U \Delta U - \frac{\dot{m} (\Delta U)^2}{2} = UL - \frac{L^2}{2\dot{m}}. \quad (2.27)$$

The expression on the right hand side follows after a substitution of  $\Delta U$  by  $L / \dot{m}$ . So, the power extracted by the lift force  $U \cdot L$  exceeds the power extracted from the flow by  $L^2 / (2\dot{m})$ . This error will be corrected by the introduction of the induced angle of attack  $i$ . The induced angle should tilt the lift force backwards until the power generated by the lift is decreased with the power surplus. Thus if we assume that  $i$  is small, then  $Lvi$  should equal  $L^2 / (2\dot{m})$ , or:

$$i = \frac{L}{2\dot{m}v} = \frac{\Delta U}{2v}. \quad (2.28)$$

It follows that the induced angle of attack decreases the geometric angle of attack by means of half the induced velocity in the far wake, in agreement with equation 2.5 of section 2.1.1 and with the argument of Lanchester. So the introduction of Prandtl's induced drag via the induced angle of attack  $i$  is equivalent to the effect of the induction factors in blade element momentum theory, which is described in the next section. This is not generally known. Reference is often made to Viterna and Corrigan [62] who propose a correction for the induced drag in addition to the effect of induction velocities calculated using blade element momentum theory. This means that they correct for induction twice.

### Aspect Ratio

The performance of a finite airfoil diminishes by a decreasing aspect ratio. The smaller the aspect ratio the larger the ratio of the lift force and the mass flow on which the force is exerted. So the velocity in the down flow increases and thus the induced drag. We should emphasise that the aspect ratio correction is equivalent to a correction for induction velocities. In fact the aspect ratio is just the geometric factor that determines the induced drag via  $c_{di} = c_l^2 / (\pi\lambda)$ . Thus it is already part of blade element momentum theory.

### 2.2.3 Blade Element Momentum Theory

This theory, sometimes referred to as strip theory, is W. Froude's [33]. It differs from momentum theory in that the forces on the flow are produced by the blades of a propeller, or wind turbine rotor, instead of an actuator disk. The theory, found in much of the literature [34, 63, 65], is based on the assumption that no interference exists between successive blade elements. In short, the theory offers a calculation scheme that iteratively brings the forces on the airfoil sections at a certain radial position into agreement with the momentum changes of

the flow through the annulus at that radial position. It yields both the forces and the axial and tangential induction factors  $a$  and  $a'$ . The axial force causes the flow to slow down by  $aU$  at the rotor disk and  $2aU$  in the far wake. The torque exerted by the flow on the rotor will cause the flow to rotate in the opposite direction with rotation speed  $a'\Omega$  at the rotor and  $2a'\Omega$  in the far wake.

One assumes a rotor with  $N$  blades and airfoil sections at radial position  $r$  with chord  $c$ . When the rotor speed is  $\Omega$  and the undisturbed wind speed  $U$ , the velocity component at the blade sections are:

$$U_{ax} = (1 - a)U, \quad U_{tan} = (1 + a')\Omega r. \quad (2.29)$$

The axial and tangential induction factors  $a$  and  $a'$  first get an initial value, for example 0. From these velocities the inflow conditions are obtained, namely the resultant velocity  $W$  and the angle of attack  $\alpha$  with

$$W = \sqrt{U_{ax}^2 + U_{tan}^2}, \quad \alpha = \arctan \frac{U_{ax}}{U_{tan}} - \beta, \quad (2.30)$$

where  $\beta$  is the blade pitch angle. Using tables for  $c_l(\alpha)$  and  $c_d(\alpha)$ , the lift  $L$  and the drag force  $D$  are found,

$$L = \frac{1}{2} \rho W^2 c_l N c \Delta r, \quad D = \frac{1}{2} \rho W^2 c_d N c \Delta r, \quad (2.31)$$

which can be expressed as an axial and tangential force

$$F_{ax} = L \cos \alpha + D \sin \alpha, \quad F_{tan} = L \sin \alpha - D \cos \alpha. \quad (2.32)$$

These forces should balance the axial and change of tangential momentum of the mass flow through an annulus of cross section  $2\pi r \Delta r$ :

$$2\pi r \Delta r U (1 - a) 2aU = F_{ax}, \quad 2\pi r \Delta r U (1 - a) 2a' \Omega r = F_{tan}. \quad (2.33)$$

In this way one can find a new estimate for  $a$  and  $a'$ , but these values are still based on the condition of undisturbed inflow. One has to go through this procedure a number of times to find more correct values for the forces and induction factors. By doing so for many radial positions and many wind speeds, the rotor performance can be calculated. The geometry can subsequently be changed until optimum performance is obtained. Relevant changes include the local pitch angle  $\beta$ , the chord  $c$ , the airfoil that determines the tables for  $c_l$  and  $c_d$  and the rotor speed.

Strip theory cannot deal with yawed conditions and wind shear, which often do occur in practice. It is therefore common practice to extend the calculation scheme by dividing the swept area not only in radial, but also in  $k$  azimuthal sections. The mass flow will decrease by  $1/k$  and the number of blades in an azimuthal section becomes  $N/k$ . Now the wind speed input can vary with altitude, to represent shear, and the relative direction of motion of the blades and the wind can be accounted for, to represent yaw.

## 2.3 Tip Correction

The flow through an actuator disk does not depend on azimuth. This disk is a theoretical concept, whereas in practice one has 2 or 3 blades on which the force is exerted. That force will therefore vary with time at any fixed azimuthal position. The smaller the ratio of the tip velocity and the wind velocity,  $\Omega R/U$ , and the fewer the blades, the greater becomes the pitch of the tip vortices and thus the variation of the induced velocities with azimuth. A correction for the non-uniform disk loading was proposed by Prandtl in 1919. It will be explained in the first section. The second section deals qualitatively with another tip correction that is required even in the case of the actuator disk.

### 2.3.1 Prandtl Tip Correction

This correction addresses the azimuthal non-uniformity of the disk loading. A small number of blades covering the entire swept area would not need the correction and an infinite number of blades in only one quarter of the swept area would need it.

Prandtl's model replaces the helices of trailing tip vortices with a series of parallel disks at a uniform spacing equal to the normal distance between successive tip vortices at the slipstream boundary (see figure 2.7). For the precise formulation reference is made to Glauert [34]. Glauert explains Prandtl's model as follows: *'In the interior of the slipstream the velocity imparted to the air by the successive sheets of this membrane will have important axial and rotational components but the radial component will be negligibly small. Near the boundary of the slipstream however, the air will tend to flow around the edges of the vortex sheets and will acquire an important radial velocity also.'*

The method of estimating the effect of this radial flow has been the following. A reduction factor  $f$  must be applied to the momentum equation for the flow at radius  $r$ , since it represents the fact that only a fraction  $f$  of the air between the successive vortex disks of the slipstream receives the full effect of the motion of these disks. If the induction factor  $a$  is defined as the value which applies when the blade passes, then the average induction factor will be  $af$ . At the locus of the blade the induction is  $aU$ , but on average the induction is  $afU$ . The momentum balance including the Prandtl tip correction yields the axial force:

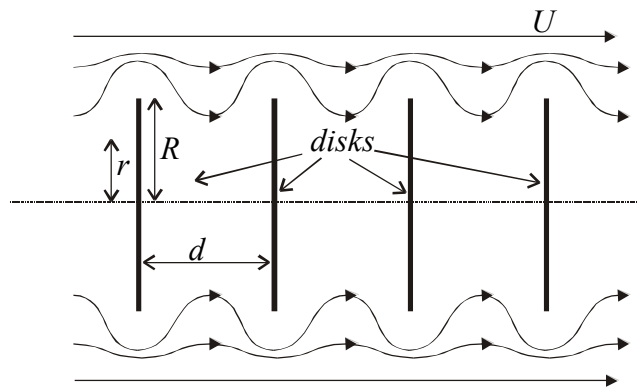


figure 2.7 Prandtl's solid disk model.

The momentum balance including the Prandtl tip correction yields the axial force:

$$D_{ax,r} = \rho A_r (1 - a_r f)_r U \cdot 2a_r f_r U \quad (2.34)$$

Here the index 'r' is added to the variables  $D_{ax}$ ,  $A$ ,  $a$  and  $f$ , in order to denote that they refer to an annulus and not to the entire rotor. The reduction factor  $f_r$  is found to be:

$$f_r = \frac{2}{\pi} \arccos \left( e^{\frac{-\pi(R-r)}{d}} \right), \quad (2.35)$$

with

$$\frac{\pi(R-r)}{d} = \frac{(R-r)NW}{2R(1-a)U}, \quad (2.36)$$

in which  $R$  is the blade radius and  $r$  is the radial position,  $d$  is the spacing between the solid disks,  $N$  is the number of blades and  $W$  is the resultant velocity. It can be seen that  $f_r$ , the tip correction, vanishes when  $N$ , the number of blades, becomes very large and we approach the theoretical concept of the actuator disk.

### 2.3.2 Tip Correction for an Actuator Disk

In theoretical treatments several definitions of the actuator disk are used. For example, Johnson [43] discusses both uniformly loaded and non-uniformly loaded actuator disks. In the case of the usually applied uniform load distribution on the disk, a pressure singularity exists at the edge of the disk. For an extensive study of this singularity we refer to Van Kuik [45]. Lanchester [46] already opposed this concept: *'At the edge it is manifestly impossible to maintain any finite pressure difference between the front and the rear faces'*. One would expect that the gradient from the high pressure side to the low pressure side, would drive the flow around the edges of the disk. This flow around the tip or edge has to exist even for an actuator disk representing a wind turbine with an infinite number of blades. It will equalise the

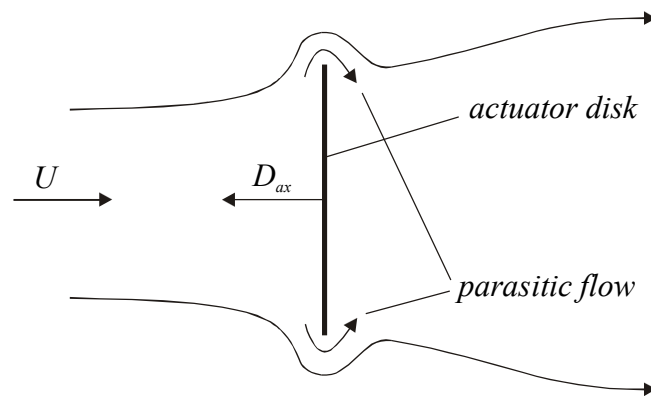


**figure 2.8** Parasitic flow around the actuator disk.

pressure discontinuity so that the loading per unit of surface on the disk decreases to zero when the edge is approached. The decrease of disk loading directly corresponds to a decrease of the extracted power. Therefore, the flow around the edges (see figure 2.8) is parasitic. It can be compared to the loss of lift of an airplane due to the span-wise flow around the tips. This loss of lift was originally called the tip correction for finite airfoils. It is discussed for example in Hoerner

[38] where the parasitic flow is accounted for via a reduction of the geometric blade span to an effective blade span. If we compare this situation to the case of a wind turbine, then it is expected that the wake will contract first behind the disk and then will rapidly expand again (see figure 2.7). Such a contraction has also been confirmed by experiments (see [60]).

It should be mentioned that the tip correction for rotors is, in the existing literature, entirely attributed to the effect of the finite number of blades. For example Johnson [43], Spera [57] and Glauert [34] attribute the tip correction wholly to the effect of a finite number of blades. In their theory the actuator disk has no loss of lift at the edges. A loss of lift at the tips of rotor blades is mentioned by Freris, but not worked out in his formulas for the tip correction [31].

So, two corrections for the tip of wind turbine blades can be distinguished. First that by Prandtl for the azimuthal variation of the induced velocity. Second a correction for the loss of lift and thus a loss of transferred power due to the span-wise/axial flow around the blade tips. The latter correction is also required for an actuator disk. It has been stated that the correction for the aspect ratio includes the tip correction [45], but this is not correct. The aspect ratio corrects for the induced drag, while the flow around the tips means that the geometric aspect ratio should itself be corrected to obtain a smaller effective aspect ratio. For a wind turbine this means that the physical diameter should be corrected to a somewhat smaller effective diameter.



## 2.4 Blade Aerodynamics

Presently it is still impossible to calculate the lift and drag characteristics of an airfoil accurately. Especially beyond the stall angle, the calculations can be off by tens of percents. For that reason airfoil characteristics still have to be determined in wind tunnels, under the assumption that in practice the airfoil will show the same behaviour as in a wind tunnel. But as shown in the preceding section, induction effects should be taken into account to make the field situation comparable to the wind tunnel situation. Section 2.5 will explain that also rotational effects need to be accounted for. This section deals with two-dimensional characteristics of airfoil sections, which involve angle of attack, lift, drag and stall. Figure 2.9 introduces the chord, the thickness and the camber of a profile; the camber line is the line with equal distance to the lower and the upper sides of the airfoil.

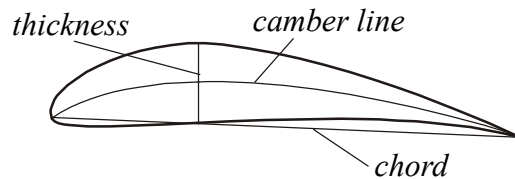


**figure 2.9** Definition of the chord, the thickness and the camber line of an airfoil.

### 2.4.1 The Angle of Attack

The two-dimensional steady angle of attack is defined as the geometric angle between the undisturbed stream lines and the chord line of the profile (figure 2.10). The lift force is by definition directed perpendicular to the undisturbed inflow direction. Undisturbed flow is defined as the flow without the influence of the profile. In two-dimensional steady flow the changes to the flow field are only induced by bound vorticity. It should be noted that the velocities induced by the bound vorticity are *not* part of induction velocities in 'Prandtl terms' (see section 2.2). The definition of the two-dimensional steady angle of attack is convenient in practice. In a wind tunnel the angle between the tunnel walls and the chord line almost equals the two-dimensional steady angle of attack (*almost*, since small corrections are required for the pressure distribution over the tunnel walls).

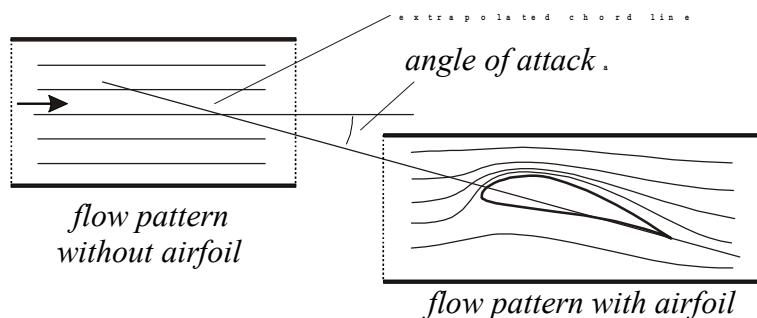


**figure 2.10** The 2d-steady angle of attack is the angle between the stream lines of the undisturbed flow on the left-hand side, with the chord line of the airfoil in two-dimensional flow on the right-hand side.

### 2.4.2 Lift and Drag

In two-dimensional steady flow the force exerted on an object consists of a component, perpendicular to the undisturbed flow, which is by definition the lift, and a component parallel to that flow which is by definition the drag. In the unsteady three-dimensional situations that occur in practice, these definitions refer to the direction of the sum of the undisturbed flow velocity and the induction velocities in Prandtl's terms. Lift is described in theory as the force exerted by a fluid flow on a bound vortex, given that the fluid flows perpendicular to the vorticity vector. The vorticity is defined as  $\boldsymbol{\omega} = \nabla \times \mathbf{v}$ . The total vorticity or circulation  $\Gamma$  in a surface  $S$  is the integral of the local vorticity over  $S$ :

$$\Gamma = \iint_S \boldsymbol{\omega} \cdot d\mathbf{S} = \oint_C \mathbf{v} \cdot d\mathbf{C} \quad (2.37)$$

The equivalence of the integral over the surface  $S$  and the integral along the closed curve  $C$  follows from Stokes' theorem. The difference between vorticity and circulation is, that vorticity is a property of an infinitesimal element of fluid, while circulation is an integral property. The physical meaning of circulation becomes clear when a line (hence a 2d-situation) of constant vorticity  $\boldsymbol{\omega}$  is considered. If  $C$  is a circle of radius  $r$  perpendicular to the line of vorticity in the centre, it follows that  $v = \Gamma / (2\pi r)$ . The lift force per unit length is related to the circulation and the inflow velocity via Joukowski's theorem:

$$L = \rho v \times \Gamma, \quad (2.38)$$

According to Joukowski's hypothesis, the effect of viscosity in the boundary layer is to cause precisely that circulation so that the stagnation point at the rear of the airfoil corresponds to the sharp trailing edge of the airfoil. For a description of this process reference is made to Batchelor [6]. Joukowski's hypothesis implies that the circulation around an airfoil under small inflow angles is almost proportional to this inflow angle. Airfoils have camber since it yields a slightly better performance regarding the lift over drag ratio. The camber also causes the lift curve of the airfoil to shift over a certain angle  $\alpha_0$ , which is the angle of attack at zero lift (see figure 2.11). Both the lift and drag per unit of span are conventionally given as dimensionless quantities after normalisation by the product of dynamic pressure and the chord  $c$  of the airfoil. The lift and drag coefficient are respectively defined by:

$$c_l = \frac{L}{\frac{1}{2} \rho v^2 c} \approx 2\pi(\alpha - \alpha_0), \quad c_d = \frac{D}{\frac{1}{2} \rho v^2 c}, \quad (2.39)$$

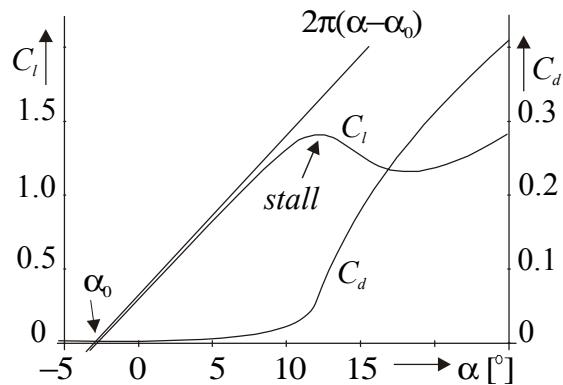


figure 2.11 Airfoil characteristics as function of the angle of attack ( $\alpha$ ).

where  $D$  is the drag force per unit span. Equation 2.39 presents the general expressions for the lift and drag coefficients and the theoretical value for the first of the situations of thin airfoils at small angle of attack. In practice the slope  $dc_l/d\alpha$  is approximately 5.7 instead of the theoretical  $2\pi$ . Typical relations for the lift and drag coefficients as a function of the angle of attack are presented in figure 2.11. In this figure it can be seen that in practice the lift curve deviates a great deal from the theoretical curve beyond approximately  $\alpha=10^\circ$ . The reason is that the flow on the suction side of the airfoil does not reach the trailing edge any more. At a certain distance from the trailing edge it comes to a standstill, causing reversal of the flow and separation. These effects, which will be explained in the next section, cause a loss of lift and a sudden increase of drag.

### 2.4.3 Stall

One sometimes holds [38] that 'an airfoil is said to stall when the lift decreases with increasing angle of attack'. But at angles beyond the stall angle, the lift first decreases and then increases again and develops a secondary maximum at an angle of attack of approximately  $\pi/4$ . Moreover under conditions of rotation the airfoil behaviour can change considerably and the  $L(\alpha)$  could even become a monotonous rising function up to an angle of attack of approximately  $\pi/4$ . And for example in [64] stall is again defined to be equal to boundary layer separation. This demonstrates that the term 'stall' is not clearly defined. The phenomena in the flow that cause the loss of lift have a clearer meaning. These phenomena are reversed flow and separation.

#### Separation and Reversed Flow

Separation refers to detachment of the boundary layer from the airfoil. The explanation for a two-dimensional situation is as follows. With increasing angle of attack the circulation increases and the suction peak near the leading edge becomes deeper. This means that the velocity just outside the boundary layer near the suction peak becomes very high. The suction peak is located near the stagnation point where the boundary layer is still very thin. Thus the velocity gradient in the boundary layer, and thereby the viscous shear stress, becomes very high. This viscous shear converts kinetic energy from the boundary layer flow into heat. When the flow has passed the suction peak, four quantities /effects will determine whether it will

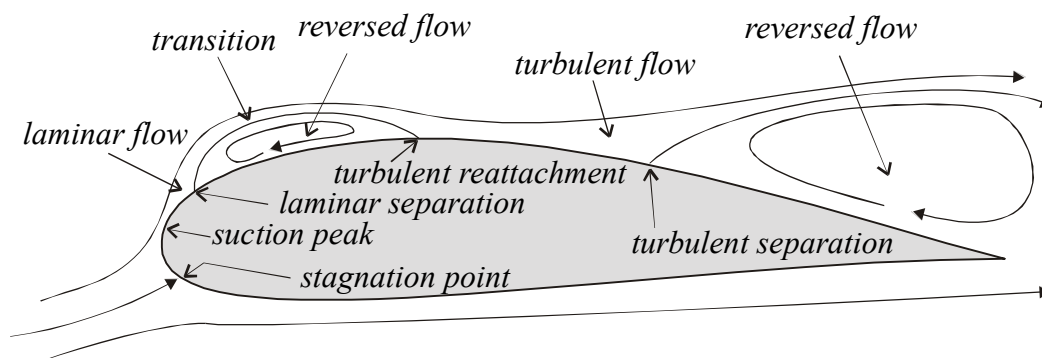


**figure 2.12** *Qualitative representation of separation types.*

reach the trailing edge. First, the remained speed (kinetic energy); second the trajectory of the viscous shear over the surface; third the trajectory of the adverse pressure gradient which decelerates the flow; and fourth the momentum that will be transferred from the main stream via viscous and turbulent stress in the boundary layer. The integral of the shear stress from the stagnation point to a certain position further downstream determines the kinetic energy losses. With increasing angle of attack the suction peak becomes deeper since the curvature of the flow around the leading edge increases. The deeper this suction the more kinetic energy is lost by shear, and at a certain angle the flow does not reach the trailing edge any more. At a certain position it comes to a standstill (not only on the surface but also above it; mathematically formulated this means that the velocity gradient normal to the wall is zero (see eq. 2.40)) and this position is called the separation line. The occurrence of two separation lines is possible in practice (see figure 2.12). Downstream from the separation line the pressure gradient accelerates the air towards the suction peak and this causes reversed flow.

Three types of separation can be distinguished. Two of them concern 'two-dimensional' flow and the third concerns the rotating case, to be discussed in section 2.5. The 'two-dimensional' types are leading edge separation and trailing edge separation.

#### Leading Edge Separation

This type of separation has two appearances: the long bubble and the short bubble. The long bubble type of leading edge separation and turbulent reattachment downstream, is a laminar separation type and gives a gradual decrease of the lift curve slope. The bubble grows with increasing angle of attack towards the trailing edge. It occurs on thin airfoil sections in combination with low Reynolds numbers  $< 5 \cdot 10^5$ . At higher Reynolds number this separation has less effect although the physical mechanism remains the same: laminar separation and immediate turbulent reattachment within the first 1% of the chord. Due to the condition of the low Reynolds number this separation type is not expected to be significant on rotors above 5m diameter.

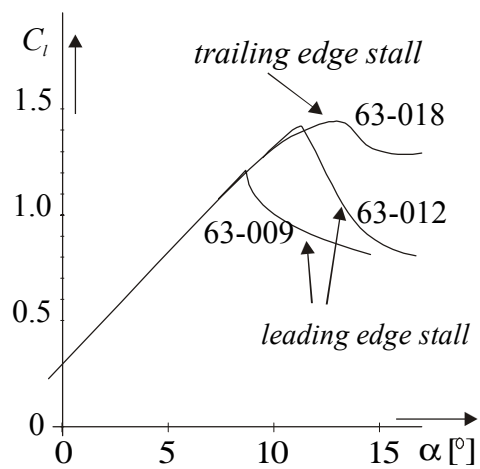


**figure 2.13** Different stall types for NACA airfoils at Reynolds  $5.5 \cdot 10^6$  [38]. The last two digits represent the thickness in percentage points of the chord.

A short bubble type can also be formed on the leading edge, which is quickly reattached. Above a certain angle of attack such bubbles suddenly burst and cause a sudden lift drop and drag increase. This occurs on thin airfoil sections with a round nose and low camber, for example the NACA 63-012 (see figure 2.13). Wind turbine blades in general have camber and are thicker, thus they probably will not suffer from this abrupt type of separation.

#### Trailing Edge Separation

The trailing edge type of separation is a gradual type of separation, which starts at the trailing edge and moves forward with increasing angle of attack. This occurs on thick or cambered airfoils with a round nose, which have a less deep suction peak, so the trailing edge becomes the preferential location for the onset of separation. This stall type is usually observed on

airfoil sections for wind turbine rotors in the wind tunnel. Airfoil sections for wind turbine blades range from 15% thickness to approximately 35% and the Reynolds number is approximately  $5 \cdot 10^6$  for a 1MW rotor of 60m diameter.

### Effective Airfoil Shape

The effective shape of an airfoil is the geometrical shape to which the displacement thickness has been added. This displacement thickness accounts for viscosity effects when the flow around the airfoil is described by Euler's potential theory. Important deviations between the lift characteristics of an airfoil and those predicted by potential theory occur when the displacement thickness becomes large, which corresponds to the occurrence of separation. As reversed flow is always the consequence of separation, the occurrence of reversed flow can be used to measure the onset of significant deviation of the lift curve slope. Thus the initial occurrence of reversed flow denotes the onset of large deviations from the theoretical lift  $2\pi(\alpha - \alpha_0)$ . With the stall flag technique we can observe such a beginning of trailing edge separation.

### Turbulent Separation

The boundary layer near the location of separation is often thought to behave as indicated in figure 2.14 [51]. Here, one streamline intersects the wall at the point of separation  $s$ . The location of  $s$  is determined by the condition that the velocity gradient normal to the wall vanishes there:

$$\left( \frac{\partial v}{\partial z} \right)_{wall} = 0, \quad (2.40)$$

in which  $z$  is the distance to the wall. This way of seeing things differs from the description given by Betz 1935 in [8]: *'Very often another phenomenon can be observed in the period of transition between normal and disturbed (separated) flow, the two states of affairs continually interchanging.'* Recently Simpson 1996 [55] came up with a more realistic model of turbulent separation. He argued that the criterion of the vanishing velocity gradient is too narrow for separation and that separation begins intermittently at a given location. The flow reversal occurs only a fraction of the time. At progressively downstream locations, the fraction of the time that the flow moves downstream is progressively less. Quantitative definitions were proposed on the basis of the fraction of the time that the flow moves downstream. Incipient detachment (ID) is defined as 1% of the time reversed flow, intermittent transitory detachment (ITD) as 20% of the time reversed flow and transitory detachment (TD) corresponds to 50% of the time reversed flow. ID corresponds to the practical situation in which flow markers such as tufts move occasionally in the reversed direction. The Simpson model agrees with stall flag observations described in this thesis (section 3.2.5) and is also confirmed by recent PIV observations in the wind tunnel [40].

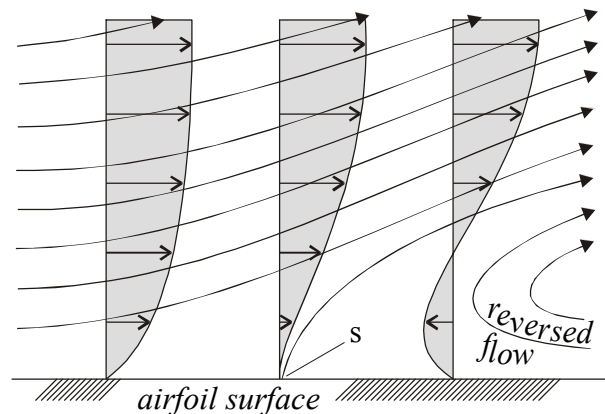


**figure 2.14** Diagrammatic representation of the boundary layer flow near the separation point [51].

## 2.5 Rotational Effects

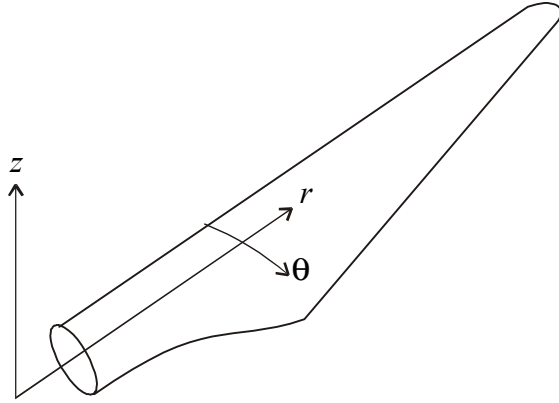


**figure 2.15** The blade in the rotating frame of reference.

This section deals with the effects of blade rotation on the aerodynamics.

### 2.5.1 Fundamental Equations in a Rotating Frame of Reference

When it is assumed that the flow about wind turbine blades is incompressible and that the viscous stress is linearly proportional to the velocity gradients, which are both generally accepted assumptions, the fundamental continuity equation and the Navier-Stokes equation for the velocity  $v$  read:

$$\nabla \cdot v = 0, \quad (2.41)$$

$$\frac{Dv}{Dt} = F - \frac{\nabla p}{\rho} + \frac{\mu}{\rho} \nabla^2 v. \quad (2.42)$$

Here,  $F$  is the external force per unit mass, and  $\mu$  is the dynamic viscosity, whereas  $p$  and  $\rho$  are as usual the pressure and the mass density of air.

To apply these equations to the situation of a rotating wind turbine blade, we will write them in cylinder co-ordinates. For the continuity equation this yields:

$$\frac{\partial v_\theta}{r \partial \theta} + \frac{\partial v_z}{\partial z} + \frac{\partial v_r}{\partial r} + \frac{v_r}{r} = 0, \quad (2.43)$$

and for the equations of motion in the direction of azimuth  $\theta$ , radius  $r$  and axis  $z$  (figure 2.15):

$$\frac{\partial v_\theta}{\partial t} + \frac{v_r \partial v_\theta}{\partial r} + \frac{v_\theta \partial v_\theta}{r \partial \theta} + \frac{v_r v_\theta}{r} + \frac{v_z \partial v_\theta}{\partial z} = F_\theta - \frac{\partial p}{\rho r \partial \theta} + \frac{\mu}{\rho} \left( \frac{\partial^2 v_\theta}{\partial r^2} + \frac{\partial v_\theta}{r \partial r} + \frac{\partial^2 v_\theta}{r^2 \partial \theta^2} + \frac{\partial^2 v_\theta}{\partial z^2} \right), \quad (2.44)$$

$$\frac{\partial v_r}{\partial t} + \frac{v_r \partial v_r}{\partial r} + \frac{v_\theta \partial v_r}{r \partial \theta} - \frac{v_\theta^2}{r} + \frac{v_z \partial v_r}{\partial z} = F_r - \frac{\partial p}{\rho \partial r} + \frac{\mu}{\rho} \left( \frac{\partial^2 v_r}{\partial r^2} + \frac{\partial v_r}{r \partial r} + \frac{\partial^2 v_r}{r^2 \partial \theta^2} + \frac{\partial^2 v_r}{\partial z^2} \right), \quad (2.45)$$

$$\frac{\partial v_z}{\partial t} + \frac{v_r \partial v_z}{\partial r} + \frac{v_\theta \partial v_z}{r \partial \theta} + \frac{v_z \partial v_z}{\partial z} = F_z - \frac{\partial p}{\rho \partial z} + \frac{\mu}{\rho} \left( \frac{\partial^2 v_z}{\partial r^2} + \frac{\partial v_z}{r \partial r} + \frac{\partial^2 v_z}{r^2 \partial \theta^2} + \frac{\partial^2 v_z}{\partial z^2} \right). \quad (2.46)$$

### Forces in the Rotating Frame of Reference

For an incompressible fluid with only one phase, the external forces in the inertial (non-rotating) reference system are usually zero. In practice the only external force is gravitational, but that force is balanced by the hydrostatic pressure gradient, so that both are left out of the equations. In a rotating frame the centrifugal and Coriolis forces appear. An observer on the blade notices radial and azimuthal accelerations on passing air elements  $d\tau$ . Therefore the centrifugal and Coriolis forces are real forces in the rotating frame of reference. If the angular velocity of the frame of reference is  $\Omega$  then the centrifugal force equals  $\rho d\tau \Omega^2 r$ . When the particle is moving in the rotating reference system with velocity vector  $\mathbf{v}$ , then the Coriolis force equals  $2\rho d\tau \Omega \times \mathbf{v}$ . The vector  $\Omega$  only has a  $z$ -component, and thus the Coriolis accelerations are:  $2v_r \Omega \theta_I - 2v_\theta \Omega r_I$ , in which  $\theta_I$  and  $r_I$  are the unit vectors in the  $\theta$  and  $r$ -direction respectively. They act on the mass element in addition to other inertial forces, which, however can be left out, as explained above. So, the Coriolis force acts in the  $\theta$ -direction and  $r$ -direction, and thus the first term on the right-hand side of equation 2.44 can be replaced by  $2\Omega v_r$ . As the centrifugal force works in the  $r$ -direction, the first term on the right-hand side of equation 2.45 can be replaced by a centrifugal contribution  $r\Omega^2$  and a Coriolis contribution  $-2v_\theta \Omega$ . In the above, it is assumed that the wing rotates in the  $r, \theta$ -plane given by  $z=0$ . But in practice the rotor blades have a small cone angle and therefore the tip rotates at a slightly negative value of  $z$ . The centrifugal and Coriolis force are thus assumed to work in the plane of the boundary layer. In short, the relevant external forces per unit of mass are:

$$F_\theta = 2\Omega v_r, \quad F_r = r\Omega^2 - 2\Omega v_\theta \quad \text{and} \quad F_z = 0. \quad (2.47)$$

### 2.5.2 Boundary Layer Assumptions

In the flow about rotating wind turbine blades the rate of downstream convection (in the  $\theta$ -direction) is much larger than the rate of transverse viscous diffusion, which means that viscosity only plays a significant role in a thin so-called boundary layer around the object. This insight will be used to estimate the order of magnitude of terms in equations 2.43-2.46. Terms of small order will then be neglected.

The thickness of the boundary layer can be estimated as follows. At the wall the velocity is 0 and at a certain distance, say  $\delta$ , perpendicular to the wall the flow velocity will be  $v_\theta$ . The velocity gradient perpendicular to the wall is therefore approximately  $v_\theta/\delta$  and the shear stress  $\tau \approx -\mu v_\theta/\delta$ . The derivative of this stress  $\partial\tau/\partial y$  equals the convective deceleration of the flow  $\rho v_\theta/r(\partial v_\theta/\partial\theta)$ , where  $\partial v_\theta/\partial\theta \approx v_\theta/(c/r)$  and  $c$  is the chord of the airfoil. Thus  $\partial\tau/\partial y = -\mu v_\theta/\delta^2 \approx \rho v_\theta^2/c$ , or  $\delta \approx \sqrt{(\mu c/\rho v_\theta)}$ , which is very small since  $\mu_{air} \approx 17.1 \cdot 10^{-6} \text{ Pa}\cdot\text{s}$ .

It follows that the shear layer of thickness  $\delta$  is small compared to the chord  $c=r\theta$ . The  $z$ -direction is perpendicular to the boundary layer where most velocity changes take place. The velocity derivatives in the  $z$ -direction are therefore relatively large:  $\partial v_\theta/\partial z$  is of the order  $v_\theta/\delta$ . Outside the boundary layer the second derivative of  $v_\theta$  in the  $z$ -direction is zero. Thus inside the boundary layer the second derivative equals the change of the first derivative, which was of the order  $v_\theta/\delta$ . Therefore the second derivative  $\partial^2 v_\theta/\partial z^2$  is of the order  $v_\theta/\delta^2$ . These results will be used to find the significant terms which yield the boundary layer equations.

### 2.5.3 Attached Flow on a Rotating Blade

For a wind turbine blade with attached flow, a typical value for the ratio of the tip speed  $\Omega R$  and the axial wind speed  $V$ ,  $\lambda = \Omega R / V$ , is approximately 7. That means that the inflow speed is close to the speed of the blade element itself being given by the radial position times the angular speed. This is true for radial positions  $r > R / \lambda$ , thus for approximately  $0.3R$  and larger. In this range the pressure distribution on the blade is roughly proportional to  $\frac{1}{2} \rho v_\theta^2$ , which is approximately  $\frac{1}{2} \rho \Omega^2 r^2$ . The radial pressure gradient will therefore be approximately  $\rho \Omega^2 r$  and due to this pressure gradient an element of air in the boundary will be accelerated in the radial direction with an acceleration of approximately  $\Omega^2 r$ . The given element will remain approximately  $c / v_\theta \approx c / (\Omega r)$  in the boundary layer and thus will develop a radial speed  $v_r$  of approximately  $\Omega^2 r c / (\Omega r) = \Omega c$ . Thus the order of magnitude of  $v_r$  is  $\Omega c$  and, in a similar way,  $\partial v_r / \partial z$  and  $\partial^2 v_r / \partial z^2$  are found to be of the order  $\Omega c / \delta$  and  $\Omega c / \delta^2$  respectively.

By substitution of  $v_\theta$  and  $v_r$  in the continuity equation and assuming  $r \gg c$  it follows that  $v_z$  is approximately  $\Omega r \delta / c$ , because it should balance the largest term which is  $\partial v_\theta / (r \partial \theta)$ . The table below lists all estimates:

parameter	estimate	parameter	estimate	parameter	estimate
$\delta$	$\sqrt{(\mu c / \rho v_\theta)}$	$p$	$\frac{1}{2} \rho \Omega^2 r^2$	$\partial p / \partial r$	$\rho \Omega^2 r$
$v_\theta$	$\Omega r$	$\partial v_\theta / \partial z$	$\Omega r / \delta$	$\partial^2 v_\theta / \partial z^2$	$\Omega r / \delta^2$
$v_r$	$\Omega c$	$\partial v_r / \partial z$	$\Omega c / \delta$	$\partial^2 v_r / \partial z^2$	$\Omega c / \delta^2$
$v_z$	$\Omega r \delta / c$	$\partial v_z / \partial z$	$\Omega r / c$		
$\Delta \theta$	$c / r$				

**table 1** Parameters and estimated orders of magnitude.

Now the Navier-Stokes equations can be written in terms of estimates instead of derivatives and unspecified forces. We will do so by giving the order of magnitude under each term. The order of magnitude of the pressure terms follows from the equations and is therefore set by the other terms. For the equation of continuity and those of  $\theta$ ,  $r$  and  $z$ -motion respectively, it follows that:

$$\frac{\partial v_\theta}{r \partial \theta} + \frac{\partial v_z}{\partial z} + \frac{\partial v_r}{\partial r} + \frac{v_r}{r} = 0 \quad (2.48)$$

$$\left( \frac{\Omega r}{c} \right) \left( \frac{\Omega r}{c} \right) \left( \frac{\Omega c}{r} \right) \left( \frac{\Omega c}{r} \right),$$

$$\frac{v_r \partial v_\theta}{\partial r} + \frac{v_\theta \partial v_\theta}{r \partial \theta} + \frac{v_r v_\theta}{r} + \frac{v_z \partial v_\theta}{\partial z} = 2 v_r \Omega - \frac{\partial p}{\rho r \partial \theta} + \frac{\mu}{\rho} \left( \frac{\partial^2 v_\theta}{\partial r^2} + \frac{\partial v_\theta}{r \partial r} + \frac{\partial^2 v_\theta}{r^2 \partial \theta^2} + \frac{\partial^2 v_\theta}{\partial z^2} \right) \quad (2.49)$$

$$(\Omega^2 c) \left( \frac{\Omega^2 r^2}{c} \right) (\Omega^2 c) \left( \frac{\Omega^2 r^2}{c} \right) (\Omega^2 c) \quad (set) \quad \frac{\mu}{\rho} \left\{ \left( \frac{\Omega}{r} \right) \left( \frac{\Omega}{r} \right) \left( \frac{\Omega r}{c^2} \right) \left( \frac{\Omega r}{\delta^2} \right) \right\}.$$

The last term in the last equation is much larger than the three preceding ones, since  $\delta \ll c, r$ , so that it is the only one of the viscous terms that needs to be retained. Further,



$$\begin{aligned} \frac{v_r \partial v_r}{\partial r} + \frac{v_\theta \partial v_r}{r \partial \theta} - \frac{v_\theta^2}{r} + \frac{v_z \partial v_r}{\partial z} = r \Omega^2 - 2v_\theta \Omega - \frac{\partial p}{\rho \partial r} + \frac{\mu}{\rho} \left( \frac{\partial^2 v_r}{\partial r^2} + \frac{\partial v_r}{r \partial r} + \frac{\partial^2 v_r}{r^2 \partial \theta^2} + \frac{\partial^2 v_r}{\partial z^2} \right) \\ \left( \frac{\Omega^2 c^2}{r} \right) (\Omega^2 r) (\Omega^2 r) (\Omega^2 r) (\Omega^2 r) (\Omega^2 r) \text{ (set) } \frac{\mu}{\rho} \left\{ \left( \frac{\Omega c}{r^2} \right) \left( \frac{\Omega c}{r^2} \right) \left( \frac{\Omega}{c} \right) \left( \frac{\Omega c}{\delta^2} \right) \right\}. \end{aligned} \quad (2.50)$$

Again the first three viscous terms are much smaller than the fourth term. Finally,

$$\begin{aligned} \frac{v_r \partial v_z}{\partial r} + \frac{v_\theta \partial v_z}{r \partial \theta} + \frac{v_z \partial v_z}{\partial z} = -\frac{\partial p}{\rho \partial z} + \frac{\mu}{\rho} \left( \frac{\partial^2 v_z}{\partial r^2} + \frac{\partial v_z}{r \partial r} + \frac{\partial^2 v_z}{r^2 \partial \theta^2} + \frac{\partial^2 v_z}{\partial z^2} \right) \\ \left( \frac{\delta \Omega^2 r}{c} \right) \left( \frac{\delta \Omega^2 r^2}{c^2} \right) \left( \frac{\delta \Omega^2 r}{c} \right) \text{ (set) } \frac{\mu}{\rho} \left\{ \left( \frac{\Omega \delta}{rc} \right) \left( \frac{\Omega \delta}{rc} \right) \left( \frac{\Omega \delta r}{c^3} \right) \left( \frac{\Omega r}{\delta c} \right) \right\}. \end{aligned} \quad (2.51)$$

Again the first three of the four viscous terms in the  $z$ -momentum equation can be neglected. In comparison with equations 2.49 and 2.50 all terms on the left hand side and the remaining viscous term are smaller by a factor of  $\delta/c$ . So, the entire  $z$ -momentum equation can be neglected with respect to the other equations and we obtain the steady boundary layer equations:

$$\begin{aligned} \frac{\partial v_\theta}{r \partial \theta} + \frac{\partial v_z}{\partial z} + \frac{\partial v_r}{\partial r} + \frac{v_r}{r} = 0 \\ \left( \frac{\Omega r}{c} \right) \left( \frac{\Omega r}{c} \right) \left( \frac{\Omega c}{r} \right) \left( \frac{\Omega c}{r} \right), \end{aligned} \quad (2.52)$$

$$\begin{aligned} \frac{v_r \partial v_\theta}{\partial r} + \frac{v_\theta \partial v_\theta}{r \partial \theta} + \frac{v_r v_\theta}{r} + \frac{v_z \partial v_\theta}{\partial z} = 2v_r \Omega - \frac{\partial p}{\rho r \partial \theta} + \frac{\mu}{\rho} \frac{\partial^2 v_\theta}{\partial z^2} \\ (\Omega^2 c) \left( \frac{\Omega^2 r^2}{c} \right) (\Omega^2 c) \left( \frac{\Omega^2 r^2}{c} \right) (\Omega^2 c) \text{ (set) } \frac{\mu}{\rho} \left( \frac{\Omega r}{\delta^2} \right), \end{aligned} \quad (2.53)$$

$$\begin{aligned} \frac{v_r \partial v_r}{\partial r} + \frac{v_\theta \partial v_r}{r \partial \theta} - \frac{v_\theta^2}{r} + \frac{v_z \partial v_r}{\partial z} = r \Omega^2 - 2v_\theta \Omega - \frac{\partial p}{\rho \partial r} + \frac{\mu}{\rho} \frac{\partial^2 v_r}{\partial z^2} \\ \left( \frac{\Omega^2 c^2}{r} \right) (\Omega^2 r) (\Omega^2 r) (\Omega^2 r) (\Omega^2 r) (\Omega^2 r) \text{ (set) } \frac{\mu}{\rho} \left( \frac{\Omega c}{\delta^2} \right). \end{aligned} \quad (2.54)$$

### The Analysis of Fogarty

Fogarty [30] further reduced this set of equations for the case of a rotating boundary layer. He argued that several terms are approximately  $(r/c)^2$  larger than other terms. At the root of wind turbine blades where  $r \approx c$ , all terms have the same order of magnitude, however at larger radial position, where  $r > c$ , even more terms can be neglected. It should be noted that the omission of these terms reduces the problem to a two-dimensional situation described by the continuity

and the  $\theta$ -momentum equations. The problem described by the two equations and the boundary conditions can be solved by any two-dimensional laminar boundary layer algorithm. The conclusions are that rotation does not influence attached flow and that the location of separation is not affected either. For that situation Fogarty described attached flow on rotating blades with only:

$$\frac{\partial v_\theta}{r\partial\theta} + \frac{\partial v_z}{\partial z} = 0, \quad (2.55)$$

$$\frac{v_\theta \partial v_\theta}{r\partial\theta} + \frac{v_z \partial v_\theta}{\partial z} = -\frac{\partial p}{\rho r\partial\theta} + \frac{\mu}{\rho} \frac{\partial^2 v_\theta}{\partial z^2}. \quad (2.56)$$

however, Fogarty noted that the small effects of rotation, predicted by the simple equations, were contrary to experience. He speculated that the engineer's observations concerned separated flow, that the effects might be larger on profiles with strong pressure gradients, that blade rotation might have more influence close to the tip and that rotational effects on a turbulent boundary layer might be more profound.

#### The Analysis of Banks and Gadd

In 1963 Banks and Gadd [5] found that rotation has a delaying effect on laminar separation. They assumed that the chord-wise velocity decreased linearly (by a factor  $k$ ) from the leading edge according to  $v_\theta = \Omega r(1-k\theta)$ . If the decrease of this velocity was very large ( $k \rightarrow \infty$ ), the rotation did not have an appreciable effect on separation. However, when the decrease was small ( $k < 0.7$ ) separation was postponed more than 10%, with the result that the pressure rise between the leading edge and the separation line was increased. Below a certain critical value for  $k$  ( $k \approx 0.55$ ) separation would never occur.

We do not think that this delay is an important phenomenon. To estimate the delay of separation we assume that velocity decreases linearly over the chord length. It then follows that  $k = r/c$ , which for wind turbine blades has a minimum value between approximately 2 and 4 at the maximum chord position. Since this is much larger than the above 0.7 or 0.55, the delay will be negligible in practice.

#### 2.5.4 Rotational Effects on Flow Separation; Snel's Analysis

In discussing the case of separated flow, Snel is implicitly using the following line of argument to find his model for separated flow on rotating blades [52, 53, personal communication]. His arguments refer to the boundary layer equations 2.52, 2.53 and 2.54.

A1 The fluid in the boundary layer is moving with the blade, thus  $v_\theta \ll \Omega r$ .

This means for the equation of motion in the  $\theta$ -direction that:

A2 The Coriolis term  $2v_r\Omega$  is larger than the co-ordinate curvature term  $v_r v_\theta / r$ .

A3 The viscous stress and the pressure gradient are small compared to the case of attached flow. The Coriolis term is dominant and should be balanced by the convective terms on the left-hand side.

And for the  $r$ -direction:

A4 The centrifugal force  $\Omega^2 r$  is dominant along with the radial pressure gradient, since the pressure is of the order  $\Omega^2 r^2$ .

A5 The convective term with  $v_r$  again is smaller than the other two convective terms; from the continuity equation it follows that the remaining terms with  $v_z$  and  $v_\theta$  are of the same order.

A6 The convective terms should balance the terms on the right-hand side, thus  $(v_\theta/r)(\partial v_r/\partial \theta) \approx \Omega^2 r$  and it follows that  $v_r \approx \Omega^2 r c / v_\theta$ .

Returning to the  $\theta$ -direction Snel argues that:

A7 The convective term  $v_r \partial v_\theta / \partial r$  should be much smaller than the Coriolis term.

A8 The remaining convective terms are of the same order. This is implied by the continuity equation. Since, if the terms with  $v_r$  are smaller than the other terms, these other terms yield  $v_\theta / c \approx v_z / \delta$ ; and by substituting  $v_z \approx v_\theta \delta / c$  in the convective term with  $v_z$  of equation 2.53 we see that the statement holds.

A9 It follows that  $v_\theta \partial v_\theta / (r \partial \theta)$  is of the order  $\Omega v_r$ , and  $v_\theta^2$  is of the order  $\Omega c v_r$ .

And for the  $r$ -direction Snel finds finally:

A10 By substituting the relation found in A9 in the  $r$ -momentum equation, it follows that  $v_\theta \approx \Omega c^{2/3} r^{1/3}$  and  $v_r \approx \Omega c^{1/3} r^{2/3}$ .

A11  $v_r / v_\theta \approx (r/c)^{1/3}$ , which agrees with A7.

A12 If  $c \approx r$ , then it follows that  $v_\theta \approx v_r$ ; when  $v_r \approx \Omega c^{1/3} r^{2/3} \approx \Omega r$  thus  $v_\theta \approx \Omega r$  which is in contradiction with the primary assumption; so the approximations are only valid for  $r/c \gg 1$ .

A13  $v_z \approx \delta \Omega c^{1/3} r^{-1/3}$ ; this follows from the substitution of  $v_r$  for  $v_\theta$  in the continuity equation, which yields  $\Omega c^{2/3} r^{-2/3} + \Omega r^{-1/3} c^{1/3} + v_z / \delta = 0$ .

parameter	estimate	parameter	estimate	parameter	estimate
$v_\theta$	$\Omega c^{2/3} r^{1/3}$	$p$	$\frac{1}{2} \rho \Omega^2 r^2$	$\partial p / \partial r$	$\rho \Omega^2 r$
$v_r$	$\Omega c^{1/3} r^{2/3}$	$\partial v_\theta / \partial z$	$v_\theta / \delta$	$\partial^2 v_\theta / \partial z^2$	$v_\theta / \delta^2$
$v_z$	$\delta \Omega c^{-1/3} r^{1/3}$	$\partial v_r / \partial z$	$v_r / \delta$	$\partial^2 v_r / \partial z^2$	$v_r / \delta^2$
$\partial \theta$	$c / r$	$\partial v_z / \partial z$	$v_z / \delta$		

**table 2** Parameters and orders of magnitude for separated flow according to Snel.

The estimated parameters are listed in table 2. They are used in equations 2.57, 2.58 and 2.59 for the boundary layer to find the order of magnitude for each term.

$$\frac{\partial v_\theta}{r \partial \theta} + \frac{\partial v_z}{\partial z} + \frac{\partial v_r}{\partial r} + \frac{v_r}{r} = 0 \quad (2.57)$$

$$\left( \Omega c^{-1/3} r^{1/3} \right) \left( \Omega c^{-1/3} r^{1/3} \right) \left( \Omega c^{1/3} r^{-1/3} \right) \left( \Omega c^{1/3} r^{-1/3} \right)$$

$$\frac{v_r \partial v_\theta}{\partial r} + \frac{v_\theta \partial v_\theta}{r \partial \theta} + \frac{v_r v_\theta}{r} + \frac{v_z \partial v_\theta}{\partial z} = 2v_r \Omega - \frac{\partial p}{\rho r \partial \theta} + \frac{\mu}{\rho} \frac{\partial^2 v_\theta}{\partial z^2} \quad (2.58)$$

$$(\Omega^2 c) (\Omega^2 c^{1/3} r^{2/3}) (\Omega^2 c) (\Omega^2 c^{1/3} r^{2/3}) (\Omega^2 c^{1/3} r^{2/3}) \text{ (set)} \frac{\mu}{\rho} (\Omega c^{2/3} r^{1/3})$$

$$\frac{v_r \partial v_r}{\partial r} + \frac{v_\theta \partial v_r}{r \partial \theta} - \frac{v_\theta^2}{r} + \frac{v_z \partial v_r}{\partial z} = r \Omega^2 - 2v_\theta \Omega - \frac{\partial p}{\rho \partial r} + \frac{\mu}{\rho} \frac{\partial^2 v_r}{\partial z^2} \quad (2.59)$$

$$(\Omega^2 c^{2/3} r^{1/3}) (\Omega^2 r) (\Omega^2 c^{4/3} r^{-1/3}) (\Omega^2 r) (\Omega^2 r) (\Omega^2 c^{2/3} r^{1/3}) (\Omega^2 r) \left( \frac{\mu}{\rho} \frac{\Omega^2 c^{2/3} r^{4/3}}{\delta^2} \right)$$

All terms of order  $(c/r)^{2/3}$  compared to the other terms become small when  $r \gg c$ . When they are neglected we get:

$$\frac{\partial v_\theta}{r \partial \theta} + \frac{\partial v_z}{\partial z} = 0, \quad (2.60)$$

$$\frac{v_\theta \partial v_\theta}{r \partial \theta} + \frac{v_z \partial v_\theta}{\partial z} = 2v_r \Omega - \frac{\partial p}{\rho r \partial \theta} + \frac{\mu}{\rho} \frac{\partial^2 v_\theta}{\partial z^2}, \quad (2.61)$$

$$\frac{v_\theta \partial v_r}{r \partial \theta} + \frac{v_z \partial v_r}{\partial z} = r \Omega^2 - \frac{\partial p}{\rho \partial r} + \frac{\mu}{\rho} \frac{\partial^2 v_r}{\partial z^2}. \quad (2.62)$$

The difference between this set of equations for separated flow and the set obtained by Fogarty for attached flow resides in the Coriolis term in equation (2.61). This term acts as a pressure gradient directing the flow towards the trailing edge. It should be noted that the neglect of terms in the case of detached flow is less justified than in the case of attached flow, since  $(c/r)^{2/3}$  decreases more slowly than  $(c/r)^2$ . Snel concludes that the parameters describing the difference between rotating and translating airfoils are  $\lambda r/R$  and  $c/r$  and that in the case of attached flow changes are expected for  $r \approx c$ , and that in the case of stalled flow at larger radii also.

The equations derived by Snel have been implemented in a program that solves the two-dimensional boundary layer equations. The calculated results have been compared with experimental data and both sets have been approximated by a single engineering result for the relation between the three-dimensional lift coefficient  $c_{l,3d}$  and the two-dimensional lift coefficient  $c_{l,2d}$ :

$$c_{l,3d} = c_{l,2d} + a \left( \frac{c}{r} \right)^b (2\pi(\alpha - \alpha_0) - c_{l,2d}), \quad \text{with } a = 3.1 \text{ and } b = 2, \quad (2.63)$$

here  $a$  and  $b$  are fitted parameters,  $\alpha$  is the angle of attack and  $\alpha_0$  is the zero lift angle.

Questions Concerning Snel's Model

In the next section we will present an alternative model and therefore we give here our motivations for our doubts about Snel's model. We have in fact 4 questions:

1. Can boundary layer theory be used in separated flow?
2. Is the order of partial velocity differentials such as  $\partial v_r / (r \partial \theta)$  equal to  $O(v_r/c)$ ?
3. What is the argument for neglecting the radial convective acceleration in the  $r$ -equation?
4. Is the model consistent?

ad. 1 To answer the first questions we will follow the example in Schlichting [51], page 24-26. Here the flat plate in parallel flow at zero incidence is analysed. The length of the plate is  $L$ , the undisturbed speed is  $U$ , (in the  $x$ -direction) the boundary layer thickness  $\delta$ . In the boundary layer, *which has not separated*, the main physical argument is that the frictional forces are comparable to the inertia forces. The velocity gradient in the flow direction  $\partial u / \partial x$  is proportional to  $U/L$ , hence the inertia force  $\rho u \partial u / \partial x$  is of the order  $\rho U^2/L$ . The velocity gradient perpendicular to the wall is of the order  $U/\delta$ , so that the friction  $\mu \partial^2 u / \partial x^2$  is proportional to  $\mu U / \delta^2$ . Since friction and inertia forces are comparable we get:  $\mu U / \delta^2 \approx \rho U^2/L$ . the separated area.

Now we ask what happens when the flow over the plate separates due to a positive pressure gradient. We return to our co-ordinates system where  $r\theta$  compares to the  $x$ -direction and  $v_\theta$  can be compared with  $U$ . Then the velocity has decreased due to friction and due to the pressure gradient until it comes to a standstill at the separation line. Beyond this point the pressure gradient drives the air backwards. Therefore at the separation line the flow must move away normal to the wall and separates. By definition the speed in the  $\theta$ -direction has become 0 here and the velocity gradient perpendicular to the wall is 0 too. Therefore, when approaching the stagnation line and beyond it in the separated area, the boundary layer assumptions no longer apply. Id est: the inertia force  $\rho v_\theta \partial v_\theta / (r \partial \theta)$  ( $\rho u \partial u / \partial x$  for the flat plate) can no longer be estimated using  $\rho v_\theta^2/c$  ( $\rho U^2/L$  for the flat plate) and, since the velocity gradient is small the frictional forces become negligible. So we showed that boundary layer theory is invalid, both in separated flow and when approaching separation. This is also mentioned in literature on separated flow [41, 64].

ad. 2 In figure 2.16 we plotted the chord-wise and radial velocity over a separated airfoil. In boundary layer theory one may estimate the order of magnitude of the chord-wise velocity gradient from  $\partial v_\theta / r \partial \theta = O(v_\theta/c)$ , but

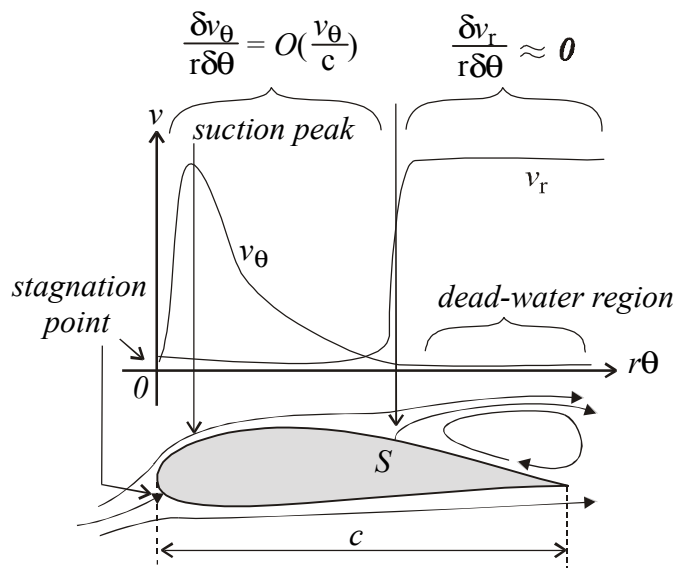


**figure 2.16** In separated flow, estimation of the order of magnitude such as used in boundary layer theory is invalid.

only in attached flow. In separated flow this may give errors. For example the order of the partial velocity gradient  $\partial v_r / (r \partial \theta)$  cannot be estimated by  $O(v_r/c)$ , with the argument that the radial speed is approximately  $v_r$  inside the separated area and approximately 0 outside the separated area. Snel's analysis uses such estimates for the second and fourth term of equation 2.59. In fact, when the partial derivative is estimated *inside* the dead-water region, we find  $\partial v_r / (r \partial \theta) \approx 0$ .

One might come up with the statement that the *order* of the partial derivatives in the dead-water region is still equal to that in the attached region, although the *magnitudes* are very different. However to reduce the Navier-Stokes equations we assume that the smaller terms can be neglected. The order of a term is not only decisive for its magnitude, the coefficient is also important. Snel's analysis is based on orders only.

ad. 3 In Snel's model the convective term with  $v_r$  is smaller than the other terms (A5), but the argument for this is lacking. In our model this term appears to be dominant.

ad. 4 In Snel's model  $\theta$ -equation leads to  $v_\theta^2 = O(\Omega c v_r)$  (A9). Then from the  $r$ -equation he has no reason (see ad. 3) to assume that any acceleration term is off smaller order than  $O(\Omega^2 r)$  so that  $v_r \partial v_r / \partial r = O(\Omega^2 r)$  and thus  $v_r = O(\Omega r)$ . If we substitute this in the term  $v_\theta \partial v_r / (r \partial \theta)$  of the  $\theta$ -equation, it follows that  $v_\theta = O(\Omega c)$ . However, the group of estimates obtained,  $v_r = O(\Omega r)$ ,  $v_\theta = O(\Omega c)$  and  $v_\theta^2 = O(\Omega c v_r)$ , is inconsistent.

### 2.5.5 Rotational Effects on Flow Separation; Our Analysis

Snel's model gave the first estimate of three-dimensional effects in stall, which have been valuable understanding rotor behaviour. The reason for an alternative model was to include the often observed and intuitively expected radial flow, which is not dominant Snel's model. Our model is valid in the separated flow and shows that the separated air flows in a radial stream with  $v_r$  as the dominant velocity. Furthermore, the new model is not based on the boundary layer theory: we use the full set of equations and do not use the property of boundary layers in which partial velocity gradients can be estimated with the ratio of differences, such as  $\partial v_r / (r \partial \theta) \approx (v_r/c)$ , which is invalid in separated flow. The model describes the separated flow on rotating blades without any effect of viscosity, which seems to be a paradox. However by studying the physics of flow separation this becomes clear. Separation occurs because the air is coming to a standstill in the main flow direction due to friction and the positive pressure gradient. Then in 2d-flow, beyond the point of separation, a dead-water region is formed. Here the frictional forces are negligible and the accelerations and the pressure gradients are small, which is illustrated by figure 3.20. Some back-flow will cause the flow to move normal to the wall at the separation line. In 3d-flow however, we have still the situation that the flow comes to a standstill in the chord-wise direction and separates due to the back-flow at a slightly larger chord-wise position. As in 2d-flow, near and beyond the stagnation line, the gradient of the chord-wise velocity normal to the wall is very small or even zero, so viscous effects and chord-wise accelerations are negligible, otherwise separation would not have occurred. This means that the pressure gradient and the Coriolis force must balance in the 3d-separated area. The difference with the 2d-situation is that a *radial* pressure gradient and a *radial* external force are also present and accelerate the separated flow in the radial direction.

Heuristics of Flow Separation about Rotating Blades

- B1 Due to viscous drag and the positive pressure gradient some air in the boundary layer will be decelerated in the chord-wise direction so that it becomes detached.
- B2 In the separated area the 'boundary layer is thick', so that the velocity gradients are small. In this case the role of viscosity becomes less important and the equations become of the Euler type.
- B3 When the flow has separated, it has come to a standstill in the chord-wise direction, and the chord-wise velocity and velocity gradient normal to the wall are small. So the chord-wise acceleration and the frictional forces are small too. Since other large chord-wise forces exist, namely the chord-wise pressure gradient and the Coriolis forces, they must be balancing.
- B4 In the absence of a thin layer with large velocity gradients, partial derivatives in the  $z$ -direction will not be much different from those in the other directions.
- B5 The centrifugal acceleration and the radial pressure gradient drive the separated air in the radial direction. The first acceleration is  $\Omega^2 r$  and the second depends on the span-wise variation of the angle of attack and of  $\lambda_r$ , but will be of the same order.
- B6 Separated air moving over the blade in the radial direction can enter attached flow at a larger radial position and thereby advances stall to a certain extent, but eventually it will leave the blade in the  $\theta$ -direction (figure 2.17).
- B7 The above radial flow experiences three chord-wise forces: the Coriolis force acting towards the trailing edge, the chord-wise pressure gradient acting towards the leading edge and a turbulent mixing stress as a result of the interaction of the chord-wise flow above the boundary layer with the radial flow. The latter effect forces the flow towards the trailing edge.
- B8 The turbulent mixing shear on the upper side of the separated flow is comparable to that of the two-dimensional case. And in that case it is negligible since the pressure distribution is flat in the separated area (see for example figure 3.20).
- B9 *The remaining counteracting chord-wise forces (Coriolis and pressure gradient) are stabilising pure radial outflow, otherwise the flow could not have separated (B3).*
- B10 The chord-wise Coriolis acceleration is constant over the chord, which means that the chord-wise pressure gradient should be constant. *This predicts a triangular shape for the pressure distribution in the separated area, as observed in experiments [9].*
- B11 The radial flow of separated air is fed at the blade root but also from both the leading edge and trailing edge. These sources are hard to quantify but their effect will be large. For this reason we cannot neglect any term in the continuity equation.
- B12 In this model the  $z$ -direction is only relevant for the control of the chord-wise pressure gradient via the displacement thickness and thus  $v_z$  remains small.

Mathematical Description of the Model

The stream of separated air is of the order of the chord in the  $\theta$ - and  $z$ -direction and as long as the blade in the radial direction. Its flux can therefore not be described by the boundary layer equations. We have to start with the complete set of fundamental equations 2.43 to 2.46. B2 suggests that terms with viscosity can be neglected. B3 implies that the chord-wise velocity can be neglected in the separated area, which is reason to neglect all terms with  $v_\theta$  except that in the continuity equation. B4 is reason to neglect the remaining  $z$ -derivatives in equations 2.45 and 2.46. We further assume that the flow is steady and that the external mass forces given by equation 2.47 are relevant. Using these approximations it follows that in equation 2.46, the term  $v_r \partial v_z / \partial r$  is the only convective term left and the entire equations is of smaller

order than the continuity equation and equations 2.44 and 2.45. The latter two remain in a much reduced form:

$$\frac{\partial v_\theta}{r\partial\theta} + \frac{\partial v_z}{\partial z} + \frac{\partial v_r}{\partial r} + \frac{v_r}{r} = 0, \quad (2.64)$$

$$\frac{\partial p}{\rho r \partial \theta} = 2v_r \Omega. \quad (2.65)$$

It follows from equation 2.65 that the chord-wise pressure gradient is a constant in the chord-wise direction if the radial velocity is constant in this area. This explains the often observed triangularly shaped pressure distributions.

$$\frac{v_r \partial v_r}{\partial r} = r\Omega^2 - \frac{\partial p}{\rho \partial r} = r\Omega^2 (1 - c_p - r \frac{\partial c_p}{2\partial r}) \quad (2.66)$$

It should be noted that equation 2.66 for the motion in the  $r$ -direction retains precisely the term  $v_r \partial v_r / \partial r$  that was neglected in Snel's model (see equation 2.62). Moreover Snel's continuity equation does not contain the terms with  $v_r$ , which are thought to be relevant in the present model.

This extremely simple model is useful for identifying the leading terms. To obtain a first estimate,  $p$  was substituted by  $\frac{1}{2}\rho\Omega^2 r^2 c_p$  in equation 2.66. Coefficient  $c_p$  will vary from almost 0 at the trailing edge to a value  $c_{p,sep}$  at the separation line. ( $c_{p,sep} \approx -3$  estimated from pressure distributions in reference [3]). We assume that  $\partial c_p / \partial r = 0$  and that separation is initiated at the trailing edge and find that:

$$v_r = r\Omega \sqrt{1 - c_p} \Rightarrow \Omega r < v_r < 2\Omega r, \quad (2.67)$$

so  $v_r$  is approximately  $\Omega r$  at the trailing edge to approximately  $2\Omega r$  at the separation line. This can be substituted in the equation for the  $\theta$ -direction in which  $p$  is also substituted by  $\frac{1}{2}\rho\Omega^2 r^2 c_p$ . If the air is separated over a fraction  $f$  of the chord, the chord-wise pressure gradient and the increase of the pressure coefficient at the stagnation line are restricted by:

$$\frac{4}{r} < \frac{\partial c_p}{r \partial \theta} < \frac{8}{r} \quad \text{or} \quad \frac{-4fc}{r} > \Delta c_p > \frac{-8fc}{r}. \quad (2.68)$$

This equation describes the decrease of the pressure from the trailing edge towards the separation line. If we assume that the pressure coefficient is 0 at the trailing edge, it equals approximately  $\Delta c_p$  at the separation line. In case of two-dimensional stall the pressure coefficient remains almost constant between the trailing edge and the stagnation line. Thus due to rotation the pressure coefficient in the separated area is on the average  $\Delta c_p / 2$  higher and the lift coefficient of the section increases by:



$$\Delta c_l = \frac{\Delta c_p f}{2} \text{ or } \frac{2f^2 c}{r} < \Delta c_l < \frac{4f^2 c}{r}. \quad (2.69)$$

We predict a linear decrease of the pressure from the trailing edge to the separation line, whereas in the case of two-dimensional flow that is constant in the separated area. In our view the adverse pressure gradient which causes separation is therefore lower. As a result of this, the separation line will be closer to the trailing edge compared to 2d-flow; this reduces the wake of the blade and less drag will be experienced.

### Orders of Magnitude

In our model we found that  $v_r \approx \Omega r$  and when we substitute this in the continuity equation we find that  $v_\theta \approx v_z \approx \Omega c$ . This can physically be interpreted as follows: mass conservation demands that the radial stream which accelerates in the radial direction, should contract in the other directions. If we substitute the estimates of the velocities in equations 2.48 to 2.51 (were we neglected the viscous terms), it follows that the system is consistent. All terms on the left-hand side of 2.49 are approximately  $\Omega^2 c$ , while the ones on the right hand side are approximately  $\Omega^2 r$  (the pressure term should equal the Coriolis term since that is the only one left!). In equation 2.50 the terms  $v_r \partial v_r / \partial r$ ,  $r \Omega^2$  and  $-\partial p / (\rho \partial r)$  are approximately  $\Omega^2 r$ , the term  $2v_\theta \Omega$  is approximately  $\Omega^2 c$ , the term  $v_\theta^2 / r$  is approximately  $\Omega^2 c^2 / r$  and the terms  $v_\theta \partial v_r / (r \partial \theta)$  and  $v_z \partial v_r / \partial z$  are approximately 0. To understand the last estimate we use our argument that  $\partial v_r / (r \partial \theta)$  cannot be approximated with  $v_r / c$  (see section 2.5.2, ad.2). Our model is valid *inside* the separated area where  $v_r$  is almost constant and the gradient is approximately 0.

### 2.5.6 Extension of the Heuristics with $\theta$ -z Rotation

The separated air above the blade will, according to the no-slip condition at the wall, form a boundary layer with a much lower radial velocity. Since this radial velocity gives rise to the Coriolis force directed towards the trailing edge this force is much reduced while the pressure gradient accelerating the flow towards the leading edge will be impressed on the boundary layer. So close to the wall the flow will accelerate towards the leading edge. At the upper side of the separated area the flow will move towards the trailing edge due to the turbulent mixing stress with the main flow. These effects will cause the flow in the separated area to spin around an axis parallel to the blade axis (next to the radial acceleration described in the section above). We call this spinning motion  $\theta$ -z rotation and deal with it as if it were independent of the above set of equations 2.64, 2.65 and 2.66.

- B13 Turbulent mixing on the upper side of the separated stream adds chord-wise momentum. The chord-wise pressure gradient acts on the entire separated stream and balances the Coriolis force and the chord-wise stress due to the turbulent mixing. This means that air in the separated stream near the blade surface is driven towards the leading edge, and the air at the upper side of the separated stream will accelerate towards the trailing edge. As a result, the air will be spinning (see figure 2.17).
- B14 The spinning motion takes places in the  $\theta$ ,  $z$ -plane so that the boundary layer equations cannot describe it: it requires the equation of motion in the  $z$ -direction.
- B15: The spinning motion in the separated stream implies that the radial velocity in the radial stream becomes more or less uniform.

B16: A negative pressure gradient towards the centre of the spinning motion is also required to produce the required centripetal forces.

Mathematical Model for  $\theta$ -z Rotation

The spinning motion can be described with the pressure gradients responsible for the centripetal force and the balancing convective acceleration terms. If we restrict ourselves to the terms required for spinning motion, we get for continuity and the  $\theta$  and the  $z$ -equations of motion respectively:

$$\frac{\partial v_\theta}{r\partial\theta} + \frac{\partial v_z}{\partial z} = 0, \tag{2.70}$$

$$\frac{v_z \partial v_\theta}{\partial z} = -\frac{\partial p}{\rho r \partial \theta}, \tag{2.71}$$

$$\frac{v_\theta \partial v_z}{r \partial \theta} = -\frac{\partial p}{\rho \partial z}. \tag{2.72}$$

The  $\theta$ -z rotation is a mechanism that is assumed to be insignificant compared to the radial flow effects described by equations 2.64 and 2.66. However, in this thesis the existence of the  $\theta$ -z rotation is important because this phenomenon is responsible for the signal of stall flags with hinges parallel to the blade axis.

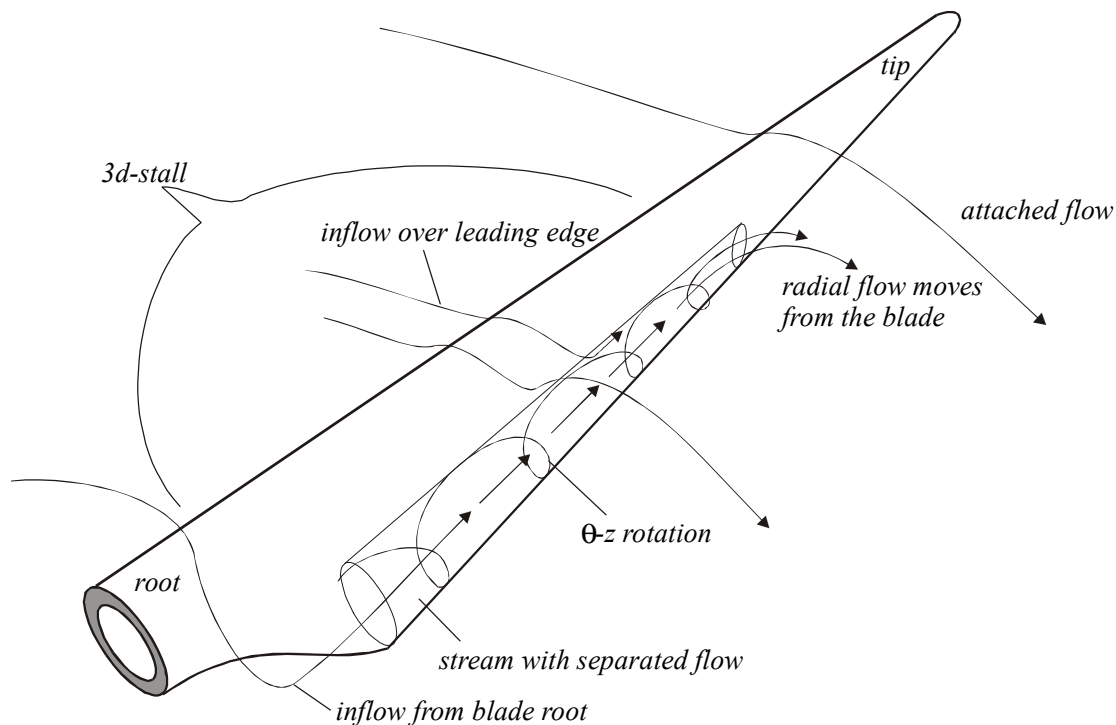


**figure 2.17** Heuristic model on the stream of separated air and the  $\theta$ -z rotation.

### Discussion of the Models on Separation

If we compare the above analysis with Snel's, the main differences are the role of radial flow and the inviscid approach. We think the radial flow is dominant because the equilibrium between Coriolis acceleration and chord-wise pressure gradient (the condition for separation) cannot give chord-wise motion. Snel's model is based on boundary layer theory, but this is not valid as we showed and as is mentioned in standard literature. It gives errors, since most partial differentials of acceleration terms were linearised to find the orders of magnitude, which is not justified. As a consequence, in Snel's model the radial convective acceleration is neglected and the other convective terms are estimated to be large. In our model, using the condition of separation, the other two convective terms are neglected and the radial convective term is the largest. The dominant role of the radial motion of separated air has been confirmed with laser Doppler measurements [10].

We neglect the viscous terms by arguing that the separated layer is thick, so we reach outside the range of validity of the boundary layer concept. The extension of our model with the  $\theta$ - $z$  rotation required terms from the Navier-Stokes equations, which are not part of the boundary layer equations.

The terms we select yield a simpler set of equations, which can even be solved analytically. We predict the increase of the lift coefficient to be proportional to  $c/r$ , which agrees with Sorensen's computational results [56]. The model also explains the triangular shape of pressure distributions on rotating blades in stall analytically [9].



### 3. The Stall Flag Method

The stall flag method is a newly developed technique by which the flow direction over an aerodynamic object can be visualised. The method is particularly useful for the visualisation of flow separation. It is comparable to flow visualisation with tufts, the tufts being replaced by the so-called stall flags. Figure 3.1 shows the application of the stall flags to a commercial wind turbine. The figure demonstrates the most relevant difference between flow visualisation with stall flags and with tufts: the visibility of stall flags is orders of magnitude better. The stall flag is a detector with a binary output signal. An optically contrasting surface (in most cases a retro-reflector) can be either visible or invisible depending on the flow direction over the stall flag. A bright light source illuminates the entire swept area of the turbine and all exposed retro-reflectors return the light to the source. An observer or (video) camera can see or record the signals even from a kilometre's distance. In practical application the stall behaviour of large commercial wind turbines can be analysed with approximately 200 stall flags installed on the rotor blades. The signals are recorded while operational conditions such as rotation speed and yaw angle are varied. From these recordings the stall behaviour of a wind turbine rotor can be determined in detail.

This chapter will deal with the method from an aerodynamic point of view in conjunction to the technical development of the stall flag. We begin with that development. In section 2 we consider the interpretation of stall flag behaviour, in section 3 the flow disturbance by that stall flag. Then in section 4 the stall flag will be compared to the tuft. For all the optical aspects of the method we refer to the next chapter.



**figure 3.1** *Application of the stall flag method to the NEG Micon 700/44m at Tehachapi, Ca. USA.*

## List of Symbols

$a$	[m]	amplitude of the sinusoidal flap deformation
$b$	[m]	width
$c$	[m]	chord
$c_d$	[-]	drag coefficient
$c_l$	[-]	lift coefficient
$c_{l,max}$	[-]	first maximum of lift coefficient
$c_t$	[-]	tangential force coefficient
$c_{t,TES}$	[-]	average tangential force coefficient during trailing edge separation
$d$	[m]	height of separated air above surface
$D$	[m]	rotor diameter
$E$	[N/m <sup>2</sup> ]	Hooke modulus of elasticity for flap material
$f$	[rad]	flap opening angle
$F_1$	[N]	force on flap due to reversed flow
$F_2$	[N]	force on flap due to main flow
$F_3$	[N]	thrust force due to stall flag
$F_{cp}$	[N]	centrifugal force on the flap
$\mathbf{f}$	[m]	vector in flap plane perpendicular to the hinge line
$g$	[m/s <sup>2</sup> ]	gravitational acceleration
$h$	[m]	height of the flap
$\mathbf{h}$	[m]	hinge vector
$\mathbf{i}$	[m]	inflow direction vector
$k$	[-]	dimensionless stall flag response
$I$	[kgm <sup>2</sup> ]	moment of inertia of the flap
$I_a$	[m <sup>3</sup> ]	second moment of area per unit width of the flap
$l$	[m]	tuft length
$m_a$	[kg/m <sup>2</sup> ]	mass per unit area of the flap
$M_a$	[Nm]	aerodynamic turning moment
$M_{cf}$	[Nm]	turning moment due to centrifugal forces
$M_E$	[N]	turning moment per unit width due to material stiffness
$M_g$	[Nm]	turning moment due to gravity
$M_p$	[N]	turning moment per unit width due to the pressure distribution
$n$	[-]	integer
$\mathbf{n}$	[m]	vector normal to flap
$p_0$	[N/m <sup>2</sup> ]	undisturbed static pressure
$p_x$	[N/m <sup>2</sup> ]	static pressure at position $x$
$r$	[m]	radial position
$Re$	[-]	chord based Reynolds number
$s$	[m]	location of stagnation point
$S$	[-]	stall flag sensitivity
$S_{cf}$	[-]	stall flag sensitivity with respect to centrifugal forces
$S_g$	[-]	stall flag sensitivity with respect to gravitation
$T$	[m]	period of deformation
$t$	[rad]	angle between flow and hinge line
$t_f$	[m]	thickness of flap

$v$	[m/s]	flow velocity
$v_0$	[m/s]	undisturbed flow velocity
$v_x$	[m/s]	velocity at position $x$
$x$	[m]	position in flow direction along the flap or chord-wise position of stall flag
$y$	[m]	span-wise position
$z$	[m]	position above surface
<b><math>a</math></b>	[rad]	angle of attack
<b><math>b</math></b>	[rad]	local pitch angle
<b><math>g</math></b>	[rad]	hinge angle
<b><math>D</math></b>	[s]	turn-over time of a stall flag
<b><math>c</math></b>	[rad]	angle between vertical and hinge vector
<b><math>r</math></b>	[kg/m <sup>3</sup> ]	air density
<b><math>w</math></b>	[rad/s]	angular velocity of switching flap or of the rotor
<b><math>\dot{w}</math></b>	[rad/s <sup>2</sup> ]	angular acceleration $d\mathbf{w}/dt$ of switching flap

### 3.1 The Stall Flag

The stall flag consists of a flap, a hinge, an optically contrasting area and a support. The support is usually a sticker sheet that can be pasted easily on the locations to be studied. The flap is fixed in a hinge-like manner to the support and can cover the optically contrasting area depending on its position. Figure 3.2 shows two stall flags in opposite states. The optically contrasting area can have a distinct colour or pattern, or it can be fluorescent or retro-

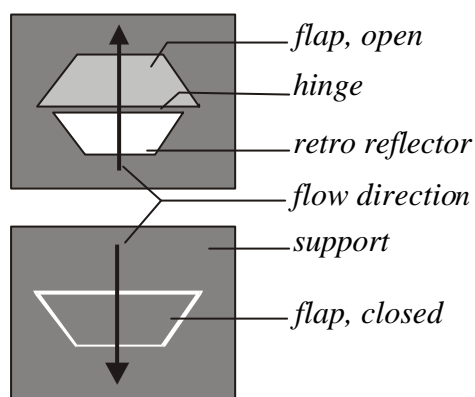


**figure 3.2** Two stall flags in the opposite extreme states.

reflective. The optical contrast can be fitted to the purpose of the measurement. In this study bright colours were used during wind tunnel measurements and retro-reflectors for field measurements. Furthermore, the contrasting area can be the support next to the flap or a side of the flap itself. A general definition of the stall flag is given in our patent (Appendix C). The stall flag behaves as a binary detector which signals or 'flags' a change of the flow direction as occurs at stall of airfoil sections. For this reason the detector was called 'stall flag'. Figure 3.3 shows an airfoil section equipped with a row of stall flags. The stall flags register the area of reversed flow. When several stall flags are pasted at different angles, the flow direction can be determined with a higher resolution. This is shown in figure 3.4.

#### 3.1.1 Controlled Evolutionary Development

The stall flag has been developed from an idea to a reliable detector by a controlled evolutionary process which took 4 years. In nature, new species are thought to come into being by random mutations in previous species, followed by a natural selection for the best ones. The successive stall flag prototypes, however, did not change in a random manner. The changes were steered by three possible arguments:

- 1) The changes should be based on the experience with previous prototypes.
- 2) The changes should do away with the observed shortcomings of previous prototypes.
- 3) The changes should incorporate new ideas, not related to the experience with previous prototypes.

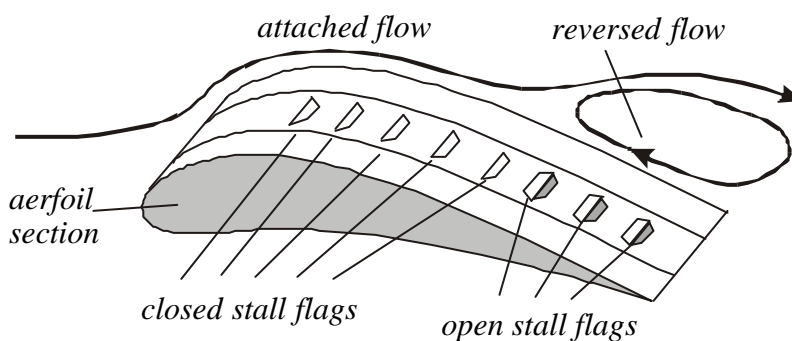


**figure 3.3** Stall flags on an airfoil section indicating reversed flow.



In the case of controlled evolution bad experiences will not be repeated and therefore the development can be faster than evolution in nature.

The idea of designing a detector for the detection of reversed flow came to the author when he tried to find the stagnation point on wind turbine blades [12]. The stagnation point depends on the angle of attack, which is a much desired

parameter for theory validation. So, at a certain moment he looked at the fur of a black sheep dog in the wind. At the stagnation point the white skin showed up because the black hair was blown outwards. This observation was important, because the visualisation was very clear and *different* from that using tufts. The 'signal' of tufts is a directional change of the tufts, the 'signal' of the fur of the dog was the appearance of the white skin in the black fur. The detection of this black/white contrast was possible from a larger distance than the determination of the directions of the individual tufts. This idea was reason to start experiments with artificial 'furs' which were called multi-tufts. Four different prototypes of these multi-tufts were made and tested in December 1993. During these tests it became clear that the aerodynamic forces on tufts are rather small compared to their stiffness. Furthermore, the visibility was not very good. These findings were reason to introduce the so-called narrow flaps, which were hinged surfaces about 1cm wide and 1 cm high. Two prototypes were made, also in December 1993. The tests with the narrow flaps led to the idea to using flaps with different colours on the upper and lower sides. The major problem was that the narrow flaps showed a rather large hysteresis. When turned over they would not switch back until the stagnation point had moved backwards over approximately twice their height. The height had to be approximately 1 cm to make the flap sensitive enough and thus the hysteresis corresponded to a shift of the stagnation point over approximately 2 cm. For a 15% thick profile with a chord of 50 cm, a 2-cm shift of the stagnation point corresponds to a 6° change of the angle of attack. Thus the hysteresis property made the narrow flaps rather inaccurate. Then, on December 19, 1993, the stagnation flap was invented.

### The Stagnation Flap

The stagnation flap was much wider than the narrow flap. Its operating principle was very different and it was free of hysteresis. Each flap was supposed to roll over in a continuous sense instead of the sudden total flip-over of the narrow flaps. The stagnation flap was pasted in an oblique manner over the leading edge of an airfoil so that one side was on the suction side of the airfoil and the other side on the pressure side. As the stagnation point moves, the flaps roll from one side to the other. The stagnation point is where the flaps stand perpendicular to the surface. The development of the first 13 different prototypes of stagnation flaps, along with several tests are also described in [12]. This work was carried out between December '93 and February '94, and resulted in increased knowledge concerning materials, adhesives and flow disturbance. One stagnation flap was also tested on a 10-m diameter wind turbine in June 1994 (see figure 3.5). This test is described by Herzke and Peinelt [37]. However, for technical reasons, it was decided to stop the further development of the stagnation flap. The main technical problems had the following causes. The stagnation

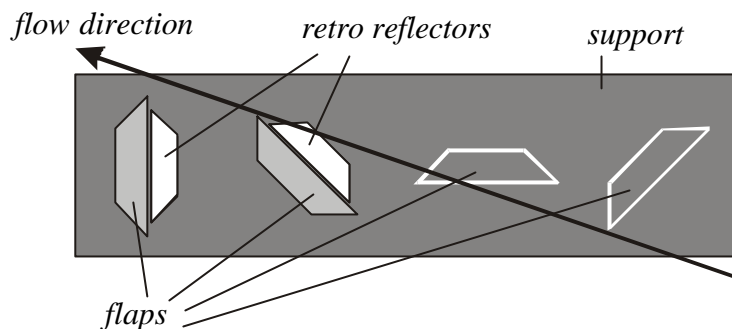


**figure 3.4** *Determination of the flow direction with stall flags.*

flaps were positioned at the leading edge, which first of all is very sensitive to flow perturbation and is difficult to record with a video camera. Second, the resolution requirements for precise localisation of the stagnation point were very high. Third, radial flow over the leading edge could greatly influence the stagnation flap.

Although the idea of the stagnation flap was no longer pursued, it returned with the idea of using flaps for the visualisation of stall. The author got the idea on the 6<sup>th</sup> of February, 1994.

The visualisation of the area of separated flow was not complicated by the three problems mentioned above related to the visualisation of the stagnation point. Furthermore, determining the area of flow separation on a wind turbine blade would be even more valuable than determining the stagnation line. Whether the flow about an aerodynamic object is separated or attached is of crucial influence on the aerodynamic loads. Discrepancies between design and practice are for a most part caused by differences between the practical blade areas of separated flow and the predicted areas of separated flow.

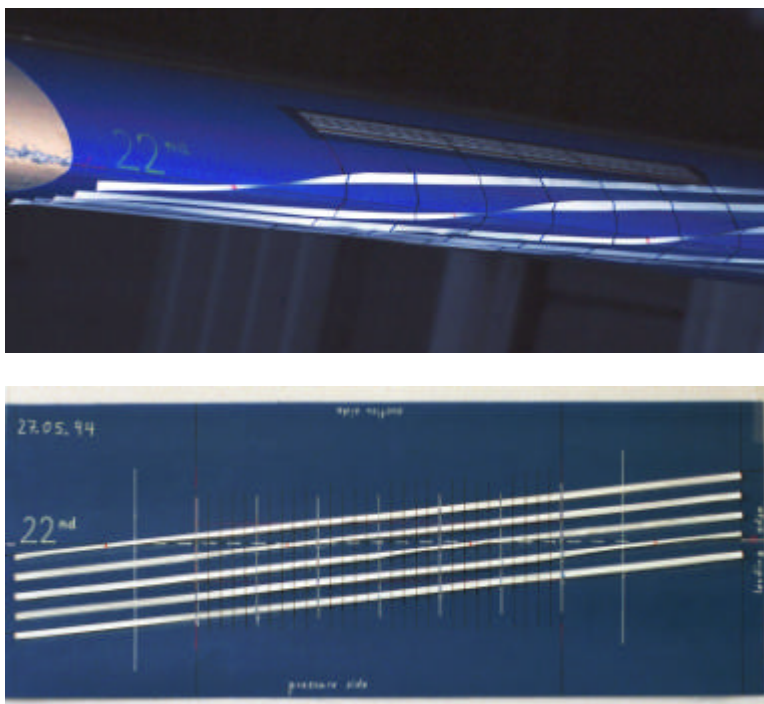


**figure 3.5** *Visualisation of the stagnation point on the leading edge of an airfoil (above). The stagnation flap separately (below).*

### The Stall Flag

The very first stall flags are shown in figure 3.6. This band with flaps was tested in the wind tunnel and showed that the drag increase was large. Furthermore approximately 50% of the flaps was lost in several minutes of wind tunnel operation. Clearly some development was necessary, but the area of reversed flow could be derived in a clear manner from the band of flaps. Solutions were found for two main problems during the development. One problem was to construct a hinge that was both extremely flexible and strong enough to survive for weeks/months on rotating wind turbine blades. The second problem was to improve the visibility of the stall flags so that detection of stall by the detectors could be from far away. This problem was essentially solved in March '95 by using retro-reflectors as optical markers. Another improvement of the visibility was obtained in December '95 when one side of the flaps was provided with fluorescent material. In December '95, hinges of polyethylene and polyurethane foils were developed: high flexibility and high strength were combined. Many different experiments with perforated foils, silk, PVC, polyester, fibres of glass or carbon had failed. The durability of the hinges was much improved by changing the shape of the flap. Beginning with prototype 11 cosine-shaped flaps were used. Stall flags of prototype 12 were used during field experiments with ECN's 25-m HAT (Horizontal Axis Turbine) in August '95. Some experiments were taken with Delft University of Technology's 10-m diameter test turbine. An experiment with a 0.45m diameter fast rotating propeller was performed in

August '95. This experiment showed that the stall flags were nearly insensitive to centrifugal forces (such an experiment was included in Appendix B). An overview of the major steps in the development is given below.

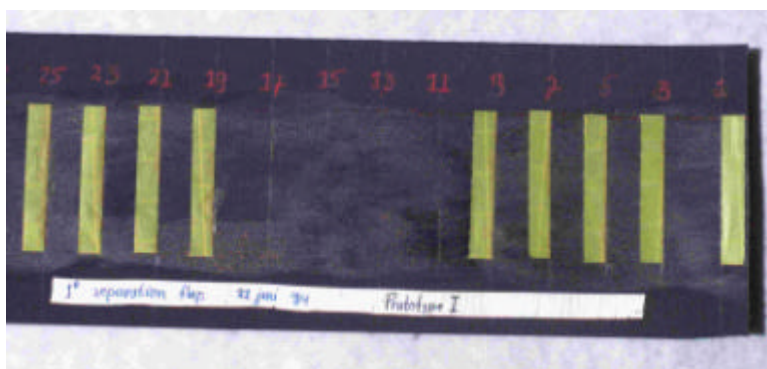


**figure 3.6** *The first stall flag.*

**detection of stagnation point [12]**

- fur of a dog shows the stagnation point November 1993
- manufacturing of first multi-tuft December 5 1993
- manufacturing of narrow flaps December 11 1993
- first stagnation flap December 19 1993
- application on 10m turbine [37] March-July 1994

**detection of stall/reverse flow**

- first idea of the stall flag February 6 1994
- retro-reflectors greatly improved visibility March 1995
- field experiment on ECN's 25m HAT July 19 1995
- test on propeller of 0.45m diameter August 1995
- experiment on commercial NedWind 30m diameter January-March 1996
- application of PE and PUR-hinges December 1995
- ECN applies for a patent on the stall flag May 1996
- first poster prize for technical relevance, innovative character and presentation at EUWEC '96 conference May 1996
- carbon fibre flaps avoid Kelvin-Helmholtz instability October 1998
- experiment on 64m NEG Micon turbine in Denmark November 1998
- experiments on rotors of LM (USA) and Aerpac (Germany) June-September 1999
- double stall explained with stall flag experiments October 1999

June 22, 1994, the first stall flag was tested in the wind tunnel. It was little more than just the idea (figure 3.6). Several flaps came loose after a short experiment in Delft University of Technology's Low Speed Tunnel. The drag coefficient of the airfoil was measured, and the increase of drag coefficient was approximately 0.02 [13].

Since October 23 1998, after 4 years of a development, stall flags of prototype 23 were produced. This prototype number corresponds to a series of stall flags of different sizes and different operational ranges concerning the flow speed. The largest stall flag of this type can be seen in figure 3.7. The latest important improvement was the change of the material of the flap from polycarbonate to carbon fibre reinforced epoxy. Due to this change, the Kelvin-Helmholtz instability of the flaps was suppressed (see section 3.2.6). Prototype 23 stall flags performed well on many large commercial wind turbines. They had a durability of approximately 1 month or  $3 \cdot 10^6$  flip-overs.

### 3.1.2 List of Recommendation

During the development of the stall flags all observations were noted on a list. Some topics in this list are given below. For the complete list, describing 24 different aspects, we refer to the technical reports [14] and [18].

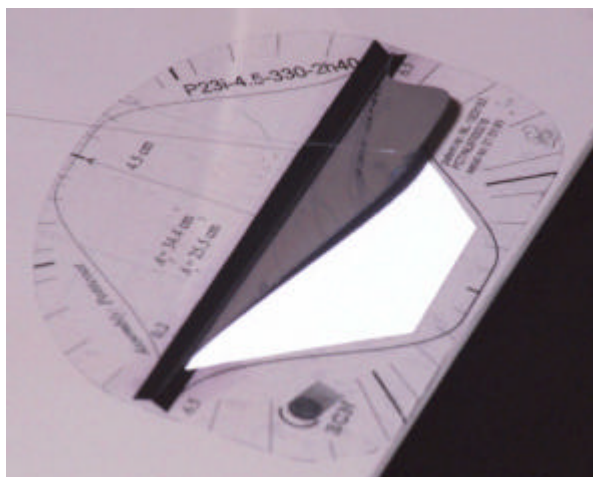


**figure 3.7** *Prototype 23, designed April 1999, (see also figure 5.3).*

- flap shape: The shape should be cosine-like, otherwise the flap comes loose at the edges.
- flap size: The size is determined by the minimum required retro-reflector size (see chapter 4).
- flap material: Carbon reinforced epoxy to yield high stiffness, which avoids self-excited motion.
- flap weight: As light as possible: thus carbon has to be used.
- adhesive: The adhesives applied should be UV-resistant, waterproof, suitable for epoxy/polyester mounts.
- support: All edges of the support should be rounded; the support should be stuck on the airfoil over its entire surface; the support should exceed the range of the flap in both positions; it should not be stretchy.
- hinge: Many different hinges are possible. The best results are obtained with a foil hinge. The material has to meet 'conflicting' demands: very strong, very flexible in the temperature range between -10°C and 50°C, UV-resistant (high demand for thin foils in direct sunlight), waterproof, polar material (otherwise it can not be pasted).
- water: Water on the stall flag can fix the flap and can decrease the efficiency of the retro-reflector. Therefore wax-like coatings can be applied to the stall flag surfaces in order to decrease adhesion with water. Another option is to use a support that absorbs water and transports it outside the flap range where it can evaporate.

## 3.2 Interpretation of Signals

The optical output signal of the stall flag is determined by the position of the flap. Therefore an analysis of the forces that drive the position of the flap should be made. We first deal with the aerodynamic forces and then with the external forces. The ratio between these two is a measure of the sensitivity which is subsequently discussed. Attention is also given to hysteresis of the flap and to self excited motion caused by Kelvin-Helmholtz instability.

### 3.2.1 Aerodynamic Forces on the Stall Flag

The aerodynamic forces on the flap are partially of the viscous type and partially of the pressure type. The viscous or frictional forces act in the plane of the flap and therefore have no turning moment with respect to the hinge. Therefore the aerodynamic forces that control the flap motion are restricted to pressure forces.

#### Pressure Forces

It is assumed that the stall flag is pasted on a surface in a fluid flow. The flow is considered to be perpendicular to the hinge parallel to the surface. The flow will stagnate to a certain extent under the flap of the stall flag (see figure 3.8). It is assumed that the pressure below the flap equals the total pressure and that the pressure above the flap equals the static pressure. Then the pressure difference equals the dynamic pressure  $\frac{1}{2}\rho v^2$ , in which  $v$  is a kind of average velocity in the boundary layer between the surface and the edge of the flap. In the boundary layer,  $v$  increases rapidly with the distance above the surface, thus the pressure under the flap increases rapidly when the opening angle between the flap and the surface increases. This angle called  $f$  is defined in figure 3.8. A global estimate of the turning moment due to this stagnation will be made. We assume that the flap is rectangular with width  $b$ , height  $h$  and mass per unit flap area  $m_a$ . The initial turning moment due to the pressure under the flap becomes:

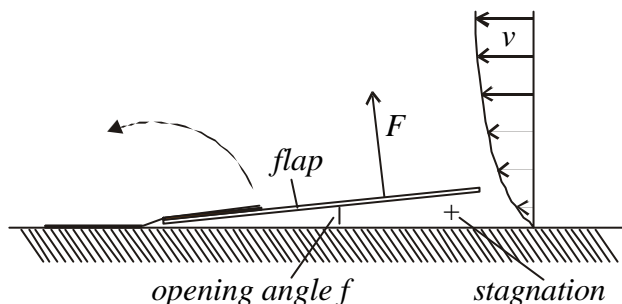


figure 3.8 The switching stall flag.

$$M_a = \frac{1}{4}h^2b\rho v^2, \quad (3.1)$$

in which we assumed that the pressure force works at a distance  $h/2$ . This initial turning moment is also a rather good estimate over a large range of positions of the flap. This follows from the drag coefficient of a flat plate (perpendicular to the flow) which is approximately 1.2 for Reynolds  $> 100$ . Thus equation 3.1 is also indicative of the range of opening angles around  $\pi/2$ . If the angle increases further to approximately  $5\pi/6$ , then the pressure coefficient

below the flap is approximately minus 0.35, for which we refer to [39]. Only when the flap is close to the surface on the down-flow side do the aerodynamic forces acting on the flap decrease rapidly. It is assumed that the turning moment on the flap equals equation 3.1 constant between 0 and  $\pi/2$  and decreases by the sine function for larger angles.

The analysis above is valid for inflow perpendicular to the hinge. We will proceed with the more general case in which the angle between the flow and the hinge is  $t$ . The blade surface is located in the  $x,y$  plane in which  $x$  is in chord-wise direction and  $y$  in span-wise direction. The distance to the surface is given by the  $z$ -ordinate. In vector notation the hinge has direction  $(x,y,z) = \mathbf{h} = (0,1,0)$  and the inflow over the stall flag has direction  $\mathbf{i} = (\sin t, \cos t, 0)$ . The vector in-plane with the flap perpendicular to  $\mathbf{h}$  is called  $\mathbf{f}$ , which is given by  $(\cos f, 0, \sin f)$ . So the flap is positioned in the  $(\mathbf{h}, \mathbf{f})$  plane. The vector normal to the flap surface  $\mathbf{n} = (\sin f, 0, -\cos f)$ . The angle between  $\mathbf{i}$  and  $\mathbf{n}$  follows from the arccosine of the dot product and equals  $\arccos(\sin t \sin f)$ , thus the angle between  $\mathbf{i}$  and the flap is  $\mathbf{a} = \pi/2 - \arccos(\sin t \sin f)$ , in which  $\mathbf{a}$  is the angle of attack of the flow with respect to the flap.

The lifting characteristics of a flat plate for  $-7.5^\circ < \mathbf{a} < 7.5^\circ$  are almost equal to the theoretical  $2\mathbf{p}\mathbf{a}$ . At approximately  $7.5^\circ$ , the flow separates and the lift coefficient  $c_l$  is approximately 0.7. For larger angles, the lift coefficient is approximately 1. It follows that if the angle between the flow over the stall flag and the hinge becomes larger than a few degrees, the lift coefficient on the flap (forcing it downwind as far as the hinge permits) is approximately 1 and yields again equation 3.1 for the turning moment. Only if the flap is close to the surface with a hinge angle smaller than a fraction of  $7.5^\circ$  the lift coefficient will be less.

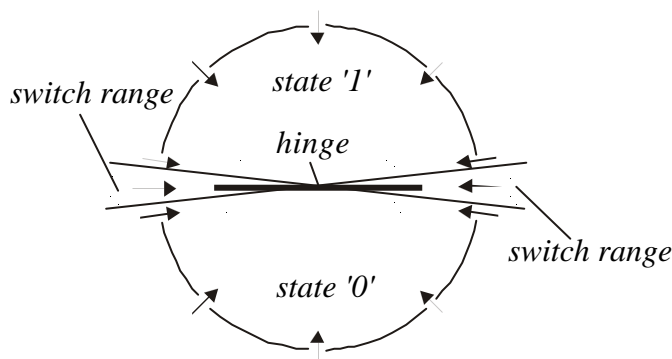


**figure 3.9** The binary distinction of the flow direction with a stall flag.

Thus the turning moment of aerodynamic forces on the stall flag is nearly quasi-static and given by equation 3.1 as long as the angle between the inflow and the hinge is not less than  $7.5^\circ$  and the flap is not pressed against the surface downwind. This means that the complete range of flow directions ( $2\mathbf{p}$ ) is divided by the hinge in two equal inflow ranges of almost  $\mathbf{p}$ . If the flow direction is along the hinge, then the stall flag will be in the switch state. This coupling between the state of the stall flag and the flow direction is shown in figure 3.9.

The above modelling is simplistic. In practical application the flow will not stagnate completely but will turn side-wards. Furthermore, the flap will be accelerated and the process becomes highly dynamic. The dynamic situation becomes even more complicated when the flap rises above the surface and separates the flow by its sharp edges. It should also be noted that flaps turn over when the flow is separating at the flap location. Such areas are often studied because so little is known about the flow characteristics in this area. Thus, if the modelling needs to be improved, all these effects should be included in a realistic sense. But it

will be shown in the successive sections that a better estimate is not required for application on a wind turbine blade.

### 3.2.2 External Forces

This section deals with external forces, which may cause systematic errors in the stall flag signals.

#### Gravity and Centrifugal Forces

These forces are certainly present when the stall flag is mounted on wind turbine blades. The centrifugal force on the rectangular flap of the previous section equals  $hbm_a\omega^2r$ , where  $\omega$  is the angular velocity of the rotor. This force will cause a turning moment with respect to the hinge which is proportional to the sine of  $f$  and to the sine of  $g$ . The first sine takes into account the opening angle of the flap and the second the angle between the hinge vector and the centrifugal force vector. The definition of the hinge angle is given in figure 3.10. It follows that the turning moment due to the centrifugal force is given by:

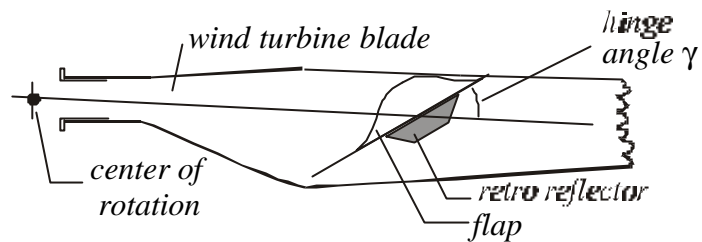


figure 3.10 Definition of the hinge angle.

$$M_{cf} = \frac{1}{2}m_a h^2 b \omega^2 r \sin(f) \sin(g). \quad (3.2)$$

It is assumed here that the centrifugal force vector is directed parallel to the support of the stall flag. In practical application a small difference exists, due to the cone angle of the rotor, due to blade deformation and due to the variation of the thickness of the blade in radial direction. The cone angle usually is less than  $5^\circ$  and in order to account for the thickness, approximately  $0.7^\circ$  has to be subtracted (for the suction side). The blade deformation depends on many parameters but will not be large. A reasonable estimate will be approximately  $5^\circ$ . It follows that all effects are small and can be neglected. Only in the case of a flap oriented down-flow with respect to the hinge (the situation in which the aerodynamic forces become small) the effects have some relevance. The small angle gives rise to a small turning moment pushing the flap against the surface.

The turning moment due to gravity follows straightforwardly:

$$M_g = \frac{1}{2}m_a g h^2 b \sin(f) \sin(c), \quad (3.3)$$

where  $c$  is the angle between the vertical upward direction and the hinge; it is assumed that the vertical is in-plane with the rotor plane.

#### Adhesion

In practical application, the flap cleaves to the support if there is water or remains of the adhesive under the flap. Adhesive forces and surface keep the pressure under the flap low, so that the flap cannot rise from the surface and becomes immobile. In reality the centrifugal force could throw the water out, the water could also evaporate or flow away when special

wax like coatings are applied to the stall flag surfaces. Adhesion may overrule any turning moment and it may cause malfunctioning of the stall flags, but if the flap surface is clean and dry it does not influence the stall flag behaviour.

### Hinge Stiffness

Stiffness of the hinge can be made insignificant. To verify the insignificance of the stiffness we test whether the flap turns over due to gravitation only. When it does we are justified in neglecting its effect, since in practical application gravity is the smallest force.

### 3.2.3 Sensitivity

The sensitivity of the stall flag  $S$  is defined as the ratio of the aerodynamic turning moment and that due to external forces. It is assumed that the flap is not immobilised by adhesion. Using equations 3.1 to 3.3 we find:

$$S = \frac{M_a}{M_g + M_{cf}} = \frac{\mathbf{r}v^2}{2m_a[g \sin(\mathbf{c}) + \mathbf{w}^2 r \sin(\mathbf{g})] \sin(f)}. \quad (3.4)$$

It follows that for a small opening angle  $f$  of the flap, the sensitivity is high and the flap will respond mainly to aerodynamics. If the opening angle becomes larger, the hinge angle  $\mathbf{g}$  becomes important. The centrifugal contribution to the external force is in general much larger than the gravitational contribution. For small  $\mathbf{g}$  the centrifugal distortion vanishes. In practical application, stall flags are mostly placed with  $\mathbf{g}=0$ . This angle is favourable for discriminating between separated and attached flow and at the same time it guarantees that there is no centrifugal distortion. Therefore if  $\mathbf{g} \approx 0$  the parameter  $S$  is determined by gravitation only, if  $\mathbf{g}$  is large, then  $S$  is determined by the centrifugal contribution. This defines  $S_g$  and  $S_{cf}$  respectively as:

$$S_g = \frac{M_a}{M_g} = \frac{\mathbf{r}v^2}{2m_a g}, \quad S_{cf} = \frac{M_a}{M_{cf}} = \frac{\mathbf{r}v^2}{2m_a \mathbf{w}^2 r} \neq \frac{\mathbf{r} \mathbf{w}^2 r^2}{2m_a \mathbf{w}^2 r} = \frac{\mathbf{r}}{2m_a}. \quad (3.5)$$

The inequality is valid since the substitution  $v=\mathbf{w}r$  is invalid in the boundary layer. If typical practical values for a P23 stall flag on a 64m wind turbine are substituted, it follows that  $S_g = 31$  and  $S_{cf} = 10$  for [ $\mathbf{r}=1.25\text{kg/m}^3$ ,  $v = 10\text{m/s}$ ,  $m_a=0.2 \text{ kg/m}^2$ ,  $g = 10 \text{ m/s}^2$ ,  $\mathbf{w}=1.8 \text{ rad/s}$  (rotor speed),  $r=10\text{m}$ ]. It follows that even for the low velocity of 10m/s, the sensitivity parameters estimate that the aerodynamic turning moment is an order of magnitude larger than that due to the external forces. The smaller the wind turbine, the larger the rotor speed. So especially in for small rotors, the flags should be placed at zero hinge angle to avoid centrifugal distortion.

### 3.2.4 Response Time

From the above it follows that the flap is mainly driven by aerodynamic forces. If only the aerodynamic turning moment accelerates the flap, the angular acceleration  $\dot{\mathbf{w}}$  becomes:

$$\dot{\mathbf{w}} = \frac{M_a}{I}, \quad (3.6)$$



where  $I = \frac{1}{3}m_a h^3 b$  is the moment of inertia of the flap. With this angular acceleration, the free edge of the flap will reach the flow velocity  $v$  after a turn-over the angle  $f = I v^2 / (2M_a h^2) = 2m_a / (3r h)$ . If we substitute typical values ( $r = 1.25 \text{ kg/m}^3$ ,  $h = 0.03 \text{ m}$ ,  $m_a = 0.2 \text{ kg/m}^2$ ) then it follows that  $f \approx 3 \text{ rad}$  or approximately  $180^\circ$ . After a complete turn the flap edge will therefore move with approximately the same speed as the flow. If we assume that the acceleration remains constant, the flap will turn over in a time  $\Delta t$  given by: this follows from  $\frac{1}{2} \dot{\omega} \Delta t^2 = \pi$ , which means:

$$\Delta t^2 \approx \frac{2\mathbf{p}}{\dot{\omega}} = \frac{2\mathbf{p}l}{M_a} = \frac{8\mathbf{p}m_a h}{3r v^2}. \tag{3.7}$$

This estimate for the turning time is only valid if the sensitivity parameter for the given situation is much larger than 1. Normalising this time by the time necessary for the flow to travel over the height of the stall flag  $h/v$ , for the dimensionless stall flag response  $k$  we get:

$$k = \frac{\Delta t}{h/v} = \sqrt{\frac{8\mathbf{p}m_a}{3r h}} \approx 7. \tag{3.8}$$

The numerical value is obtained by substitution of the above data. So the flap turns over in a period which corresponds to the time required for the flow to travel approximately 7 times the height of the stall flag.

### 3.2.5 Hysteresis and the $h/2h$ -Model

The classic way to think about separation is to assume that the velocity profile in the separated area is steady [51]. The flow in the lower part is reversed and higher up it is still in the main flow direction (see also section 2.4.3 and figure 2.13). If such a situation existed, then stall flags could show significant hysteresis depending on the height of the flap. Imagine

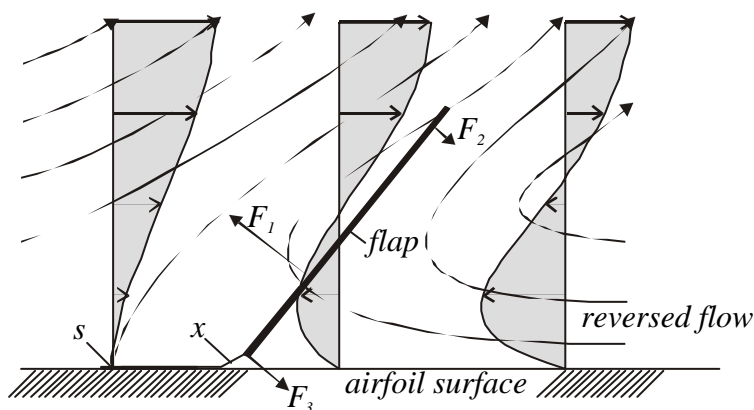


**figure 3.11** In the classical stationary boundary layer of separated flow, the flap is bi-stable. The disturbance to the flow due to the flap is not shown. In this model the flap adds thrust to the profile.

the situation of figure 3.11. The flap would remain in the half-opened situation as shown in the figure. The flap would initially turn over, but will become obstructed by the main flow at a higher altitude. At the position of equilibrium the turning moment due to force  $F_1$  exerted by the reversed flow equals the opposite turning moment of the force  $F_2$  due to the main flow direction. However, if the flap had already turned over completely in the past, it would also be in a stable situation. A model, called the  $h/2h$ -model, was set up to model the hysteresis of the stall flag in

the classic model with the stationary boundary layer. The  $h/2h$ -model relates the height  $d$  of the separated flow above the airfoil to the state of the stall flag with flap height  $h$  at the same position (see figure 3.12). The relation is given by table 3.1 for a stall flag in two-dimensional flow, with its hinge line perpendicular to the flow direction. Going down the table, the stall flag signals are listed while the position of separation  $S$  first shifts to the left and then to the right in figure 3.12. The height of separation at locus  $x$  is  $d$ , and it can be seen that the stall flag signal with increasing  $d$  ( $0 \rightarrow 2h$ ) differs from the signals with decreasing  $d$  ( $2h \rightarrow 0$ ). This difference is caused by the hysteresis.

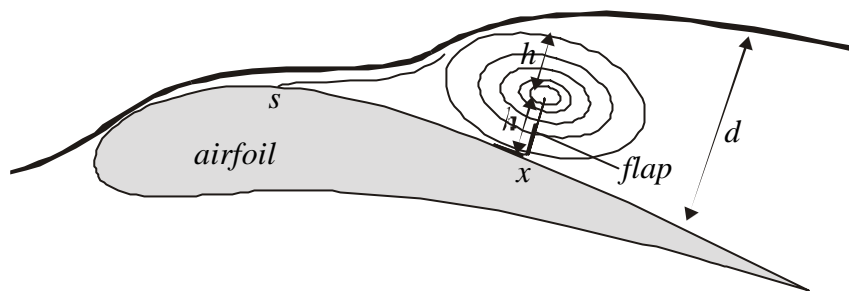


figure 3.12 The  $h/2h$ -model.

### Thrust

From the situation of the steady velocity profile in figure 3.11 it can be seen that the force  $F_1$  should be larger than  $F_2$  in order to yield an opposite but equal turning moment. This means that half opened stall flags add a thrust force  $F_3$  in the main flow direction on the object.

### Simpson Model

In the Simpson model (see section 2.4.3 on stall and [55]) the reversed flow occurs stochastically and separation is classified by means of the fraction of the time the flow is separated at a certain location. The stochastic behaviour will oppose the locking of the flap of a stall flag in a bi-stable state. Therefore systematic deviations in the stall flag behaviour will vanish with increasing unsteadiness. It will be shown by means of two wind tunnel experiments with stall flags that the Simpson model is preferred over the classic model.

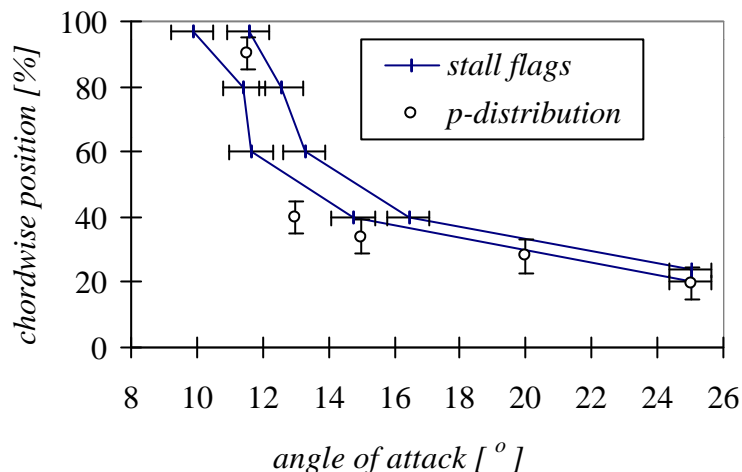
### Wind Tunnel Measurements

The hysteresis behaviour of the stall flags was measured in the wind tunnel on a 30% thick airfoil (DU97w300,) especially designed for wind turbine blades [Timmer & van Rooij, IW

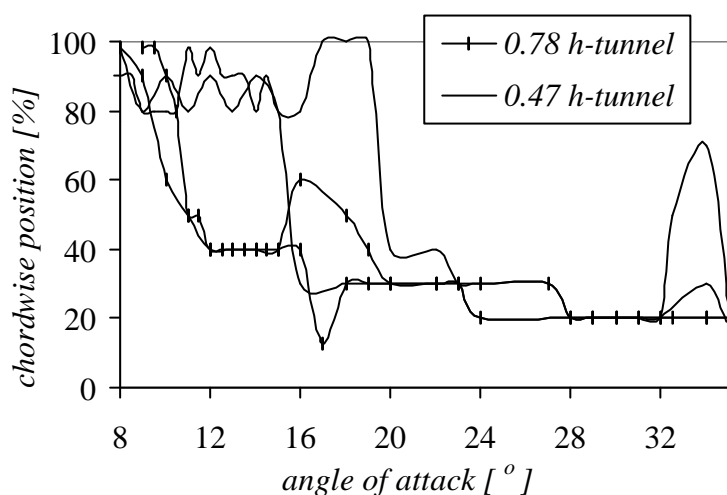
condition	state	signal	
$d \gg 0,$	$S > x$	closed	0
$d (0 \rightarrow 2h)$	$S < x$	half open	$\frac{1}{2}$
$d (> 2h)$	$S < x$	open	1
$d (2h @ 0)$	$S < x$	open	1
$d \gg 0,$	$S > x$	closed	0

table 3.1 The criteria that determine the stall flag signal based on the  $h/2h$ -model. Going down the table signifies that the separation height first increases and then decreases again. It can be seen that the stall flag signals with equal conditions depend on the past conditions.

98003R, 1999]. Pressure measurements and wake rake traverses with stall flags pasted on the airfoil were taken in Delft University of Technology's Low Speed Tunnel. To determine the hysteresis the airfoil was equipped with five stall flags, respectively at  $0.20c$ ,  $0.40c$ ,  $0.60c$ ,  $0.80c$  and  $0.97c$ . The chord of the airfoil was 60 cm and the height of the flaps of the stall flags was 2 cm. The Reynolds number was  $2.0 \cdot 10^6$  while the angle of attack was increased from  $0^\circ$  to  $25^\circ$  and then reversed for 5 times. The stall flag signals were recorded with a video camera and the angle of attack (uncorrected for tunnel influences) was spoken and recorded on



**figure 3.13** Hysteresis of the airfoil and the stall flags. The curves are passed clockwise. The average hysteresis is approximately  $1.5^\circ$  angle of attack.



**figure 3.14** Equal rows of stall flags (1 cm high) at different span-wise locations show large differences caused by three-dimensional flow. All loops above  $22.5^\circ$  are clockwise, all loops below this angle are counter clockwise.

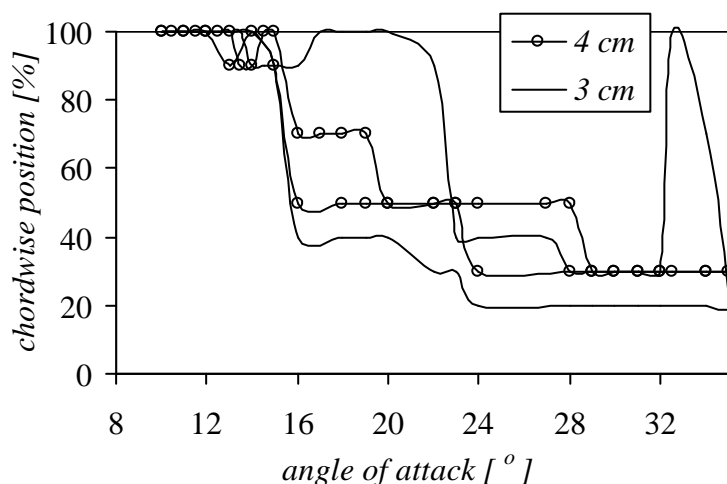


**figure 3.15** Hysteresis of stall flags with flaps of 3 and 4 cm height at respectively 39% and 56% of the height of the tunnel. All loops are clockwise.

the audio channel of the camera. The angle of attack changes at a constant rate of  $0.875^\circ/s$ . Because the time between successive frames of the video was precisely 40 ms, the changes of angle of attack between changes of the stall flag signals could be determined rather precisely by counting the number of video frames. Figure 3.13 shows the results averaged over the 5 sweeps. In steady conditions, thus without pitching, the stall flag signals were not steady in separated flow. They could close for several seconds and then suddenly flip over and back in a fraction of a second. During the measurements, it was observed that several stall flags

showed a behaviour indicating unsteadiness. The location of separation was also estimated from the flat region of the pressure distributions (the reading error was approximately  $0.05c$ ). The errors in the stall flag curves were  $0.25^\circ$ , which is the difference between the adjusted  $\alpha$  and the  $\alpha$  recorded by the video camera. Furthermore, an error of  $0.4^\circ$  was added, to represent the average standard deviation of the realisations of the 5 sweeps. It should be noted that the observed hysteresis of the stall flag signals could be due to stall flag hysteresis or due to hysteresis of the flow around the airfoil. The  $h/2h$  model predicts that the stall flag hysteresis increases proportionally to the height of the flap. Such an experiment has been carried out on a DU91w250 airfoil, also of 60cm chord. A new advantage of the stall flags was discovered. Two rows of small stall flags ( $h=1$  cm) were pasted at different span-wise locations and showed very different behaviour (see figure 3.14). If the flow would had been two-dimensional, as is expected in the wind tunnel, then the stall flag signals would have to be independent of the span-wise position. Thus the stall flags very clearly "warned" the experimenter that the flow was, to a large extent, three dimensional. This means that the results of tunnel measurements above an approximately  $9^\circ$  angle of attack do not represent two-dimensional data and are difficult to interpret. Figure 3.14 also shows that the position of the separation line does not move monotonously in one direction. The observations were consistent with the intermittent behaviour of separation as modelled by Simpson. This confirmation of Simpson's model is also a rejection of the  $h/2h$ -model, being based on classic steady velocity profiles. Although the three-dimensional character of the flow makes the interpretation difficult, the hysteresis of stall flags with flap heights of 3 and 4 cm turned out to be significantly different. The results presented in figure 3.15 show that the stall flags with the lower flaps demonstrate more hysteresis, while on the basis of classic profiles less was expected.

### Discussion/Conclusions

The  $h/2h$  model and the classic separated boundary layer model of figure 3.11 have to be rejected. Instead, the flow behaved unsteadily and three dimensionally to a large extent in separated conditions. The character of the flow was more like that predicted by Simpson. His intermittent stall behaviour was also confirmed by the recent experimental data from particle image velocity experiments of Holm and Gustavsson [40].

### 3.2.6 Kelvin-Helmholtz Instability

The stall flags with prototype numbers lower than 22 showed a self-excited whipping motion even in attached flow. This behaviour has also been observed from tufts, [23]. The self-excited whipping motion disturbs the interpretation of tuft signals and is likely to increase the flow disturbance. The stall flags suffered from the same problem and from the loss of flaps, which were smashed to pieces by violent collisions against the blade surface. The cause of this motion was ascribed to the Kelvin-Helmholtz instability of waves in two-phase flow [31]. Here, an initial small curvature of the flap surface causes the pressure to decrease above convex parts, and to increase above concave parts, so that the deformation tends to increase (see figure 3.16). This instability also causes the well-known waves in normal flags in the wind. We found that the instability vanishes when the stiffness of the flap material exceeded a critical value. For this reason the stiffness of the flaps was increased by changing the conventional polycarbonate material to carbon fibre reinforced epoxy. These carbon flaps were applied as stall flags for prototype numbers 23 and higher. This provision reduced the flow disturbance a great deal and increased the stall flag lifetime by a factor of about 10.

The required stiffness of the flap material can be calculated. We assume that the flap is an infinite surface with thickness  $t_f$  and made of a material with elasticity-modulus  $E$ . The flap is subject to uniform flow of velocity  $v_0$  and static pressure  $p_0$  on the upper side and no flow on the lower side (see figure 3.16). The deformation of the flap is initially very small, and therefore the pressure forces act in the vertical direction only. We then assume that the deformation  $u(x)$  is sinusoidal with period  $T$  and amplitude  $a$ . In the text books on the Kelvin-Helmholtz instability, it is also assumed that the air flow is affected up to an altitude equal to the period  $T$ . With the continuity equation the flow speed at location  $x$  is found to be:

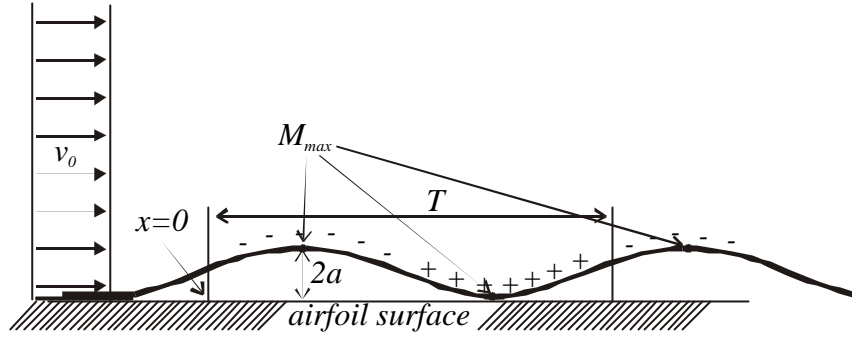


figure 3.16 Kelvin-Helmholtz instability.

deformation of the flap is initially very small, and therefore the pressure forces act in the vertical direction only. We then assume that the deformation  $u(x)$  is sinusoidal with period  $T$  and amplitude  $a$ . In the text books on the Kelvin-Helmholtz instability, it is also assumed that the air flow is affected up to an altitude equal to the period  $T$ . With the continuity equation the flow speed at location  $x$  is found to be:

$$v_x = v_0 \frac{T}{T - a \sin(2\pi x/T)}. \quad (3.9)$$

When the velocity  $v_x$  and  $v_0$  are linked by the Bernoulli equation:

$$p_x = p_0 + \frac{1}{2} \rho (v_0^2 - v_x^2). \quad (3.10)$$

So the pressure distribution over the flap surface is known and can be used to calculate the turning moment for the flap material. From the figure it can be seen that the turning moment for the flap is 0 for  $x=nT$  where  $n$  is an integer. Thus if we regard an arc of the sine from 0 to  $T/2$ , then at both ends of the arc the turning moment is zero and the force is half the opposite vertical force due to the pressure distribution. The turning moment per unit width due to the pressure distributions  $M_p$  will have a maximum for  $x=T/4+nT$ . The numerical value is equal to:

$$M_p = \int_{x=T/4}^{x=T/2} \left(\frac{T}{4} - x\right) p_x dx + \frac{T}{4} \int_{x=T/4}^{x=T/2} p_x dx \approx \frac{\rho v_0^2 T}{4} \left(\frac{3 - \pi}{2\pi}\right), \quad (3.11)$$

where  $a \ll T$ . This inequality is true since the initial amplitude of deformation  $a$  can be as small as we like. The strain in the flap material opposes the deformations. This strain depends on the radius of curvature at the same position  $x = T/4+nT$ , which for the sinusoidal deformation is equal to the reciprocal of  $d^2u/(dx)^2$  or  $a^{-1}$ . It then follows for the turning moment per unit width due to the strain in the flap material [48] that:

$$M_E = a I_a E, \quad (3.12)$$

in which  $E$  is the  $E$ -modulus for the flap material and  $I_a$  is the second moment of area per unit width, which equals  $t_f^3/12$ .

The condition for to avoiding the Kelvin-Helmholtz instability becomes:

$$M_E > M_p \Leftrightarrow I_a E > \frac{rv_0^2 h}{2} \left( \frac{3-p}{2p} \right) \quad (3.13)$$

From this equation it can be seen that  $I_a E$  should increase by the square of the velocity in order to avoid instability. It also can be seen from equation 3.11 that the turning moment due to the pressure distribution increases proportionally to the period  $T$  of the deformation. The longest period of deformation possible in a flap of height  $h$  will be approximately equal to  $2h$ . This value for  $T$  was substituted in the inequality 3.13. For the stall flags applied on the blades of a wind turbine, condition 3.13 required that a very stiff material had be used to keep the flap thin. This has been the reason for using carbon fibre reinforced epoxy for the flaps. It should be noted that tufts have hardly any stiffness and therefore develop the Kelvin-Helmholtz instability already at very low flow speeds. Crowder [24] did not associate the self-excited motion of tufts with the Kelvin-Helmholtz instability, but knew that the stiffness could avoid the instability. Therefore he developed the so-called flow cones (see figure 3.21). The flow cones however, are more sensitive to centrifugal deviations and may cause large flow disturbances.

### 3.2.7 Observations

It is clear by now that the stall flag signal is dominantly driven by aerodynamics when the sensitivity parameters are much larger than 1. In the case in which only the flow direction determines the stall flag signal, the area of separation can be determined over the entire wind turbine rotor. The prediction of wind turbine behaviour is accurate when the flow about the blades is attached, but at high wind speeds, when separation can occur, the predicted the power can be off by as much as 30% [22]. In practical application the separated area does not agree with the calculated area. Using the stall flags the unexpected can be seen and different types of separation can be distinguished. This is shown in figure 3.17. In attached flow all stall flags are closed. When separation just starts at the trailing edge, the stall flags there will flap over, while the flags at smaller chord-wise positions are still closed. Remember (chapter 2, section 5) that separation can be postponed. Postponement can be observed with stall flags at the trailing edge. When the separation line progresses towards the leading edge (probably in an intermittent way) the flags passed by the line will open. When full airfoil stall (or leading edge stall) occurs, the stall flags positioned at less than  $0.2c$  will also flap over. Another typical observation at very large angles of

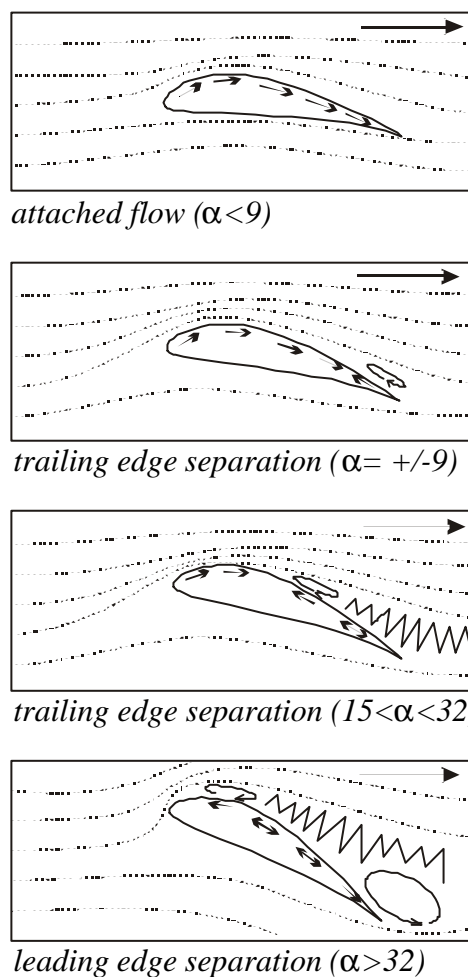


**figure 3.17** Interpretation of stall flag signals. The angles are indicative only.

attack ( $>32^\circ$ ) is that stall flags downstream  $0.8c$  can close again because of the vortex at the trailing edge (see figure 3.17).

The signals of the stall flags were compared to pressure measurements in the wind tunnel for two different airfoils used in wind turbine blades: the DU91w250 and the DU97w300. From these measurements, a semi-quantitative relation was derived between the flow types given by the stall flags and pressures measured (see figure 3.20). Stall flags positioned in the 'flat' part of the pressure distribution were always open and in other parts were always closed. When the stall flag at  $0.90c$  was open and the one at  $0.80c$  was closed, the airfoil operated at the first maximum of the lift coefficient  $c_{l,max}$ . This could be a general phenomenon, since these stall flag signals mean that significant decambering 'just started' at the trailing edge. When this starts the drag coefficient  $c_d$  also increases rapidly. The tangential force coefficient  $c_t = c_l \sin(\mathbf{a+b}) - c_d \cos(\mathbf{a+b})$  is added to table 3.2, in which various cases of the stall flag signals are listed. The stall flag indicate when separation of the trailing edge is initiated. Then we define the tangential force coefficient to be  $c_{t, TES}$ , and this value remains nearly constant ( $\pm 0.05$ ) when the separation line moves forward. When the flow on the leading edge also separates, however,  $c_t$  suddenly drops by approximately 0.2. This means that the tangential force on a blade section remains approximately constant in trailing edge stall, so the power produced by the rotor is constant. But when the flow at the leading edge separates, the tangential forces drops and can even become slightly negative, thus the power of the rotor is reduced.

stall flag signal			coefficient	flow type
$x/c < 0.2$	rest	$x/c > 0.8$		
0	0	0	$c_t = 2pa, c_d < 0.02$	attached flow
0	0	1	$c_t = c_{l,max}, c_d > 0.1$	initial separation
0	1	1/0	$c_t \approx c_{t, TES}$	trailing edge separation
1	1/0	1/0	$c_t \approx c_{t, TES} - 0.2$	full airfoil separation
1	1/0	0	$c_t \approx c_{t, TES} - 0.2$	deep stall

**table 3.2** *Indicative correspondence of stall flag signals and aerodynamic coefficients.*

## 3.3 Flow Disturbance

The stall flags are meant to detect the areas of flow separation on aerodynamic objects. They should not disturb the separation phenomenon to a large extent. Although wind tunnel experiments show that this is the case, one should always be suspicious about possible disturbances. It can easily be checked whether certain stall flags change the separation phenomenon. One should install other stall flags downstream from the ones suspected. If their signals are independent from the ones upstream, it can be concluded that the latter do not cause significant disturbance. After this general remark, the possible flow disturbance due to the stall flags will be discussed in more detail. First the influence of the stall flag on transition will be discussed, then the drag increase is measured and finally the influence on the pressure distribution will be described.

### 3.3.1 Transition

Transition depends on roughness, pressure gradient, turbulence and fluid properties such as the Reynolds number. Not much is known in detail about the factors controlling this mechanism [1,51], and therefore only semi-theoretical or empirical models exist to analyse the influence of roughness. Transition involves a change in the skin friction. In laminar flow the skin friction is approximately proportional to  $v^{1.5}$ , but in turbulent flow it is  $v^{1.85}$ . The presence of stall flags may therefore introduce additional viscous drag. Early transition could also postpone separation and thereby reduce the drag an order of magnitude. Thus, if the stall flags do affect the location of transition, both drag and lift characteristics may be affected.

#### Expected Influence on Transition

Abbott gives the minimum height of a cylindrical disturbance (0.9 mm diameter at  $0.05c$ , with its axis normal to the surface) necessary to cause premature transition [1]. This height becomes less when the (chord based) Reynolds number increases (to 0.75mm for  $Re = 2.5 \cdot 10^6$  and 0.38mm for  $Re = 5 \cdot 10^6$ ). The position of lowest pressure in Abbott's figure was  $0.7c$ . Wind turbine blades rarely operate at Reynolds numbers larger than  $5 \cdot 10^6$ , and this would imply that our stall flag height (0.3 mm) is too low to affect transition. However, the shape of the object causing flow disturbance is also important, and the stall flag has surface roughness. Furthermore, in Abbott's case, the position of lowest pressure was far behind the disturbance, which stabilised the flow. At conditions more comparable to wind turbine aerodynamics nearby or in separation, the lowest pressure will be located near the leading edge ( $<0.1c$ ), so that transition will take place much sooner. This explains why wind tunnel measurements showed that stall flags caused transition when located in areas of laminar flow (see figure 3.20). So stall flags cause transition when placed in laminar flow. However, when stall flags show separation, the flow has become turbulent far upstream if the stall flag position and thus no flow disturbance via transition takes place.

#### Influence on Transition in Practical Application

Commercial wind turbine blades often already have a leading edge roughness of approximately 0.5mm due to the manufacturing process [22]. Blades produced with very smooth leading edges will become contaminated by insects within a few months (depending



on the site and the season). This contamination soon reaches a thickness of 0.5mm [22]. On these airfoils, the height of the stall flags (0.2-0.4mm) is regarded as being relatively small compared to other disturbances. When studying the phenomenon of stall using stall flags, the airfoils are operating at large angles of attack. This means that the suction peak is located at a position  $< 0.05c$ , thus at the location of the natural roughness. The positions of the stall flags ( $>0.1c$ ) are much less sensitive to flow disturbance.

For wind tunnel experiments roughness is simulated by a tripwire with a diameter of 2 mm on the leading edge [58]. NACA [1] applies a standard roughness given by 0.30mm Carborundum grains over the first  $0.08c$  on the suction and pressure side, where the grains cover 5 to 10 percent of the area. At Delft University of Technology [49] a zigzag tape of 0.32mm height at  $0.05c$  on the suction side is used. The profile Reynolds numbers varied between  $1 \cdot 10^6$  and  $6 \cdot 10^6$  for these experiments. Compared to these types of simulated roughness, the disturbance of the stall flags is regarded to be small.

### 3.3.2 Drag Increase

The drag increase due to the presence of stall flags and tufts on the suction side of an airfoil was measured in the low-speed low-turbulence wind tunnel of Delft University of Technology. Traverses were made with a wake rake, and stall flags or tufts were placed on a perfectly smooth 30% thick airfoil of 65 cm chord at a Reynolds number of  $2.0 \cdot 10^6$ . The airfoil called DU97w300, was specially designed for the root section of wind turbine blades. The stall flags used for these experiments were of the type P17-2. The most important characteristics are the dimensions of the flap which were 2 cm high,  $125\mu\text{m}$  thick polycarbonate and 8 cm wide. For more detail reference is made to [14]. It should be noted that the applied stall flags still suffered from the Kelvin-Helmholtz instability, and thus showed relatively large drag increase compared to stall flags with the carbon flaps.

#### Results

The traverses measured with the wake rake are shown by figures

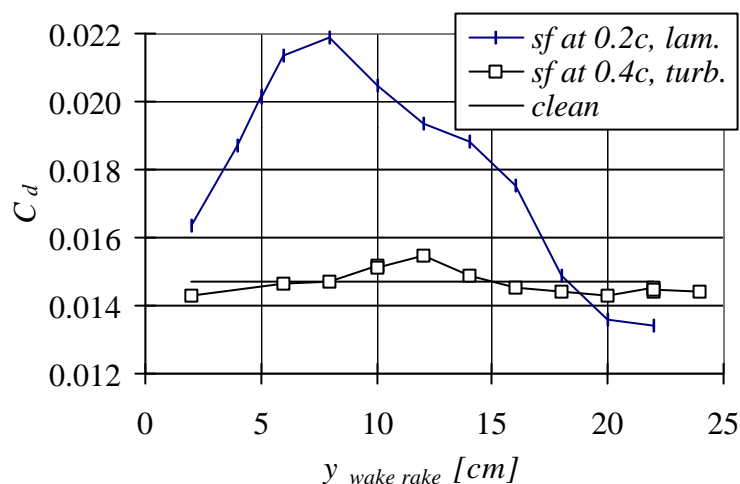


figure 3.18 Drag increase due to a stall flag in laminar and turbulent flow at an angle of attack of  $9^\circ$ .

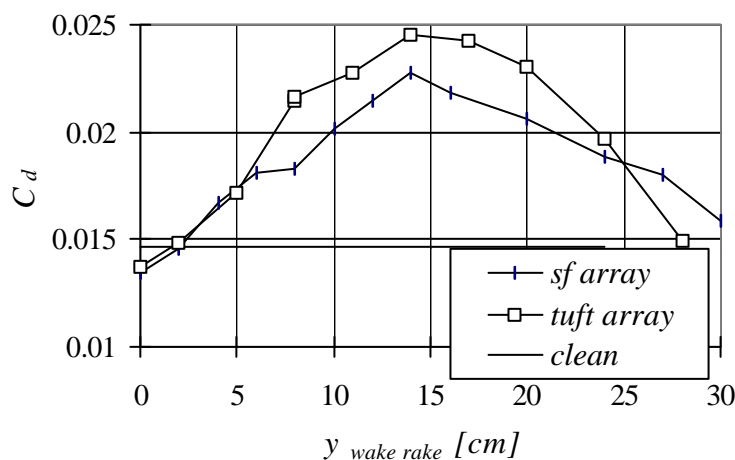


figure 3.19 Comparison of the drag increase due to row of stall flags compared to that due to a row of tufts, again at an angle of attack of  $9^\circ$ .

3.18 & 3.19. It can be seen that the drag increase for a stall flag located in laminar flow is large when compared to that of the clean airfoil. When the stall flag is located further downstream in the turbulent boundary layer, the drag increase vanishes. An overview of the results is given in table 3.3.

DU97w300, $Re=2.0 \cdot 10^6$ , $\alpha=9^\circ$	$c_d$ -increase
single stall flag at $0.2c$ in laminar flow	0.009
single stall flag at $0.4c$ in turbulent flow	0.0008
6 stall flags at $0.2, 0.4, 0.6, 0.8, 0.9$ and $0.95c$	0.016
6 rows of tufts at $0.2, 0.4, 0.6, 0.8, 0.9$ and $0.95c$	0.020

**table 3.3**  $C_d$ -increase due to stall flags. The clean airfoil had a drag coefficient of 0.145. It is assumed that the  $c_d$ -increase is concentrated over the width of the flap (8 cm) or tuft-row (8 cm). The values for the array of 6 stall flags or the 6 tuft rows are indicative only: the support layers of the stall flags or tufts puffed up during the measurements because the support layers were only fixed at their edges. At each of the indicated chord-wise positions in the last row, three tufts of 1 mm times 4 cm were located.

These results depend on the conditions. At larger angles of attack, transition would have been located closer to the leading edge and the stall flag at  $0.2c$  would have been located in turbulent flow. Thus a drag increase like that of the stall flag at  $0.4c$  is expected. Furthermore the perfectly smooth airfoil did not represent the actual wind turbine blades, which would experience turbulent flow closer to the leading edge at equal inflow conditions. The third reason, why the drag increase would be even smaller in practical application than the listed values, is that the stall flags do not cover the entire span. For optical reasons (see chapter 4) the maximum number of stall flags on a line from tip to tip is approximately 90, which means that the span-wise distance between the stall flags is typically  $D/90$  (depending on the resolution of the video camera). From optical reasons it follows also that the stall flags should have a width of approximately  $D/500$  of the diameter in order to remain visible. Combination of these numbers yields that the stall flags cover approximately 20% of the span when the maximum number is applied. We conclude that the most realistic value for the drag increase for real wind turbine blades is that of a single stall flag in turbulent flow and that this value will be 5 times smaller when averaged over the span. Thus it follows for the drag increase for wind turbine blades with the maximum number of stall flags in turbulent flow that  $Dc_d \approx 0.002$ . As the drag coefficient of real airfoils is rarely less than 0.01, and as the drag in those cases is in general much smaller than the lift, it follows that the drag increase due to the stall flags can be neglected.

### 3.3.3 Influence on Pressure Distributions

Measurements were taken to find relations between the stall flag signals and the pressure distributions, and to see whether the pressure distributions change when stall flags are placed at different locations. Flags were deliberately placed approximately 1 mm apart from the pressure holes. If no flow disturbance occurred at this distance, then it would certainly not occur further away from the flags. In total 5 stall flags were placed on a 30% thick DU97w300 airfoil with their hinges at chord-wise positions:  $0.2c$ ,  $0.4c$ ,  $0.6c$ ,  $0.8c$  and  $0.9c$ . Pressure distributions were measured with these flags and without them. Angles of attack were  $-4^\circ$ ,  $0^\circ$ ,  $5^\circ$ ,  $10^\circ$ ,  $11.5^\circ$ ,  $15^\circ$ ,  $20^\circ$  and  $25^\circ$ . In all cases the Reynolds number was  $2.0 \cdot 10^6$ . No corrections were made for tunnel effects because only the differences between the situations with and without stall flags were important. Figure 3.20 shows the most interesting pressure distributions for  $5^\circ$ ,  $11.5^\circ$ ,  $15^\circ$  and  $20^\circ$  with and without stall flags. The immediate

conclusion is that they are hardly influenced by the stall flags pasted nearby. In the case of  $5^\circ$ , a premature transition due to the stall flags can be seen. For the clean airfoil it occurred at  $0.34c$ , while it already occurred at  $0.2c$  when stall flags were present. In the case of large angles ( $20^\circ$  and  $25^\circ$ ), the flow became three dimensional, which was concluded from visualisation with tufts. Then also, the pressure distributions were hardly influenced. The maximum change of the pressure due to the stall flags has been quantified. The average difference and the standard deviation between the pressures measured without and with stall flags are given in table 3.4. In the table the two-dimensional flow situations at low angles are separated from the less reproducible three-dimensional flow situations at large angles. In the table the differences are given by the sum of the influence of the stall flags plus the reproduction error. Our conclusion is that the effect of stall flags on the pressure distribution can be disregarded.

quantity	$\alpha=4/0/5/10/11.5\&15$	$\alpha=20\&25$
absolute average difference in $c_p$	0.002	0.04
standard deviation of difference above	0.02	0.06

table 3.4 Influence of the stall flags on the pressures measured.

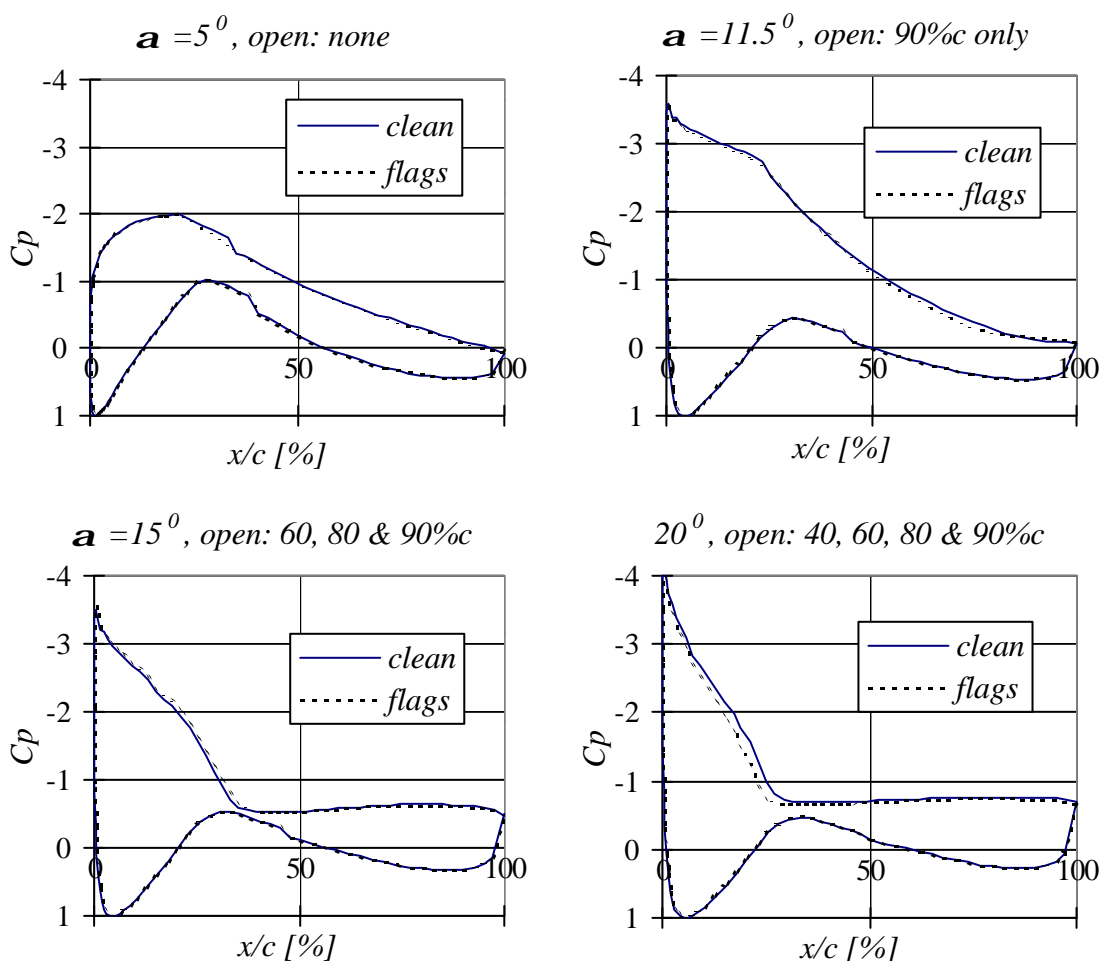
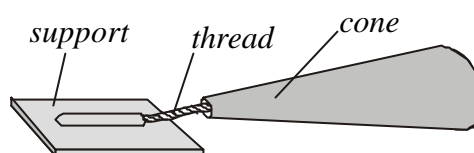


figure 3.20 Pressure distributions with and without stall flags. It can be seen that the flow perturbation is minimal and that the stall flags in the flat range of the pressure distributions indicate reversed flow.

### 3.4 Tufts and Stall Flags Compared

When the first paper including flow visualisation with tufts was published in 1928 [36], it was already denoted as a standard technique. Since then improvement of the tuft technique has been topic of many studies. An overview can be found in the Handbook of Flow Visualisation, chapter 'Tufts' by Crowder [23]. The improvements of the tufts technique focussed on: visibility enhancement, reduction of flow disturbance, reduction of external force dependence (centrifugal forces) and avoidance of the self-excited whipping motion. This was reason to invent 'fluorescent mini tufts' in combination fluorescence photography. Both the visibility was improved and the flow disturbance and the influence due to external forces were reduced. Self-excited motion was avoided with flow cones (see figure 3.21). Retro-reflective tape could be applied to these cones which much improved visibility. Such a retro-reflective cone comes close to the stall flag, but the latter has three significant advantages.



**figure 3.21** *The flow cone of Crowder [13].*

First, the stall flags are predominantly driven by pressure forces, which only act when the stall flag switches between states. When the flap is flat on the surface, there is hardly any interaction with the flow, whereas the flow cone is mainly drag-driven under all conditions. Second, the on-off character of the stall flag signals enables easy and even automated detection of the separated area on objects up to 100m diameter (see chapter 4). Third, the stall flag is, in most applications, little influenced by external forces. These forces are attenuated according to the sine of the opening angle of the flap, and when the hinge angle is zero, there is no influence by the centrifugal force. The tuft, however, is subject to a strong turning moment by centrifugal force in attached flow. On small rotors large directional deviations and large flow disturbance should be expected. Flow visualisation with tufts on an entire rotor blade of 6.5m span was shown to be possible, but the tuft signals could not be detected automatically [29]. Whether tufts directed towards the tip meant radial flow or 'slow reversed flow' could not be detected. For example in [61] the authors conclude that the flow is separated when they observe tufts pointing in radial direction on a blade of 0.6m span, but in fact they were misled by the large centrifugal force. When the centrifugal force gives the tufts a deviation side-wards from the flow direction, they start acting as effective vortex generators and so postpone separation. This was observed on a 100-m diameter rotor [12]. From equation 3.4 it can be seen that the ratio of aerodynamic and centrifugal force becomes larger for smaller rotors, so for the 0.6m span blade we expect huge flow disturbance by the tufts. An overview of the characteristics of the stall flag and the tuft is given in table 6.1 in chapter 6.

## 4. Optical Aspects of Stall Flags

We have seen that the detection of separated areas on the blades of wind turbines is crucial for the understanding of the stall behaviour. We also showed that our new indicator, the stall flag, is very well suitable for responding to flow separated by the change of the position of the flap. But still the state of a stall flag should be read out somehow. In fact the optical and contactless read out of the stall flag state is one of its principal benefits. In this chapter we deal with many options that can be made. Where should we put the retro-reflector. Underneath the flap or on the flap? And how large should the reflector be and what type should we use?

We then model the stall flag and the recording system for the most beneficial options. Our model is based on basic optical theory [25] in conjunction with experimental data. The model is subsequently used to calculate the optimum configuration and we finally compare the optical properties of the stall flag to those of tufts.

## List of Symbols

$a$	[-]	aperture
$A$	[m <sup>2</sup> ]	size of contrasting area
$AD$	[-]	Absolute Demand on visibility
$c$	[m]	blade chord
$d$	[m]	distance between camera/light source and contrasting area
$d_e$	[m]	effective diameter of image of a contrasting area
$d_h$	[m]	horizontal distance to turbine
$d_L$	[m]	diameter of the camera lens
$d_R$	[m]	diameter of the contrasting area of the stall flag
$d_{\lambda a}$	[m]	diameter of first order maximum of diffraction image of a point
$D$	[m]	diameter of the rotor
$D_{CCD}$	[m]	diameter of the CCD-chip
$D_{min}$	[J/m <sup>2</sup> ]	minimum detectable exposure
$E_i$	[W/m <sup>3</sup> ]	spectral irradiance of image of contrasting area
$E_{sun}$	[W/m <sup>3</sup> ]	spectral irradiance from the sun assuming an air mass of 1.5
$E_S$	[W/m <sup>3</sup> ]	spectral irradiance from the artificial source
$f$	[m]	focal length
$f_{L,B}$	[-]	Lambertian reflected fraction of the blade area
$f_L$	[-]	Lambertian reflected fraction of contrasting stall flag area
$f_{R,\theta}$	[-]	retro-reflected fraction of irradiance under angle $\theta$
$f_{R,\zeta}$	[-]	retro-reflected fraction of irradiance under angle $\zeta$
$h$	[m]	hub height
$I_{L,\theta}$	[W/msr]	Lambertian spectral intensity of contrasting area as secondary source
$I_R$	[W/msr]	spectral radiant intensity of the retro-reflector acting as secondary source
$I_S$	[W/msr]	spectral radiant intensity of the source
$I_{sf}$	[W/msr]	spectral radiant intensity of contrasting area of the stall flag as secondary source
$k$	[sr]	(space angle per unit cross section) per square distance to the source
$M$	[-]	magnification
$N_{CCD}$	[-]	resolution of CCD-chip expressed in # pixels on a line
$r$	[m]	radial position
$R$	[m]	rotor radius
$RD$	[-]	Relative Demand on visibility
$v_i$	[m/s]	velocity of the image over the detector area
$v_{tip}$	[m/s]	tip speed
$\beta$	[°]	pitch angle
$\beta_t$	[°]	total pitch angle
$\delta$	[rad]	half maximum cone angle of retro-reflected flux
$\Delta t_L$	[s]	illumination time of Lambertian reflective image of contrasting area
$\Delta t_p$	[s]	pulse duration of artificial source
$\Delta t_R$	[s]	illumination time of retro-reflective image of contrasting area
$\Delta t_s$	[s]	shutter time
$\epsilon_{Bi}$	[J/m <sup>2</sup> ]	exposure of the blade images

$\epsilon_{Ri}$	[J/m <sup>2</sup> ]	exposure of the reflector images
$\eta_D$	[-]	spectral sensitivity of the detector
$\eta_F$	[-]	filter spectral transmission
$\eta_L$	[-]	lens transmission
$\eta_S$	[-]	bundle efficiency of the source
$\theta$	[rad]	entrance angle between irradiance and normal to contrasting area
$\varphi$	[rad]	half maximum cone angle of the bundle of the artificial source
$\Phi_D$	[W/m]	spectral radiant flux from contrasting area incident to the detector lens
$\Phi_{i,S}$	[W/m]	spectral radiant flux of the source incident to the contrasting area
$\Phi_{i,sun}$	[W/m]	spectral radiant flux of the sun incident to the contrasting area
$\Phi_S$	[W/m]	spectral radiant flux of the source
$\Phi_{D,B}$	[W/m]	spectral radiant flux from the blade surface incident to the detector lens
$\lambda$	[m]	wavelength of radiation
$\zeta$	[rad]	angle between solar irradiance and normal to contrasting area

## 4.1 Principles of Detection

The stall flag has two optically different states that are assumed to correspond to ranges of flow direction (see figure 4.1 and 3.9). When a contrasting area is visible, the signal will be called ‘1’ and otherwise ‘0’, so the stall flag is a binary detector. The principle for detection is whether the contrasting area shows up or not. A tuft in comparison shows up all the time, and the detector should read the direction in which the tuft is pointing, which is much less clear (see figure 4.1). The text below discusses many ways to detect the binary stall flag signals.

### 4.1.1 Detectable or Visible

The stall flag signals can be observed by a detector (e.g. a video camera) or by the human eye. In the first case we speak about detection and in the second case about visibility. Detection is expressed in radiometric units and visibility in photometric units. We start the analysis by a radiometric analysis and derive then photometric results by multiplication by the spectral sensitivity of the detector or the human eye. Depending on the results, the signals will be concluded to be detectable or visible. Detection is more important because the human eye cannot follow the signals of hundreds of stall flags simultaneously. However, it is beneficial if the signals are visible too. Visibility allows an immediate check of the signals and draws the attention to uncommon events that may prompt the experimenter to adapt the measuring scheme.

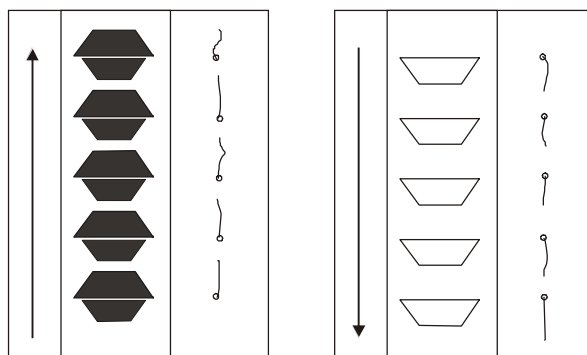


**figure 4.1** *Stall flags and tufts at equal conditions. On the left-hand side the flows moves upward, on the right-hand side it is reversed.*

### 4.1.2 Active or Passive

The stall flags are passively responding by the optical signal they give, but they may be made active to signal their turning over. One could connect an electric switch or optical sensor to each flag for example, and detect the state of that flag through a direct electric signal, fed into a computer via a data bus. This would require wires to each stall flag, however. We know from experience that this complicates instrumentation so much that the technique becomes prohibitive for application on a commercial wind turbine. Moreover, the computer would have to rotate with the turbine rotor or, if one wants to put the computer on the ground, electronic / optical slip rings or radio transmission techniques would be needed. This adds even more complexity.

Another option is to give each flag its own power supply so that it can send an active optic or radio signal to the ground and does not need wires. A battery, possibly in combination with a solar cell, can be used. It may be difficult however, to keep the flag then thin enough to not disturb the flow. The device should also be durably resistant to high centrifugal loads and to



rain during a period of minimally three weeks. These constraints are severe, however. In this thesis we restrict ourselves to the stall flag that operates passively.

#### 4.1.3 Stall Flag Positioning

Stall flags are applied to indicate the flow direction over the surface area of an object and in particular to indicate the area of reversed flow. We can use two types of stall flag patterns to find such areas. In the first, called the discrete pattern, a number of stall flags is pasted on the object on known positions. From the individual responses of the stall flags, one then knows where the flow type changes. The second way, the continuous pattern, is to cover the entire surface of the object with a sheet of stall flags placed closely together. In this case the positions of the particular stall flags are not known. Just the area on the object that 'lights up' corresponds to the area of the different flow type. The spatial accuracy of the luminous area follows from the accuracy of the recording system, while the accuracy obtained by the discrete patterns follows from the pasting accuracy.

Other differences are that the discrete pattern requires much less stall flags (is thus cheaper) and that it disturbs the flow less. However, stall flags might become less expensive (presently they cost 40Euro) and then the continuous option could become favourable, since it is easier to implement.

#### 4.1.4 Type and Locus of Contrasting Area

In practice the difference in visibility is obtained by application of retro-reflective foils or diffuse reflecting foils. The latter ones can be black, white, coloured or fluorescent. Reflection properties such as mirrored reflection, polarisation or phosphorescence are not used since no beneficial effects are expected from such materials. Optical differences based on diffuse reflection can be used without artificial light source, using daylight instead. When measurements take place on rather small objects (in particular in the wind tunnel) diffuse reflection gives good results. Retro-reflection is only useful with an artificial source and provides good results even on large wind turbines. When sunlight gives too much background, the measurements have to be taken at night. Both in the case of diffuse reflection and retro-reflection, stall flags of different colours can be used. Colours can be used to discriminate different types of stall flags or different angles of orientation of stall flags. Also it can be used to increase the resolution. The three colours of detection of a colour camera can be analysed independently. Thus three stall flag patterns, each using a different colour, can be detected simultaneously by a colour CCD-camera.

The contrasting area can be applied to several surfaces of the stall flag: at least three options exist: the support under the flap at one side, the flap at one side and both the flap and the support at one side, so that they work together. The strongest signal is obtained in the last case, but the stall flag becomes thicker and the flap becomes heavier. A thicker stall flag increases flow perturbation, and a heavier flap is slower and more sensitive to the centrifugal force. The strength of the stall flag signals depends, via the entrance angle, on stall flag hinge angle (figure 3.10), the flap opening angle (figure 3.8) and the rotor azimuth angle. This was studied for the different positions of the contrasting area in [13]. We will only rephrase the main result: the signal from the flap varies much more with azimuth than the signal from the support. So, for several reasons we advise to apply the contrasting area on the support only.

### 4.1.5 Retro-reflection

Most stall flags are provided by a thin retro-reflective sheet as contrasting area. Therefore several properties of retro-reflectors will be given.

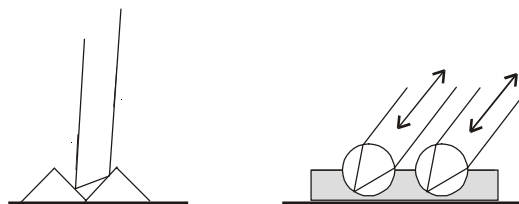


**figure 4.2** On the left-hand side the open cube edge retro-reflector and on the right-hand side the open sphere type retro-reflector, where the focal distance of the spheres equals their diameter.

#### Refraction or Reflection

Retro-reflection can be based on refraction or reflection. In the case of refraction, small spheres that act as lenses, with the property that their diameter equals their focal lengths, are pasted in white or reflective paint (see figure 4.2). A parallel incoming light beam focuses on the other side of the sphere, where it is reflected on the paint and returns to its origin. In the case of reflection the incoming light-rays are mirrored on three perpendicular reflectors (as the edge of a cube seen from inside) which return the ray in a direction parallel to the incoming direction. Retro-reflection, based on refraction in spheres, does not depend on direction of polarisation and it is isotropic. The latter property means that the retro-reflector can be rotated around its normal vector without any change of the retro-reflected beam. The cube-edge retro-reflectors are anisotropic and their efficiency is dependent on the polarisation of the incident beam. Thus the intensity of the returned beam depends on the blade azimuth too.

#### Open or Closed Geometry

Both the retro-reflectors of the refractive and the reflective type are available with open and closed geometry. Open means that the spheres or ‘cube edges’ form the surface of the reflector; closed means that the surface is a transparent protective sheet, which covers the cubes or spheres, or is part of them. Open retro-reflectors have a much higher efficiency for large entrance angles, closed types remain operational when wetted and are much less sensitive to contamination. The efficiency of closed types depends on the direction of polarisation of the incident beam.

#### Divergence

Due to small geometric imperfections of the retro-reflector and because of dispersion and diffraction, the retro-reflected ray will in general not be retro-reflected exactly parallel to the incoming ray. In the data sheets of retro-reflective foils often the fraction of the incoming beam that is retro-reflected within a cone around the incoming beam with half maximum cone angle  $\delta$  of  $0.2^\circ$  is specified (see figure 4.3). This fraction  $f_{R,\theta}$  (of approximately 1%) depends much on the entrance angle  $\theta$ . Although the returned fraction is small in absolute sense, the factor  $f_{R,\theta}\delta^2$  which occurs in the intensity is higher than the corresponding factor in the intensity of a perfect diffuse or Lambertian reflector of equal size with efficiency  $f_L$ .

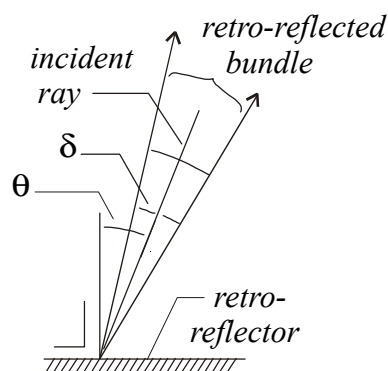


**figure 4.3** The entrance angle  $\theta$  and the half maximum cone angle  $\delta$ .

For commercially available thin retro-reflective sheets this factor is approximately  $10^3$  ( $f_{R,\theta} = 0.01$ ,  $f_L = 0.8$ ,  $\delta =$

$3.5 \cdot 10^{-3} \text{ rad} = 0.2^\circ$ ). This clarifies why small retro-reflective surfaces can be seen from a large distance. We use retro-reflective sheets in order to keep the stall flag thin, so that the flow will not be disturbed. However, if we would have accepted a few millimetres thickness, then special retro-reflective prisms could have been applied. For example in [28] a corner cube retro-reflector of 13mm diameter and 6mm height is mentioned, which returns over 90% of the incident radiation with an angular deviation of less than 3 arc second, so that  $f_{R,\theta} \delta^2 = 5 \cdot 10^9$ . This factor is high enough to make stall flag signals detectable even in bright daylight. But the current price of these prisms is approximately \$130,-, while a retro-reflective sheet costs approximately \$50,- per square metre, which is another argument not to use the prisms.

Figure 4.4 shows the entrance angle dependency for a spherical open retro-reflector. It can be seen that the open type has a higher efficiency for large entrance angles. Therefore this type (# 3M8850) is usually applied for the stall flags. For calculations the following relation for the entrance angle dependent efficiency is used:  $f_{R,\theta} = 0.016$  for  $0^\circ < \theta < 15^\circ$ ,  $f_{R,\theta} = 0.016 \cdot (1.36 - 0.022 \theta)$  for  $15^\circ < \theta < 50^\circ$ ; this relation is also shown in figure 4.4. The projected area in the direction of the incoming beam decreases by the cosine of the entrance angle. This is another reason why the stall flag signals become smaller when the entrance angle is decreasing. The product  $f_{R,\theta} \cos \theta$  expresses the net entrance angle dependent intensity of a stall flag based on retro-reflection.

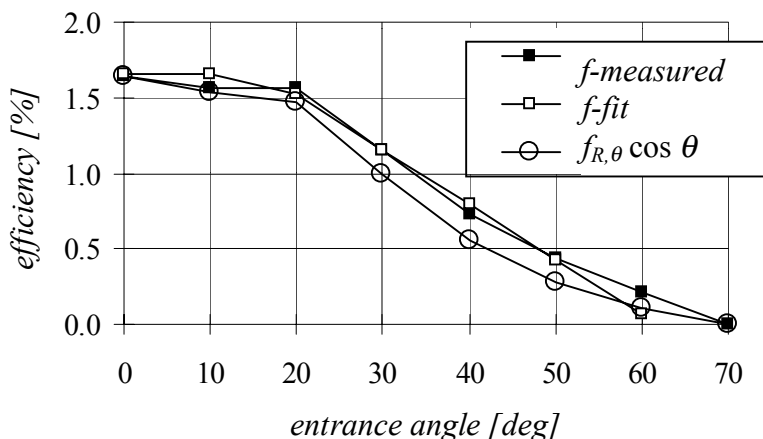


**figure 4.4** Retro-reflector efficiency as a function of entrance angle.

#### 4.1.6 Differential Detection

The outstanding property of stall flags is their good visibility and low resolution demands. However, when the wind turbines are large, even the signals of stall flags are not strong enough to detect in daytime. For this reason we mention a differential method to increase the sensitivity of detection. The method proposed is derived from the standard method to improve the signal to noise ratio in phenomena occurring at a certain prescribed frequency. This standard method prescribes the application of a high frequent stroboscopic light source. During each recorded video frame the source should produce a sequence of pulses and a lock-in amplifier in the camera should in phase amplify the variation of the stall flag signals. However, a CCD-camera provides a time integrated value for the brightness of each pixel, so that brightness variations during the exposure can not be detected and therefore this option fails.

A second option is using two cameras that observe the rotor through the same lens via a beam splitter. The shutters of the cameras are synchronous but slightly out of phase. While the shutter of one camera has just closed and the other is still open, a strong pulse of radiant

energy from an artificial source is supplied. Subsequently both images are subtracted and only the influence of the artificial source remains. Application of this difference method would however much increase the experimental complexity, which is fatal for field experiments. During the night the signals appear to be easily detectable without taking resource to a differential method. In practice this turns out not to be a severe restriction, so it was decided to maintain the method of direct detection.

## 4.2 Quantifying Stall Flag Signals

We will calculate the detection and visibility of the contrasting area of the stall flag by following the radiation from the source to the stall flag and from there to the CCD-chip or the human eye. The primary sources of radiant energy are the sun and the artificial source. The contrasting area acts as a secondary source that reflects a part of the incident radiant flux of which again a part is received by a camera or by an observer behind the turbine. We can model it as a disk of diameter  $d_R = \sqrt{4A/\pi}$ , when  $A$  is the area, since the image of a stall flag is so small that the precise geometry is lost. It will be shown that the strength of stall flag signals can be described by two numbers: the absolute ( $AD$ ), in which the sensitivity of detection is taken into account and the relative ( $RD$ ) which accounts for the background. If both numbers are larger than 1 then the stall flag signals are detectable.

### 4.2.1 Sources of Radiation

The exposure of the stall flag image will be calculated by assuming that we have two sources: the sun and an artificial source. The spectral irradiance from the sun  $E_{sun}$  is shown by figure 4.6. It is roughly equivalent to the radiation of a black body of 6000K. The spectral radiant intensity of the artificial source  $I_s$  depends on the type. When that artificial source has a total radiant spectral flux  $\Phi_s$ , of which a fraction  $\eta_s$  is bundled isotropically with half-maximum angle  $\varphi$ , its spectral intensity and irradiance are:

$$I_s = \frac{\eta_s \Phi_s}{2\pi(1 - \cos \varphi)}, \quad (4.1)$$

$$E_s = \frac{kI_s}{d^2}, \quad (4.2)$$

where  $d$  is the distance of the source, and  $k = 1$  unit space angle.

### 4.2.2 Intensity of Stall Flag Signals

The reflective properties of the contrasting area depend on the wavelength of the radiation  $\lambda$  and the angle  $\theta$  between the normal of the contrasting area and the irradiance. To include both the diffuse and retro-reflective properties, we assume that the area reflects a spectral fraction  $f_L$  as a Lambertian source and a fraction  $f_{R,\theta}$  as a retro-reflector. Both fractions are functions of the wavelength. The fraction  $f_{R,\theta}$  also depends on the entrance angle  $\theta$ . It is assumed that  $f_{R,\theta}$  is retro-reflected isotropically within a bundle with divergence  $\delta$ , which also is a function of  $\lambda$ . Stall flags with optical differences due to diffuse or retro-reflective properties can be modelled by changing the fractions.

### Lambertian Contribution

The spectral radiant fluxes reflected by the stall flag depend on the irradiance from the sun  $E_{sun}$  under angle  $\zeta$  and on that from the artificial source under angle  $\theta$ . They are given by:

$$\Phi_{i,sun} = E_{sun} A \cos \zeta \quad , \quad (4.3)$$

$$\Phi_{i,S} = E_S A \cos \theta \quad . \quad (4.4)$$

The stall flag will reflect a fraction  $f_L$  as a Lambertian source, so the excited Lambertian spectral flux  $\Phi_L$  and Lambertian spectral intensity  $I_{L,\theta}$  become:

$$\Phi_L = f_L (\Phi_{i,sun} + \Phi_{i,S}) \quad , \quad (4.5)$$

$$I_{L,\theta} = \frac{\Phi_L \cos \theta}{2\pi} \approx \frac{f_L \Phi_{i,sun} \cos \theta}{2\pi} \quad . \quad (4.6)$$

If we compare the contribution from the sun ( $< 1 \text{ kW/m}^2$ ) to that from the artificial source ( $< 1 \text{ kW/swept rotor area}$ ) then the first is many hundred times larger, for a small turbine of 10m diameter already. Therefore the diffuse contribution from the source can be neglected with respect to that of the sun during the day, which justifies the approximation in equation 4.6. If the solar flux becomes much less than  $1 \text{ kW/m}^2$  the two Lambertian fluxes may become comparable, but then Lambertian contribution to the stall flag signal is in practice too small to be detected.

### Retro-reflective Contribution

The retro-reflective fractions depend on the entrance angle. Therefore it follows for the retro-reflected spectral excited flux that:

$$\Phi_R = f_{R,\zeta} \Phi_{i,sun} + f_{R,\theta} \Phi_{i,S} \quad , \quad (4.7)$$

where  $f_{R,\zeta}$  is the retro-reflected spectral fraction of sunlight with direction of incidence  $\zeta$ . Since the retro-reflected light is concentrated in the narrow bundle directed backwards to the source, two bundles of high intensity can be discerned, one towards the sun and one towards the artificial source:

$$I_{R,sun} = \frac{f_{R,\zeta} \Phi_{i,sun}}{2\pi(1 - \cos \delta)} \quad , \quad (4.8)$$

$$I_{R,S} = \frac{f_{R,\theta} \Phi_{i,S}}{2\pi(1 - \cos \delta)} \quad . \quad (4.9)$$

In practice the directions to the detector and the sun are very different, while those to the detector and the artificial source are almost similar. Therefore the detector receives very low intensity from the sun, but high intensity from the source, so only equation 4.9 is relevant.

### Stall Flag Spectral Intensity

From equations 4.6 and 4.9 it follows that the radiant intensity of the stall flag is given by:

$$I_{sf} \approx I_{L,\theta} + I_{R,S} \approx \frac{f_L \Phi_{i,sum} \cos\theta}{2\pi} + \frac{f_{R,\theta} \Phi_{i,S}}{\pi\delta^2}. \quad (4.10)$$

Here the approximation  $1 - \cos\delta \approx \frac{1}{2}\delta^2$  is used, since typical values of  $\delta$  are less than  $1^\circ$ . It is also assumed that the detector is in the bundle with divergence  $\delta$ .

### 4.2.3 Stall Flag Image Size

The image of a stall flag is determined by geometric magnification, diffraction and detector resolution. The contributions of these three effects to the image size are estimated below.

From a geometric point of view the image of the contrasting area has a diameter of approximately  $Md_R\sqrt{\cos\theta}$ , where  $M$  is the geometric magnification factor of approximately  $10^4$ ,  $d_R$  is the area diameter of 0.04m and  $\theta \approx \pi/6$  rad. This is of the order of the wavelength of the light, so that diffraction becomes significant. Diffraction depends on the wavelength  $\lambda$  and of the numerical lens aperture  $a$ . We assume that the image of a point has a diameter  $d_{\lambda a} = 2.44\lambda a$ , which corresponds to the Airy disk [2].

In practice the image is formed on a CCD-chip with a limited resolution. We define the number of pixels on a line on the CCD-chip as the resolution, denoted by the parameter  $N_{CCD}$ , which in practice has a value of approximately 600. The image of a (bright) point source exposes at least  $2 \times 2$  pixels (due to imperfections of lens and electronics). Therefore details smaller than  $2D/N_{CCD}$  will not be significant, if the rotor of diameter  $D$  is imaged on the chip. For a rotor of 60m diameter  $2D/N_{CCD} \approx 20$  cm, while the contrasting area of a stall flag for such a rotor has a diameter of approximately 4 cm. Thus the image size becomes  $2MD/N_{CCD}$  larger due to the limited resolution, which means an increase of the image area by a factor of 25 for the case above (see figure 4.5) .

To obtain the image size of the retro-reflector  $d_i$ , we assume that it equals the root mean square sum of the size due to resolution ( $2MD/N_{CCD}$ ), diffraction ( $d_{\lambda a}$ ) and geometric scaling under an angle  $\theta$  ( $Md_R\sqrt{\cos\theta}$ ):

$$d_i^2 \approx M^2 \left( d_R^2 \cos\theta + \frac{4D^2}{N_{CCD}^2} \right) + d_{\lambda a}^2. \quad (4.11)$$

### 4.2.4 Image Spectral Irradiance

The optical axis of the lens is put parallel to the incident flux. In that case the spectral radiant flux falling on the detector lens due to a single stall flag  $\Phi_D$  becomes:

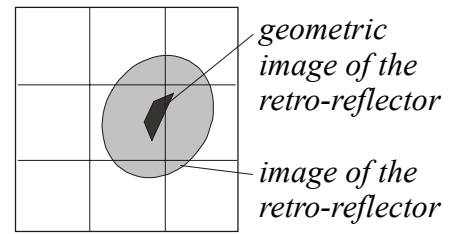


**figure 4.5** A fraction of a CCD-chip with only 9 pixels. The geometric image of a stall flag reflector is much smaller than a single CCD-pixel.

$$\Phi_D = \frac{kI_{sf}}{d^2} \pi/4 d_L^2 = \frac{\pi k I_{sf} M^2}{4a^2}, \quad (4.12)$$

if  $d_L$  is the diameter of the lens. The expression on the right-hand side follows from the substitutions  $a=f/d_L$  and  $f \approx Md$ , in which  $f$  is the focal length of the lens.  $M$  approaches  $f/d$  when  $f$  becomes much smaller than the object distance  $d$ . Since typical values for  $f$  and  $d$  are respectively 3cm and 100m, the approximation is valid. The flux  $\Phi_D$  will be filtered by a filter with spectral transmission  $\eta_F$  and subsequently a fraction  $\eta_L$  (the transmission of the lens) is distributed over the effective image size of the contrasting area.

The irradiance  $E_i$  at the effective image of the contrasting area follows from the ratio of the flux that passed the lens and the effective image size, assuming that the spectral radiant flux is homogeneously distributed over the effective image area:

$$E_i = \frac{\eta_F \eta_L \Phi_D}{\pi/4 \pi d_i^2} = \frac{k \eta_F \eta_L I_{sf} M^2}{a^2 d_i^2}. \quad (4.13)$$

#### 4.2.5 Image Spectral Exposure

The exposure, the product of the irradiance and the exposure time, is not a trivial factor, since the exposure time depends on many parameters.

##### Exposure Time

The exposure time is determined by three time intervals: the shutter time of the detector  $\Delta t_s$ , the pulse duration of the artificial source  $\Delta t_p$  and the time it takes for the image of the stall flag to move over approximately  $d_i/2$ . We will explain that it can differ for the diffuse and retro-reflective part of the flux. In practice the magnification is adjusted so that the rotor fills the entire field of view of the detector. The speed of a stall flag on radial position  $r$  on a turbine of radius  $R$ , which is rotating with angular velocity  $\Omega$ , is  $\Omega r = \Omega R r/R = v_{tip} r/R$ . So the speed of its image on the detector becomes  $v_i = v_{tip} M r/R$ . The image travels over  $d_i/2$  in a time interval  $d_i/2v_i = 1/2 d_i R / (r M v_{tip})$ . Thus the exposure time of the diffuse reflected part (from solar origin) of the stall flag signal is determined by the minimum of  $d_i/2v_i$  and  $\Delta t_s$ , while the exposure time of the retro-reflected part (from artificial origin) of the intensity of the stall flag signal is determined by the minimum of  $d_i/2v_i$ ,  $\Delta t_s$  and  $\Delta t_p$ .

##### Contrasting Area

For the exposure  $\epsilon_{R,i}$  of the effective image of the contrasting area we get:

$$\epsilon_{R,i} = \frac{4k \eta_F \eta_L M^2}{a^2 d_i^2} (I_{L,\theta} \Delta t_L + I_{R,S} \Delta t_R), \quad (4.14)$$

with  $\Delta t_L = \min(d_i/2v_i, \Delta t_s)$  and  $\Delta t_R = \min(d_i/2v_i, \Delta t_s, \Delta t_p)$



### Background

We assume that the background is formed by white wind turbine blades, which only reflect sunlight in a Lambertian manner. In this case the image of the object (the blades) is large compared to a CCD-pixel and to the wavelength, so that both the camera-resolution and diffraction do not significantly enlarge the geometrical image size. Therefore an area of the turbine blades of diameter  $d_B$  at an angle  $\theta$  is imaged as an area of diameter  $Md_B\sqrt{\cos\theta}$ . This means that the spectral irradiance of the image of the blades  $E_{B,i}$  is:

$$E_{B,i} = \frac{\eta_F \eta_L \Phi_{D,B}}{\pi/4 M^2 d_B^2 \cos\theta} = \frac{k \eta_F \eta_L f_{L,B} E_{sun} \cos\zeta}{8a^2}, \quad (4.15)$$

where  $\Phi_{D,B}$  is the spectral flux, incident on the detector lens from the area of the turbine blades, and  $f_{L,B}$  is the fraction of solar radiation that is Lambertian reflected by the white blades. The derivation of 4.15 from equations 4.12, 4.6 and 4.3 is straightforward. The spectral exposure of the white blades equals the product of  $E_{B,i}$  and the shutter time  $\Delta t_s$ .

$$\epsilon_{B,i} = E_{B,i} \Delta t_s \quad (4.16)$$

### 4.2.6 The Absolute Demand

We now derive the minimum incident radiant energy per unit area that can be detected, that is: the minimum exposure of the stall flag image. To this end the product of the spectral exposure of the image of the contrasting area and the spectral sensitivity of the detector should be integrated over the sensitive detector range, limited by  $\lambda_{min}$  and  $\lambda_{max}$ , and then needs to exceed a certain threshold. This ratio, which should be larger than 1 is called  $AD$ . For example: the image of a stall flag on a photograph should expose the film above its minimum exposure level. In equation form the absolute demand yields:

$$AD = \frac{\int_{\lambda_{min}}^{\lambda_{max}} \epsilon_{R,i} \eta_D d\lambda}{D_{min}} > 1, \quad (4.17)$$

in which  $\eta_D$  is the spectral detector sensitivity and  $D_{min}$  is the minimum integrated detector exposure that provides a detector response above noise level.

To optimise stall flag signals based on retro-reflection, we use the analysis above to rewrite the relation for the absolute demand as a function of the independent parameters. We assume that the stall flag image size  $d_i$ , the divergence angle of the retro-reflected radiation  $\delta$ , and the reflected fractions  $f_{R,\theta}$  and  $f_L$ , the efficiency of the source  $\eta_S$  do not depend much on the wavelength and obtain:

$$AD = \frac{2k^2 M^2 \eta_L \eta_S f_{R,\theta} \Delta t_R A \cos\theta}{\pi^2 a^2 d^2 \delta^2 d_i^2 (1 - \cos\varphi) D_{min}} \int_{\lambda_{min}}^{\lambda_{max}} \eta_D \eta_F \Phi_S d\lambda. \quad (4.18)$$

In practice the bundle of the source (with half maximum cone angle  $\varphi$ ) is adjusted in such a way that most of the radiant flux is homogeneously distributed over the swept area of the rotor ( $\frac{1}{4}\pi D^2$ ). Therefore we replace  $2\pi(1-\cos\varphi)d^2$  by  $\frac{1}{4}\pi D^2$ . This means that the optics of the artificial source is adapted in such a way that the irradiance of the swept area of the turbine does not change with distance between source and turbine. We also replace  $M=f/d$  by  $D_{CCD}/D$  and  $d_{\lambda a}$  by  $2.44\lambda a$  and obtain a useful expression for the optimisation of the stall flag detection system:

$$AD = \frac{4k^2\eta_L\eta_S f_{R,\theta}\Delta t_R \cos\theta}{\pi a^2 \delta^2 D^4 \left( \frac{\cos\theta}{D^2} + \frac{4}{d_R^2 N_{CCD}^2} + \frac{(2.44\lambda a)^2}{D_{CCD}^2 d_R^2} \right) D_{min}} \int_{\lambda_{min}}^{\lambda_{max}} \eta_D \eta_F \Phi_S d\lambda. \quad (4.19)$$

#### 4.2.7 The Relative Demand

The image formation in the detector will be affected by scattering on particles in the air, internal reflections of the lens, dispersion, diffraction and other effects. As a result there will be a background. So, the ratio of the stall flag image and the background, which we call the relative demand or  $RD$ , should be larger than unity:

$$RD = \frac{\int_{\lambda_{min}}^{\lambda_{max}} \epsilon_{R,i} \eta_D d\lambda}{\int_{\lambda_{min}}^{\lambda_{max}} \epsilon_{B,i} \eta_D d\lambda} > 1, \quad (4.21)$$

where  $\epsilon_{B,i}$  is the spectral exposure of the blade image. When the differential recording principle described in section 4.1.6 is used the factor can be much less than 1.

Using similar substitutions as in the calculation of  $AD$ ,  $RD$  is found to be:

$$RD = \frac{32k\eta_S f_{R,\theta}\Delta t_R \cos\theta}{\pi f_{L,B}\Delta t_s \delta^2 D^4 \cos\zeta \left( \frac{\cos\theta}{D^2} + \frac{4}{d_R^2 N_{CCD}^2} + \frac{(2.44\lambda a)^2}{D_{CCD}^2 d_R^2} \right) D_{min}} \frac{\int_{\lambda_{min}}^{\lambda_{max}} \eta_D \eta_F \Phi_S d\lambda}{\int_{\lambda_{min}}^{\lambda_{max}} \eta_D \eta_F E_{sun} d\lambda} > 1 \quad (4.22)$$

#### 4.2.8 Visibility

The above relations for detection can be converted to relations for visibility for the average human eye by replacing the resolution  $N_{CCD}$  by  $N_H$ ,  $\eta_D$  by  $\eta_H$  and  $D_{min}$  by  $H_{min}$ . The parameter  $N_H$  is the resolution of the retina of the human eye,  $\eta_H$  represents the spectral sensitivity of the human eye and  $H_{min}$  is the minimum luminous exposure that can be clearly seen. The human

eye adapts its sensitivity to daylight vision or night vision (the corresponding sensitivity spectra or efficacies being called photopic and scotopic respectively), but this adaptation changes the resolution much. Visibility is and remains a subjective property, but the relations can be helpful to roughly check if the signals will be visible. In practice the signals of retro-reflective stall flags can be seen very well, even when they are too low for the CCD-camera. The main reason is that the image of the retro-reflector is not much enlarged (see equation 4.9) due to poor resolution such as is the case in the CCD-camera. The resolution of the human eye can be compared to that of a CCD-chip with approximately 3000 pixels on a line. However, this number should be used with great care: it differs from eye to eye, it decreases rapidly when moving away from the macula lutea, it also decreases largely when the eye adapts to night vision and most important the brain plays an important role. The sensitivity spectra for a 'normal' CCD-camera and the human eye are given together with the solar spectrum in figure 4.6.

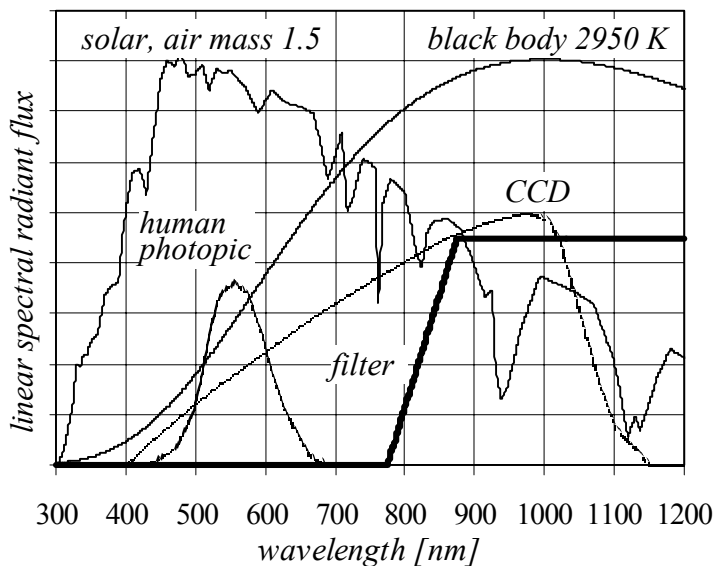


**figure 4.6** Sensitivity spectra for a 'normal' CCD-camera, a black body radiator at 2950K, a filter and spectral radiant flux of solar radiation at Air Mass ( $AR$ ) = 1.5.

## 4.3 Optimisation

Stall flags based on diffuse reflection need no artificial source and therefore are to be preferred above the retro-reflective ones. We therefore first deal with diffusely reflecting stall flags, only then with retro-reflective ones. It will be determined how the optimum combination of light source, detector, retro-reflector, filter etc. can be determined. For a complete overview of practical options reference is made to [18].

### 4.3.1 Diffuse Reflection

In the case of diffuse reflective stall flags the maximum intensity from the stall flags will be comparable to that of the white turbine blades: both reflect a large fraction of the ambient irradiance. For that reason stall flags based on diffuse reflection are preferably combined with a black support, which reduces the excitation around the stall flag (and thus the irradiance from the immediate neighbourhood). To take maximum profit of this effect, the image of the support should be approximately  $4 \times 4$  CCD-pixels if the stall flag image is approximately  $2 \times 2$  pixels. In practice this corresponds to a square with edges of  $4 \cdot D/N_{CCD} = 60\text{cm}$ , for a 60 meter diameter wind turbine and a detector resolution  $N_{CCD} = 600$ . This size is too large to manage easily, however.

The excitation from the black support in the sensitive spectral ranges of a CCD-chip or the human eye is almost 0 and therefore one expects that the relative demand is always fulfilled. But, in practice internal reflections and so on will blur the image and will increase the exposure of the black support. As a rule of thumb we assume that the exposure of a support of the size calculated above is approximately 10 times less than that of the white turbine blades. So we assume that a stall flag

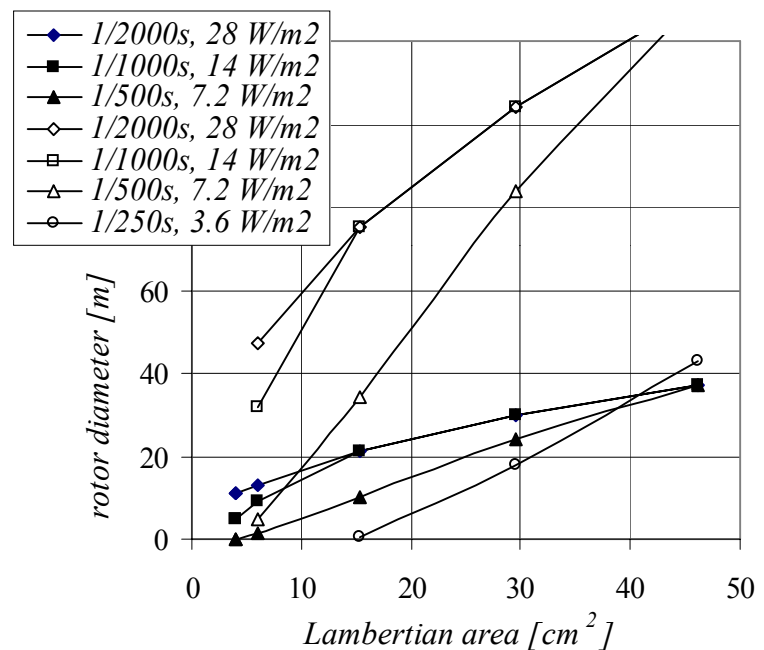


**figure 4.7** Simulation of the detection of a diffuse reflecting stall flag located at a blade tip. The settings were  $N_{CCD}=576$  for the filled symbols and 3000 for the open symbols,  $v_{tip}=55\text{m/s}$ ,  $a=2.0$ ,  $RD=0.1$ ,  $D_{min}=2.0 \cdot 10^{-6} \text{ J/m}^2$ . The legend shows the shutter time and the solar irradiance to obtain  $AD = 1$ . The curves show the maximum rotor diameter for which detection is possible. A better resolution improves detection largely. Motion blur causes that the high resolution curve with 1/250s shutter time is so low.

based on diffuse reflection is detectable/visible if the  $AD$ -value  $> 1$  and the  $RD$ -value  $> 0.1$ . The contrasting area of the diffuse reflective stall flags is more than twice as large as that of retro-reflective stall flags, since both the flap and the support under the flap in stall flag state '0' can be covered with reflective foil.

Using the relations for the absolute and relative demand derived above, simulations were carried out for typical stall flags on wind turbines of varying diameter. The results are shown in figure 4.7. The signals detected for a digital consumer video camera (1998) and by the human eye (which approximately equals that of a  $24 \times 36 \text{mm}^2$  slide) were simulated. For this reason  $N_{CCD}$  was set to 576 and 3000 respectively. The figure shows that stall flags of a contrasting area of  $15 \text{cm}^2$  can be applied on turbines of 20m diameter requiring a background irradiance of  $14 \text{W/m}^2$  or more. During the day such a background level is usually available (the irradiance from the sun in the Netherlands is approximately  $1 \text{kW/m}^2$  at noon in the summer). A turbine of 40m diameter already requires stall flags with contrasting areas of  $50 \text{cm}^2$ , which is rather large. Thus even in theory diffuse reflective stall flags are only detectable on small wind turbines. The figure shows that in the case of a much higher resolution, detection can be obtained even for turbines of 80m diameter with stall flags of  $30 \text{cm}^2$  only. So, with the high resolution, diffuse reflective stall flags are detectable even on large wind turbines, which seems an interesting option for the future, but in practice we will have severe disadvantages. The sun can be roughly in front of the turbine, so that it is a black silhouette in the bright sky for the camera behind the turbine. Or when the blades turn occasionally in the shadow areas the automatic image analysis would become very complicated. Furthermore light conditions change continuously due to passing clouds, and obviously measurements can not take place at night.

#### 4.3.2 Retro-reflection

From the integrals in formula 4.22, we see that spectral filtering can increase  $RD$  orders of magnitude. The filter can be chosen in such a way that the transmission is high at wavelength where the source spectral intensity is high and low where the sun has high spectral intensity. The source should emit most flux in narrow bandwidths, located in the sensitive spectral range of the detector and at wavelengths of low solar flux.

From both the relation for  $AD$  and  $RD$  it can be seen that they do hardly depend on the distance between detector and turbine: the only implicit dependency is that the retro-reflector efficiency increases by the distance because the entrance angle decreases. Furthermore it can be seen that  $AD$  drops by the second power of the rotor diameter  $D$  and for larger rotors even by the fourth power of  $D$ . The switch-over from second to fourth power (equal contributions) takes place for  $D = 6.7 \text{m}$  for usual detector settings ( $a = 2.0$ ,  $\theta = 20^\circ$ ,  $d_R = 2.8 \text{cm}$ ,  $D_{CCD} = 8 \text{mm}$ ,  $N_{CCD} = 576$ ,  $\lambda = 700 \text{nm}$ ). For a photo camera with  $24 \times 36 \text{mm}$  slides the switch-over occurs for  $D \approx 42 \text{m}$ , in which case the settings were ( $a = 2.0$ ,  $\theta = 20^\circ$ ,  $d_R = 3.6 \text{cm}$ ,  $D_{CCD} = 24 \text{mm}$ ,  $N_{CCD} = 3000$ ,  $\lambda = 700 \text{nm}$ ). We conclude that the retro-reflective stall flag signals are very easy to detect for small rotor diameters. Stall flags based on diffuse reflection can only be applied to small rotors and have even in those cases several disadvantages. Thus, also for small rotors retro-reflective stall flags are recommended. Only when all sources of radiation can be controlled, for example in a wind tunnel, diffuse reflection might be preferred. Then the signals become less entrance angle dependent and the sources do not need to be located close to the detector.

### 4.3.3 Summary

To get an overview of optimisation possibilities, table 4.1 shows the power by which parameters act in both  $AD$  and  $RD$ . We see that both decrease by the fourth power of  $D$  for large turbines. So it is beneficial to decrease the field of view of the CCD-camera as much as possible: the tips of the turbine can be cut off for the vertical upward and downward positions without much loss of information. After this measure most improvement can be expected from better retro-reflectors. The divergence angle  $\delta$  and the size of the retro-reflector  $d_R$  are optimisation parameters of a second power. Increasing the retro-reflector efficiency helps in a linear sense, and presently the retro-reflected fraction is less than 2%, so much improvement is possible. Then much profit can be derived from the parameters denoted with 'integral'. A clever combination of spectral radiant flux of the source and the filter regarding the fixed spectrum of the sun can much improve  $RD$ . This requires sources with a high radiant flux in a narrow bandwidth, but such sources often are not practical or very expensive. In [18]  $AD$ ,  $RD$  and prices of 17 different sources were calculated. Among these sources were sodium and mercury lamps of the high and the low (monochromatic) pressure type, several LASERS and LEDs, a krypton flash lamp and a 'normal' halogen lamp. The calculations showed that by far the best option was the halogen lamp. It provides high  $AD$  and  $RD$  for low cost. Figure 4.6 shows that the CCD-chip is very sensitive in the near infra red part of the spectrum and the halogen lamp, being a black body radiator at 2950K, produces most radiation in the same spectral range. Therefore the combination is good. We also expect good results from the flash lamps, since they do not radiate when the shutter of the detector is closed (which is most of the time), so that the needed power is approximately 50 times less. However, standard powerful flash units do not yet have short enough repetition frequencies and would complicate the set-up since synchronisation and high voltages would be required.

parameter	$AD$	$RD$
$D$ (large rotors)	-4	-4
$\delta$	-2	-2
$d_R$	2	2
$N_{CCD}$	2	2
$f_{R,\theta}$	1	1
$\theta$	-1	-1
$\Phi_S$	1	integral
$\eta_F$	1	integral
$\eta_D$	1	integral
$E_{sun}$	0	integral
$\eta_S$	1	1
$a$	2	0
$\Delta t_R (\leq \Delta t_S)$	1	1
$\Delta t_S$	0	-1
$D_{min}$	1	0
$\eta_L$	1	0
$f_B$	0	-1
$d$	0	0

**table 4.1** Approximate powers of the different parameters determining the retro-reflective stall flag signals. 'Integral' refers to the integrals over the spectrum in equations 4.19 and 4.22. It can be seen that the stall flag signals are independent of the distance to the turbine  $d$ .

## 4.4 Application on a Wind Turbine

When stall flags are applied on a wind turbine rotor, one needs to be certain that changes of the rotor's azimuth don't affect the detection of the signals. This may happen since the entrance angle varies and the distance between detector and stall flag changes. Such variations will depend on the radial and chord-wise position of the stall flags. By measuring the signals of contrasting areas at a few extreme positions, such a certainty can be achieved however, and we will show this below.

### Extreme Positions

In theory the extreme positions can be found by considering all geometric factors (total pitch angle, tilt angle, cone angle, deformation angles, yaw angles etc.) and all optical factors (light distribution in the rotor plane, bundle quality as function of half maximum cone angle, detector lens aperture changes with focal length etc.). However, this is cumbersome and also not very accurate, since many relations are unknown in practice. Therefore we focus on the most important factor: the entrance angle of the retro-reflector, which varies with changing azimuth and thus depends on the azimuth. The relation between entrance angle and efficiency has already been presented by the curve ' $f \cos(\theta)$ ' in figure 4.4. The entrance angle can be influenced by increasing the horizontal distance between the recording unit (source + detector) and the wind turbine and, of course, by adapting the stall flag pattern. The latter option is not desirable, as the stall flag positions are set by the positions where we want to learn more about the aerodynamics.

The entrance angle can be estimated by adding of two angles, namely the angle between the main rotor axis

and the ray from the source to the rotor centre, and the angle between the normal of the retro-reflector and the rotor axis. When the rotor blades are set in horizontal position these angles add linearly, and in other positions they add to a smaller value. For an estimate of extreme angles the horizontal blade position is therefore studied.

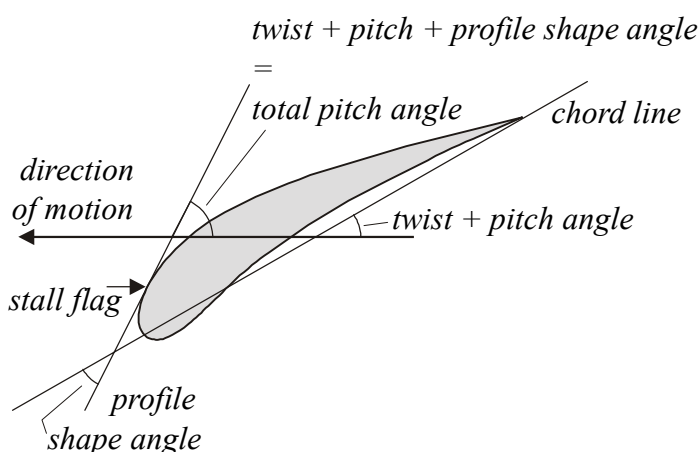


**figure 4.8** *Definition of the total pitch angle  $\beta_i$ .*

The angle between the normal of the retro-reflector and the rotor plane will be called the total pitch angle  $\beta_i$ , which includes twist, pitch and profile contour angle. The total pitch angle is defined by figure 4.8. To derive the extreme total pitch angle we start by analysing a typical thick and a thin wind turbine airfoil section as shown by figure 4.9. The thick profile applies to the root of wind turbine blades, and the thin profile to the tip section. In practice stall flags are mostly placed between  $0.2c$  and  $1c$  on the suction side of a profile (at locations where we

expect separation). From the figure it follows that the angle between the blade surface and the chord line varies between  $0.2c$  and  $1c$  from  $+7^\circ$  to  $-12^\circ$  for the thick profile and from  $+9.5^\circ$  to  $-12^\circ$  for the thin profile. Although many different profiles are used for wind turbine blades, the total pitch angles do not vary significantly if equal radial and chord-wise position are compared.

The pitch angle of a typical wind turbine is approximately  $0^\circ$  at the tip and approximately  $10^\circ$  at the root of the blade. Therefore the total pitch angles vary between  $+17^\circ$  and  $-2^\circ$  at the blade root  $r/R \approx 0.2$  and between  $9.5^\circ$  and  $-12^\circ$  at the blade tip  $r/R \approx 1$ . In both cases the values were given for respectively the leading edge and approximately  $0.7c$ . It follows from these values that the worst angles occur at  $0.7c$  on the tip ( $|\beta_t| \approx 12^\circ$ ) and at the leading edge of the root ( $|\beta_t| \approx 17^\circ$ ). So the position at the root is the extreme one regarding the entrance angle.

Later in this analysis we will return to the tip position, because the tip position could also become an extreme one in practice (the irradiance at the tips is usually less than in the centre due to the more or less Gaussian intensity distribution of the source). The tips can also become extreme positions because of the high speed, which smears out the images of tip-retro-reflectors and so decreases effectively the exposure time. One may note as well that the tip has the largest distance to the source (and thus has the lowest irradiance) when the blade is upward.

We return to the extreme position at the blade root. When the blade is horizontal and is moving upward, the entrance angles will be at the maximum and approximately equal to  $\theta = |\beta_t| - \theta_t + \arctan(h/d_h)$ , in which  $\theta_t$  is the tilt angle and  $h$  and  $d_h$  are the vertical distance and the horizontal distance between the rotor centre and the detector respectively. Since the entrance angle dependency of a retro-reflector signal is known, we can determine the signal as a function of  $h/d_h$ . In the previous section it was explained that the signal increases by distance and that it approaches its maximum at approximately  $d_h = 8h$ . The optimum distance is finite due to the tilt angle of the turbine and because of the property of the retro-reflectors that the retro-reflection efficiency is already maximal for approximately  $10^\circ$  entrance angle. In practice the optimum occurs at a shorter

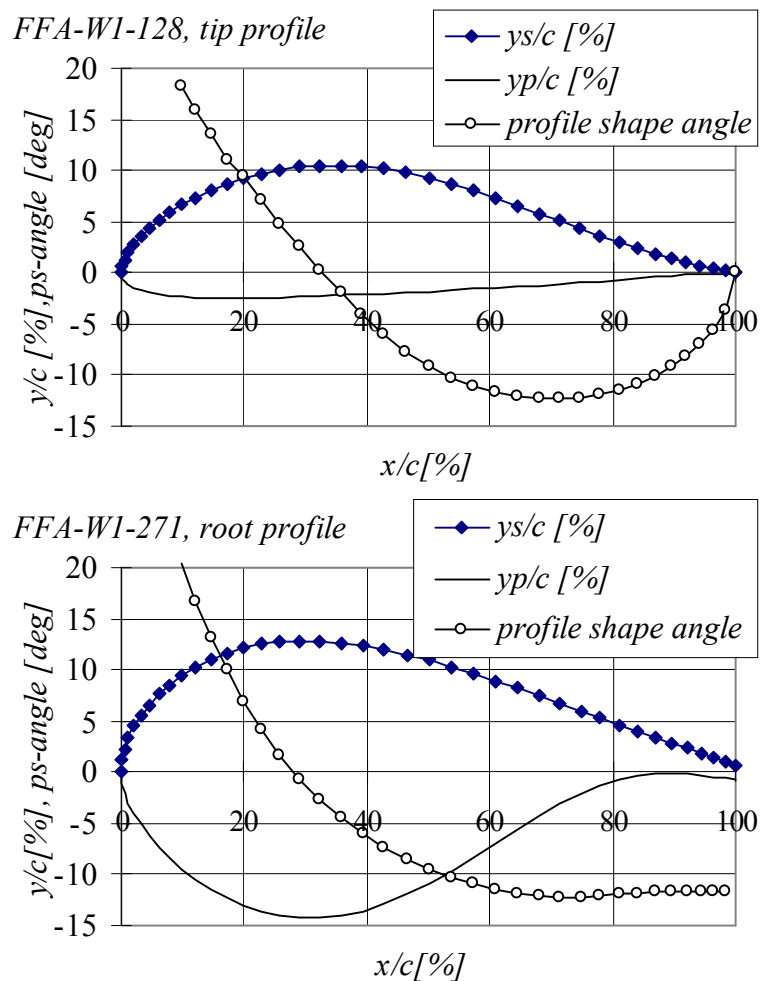


figure 4.9 The contour angles of a typical thick and a thin wind turbine airfoil section.



horizontal distance for reasons already mentioned (the aperture usually decreases by focal length and the bundle efficiency of the source armature decreases by decreasing bundle divergence). We recommend a horizontal distance between  $3h$  and  $6h$ .

Practical Proof for Detection:

The detection of the stall flags depends on many parameters of which some are unknown. Calculations can help to optimise stall flag signals and to predict the performance of many different sources of radiation, but detection in practice is never guaranteed by our formulas. We therefore recommend to past retro-reflectors (stall flags without flaps) of the size that is used for a stall flag on the trailing edge of the tip ( $r/R=1$ ,  $|\beta_t|\approx 12^\circ$ ) and at the leading edge of the root ( $r/R=0.2$ ,  $|\beta_l|\approx 17^\circ$ ). If they are detectable over the entire azimuth range, then any stall flag signal on positions ( $r/R<1$ ,  $0.2<x/c<1.0$ ) is also guaranteed to be detectable.

## 4.5 Tufts Signals

### Signal Strength

We define the signal strength as the ratio of radiant intensities excited by a flow indicator for attached and separated flow. For a retro-reflective stall flag this typically is as high as  $10^3$ . Tufts do not display intensity differences and therefore have signal strength 1. The signal of tufts has to be derived from the direction in which they are pointing and this sets high demands on the detector resolution.

### Resolution

A rather precise image of the tuft needs to be formed to distinguish its direction. The image of the tuft has to cover at least  $10 \times 2$  CCD-pixels, and since the tuft can turn in all directions, an area of approximately  $20 \times 20$  pixels is required. For a CCD-chip of approximately 600 pixels on a line, the maximum number of tufts on a line is approximately 30. However, the number of stall flags on a line, which each only need  $4 \times 4$  pixels, can be 150, so that the resolution requirements are  $(20 \times 20)/(4 \times 4) = 25$  times less. The image of the tuft is 10 pixels long, thus the real tuft should be  $10\text{pixels}/600\text{pixels} \times \text{rotor diameter}$  long. For a 60m diameter wind turbine this gives a length of approximately 1 meter, which is not realistic. For realistic tufts ( $2\text{mm} \times 5\text{cm}$ ) the maximum diameter of the turbine would have to be between 1.2 and 3m, much smaller than current commercial rotors are. For such small rotors one should expect flow disturbance and a high centrifugal deviation.

To solve this resolution problem, one can think of a rotating camera that follows only a single blade. In that case special engineering is required to fix the camera vibration free to the rotor and to transfer the signals without loss of quality to the ground. One should also protect the camera(lens) against contamination, moisture, high accelerations and lightning. Automatic image processing would become almost impossible, since the exposure varies much with azimuth: one moment the camera looks into the sky and a moment later to the ground. It would also be difficult to program a computer to automatically follow the tufts and read their directions. In our opinion tufts in combination with a rotating camera on a commercial wind turbine are not a realistic option. However, some tuft experiments on small wind turbines have been carried out.

Crowder [23] describes experiments with thousands of flow cones on the MOD II wind turbine of 100m diameter. Such cones are mentioned in section 3.4 and shown by figure 3.21. Although the centrifugal deviation decreases when the turbine becomes larger, he still observed a deviation of approximately  $20^\circ$ , which was initially considered to be acceptable. Later, wind tunnel experiments showed that the filaments acted as very effective vortex generators due to this sideward deviation and that the flow behaviour was altered substantially. Crowder used a large photo camera with an effective resolution of approximately 6000 times 9000 points. He had difficulties with motion blur but solved that later with a powerful flash lamp. Using this set-up he could take pictures of approximately half a rotor blade. The dynamic behaviour could not be followed and image analysis could not be done automatically. He concluded that the utility of flow cones for such rotating applications is limited considerably by their relatively high mass.

We stress that even with Crowder's very high resolution imaging, only a part of a blade could be observed. The flow on a wind turbine, especially at separated flow is highly dynamic. What one sees at one particular moment is not very interesting. Hundreds of images need to be analysed to find the dynamics of the flow. Therefore visualisation of a part of a rotor blade in a few instants does not give the information we are looking for. We need visualisation of the entire swept area during a considerable period with a sufficiently high image rate. Analysis of the obtained sequences of hundreds or thousands of frames is only possible with the aid of a computer. And then we take much advantage of the binary signals of the stall flags.

#### Motion Blur

For stall flag signals motion blur is not a problem and even an advantage. This blur causes light tracks where detector is in state '1' and darkness (nothing) in state '0', so that states can be derived from the images. This enables the application to fast rotating propellers in quasi steady operation: the average stall pattern can be obtained from a picture that is exposed for many revolutions (see the propeller experiment in appendix B).

For tufts however, motion blur over a fraction of the tuft length completely destroys the information. Even when the camera follows the object under study, or when the object does not move, information vanishes due to motion blur. This is due to the self-excited motion (Kevin-Helmholtz instability) of tufts, which was described in chapter 3.



## 5. Stall Flag Experiments

We begin by explaining the way stall flag experiments are set-up, carried out and analysed. The focus was initially on the solution of practical problems such as hinge durability and light source optimisation, but after about 10 experiments on wind turbines, the focus was shifted to aerodynamic questions. However, the development of the technique has not stopped. Recent novelties are a retro-reflective sphere on a line fixed to the nacelle to optically measure the yaw error, and an anemometer with retro-reflector, placed on the nacelle, that sends a wind speed signal to the video camera. Section 5.2 presents the first field experiment on a turbine of considerable size. We show the extent of the stall area and how the stall behaviour of this turbine was seriously disturbed by the sensors applied to measure the angle of attack. Section 5.3 deals with the peculiar stall behaviour of wind turbines in California, which will be discussed in light of chapter 2. For two additional experiments we refer to appendices A and B. The first aims at improvement of the power curve of a commercial rotor; the second demonstrates the fast response of the stall flag, the independence of centrifugal force and the advantage the method can gain from motion blur.

## 5.1 The Standard Procedure

### 5.1.1 Instrumentation of the Turbine

During the instrumentation four types of devices are installed on the wind turbine: the stall flags, the reference reflectors, a wind direction indicator and a wind speed indicator. It takes about 12 hours to install everything on the turbine if the work is done by two people in the basket of a crane. The instrumentation is non-intrusive and it can be easily removed. Pasting the stall flags on a 64m diameter turbine has also been tried by absailers; two men were fixed with ropes to the main shaft and sailed down along the blade, but the wind caught them and they were moving too quickly to stick anything on the blades accurately. Another possibility is to lift a person with a small multi-compartment helium filled balloon (see figure 5.1). The man and the balloon are fixed to a weight and the connecting rope is also used to control the altitude. We have only used a crane to instrument the blades. The method is as follows. One blade is put in a downward vertical position and the people in the basket move towards the blade tip. There they attach a measuring rope that will indicate the distance to the tip. They then move to the blade root fixing the rope every two metres. At the blade root they start pasting the stall flags and reference reflectors (and flow manipulators like vortex generators) while using

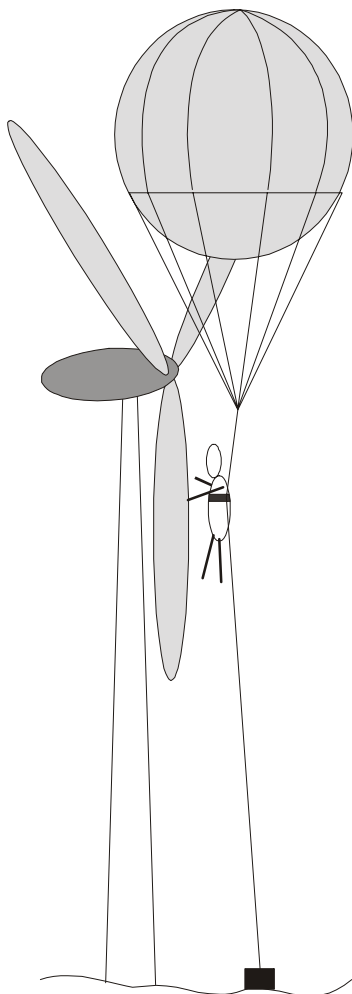


**figure 5.1** Possibility to instrument the turbine.

a second measuring rope to determine the chord-wise position. They continue moving downward and remove the rope that measures the tip distance. The orientation angle of the stall flags is adjusted by eye, or if accuracy demands it, a line fixed to the rotor shaft is used as reference. This procedure is repeated for each blade. The stall behaviour is largely dependent on the yaw error and the wind speed, therefore two devices are applied to record these signals with the video camera too.

#### Retro-reflective Sphere

A retro-reflector is pasted at the centre of the rear end of the nacelle and here also a thin line of about one blade radius length is also attached, see figure 5.2. At its other end we attach a retro-reflective sphere of foam, which simply moves freely with the wind. When the video camera in the field behind the rotor detects the foam sphere vertically below the rear of the nacelle, the wind is directed straight. This gives a reliable indication of any yaw error.

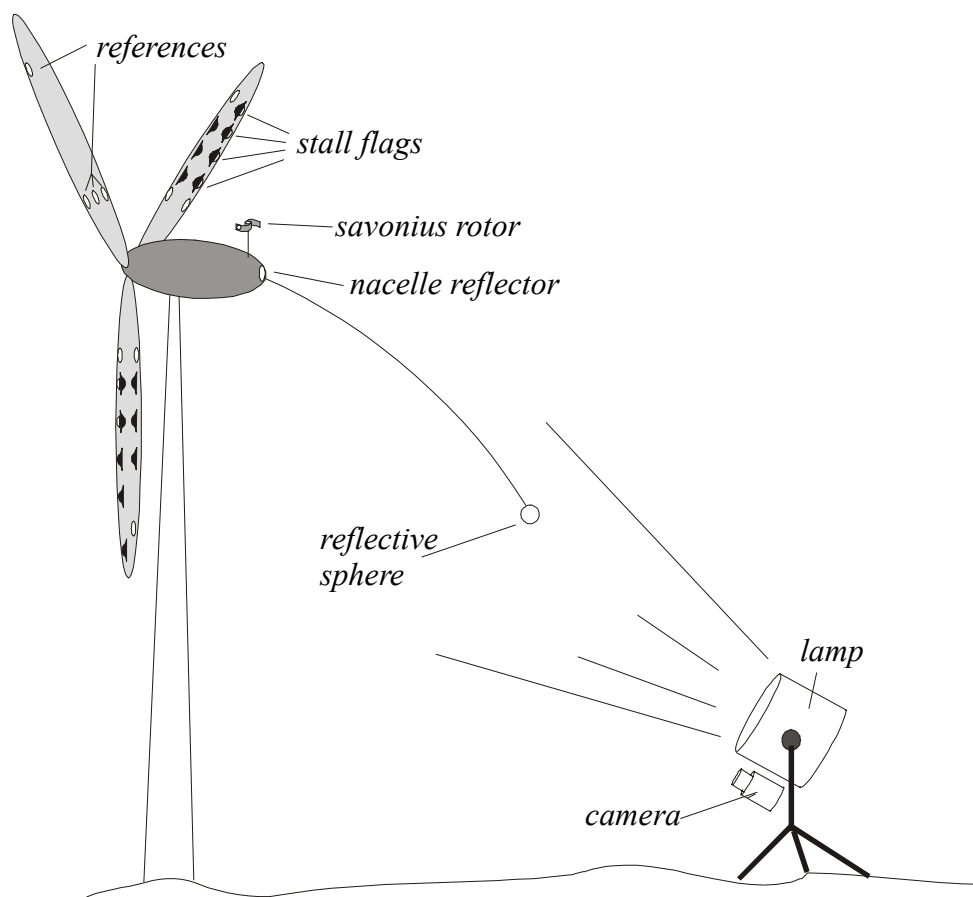


**figure 5.2** Set-up of a stall flag measurement, not on scale.

### Savonius Anemometer

During the most recent experiments reported here we also attached a 35cm diameter 3-bladed Savonius rotor to the nacelle. One blade was made retro-reflective, so that optical pulses were produced with a frequency in proportion to the wind speed. The video camera records the signal, the yaw error and the stall pattern simultaneously. The Savonius rotor is attached about 20cm above the nacelle, where the wind is strongly disturbed (see figure 5.2). Still its signal, which often is the only wind speed indicator, is relatively significant.

#### 5.1.2 Stall Flag Pattern

The stall flag pattern is determined by the objectives of the experiment and the technical restrictions. We discuss the most important aspects.

#### Different Experiments on Different Blades

The experiments often aim at determining the influence of a certain change, e.g. the effect of an additional row of vortex generators on the blades. Since the wind speed and direction can vary, it makes little sense to compare measurements just before and just after that change. The observed differences could be due to a different wind direction, wind speed, turbulence level and, if much time has passed between the measurements, by different blade soiling, humidity etc. For this reason we have used another method. We make a change on one or two of the

three blades and compare the behaviour of the blades. Thus we assume that the clean blades behave in the same way. If there is doubt, we can test this with a stall flag experiment. Then we keep one blade unchanged for reference and we make changes to the remaining blade or blades. We often keep the positions, types and orientations of the stall flags on the different blades constant, so that the differences we see are not caused by the different stall flag positions. The outcome of experiments may be affected by the mutual influence of the blades. But the eventual error is much smaller than that caused by a time lag between experiments.

**Stall Flags**

The resolution of our camera (digital video camera with 420.000 pixel full frame on a 1/3 inch CCD-chip) requires that the distance between the stall flags is approximately the rotor diameter divided by 90 (if the field of view encompassed just the entire rotor). The stall flags can be located anywhere between  $0.1c$  and the trailing edge and over the entire blade span. These spacing requirements mean that in chord-wise direction three rows of stall flags can be placed on the inner part of the blade and two rows on the outer part. If the operational range of vortex generators is studied, a recommended position for the stall flags is immediately down flow from the vortex generators. The size of the rotor sets the minimum stall flag size that can be detected. Larger stall flags can always be applied, for example to measure the thickness of the sheet of reversed flow. Table 5.1 gives an overview of the different stall-flag designs and their range of application. Figure 5.3 shows the support of the largest stall flag.

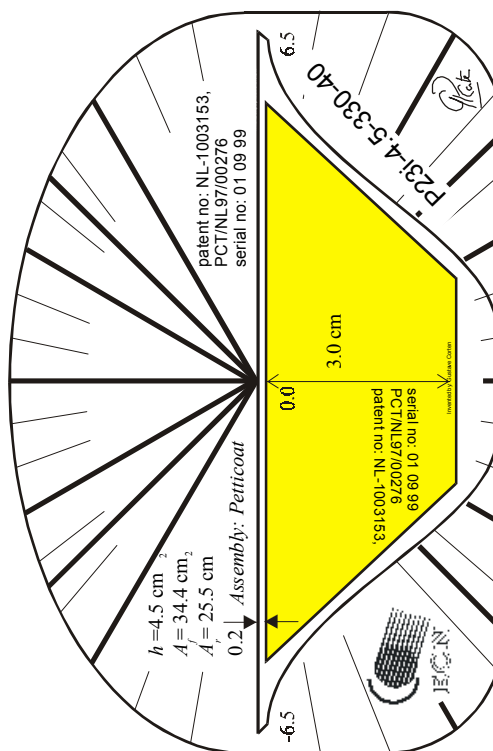


**figure 5.3** The largest stall flag scaled to 70% (see also figure 3.7).

Flap height width		rotor diameter	type of stall flag							
[cm]	[cm]		[m]	230-2h40 <sup>1</sup>		230-h40		125-h40		125-h25
[cm]	[cm]	[m]	[m/s]	[m/s]	[m/s]	[m/s]	[m/s]	[m/s]	[m/s]	[m/s]
4½	7.2	< 80	157	126 <sup>2</sup>	157	126	85	67	85	67
3	6.8	< 50	193	128	193	128	103	68	103	68
2	5	< 35	-	-	-	-	126	80	126	80
1	6	< 25	-	-	-	-	179	73	179	73
0.5		< 5	-	-	-	-	-	-	309	218

<sup>1</sup> In this number,  $A-BhC$ ,  $A$  is the thickness of the carbon flap in  $\mu\text{m}$ ,  $B$  is the number of hinge foils and  $C$  is the thickness of the hinge foil in  $\mu\text{m}$ .

<sup>2</sup> The first number is the speed limit to avoid Kelvin-Helmholtz instability in height direction, the second for avoiding it in width direction.

**table 5.1:** Different stall flags and their operational ranges



The type of stall flag is determined by the local flow speed expected. The higher the speed the stiffer the flap of the stall flags needs to be (see section 3.2.6). So we use for example type 230-2h40 at the tip and 125-h40 at the root.

The angle  $\gamma$  (defined in figure 3.10) under which the stall flag is installed is  $0^\circ$  in most cases. This choice makes a clear distinction of flow from leading edge towards the trailing edge or in the reverse direction possible; in this case the flap position is not influenced by the centrifugal force. Other angles are used if more resolution in flow direction is required.

### Reference Markers

These markers (which are retro-reflectors without flaps and thus are always visible) are used by the image processing software to follow the blades and to find the positions of the stall flags. The size of the reference marker should be twice the retro-reflective area of the stall flags, which size is set by the rotor diameter (chapter 4). The references also serve to recognise the different blades by placing them in different ways on the different blades. For the most recent experiments we used 3 references per blade and one more on one blade for identification (figure 5.2). The three references define the blade co-ordinate system for the image processing software. Therefore they should have a large mutual spacing in chord-wise direction and in radial direction; for this we use two markers near the largest chord and one marker at the tip.

The nacelle gets a reference marker at its rear end. This marker is used for determining the yaw angle (in combination with the reflective sphere) and to detect vibrations of the camera or nacelle.

### 5.1.3 The Measurements

After the instrumentation of the turbine, we wait for twilight. Then we position the camera and light source down-wind at a distance of about 4 times the height of the nacelle behind the turbine. The source has to be adjusted until it homogeneously illuminates the swept area and the camera has to cover that arc completely (a few tip chords may be cut off at the upper and lower side). We prefer a recording of the stall behaviour while the wind speed is slowly increasing from about 5 to 25 m/s, but we cannot control the wind. Therefore we have to work with a few different mean wind speeds over several evenings of taking measurements. Such recordings of ‘steady’ operation at a constant wind speed give the most reliable information, but often the interesting wind speeds do not occur during the ‘short’ measuring period. Therefore we experimented with recordings while starting and stopping the wind turbine to simulate wind speed variations.

### Starts and Stops

The idea is that we simulate a wind speed variation at constant rotation speed with a rotation speed variation at constant wind speed. In both cases we can get the same range of  $\lambda = v_{tip}/U = \Omega R/U$  values. The highest  $\lambda$  is obtained when the turbine reaches the maximum (nominal) rotation speed. So the wind speed should not be too high, say less than 10 m/s, to get the entire  $\lambda$ -range of interest. This procedure has one drawback: the induction of the turbine will not be in equilibrium with its operational state. When it starts, the induction will increase with a significant delay, and vice versa, there will be too much induction during a stop. The slower the change of the rotation speed of the rotor the smaller this error will be.

Its maximum value can be estimated by comparing the cases of steady induction and no induction. Since the start torque is much less than the brake torque, a start is slower than a

stop. So we prefer starts. Stops are also inconvenient since the tips are often deployed (turned over 90°) to serve as aerodynamic brakes. Turbines with a two speed drive train can be forced in low speed at relatively low wind to obtain a second interesting  $\lambda$ -value.

### Yawing

One can turn the turbine during the recordings to see the effect of a variation of the angle of attack on azimuth. This can be helpful in analysing dynamic effects (how fast do stall areas come and go). Using the yaw error and our extended blade element momentum theory (section 2.2.3), we can estimate the variation of the angle of attack along the blade on azimuth, and we can see its influence from the stall flag signals. Such measurements are difficult to interpret, but they turn out to be of great value in understanding the phenomenon of ‘double stall’.

### 5.1.4 Image Analysis

The image analysis starts with a fast assessment of the applicability of video recordings. A few interesting shots (often starts) are transferred over a firewire 1394 data bus from the digital video camera to a hard disk. These shots incorporate about 1500 frames, which is about one minute of video (although they sometimes take 10 minutes). Then the video file is converted into a sequence of separated video frames, each stored as a jpg-file. These files are successively opened by an image analysis program especially written for the application. This program starts with a conversion to 8-bit (256 values) black and white scale and subsequently sharpens the images. The process of data extraction is explained below.

### User Interaction

Each frame can be described as a black surface with about 10 to 300 bright spots from the visible reflectors. It turned out to be difficult to program a computer so that it would automatically find which spot refers to which stall flag or reference marker or other object. The user has to assist the computer in the interpretation of the first two frames, after which it will process the successive thousands. He has to point with a mouse to each reference reflector, the reflective sphere, the nacelle reflector and the anemometer. The computer reads the stall flag positions from an input file and finds them since it knows the positions of the reference reflectors. This procedure has been implemented with success. We will explain a few important aspects of the image analysis.

### Reference Reflectors

After two frames of user interaction the computer has the co-ordinates of the reference reflectors in two successive frames. From this it estimates the rotation speed and centre of rotation so that it can estimate the positions of the reference reflectors in the next frame. It will search for each reflector within a circle around the estimated position. All pixels above a certain threshold in the circle are used (weighted average) to find the measured position. The error between estimated and measured position is stored for each reference reflector separately as a moving average. The reference positions in all remaining frames are estimated by rotating the reflector around the rotor centre and adding the partly systematic error. This procedure implicitly corrects for perspective (the reflectors do not follow circular paths since the camera monitors from below), lens errors and low frequency vibrations. When a rotor blade disappears behind the tower it can remain invisible for 20 frames or so. In this period the estimated positions are based on the preceding estimates and the reference reflector will

only be found when it re-appears, when the procedure is very accurate. In practice it was proven that the program could find the blade after it disappeared for dozens of frames and sequences of thousands of frames could be processed automatically. This enabled statistical analysis of the dynamic stall patterns.

### Stall Flags

The computer should get the positions of the stall flags relative to the reference reflectors from an input file or by user interaction. Using this data it can precisely search for stall flag signals at the locations of stall flags. This procedure very effectively avoids the computer mistaking passing insects, rain droplets or sand particles for stall flag signals. When an insect flies over a stall flag in state '0', the computer sets the signal incorrectly to '1', but this is a rare event which only slightly affects the statistics.

### Reflective Sphere and Anemometer

Special subroutines follow the retro-reflective sphere and the Savonius rotor anemometer. The positions of these objects in each new frame are also estimated by extrapolating their tracks. The Savonius rotor on the nacelle can move through the frame because of camera vibrations, turbine yawing and tower bending. The extrapolation procedure only allows for small and slow movements of the Savonius rotor and much faster variations of speed and direction of the sphere. These differences are used to distinguish the objects when they come very close to each other or even completely overlap. The retro-reflective sphere in particular often crosses other sensitive positions (where the computer calculates positions of references or stall flags) without causing problems for a correct continuation.

### Vibrations

Measurements are sometimes carried out during high wind speeds. Then the tripod holding the lamp and the camera vibrates in the wind. Our video camera has an optical image stabiliser which filters most of these vibrations, so the recordings are stabilised to some extent. But sometimes, when severe vibrations occur, the image analysis may miss a reference reflector. These situations can be avoided when the retro-reflector on the nacelle is also followed. The translation made by this reflector should be added to the estimates for all other reflectors. Such a procedure can deal with most vibrations. However, when the camera vibrates in a rotational way around an axis parallel to its optical axis, this procedure will not help.

### 5.1.5 Experimental Data

Presenting graphs of the angle of attack  $\alpha$ , when stall sets in, or the tip speed ratio  $\lambda$  as a function of radial position  $r/R$  is valuable. These will be discussed in section 5.3 and in appendix A. Here we will give only a list of the data that become available from the video recordings.

- a. The frame number representing time.
- b. The state of each stall flag (0= closed, 1= open, t= behind tower, m = outside field of view).
- c. The rotation speed of the Savonius rotor by which the wind speed is estimated.
- d. The co-ordinates of the reflective sphere relative to the rotation centre.
- e. The yaw error as obtained from the nacelle reflector and the reflective sphere.
- f. The azimuth angle of each blade independently.

- g. The rotation speed from the derivative of the azimuth.
- h. The in-plane blade bending and from this eventually lead-lag vibrations.

Using these data we will try to find answers to the following questions:

1. What is the effect of vortex generators or stall strips? In which angle of attack range are they operational and how large is the blade area they influence.
2. Does the rotor stall before rated wind speed?
3. If overpower occurs, which rotor areas are still attached?
4. Is stall occurring at the leading edge or at the trailing edge?
5. How does the separated area extend with increasing wind speed?
6. How is the separated area influenced by shear, yaw, tower passage?
7. How are separated areas affected by turbulence, transition, blade contamination, rain etc?
8. What is the thickness of the separated area? (This can be measured with different flap heights.)
9. What kind of lead-lag modes do occur and what are their amplitudes?
10. Does the tower display side-ward bending?

## 5.2 Proof of Concept Using a 25m HAT

We have done small scale experiments, one of which is described in appendix B, where the response of stall flags and the reliability of their signals have been studied under actively controlled flow conditions. In the present section the first field experiment is discussed with stall flags on a turbine of reasonable size (28m diameter). It began April 4, 1995. We used stall flag prototype 5 and the later prototype 6 for this experiment at the 25mHAT of ECN, which is described in detail in [22] and [15]. With a few hours of preparation we saw reversed flow over the area of the blades of a full scale wind turbine.

The 25mHAT was the ECN test turbine between 1981 and 1998. It was used for many experiments, including some with stall flags. The main characteristics of the turbine are listed in table 5.2.

nominal power	300kW	cone angle	5°
rotor speed	20-55rpm	tilt angle	5°
hub height	22.4m	pitch angle	-12 to +80°
number of blades	2	profile	NACA4426-4418
rotor diameter	27.7m	wind	2.3D, H, upwind

**table 5.2** Data on the ECN 25mHAT test turbine.

### Proof of Concept

However, it took until March 1997 before we recorded the stall behaviour of an entire blade of the turbine. We applied the second series of stall flags of prototypes 15 and 16 [18], of which 200 were used. The flow behaviour over one blade, equipped with 57 flags (see figure 5.4) will be analysed. Properties of those flags are given in table 5.3. To be able to distinguish leading edge stall and trailing edge stall, stall flags were placed at two chord-wise positions: 20%c and 80%c. The blade was also used for pressure and angle of attack measurements. The positions for the (connectors of the) angle of attack probes are also indicated, the pressure tabs were located 50 cm towards the root with respect to each probe connector.

overall weight	< 1.0 g	hinge flexibility	< 10 · 10 <sup>-6</sup> Nm
flap weight	0.13 g	retro-reflective area	6 cm <sup>2</sup>
thickness	< 0.4 mm	flap area	9.4 cm <sup>2</sup>
flap fabric	polycarbonate	flap height	2 cm

**table 5.3** Characteristics of the prototype 16 stall flags.

The geometry of the rotor (Aerpac 25 WPX), is given in table 5.4. The profile of the blades varied from NACA4426 at the root to NACA4418 at the tip. In the wind tunnel (Re=3·10<sup>6</sup>) they stall at an angle of attack between 11° and 13°.

pos. [m]	chord[m]	thickn. [%c]	twist[°]
4.06 root	1.47	26.3	12.2
5.16	1.42	22.8	8.3
8.91	0.99	19.9	4.1
11.41	0.70	18.6	4.8
13.83 tip	0.43	-	0.0

**table 5.4** Geometric data of the Aerpac 25 WPX blade [50].

Analysis

A measurement at an average wind speed of 12 m/s and a rotational speed of 35 rpm will be presented. There was no yaw error. At five different pitch settings the non- averaged stall flag signals were determined from the video frames of two revolutions. The selected revolutions were always spaced about 12 seconds apart in time. In this early phase of our work 340 video frames were analysed manually. For example, the leading edge signal of figure 5.4 had to read as (from root to tip): 00011 11111 11010 01000 00010 0000. The total number of video frames was divided into six groups, each defined by a selected number of visible stall flags (1's). The larger this number, the larger the area flagged by the stall flags or the more the stall area has extended. Three groups, containing 0-5, 6-15 and more than 16 visible stall flags, do represent the extension of stall over the trailing edge, since the trailing edge stall flags switch over first. For the leading edge the groups contained 16-25, 25-35 and >35 visible stall flags. The leading edge groups have on average more visible stall flags, since the vast majority of the trailing edge stall flags are already in state '1'. The probability that a stall flag is open (p-open) is determined by averaging the stall flags signals within a group.

Results

The extension of the stall area over the leading edge is given in figure 5.5. The figure shows a few high peaks, which turn out to coincide with the position of the angle-of-attack sensor or the connectors for these sensors (see figure 5.4). These connectors thus severely disturb the flow, but the disturbances are local and confined to a narrow radial range. In all cases only one stall flag on the leading edge is severely disturbed. The signals for the trailing edge showed the same disturbances [15]. We exclude them in the rest of our analysis. (They pertain to flags, 5, 16 and 24 on both the leading and the trailing edge,

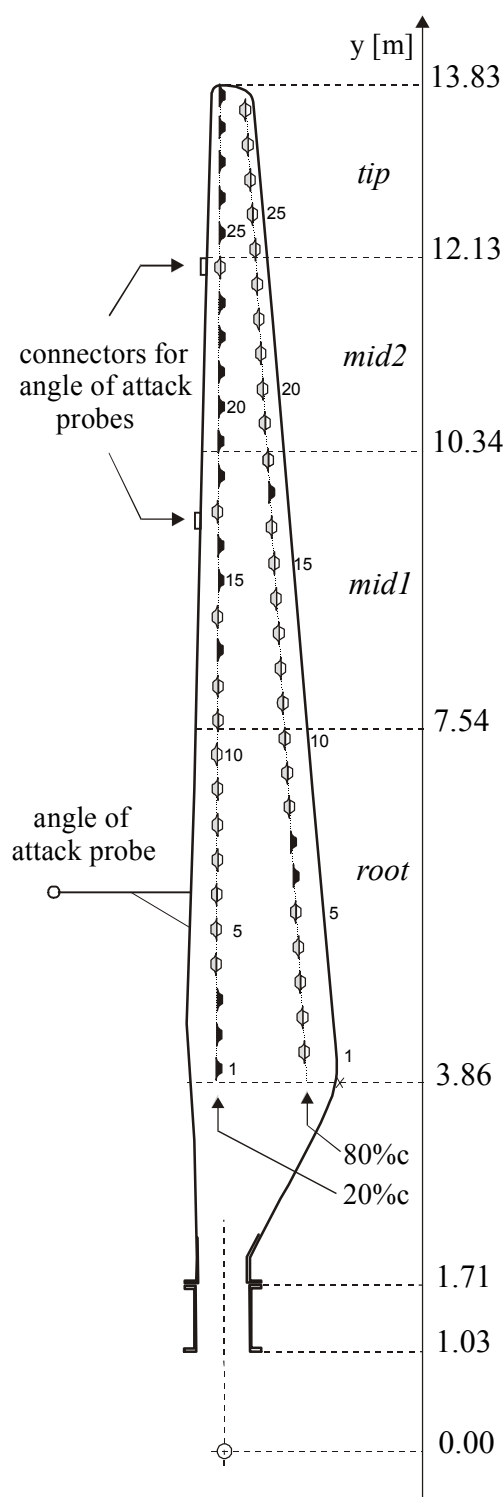


**figure 5.4** Stall flag pattern on the instrumented blade of the 25mHAT. The stall flags are pictured on a scale 4 times larger.

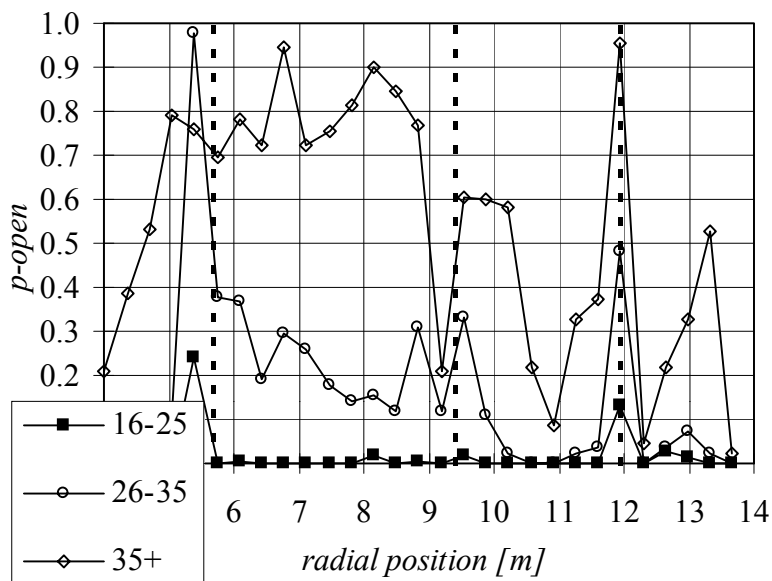


**figure 5.5** *Extension of the stall flag signals on the leading edge. The three dotted vertical lines indicate the positions of the inflow angle sensors or connectors. The peaks in the signals coincide with those positions. The influence of each disturbance seems to occur at a slightly smaller radial position than that of the disturbance itself. The disturbances increase  $p$ -open, except of that at approximately  $r=9.5m$ , where  $p$ -open dropped. The influential range of the disturbances is restricted to about 1 stall flag spacing, which is about half a chord.*

flow is expected, as is theoretically explained in chapter 2. Another explanation follows immediately from figure 3.17: for very large angles of attack the flow over the trailing edge is again directed towards the trailing edge, so a stall flag will be closed. To find which of these explanations is correct, we could have installed several stall flags with a large hinge angle of for example  $135^\circ$ . In the case of radial flow these stall flags would be closed, and in the case of attached chord-wise flow towards the trailing edge they would be open. Regretfully, there was no opportunity to do such an experiment.

### Conclusions

At any rate, we did prove the easy applicability of the stall flag method to a wind turbine in the field. Detailed dynamic (location and time dependent) data on the stall behaviour were obtained. We saw a large stall delay near the blade root. We also saw severe disturbances of the flow at the pressure probes near the angle of attack sensors, which means that the measured pressures do not represent a normal situation.

at radial positions of 5.30, 9.15, 11.95 and 5.48, 9.33, 12.13 metres for the leading edge and the trailing edge respectively.) After this exclusion, we come to figures 5.6 and 5.7.

Noting that the angles of attack increase towards the blade root, we infer that the stall area starts at the root and extends towards the tip. This agrees with the figures for radial positions larger than 5-6 metres. At the root section stall hardly develops and at the tip the signals are very spiky. We have no explanation for these tip signals, but the root signals suggest that rotation delayed the occurrence of stall. There could be other causes, however. The stall flags on the trailing edge were pasted parallel to this edge, so close to the root the hinge angle is about  $15^\circ$ . In pure radial flow, such flags will close, and in deep stall radial

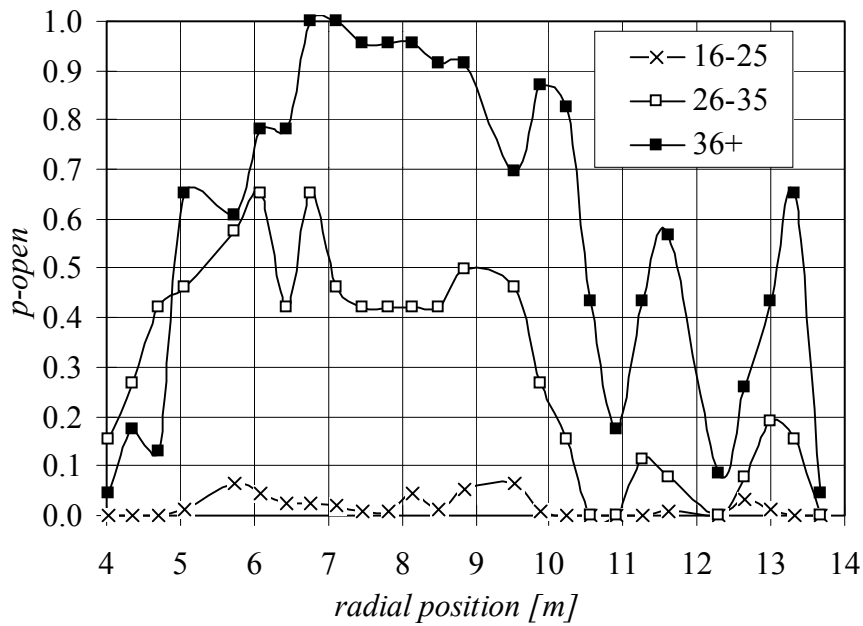


**figure 5.6** Extension of the stall flag signals on the leading edge, after exclusion of the three disturbed stall flags. The figure shows that stall at the root section is delayed. The spiky behaviour at the tip could not be attributed to a specific cause.

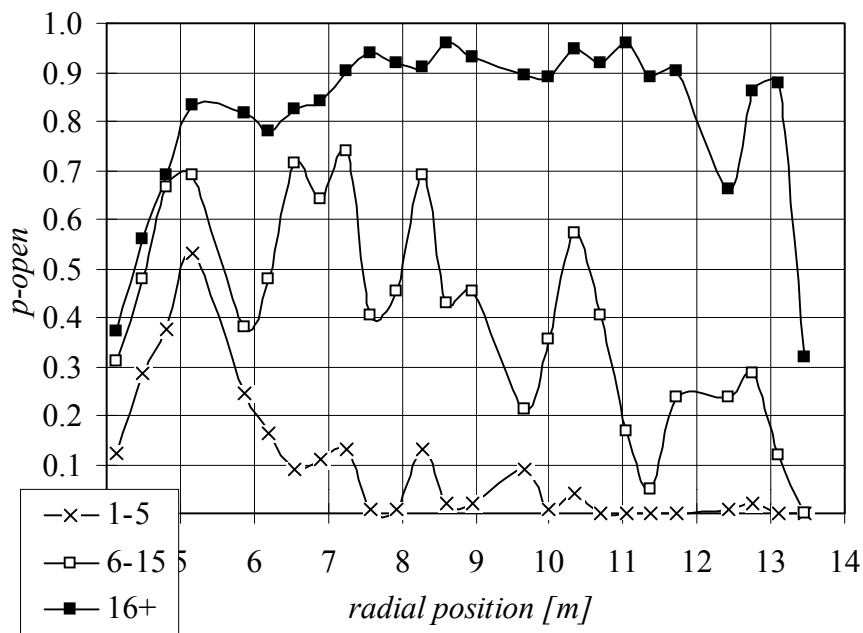


**figure 5.7** Extension of the stall flag signals on the trailing edge, after exclusion of the three disturbed stall flags. It can be seen that stall starts at about 5 m radius and extends outwardly, while  $p$ -open does not increase much at the root. Here we do not see strange effects when approaching the tip.



## 5.3 Multiple Power Levels

About 15 years ago the first observations were made that wind turbines apparently could have more than one power level in the same wind. The first publication on the phenomenon was made by Madsen [47]. At several turbine parks in California one noticed different power levels, of which the lowest was about half the design-level, see figure 5.8. The phenomenon, often referred to as ‘Double Stall’ or ‘Multiple Stall’ demonstrates the production losses (up to 25%) that may be involved. Several initiatives were taken to understand and solve the problem, for example the study of Dyrmoose and Hansen [27], the Joule project on Multiple Stall [54] and the analyses published by Risø [35,3].

Since the cause remained uncertain, we studied a 44m HAT at a Californian site as well. Our project started with an inventory of existing and new hypotheses, yielding a list of 10 hypotheses [22]. All hypothetical causes were based on contradictory events related to

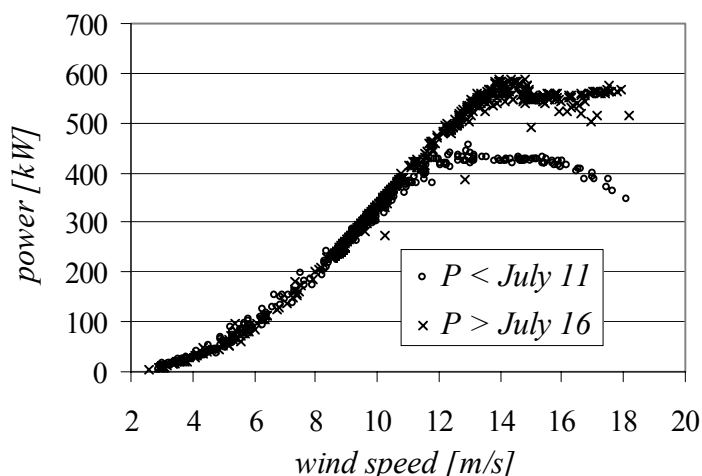


**figure 5.8** This figure shows an example of the power levels measured by Oak Creek Energy on a NEG Micon 700/44. The cause of this behaviour was unknown.

stall. We therefore carried out stall flag measurements on a turbine that clearly showed the problem: a NEG Micon 700kW turbine owned by Oak Creek Energy. Our working hypothesis was ‘the Tip Commands’, a model that seemed to give a good description of what might happen, but at the end of the project we came up with the ‘the Insect Hypothesis’. We first explain these hypothesis and then present the experimental results. At different sites and at different moments there can be different causes for multiple power levels. On September 3, 2000 we formulated the first possible cause not related to stall. It is described by the Terrain Concentration Model.

### 5.3.1 The Tip Commands Hypothesis

Here the phenomenon is attributed to the stalling of the blade tips [17]. Figure 5.9 presents a plausible sequence of flow states on the blade. The idea is that during high wind speed the stall area expands and shrinks in radial direction with the wind speed variations (the upper two blades in the figure). Thus somewhere on the blade a border exists with stalled flow on one side and attached flow on the other side. At this border the two flow types are competing. The attached flow sucks air from the separated flow and thus favours attachment of the separated area. Vice versa the separated area ‘pushes’ air into the attached region and so

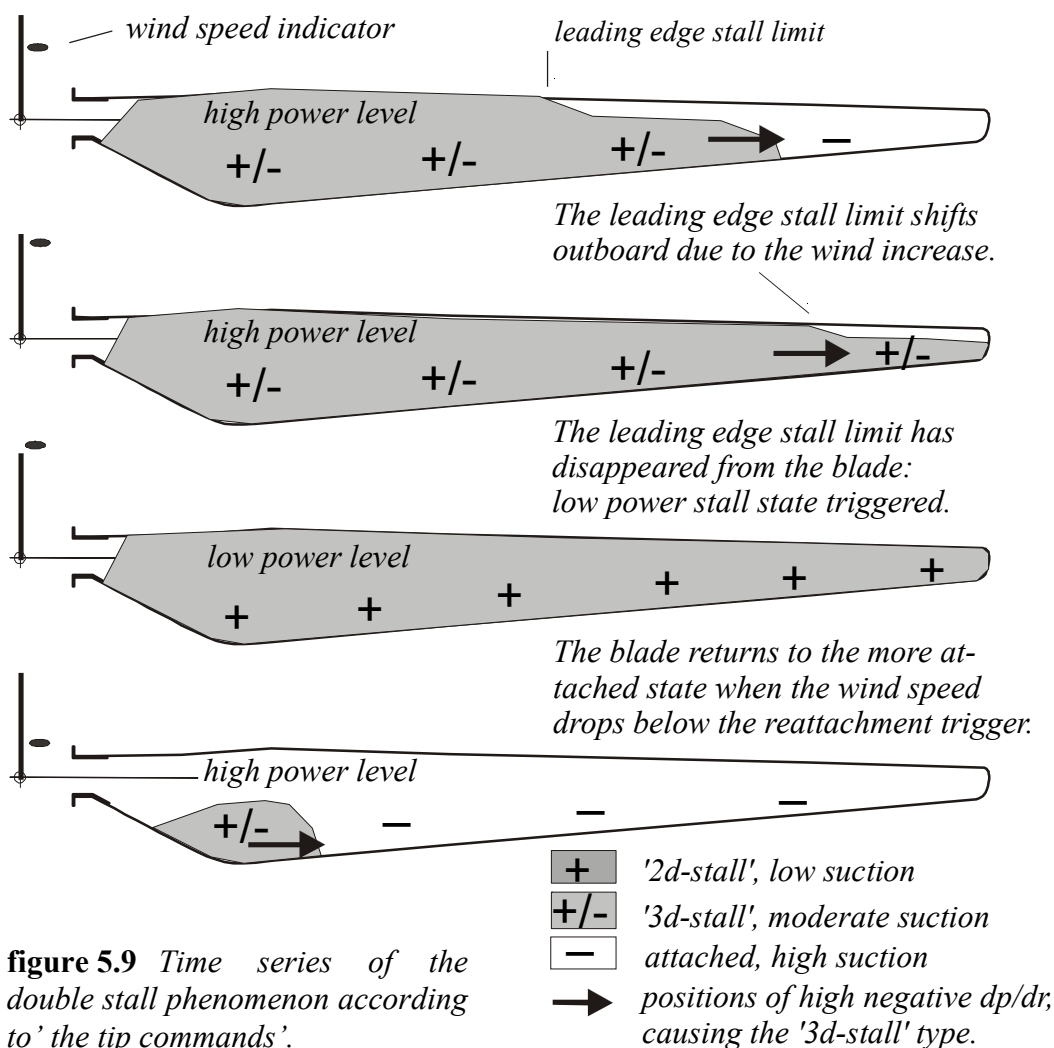


figure 5.9 Time series of the double stall phenomenon according to 'the tip commands'.

favours stall. Thus the border shifts until it arrives at a position where both effects are in balance. When the wind speed changes, the equilibrium is disturbed. The border will move towards the tip when the wind speed is increasing, and towards the root when it is decreasing. This process is, however, disturbed when the border shifts in a strong gust from the tip (see the third blade). Then the attached area has vanished, so that the suction of the attached flow does not help to reattach the flow when the wind speed is reduced again. Thus in a strong gust, the blade locks into the full blade stall state and from then on it will produce less power, or in other words, *the tip commands* the flow state on the remainder of the blade. It only switches back to the partly stalled state when the wind speeds greatly decreases (see the lower blade in figure 5.9 and the trigger mechanism of figure 5.10). So in this hypothesis every blade can have two states, one with the tip attached, one with the tip stalled. For a three-bladed rotor this may explain a maximum of 4 stall levels, one with all blades

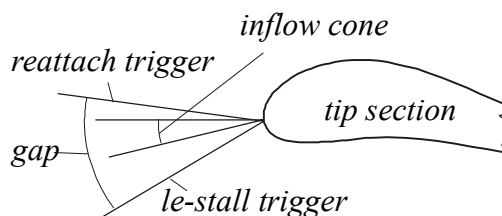


figure 5.10 The blade tip with the inflow cone and the triggers.

in the high power state and then three with 1, 2 or 3 blades in the lower power states. Most airfoil sections tested in a wind tunnel show bi-stable hysteresis in stall. When we turn the section to larger inflow angles until leading edge stall takes in, then we have to turn backwards over several degrees before the flow reattaches. In the above model this bi-stable stall cannot occur as long as there are both a stalled and an attached section on the blade. Therefore we think that the double stall hypothesis that has been put forwards in [3,4], which is based on bi-stable behaviour, cannot be explained without an additional assumption such as ‘the tip commands’.

### 5.3.2 The Insect Hypothesis

Here the phenomenon is attributed to the weather-dependent flying behaviour of insects. Figure 5.11 explains the mechanism in a diagram. It is assumed that the contamination of wind turbine blades increases only when insects are flying during turbine operation. Insects mostly fly when there is no rain, little wind and when it is not too cold, at temperatures above 10°C. If the turbine operates under these conditions, insects will increasingly contaminate the blade near the stagnation line. [Insects with a mass density much larger than air, follow a straight path when they crash on the frontal area of the airfoil near 0%*c*; at low wind speed (small angles of attack) the stagnation point is also near 0%*c*.] Here the flow is insensitive to contamination so that the power is not affected. [The flow speed near the stagnation point is low, so that the viscous shear is small, furthermore the negative pressure gradient beyond the stagnation point is stabilising the flow, which means that the flow will be almost independent of the contamination level near this point.] Above a certain wind speed, when insects rarely fly, the contamination remains constant. At high wind speed, the angle of attack along the blade is large and the suction peak has shifted to the contaminated area. [The flow speed in the suction peak is high, so that contamination causes high frictional drag in the boundary layer; moreover the positive pressure gradient beyond the suction peak destabilises the flow, which means that the flow will come to a standstill already at smaller angles of attack and thus will stall sooner.] Now the flow disturbance depends a great deal on the level of contamination, which shows itself as a decrease of the stall angle depending on the level of contamination. The smaller the stall angle, the lower the power level. This can also explain two or more power levels. The design level will be reached again when the blades are cleaned or when it rains during turbine operation.

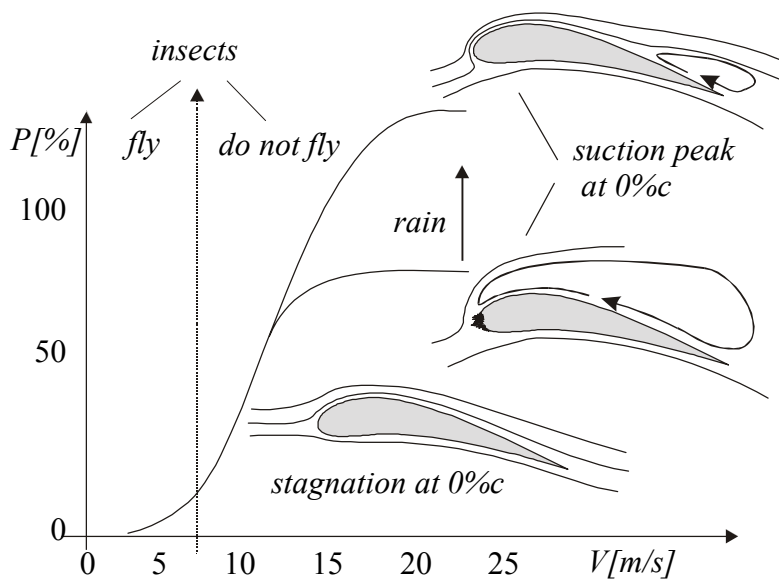


figure 5.11 The Insect Hypothesis.

5.3.3 Experiment with a 44m HAT

This section presents the experimental validation of the multiple-power-level hypotheses. In fact the above insect hypothesis was made half-way the experiments. It gave rise to further experiments to make sure that it was correct.

Set-up

In the project several stall flag measurements were performed with three different patterns of vortex generators, stall flags etc. on the rotor. We only present the most important measurements.

The corresponding

configuration is shown in figure 5.12. The leading edge of blade 1 was cleaned from root to tip between  $-20\%c$  (pressure side) and  $20\%c$ . Artificial roughness was applied on blade 2 from root to tip at  $0\%c$ . For the roughness a zigzag tape (0.5mm period) with a maximum thickness of 1.15mm and surface roughness of 0.8mm was used. The tape was 0.5cm wide between  $0.7-1.0R$  and 1.5cm between  $0.2-0.7R$ . All vortex generators of blade 3 were removed. This blade was not cleaned. The leading edges of blades 2 and 3 were contaminated with insects to a depth of about 0.3mm. The roughness was about the same over the entire span and was located at chord-wise positions smaller than  $5\%c$  on both the suction and the pressure side. The density of these disturbances was about 100 insects per square metre.

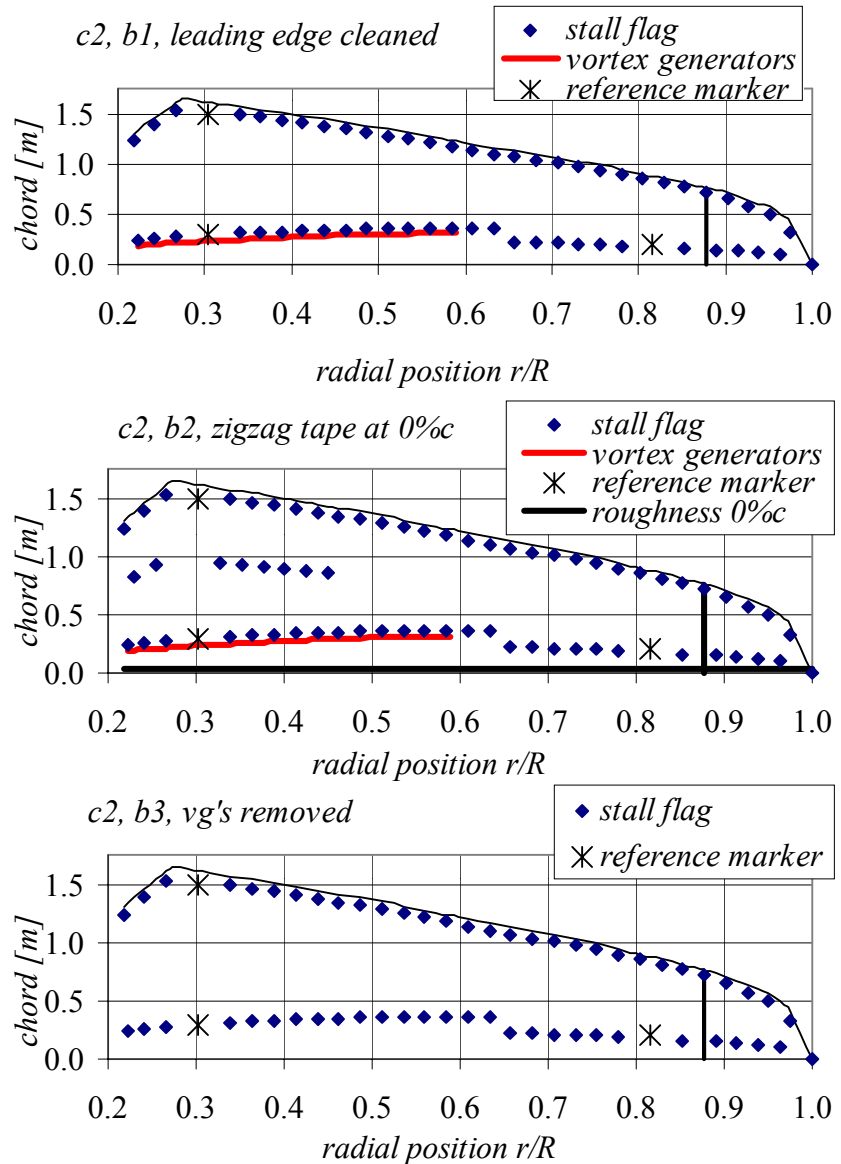


**figure 5.12** Configuration of the second measurement. The leading edge of blade 1 was cleaned. Zigzag tape was put on that of blade 2. The vortex generators of blade 3 were taken off.

5.3.4 Validation of The Tip Commands Hypothesis

This hypothesis implies that the tip may lock into a stable stalled state in high wind speed. We took measurements at 18 m/s average wind speed and we even yawed the turbine over 35°. Under these conditions the tip angle of attack varies between about 13° and 18° depending on the azimuth. Figure 5.13 shows two revolutions of the rough stall flag signals. These revolutions are representative of the results of some hours of testing, but do not show any sign of locking behaviour. The stall pattern ‘continuously’ follows the changing inflow conditions, although there might be some delay. This was the reason to believe that the double stall mechanism suggested by ‘the Tip Commands’ was not responsible for the multiple power levels of practice. In fact the command-mechanism was not yet triggered, since as figure 5.13 shows, the leading edges (0.2c) of the tips were still in attached flow.

But part of the model is confirmed: the blade did not show bi-stable hysteresis but a continuous behaviour as was expected from the model. This implies that the hypothesis in [3,4], which is based on bi-stable behaviour, is an unlikely candidate.

The figure shows another result: the stall flag pattern at the leading edges moves towards the tip with about 13 m/s. This observation *indirectly* confirms the that the radial flow speed in the stall area can be large (section 2.5.4). It is *indirect*, since we see the movement of the borders between separated and attached areas, not the radial motion of the air inside the separated areas.

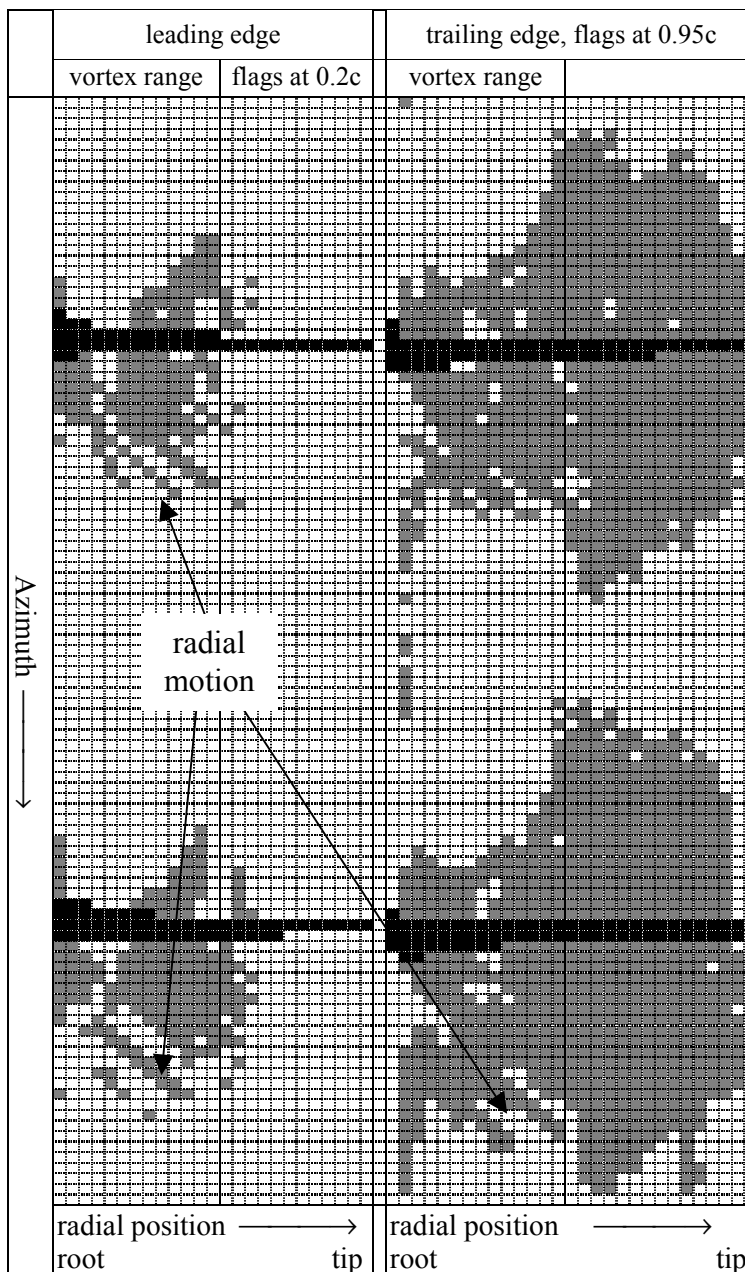


**figure 5.13** Two revolution of the rough stall flag signals (25 Hz) of blade 1. The grey area is where the stall flag indicates reversed flow, the white area is attached flow, the tower passage is black. The rotor speed is 27 rpm, the wind speed 18 m/s and the yaw error 35°. The radial speed of the stall areas is about 13 m/s.

5.3.5 Validation of the Insect Hypothesis

The video with the stall flag signals was analysed with the image processing program. After sorting out the frames on tip speed ratio  $\lambda = \Omega R/U$ , the  $\lambda$ -value at which the stall flag switched between its two states was statistically determined. The variation of  $\lambda$  was caused by changes of  $\Omega$  during starting and stopping the turbine. Figure 5.14 shows plots of the artificial wind speed  $\Omega R/\lambda$  versus radial position. The speeds are called artificial since it was not the wind that was changing but the rotation speed.

Stall Flag Results

We see in figure 5.14 that most stall flags on the leading edge of the rough blade switch over at 17 m/s on average, while those on the clean blade switch over at 21 m/s on average. It follows from this and other figures [22], that the roughness causes a large advance of stall in the wind speed range of 11 m/s to 25 m/s. As the influence extends over the entire span of all blades it can easily affect the power by dozens of percentage points. Therefore it can explain the multiple power levels.

Time series of PV-data

Time series of the power  $P$  and the wind speed  $V$  of four different turbines were studied in detail in order to validate the Insect Hypothesis [22]. The power levels appeared to become lower after each period of low wind speed. This confirms the Insect

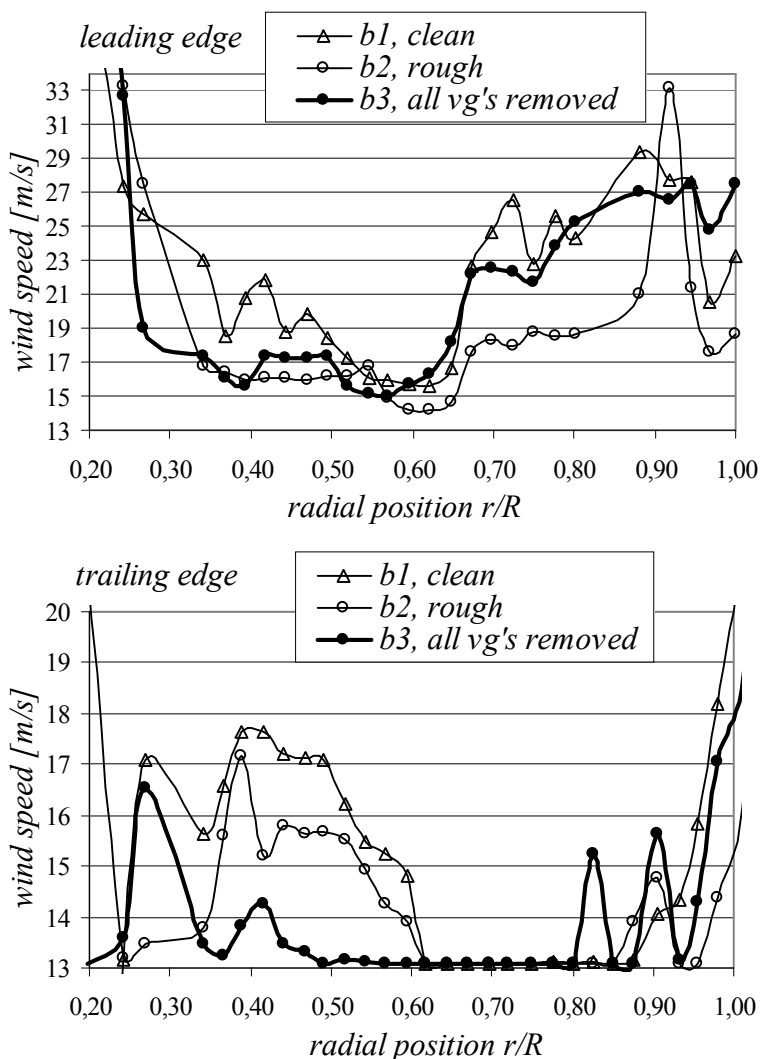


**figure 5.14** Plots of the wind speed against the radial position. The important observation is the large difference of the leading edge signals of blade 2 with roughness, compared to the other blades. Between 0.65R and the tip blade 2 stalls at about 18 m/s while blades 1 and 3 stall at about 25 m/s neglecting the peak in the signal of blade 2. This advance of leading edge stall corresponds to power losses of dozens of percents. The peak at about 0.92R corresponds to the first stall flag at larger radial position than the tip division. The centre of this stall flag is about 22 centimetre apart from the slit. The flow is largely influenced by the transient or the leakage through the slit. The trailing edge signals clearly show the delay of stall due to the vortex generators.

Hypothesis, since the contamination increases during each period of low wind speed (insects fly) and this progressively reduces the stall level. We also observed one period of no wind, after which the power did increase. However it was discovered that the blades had been cleaned by lots of rain. So in this case the Insect Hypothesis was also confirmed.

Influence of Artificial Roughness on Power

After gaining confidence in the hypothesis, a crucial experiment was carried out. Roughness (the same as before) was applied on the leading edges of all three blades, from 0.55R up to the tip of a turbine numbered 12-12. Another turbine, numbered 12-14, located 50 metres away, was left unchanged. We measured the power to see if different power levels would be obtained above rated wind speed, while the levels would be equal below rated wind speed. The results are shown in figure 5.15. We started taking measurements on October 8, 1999. On October 12 turbine 12-14 was cleaned, although it had not been very contaminated. Its power level increased by about 50 kW. Then, on October 34 (we continue on the October scale), the artificial roughness on turbine 12-12 was removed and the blades were cleaned. The power increased by about 250 kW to the same level as turbine 12-14. When comparing figure 5.15 with the demonstration of the multiple power levels in figure 5.8 we see that they are similar, which confirms the Insect Hypothesis.

Arguments against the Hypothesis

Can the Insect Hypothesis be refuted? One may argue that contamination is a continuous process and that the stall level would therefore change continuously rather than showing discrete levels. In fact jumps from one power level to another are observed (e.g. the jump in figure 5.16), and how can this possibly be explained by blade contamination? But this first argument is not valid, since contamination only occurs when insects fly and they do not fly when the turbine operates at its stall level. The jumps between power levels need not contradict the hypothesis either. They could be explained by ‘the Tip Commands’, but we have already shown that this model is not satisfactory. Within the Joule project ‘MUST’ such a jump was observed once. The power jumped down to 75% along with a 20° change of the

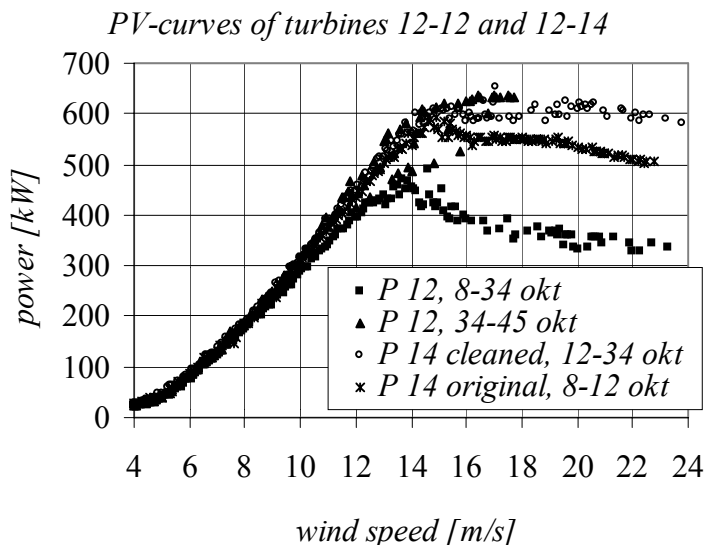


**figure 5.15** The power curves of turbines 12-12 and 12-14. The measurements started on October 8 1999, On October 14 turbine 12-14 was cleaned and the power went up by approximately 50 kW. On October 34 the artificial roughness was taken away from turbine 12-12 and the blades were cleaned. Then 12-12 produced like 12-14. The power level was clearly roughness dependent, while the power below the rated value was much less affected. The level of 350 kW corresponded to the lowest level measured during normal operation with lots of bugs on the leading edges. The two data points of 12-12 between 34 and 45 October at 500kW and 530kW are rather low with respect to the other points, however both represent only a single measurement.

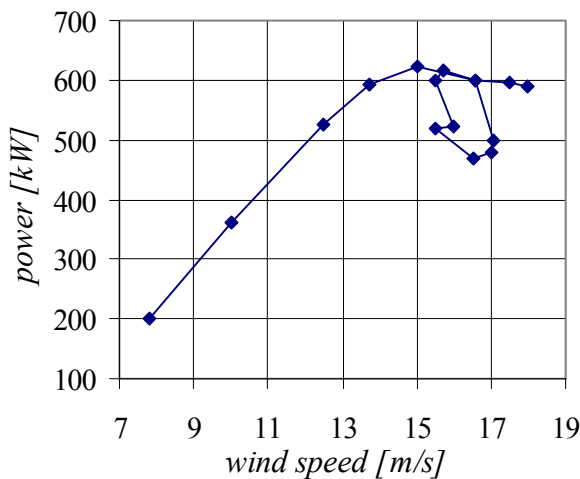


**figure 5.16** Example of a jump between power levels observed by Risø. The wind speed was measured on the nacelle and the points represent 10 minute averaged values. The yaw error was not measured (personal communication with F. Rasmussen). Therefore this jump could be caused by a temporal yaw error. Reference for the figure: Madsen, H.A.; Bak, C.; Fuglsang, P.; Rasmussen, F. 'The Phenomenon of Double Stall', EWEC 97, Dublin.

wind direction and it returned to the initial level when the wind turned back to its initial direction. We therefore think that this jump was caused by a failure of the yaw mechanism of the turbine. A turbine with a large yaw error should have large power variations. These are approximately proportional to  $\cos^3 \theta_y$ ,  $\theta_y$  being the yaw error, which gives  $(0.94)^3 = 0.83$  for  $\theta_y = 20^\circ$  or a reduction of  $(0.996/0.906)^3 = 0.75$  for  $\theta_y$  changing from  $5^\circ$  to  $25^\circ$ . The wind direction always varies around its average, and this causes power variations that depend on the yaw error. Indeed, the measurement showed that the amplitude of the power variations became much higher after the wind direction change. So the jump could even quantitatively be ascribed to a yaw failure. One more argument against contamination is that wind tunnel experiments [59] have shown that roughness on the blades would not have large effects. But the roughness is often simulated at  $5\%c$ , while the insects mainly contaminate the airfoils around  $0\%c$ . This is a more sensitive domain, since it corresponds to the suction peak area at high inflow angles. Thus this argument is not valid either.

### 5.3.6 The Terrain Concentration Hypothesis

This hypothesis is very recent. It presents another possible cause, which also affects the power at low wind speed, of multiple power levels. Not being related to stall, it does not explain the above stall observations, but it may explain multiple power levels. We assume that in hilly terrain, the surroundings of the turbine can act as a concentrator. The concentration principle has been discussed by De Vries in 1979 [63]. A concentrator is a device that decreases the static pressure at the rotor disk. Using Bernoulli's equation, one sees that the speed at the rotor increases to  $U_0 + U_+$  when the pressure  $p_0$  decreases to  $p_-$ :

$$p_0 + \frac{1}{2} \rho U_0^2 = p_- + \frac{1}{2} \rho (U_0 + U_+)^2 \quad (5.1)$$

One might think that the turbine can therefore extract a factor of  $((U_0 + U_+)/U_0)^3$  more energy, but then one forgets that the flow still has to move away from the turbine and will slow down by opposing the pressure gradient. In fact, the increase of the kinetic energy per unit air mass moving into the concentrator corresponds precisely to the static pressure drop, so precisely this energy is also required to let the flow move out of the low pressure area induced by the concentrator (see figure 5.17). Thus the increase of the kinetic energy *per unit air mass* cannot



be extracted, but since the mass flow increased by  $(U_0+U_+)/U_0$ , the rotor can extract more energy. Now we return to the Terrain Concentrator hypothesis. When the terrain around a turbine has such a shape that it can act as a concentrator, and, since the turbine will turn with the wind and the terrain will not, the concentration will depend on the wind direction. At a certain wind direction the terrain will therefore concentrate the mass flow and at another wind direction it won't (see figure 5.18). An anemometer nearby the turbine, or on the nacelle, cannot make a difference between those situations. And we as observers, not aware of the terrain concentration, do expect the power that corresponds to the wind speed indicated by the anemometer speed  $U_a$

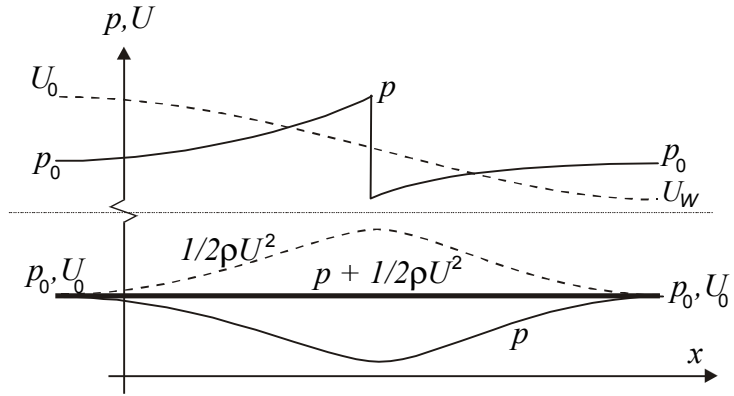


figure 5.17 The lapse of pressure and speed for a wind turbine and a concentrator.

$$P = c_p \frac{1}{2} \rho A U_a^3, \tag{5.2}$$

but the wind speed at the anemometer consists of an undisturbed wind speed and a concentrator induced speed,  $U_a = U_0 + U_+$ , so the power that can be extracted is

$$P_c = c_p \frac{1}{2} \rho A U_0^3 \frac{U_0 + U_+}{U_0} \text{ and not } P = c_p \frac{1}{2} \rho A (U_0 + U_+)^3. \tag{5.3}$$

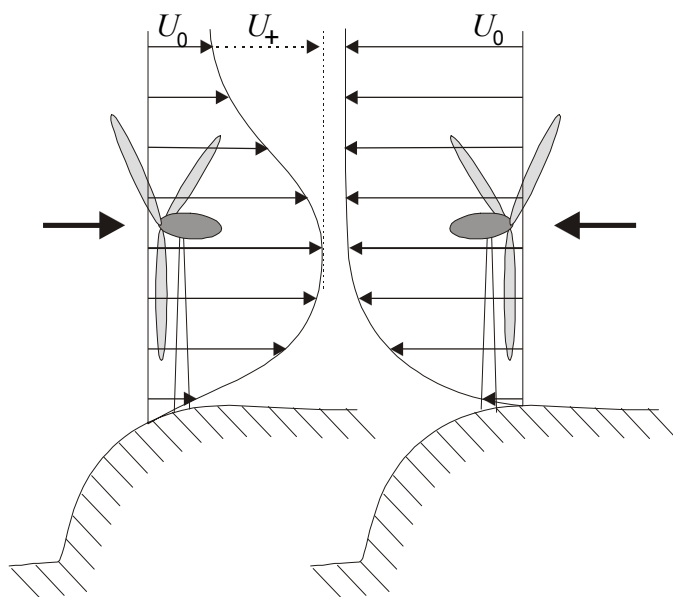


figure 5.18 The terrain concentration hypothesis. The wind speed measured on the nacelles of both turbines are equal, but the turbine on the left-hand side can extract less energy.

Furthermore, in the case of concentrated flow, for which the turbine is not designed, it will operate near  $a=1/3$  induction speed (where  $a$  is based on  $U_0+U_+$ ). So it extracts too much energy per unit air mass and may enter the less efficient turbulent wake state where it will extract even less energy.

For an efficient concentrator  $U_+$  can be almost  $2U_0$ , and for a terrain we expect a maximum of  $U_+ = \frac{1}{2}U_0$ . In that case the turbine produces power proportional to  $U_0^3(U_0+U_+)/U_0 = 3/2U_0^3$ , while we expect  $(3/2U_0)^3 = 27/8U_0^3$ , which is a factor of  $9/4$  more. This means that the obtained power will be

about half the expected power. This mechanism is not restricted to stall controlled turbines but will affect pitch regulated turbines as well.

Also the scale of the pressure field, induced by the concentrator relative to that induced by the turbine, is important. When they have the same scale the above analysis holds. But when the concentrator has a much larger scale, so that the entire pressure lapse induced by the turbine takes place in the low pressure zone of the concentrator, the power at the turbine increases by a third power of  $(U_0+U_+)$ . So Terrain-Concentration can have a great deal of influence on the power, depending on the size of the turbine compared to that of the concentrator and depending on the efficiency of the terrain as concentrator.

### 5.3.7 Conclusion on Multiple Power Levels

The occurrence of multiple power levels can be explained by the 'Insect Hypothesis', which states that these levels correspond to different degrees of contamination. A low contamination level decreases the power to 92% of the design value, a high level decreases it to 55%. The Hypothesis has been validated in three crucial experiments, which are the observation of the decrease of the stall angle due to contamination, the progress of the power level over time that showed a decrease after each period of low wind and the experiment with artificial roughness on a turbine, which power curve dropped in a way similar to the multiple power level observations. Although the Insect Hypothesis explains the multiple power levels, there can be other causes. The Terrain-Concentration hypothesis, for example, predicts multiple power levels even *below* the rated power, both for stall controlled and *pitch regulated* wind turbines.

## 5.4 Comparison with Theory

We now compare the measured power curves shown in figure 5.15 with theoretical curves for the same rotor. The theoretical curves are calculated using classic strip theory (see section 2.2.3) and they are shown in figure 5.19a.

**figure 5.19a** Three calculated power curves. One without a correction for rotational effects '2d', one according to Snel's model and one according to the new analytic model of Corten.

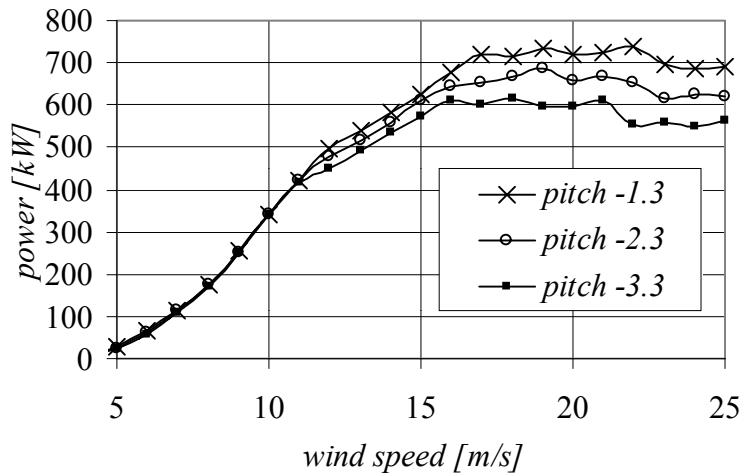
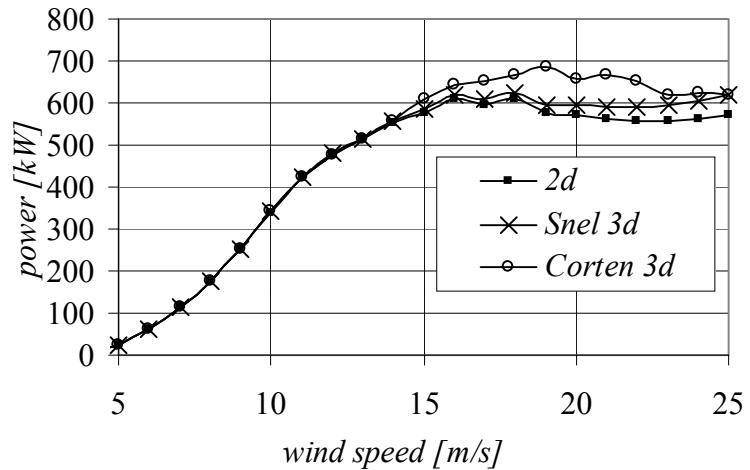
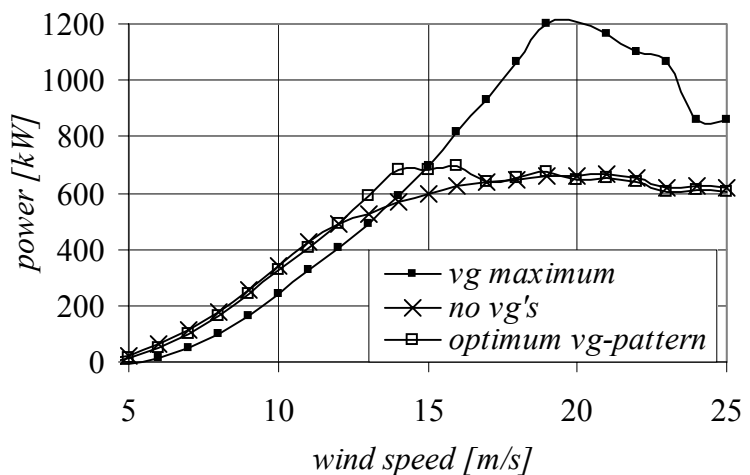


**figure 5.19b** Here we display the effect of the pitch angle on the power curve. Every degree changes the power level by about 10%. We used the Corten 3d-model.

**figure 5.19c** Power curve calculations for three different vortex generator configurations. One curve is without vg's, one with an optimised configuration with more output around 14 m/s and one with vg's placed over the entire leading edge at about 0.15c. We used the Corten 3d-correction. Watch the scale.



We also show the curves predicted by the approximations discussed in section 2.5. According to Snel's theory the stall level would shift by 5% and according to Corten's theory by 10%. Since both shifts are smaller than the spread shown in figure 5.15, it cannot be decided which of the two is superior. Even the 2d-strip theory is useful. Differences in the theories appear to be less important than differences in the experimental conditions.

This is illustrated in figure 5.19b, where the effect is shown of a change of the pitch angle, being no less than 10% per degree. One should know that this angle can hardly be determined to a precision of  $1^\circ$ , and that the twist also varies on the order of  $1^\circ$ , from blade to blade. Small deviations from the ideal blade shape (as pursued in production) can have important consequences; we have noticed, for instance, that a minute ridge near the leading edge of the airfoil did act as a stall strip. Another illustration is given in figure 5.19c, where the strong effect of vortex generators is shown. These can double the turbine power level.

Without further illustrations we recall the effects of fly-induced roughness. Even a little contamination can lower the power by 10%, and a lot of contamination can halve it. We also recall the yaw error of  $20^\circ$ , which reduced the power by 20%. Yaw errors of that magnitude may be expected in complex, hilly terrain. Even larger effects can be expected when the terrain has a concentrating effect at the turbine. Turbines are often put in locations where profit can be taken of the natural concentration. This may effect the power, even below rated, by as much as 100%, although we will use 25% as possible value in our conclusion. For the sake of completeness, we finally mention effects of air density and, perhaps turbulence. The density of air, which linearly enters the transfer of momentum and power, varies only by a few percent (at most 10% when a storm depression passes), so the effect is mostly small and may be neglected. However, at some turbine sites in Canada the density can rise to  $1.47 \text{ kg/m}^3$ , while the mean value is 1.28, with an effect on the power level of 15%. Turbulence has been invoked to explain the multiple power levels [54] without making clear how this can possibly work. We propose not to neglect the effects of turbulence, but to ignore them.

Our conclusion must be that the theoretical modelling in chapter 2 falls short in the description of the stall phenomena. Irrespective of the choice of approximations in the solution of the Navier-Stokes equation, the theory addresses only a small part of the complex process of flow separation.

## 6. Conclusions

Let us summarise. Wind turbines need a control mechanism to limit the power to a designed maximum, which is reached at a certain rated wind speed. Designers therefore tried to combine a constant rotor speed with a clever rotor geometry that inherently controls its power via flow separation. In this way, the power control becomes an intrinsic property of the rotor. About 50% of all turbines use this mechanism called stall control. However, in practice the power level can deviate tens of percent both above and below the design level.

### Models on Stall Behaviour

To design rotors with a more accurate power levelling one needs precise models on the separation behaviour. The heuristic model we propose considers rotational effects on the flow separation. We use Euler equations, since the separation layer is thick. We find an analytic solution wherein the contribution of the radial velocity, which is neglected in other models, is stressed. Present models on flow separation yield corrections for rotation that influence the power level of wind turbines by about 10%. Regrettably, none of the models addresses the major effects on the power of vortex generators (+100%), stall strips (-50%) and contamination (-50%). The first two affect only a part of the rotor, so the uncertainties introduced are approximately 20% and 10% respectively. Furthermore, flow separation follows from an instability, so that small disturbances can have large effects. However, in the models all small terms were neglected, in order to simplify the equations. Of course one may retain all the terms of the Navier-Stokes equations and solve them numerically. It should be realised however, that the computer code needs the precise rotor geometry as input, including the vortex generators and even the roughness caused by the insects on the blades. And the latter is one of the relevant dependencies that change with time. Therefore, we have quite a problem with the input data. Even if this problem could be overcome, one would need a great deal of computing time. So far, only the separation properties of airfoil sections, simplified to a two-dimensional set-up have been correctly computed, but only for the case of attached flow. Sometimes entire wind turbine blades were simulated [56], but in these cases, the modelling of turbulence had to be adapted until some correlation with the observations was reached. However, those observations did not include the real separation behaviour of the blades, so the correlation with practice was in fact unknown. Moreover, even if the stall characteristics of a rotor could be calculated precisely, it would still be impossible to design the rotor so that it had a constant stall level.

### Systematic and Time-Dependent Deviations

We have in fact found many reasons for the deviation between the designed power level and that of practice. A perfect design should account for the effects mentioned above, and many more. We have an influence of the power of 10% per degree blade pitch, and about 5% for the twist uncertainty. Vortex generators and stall strips account for 20% and 10% uncertainty respectively. A yaw error of 20° can cause a power decrease of 20%<sup>t</sup>, the terrain shape can also influence by 25%<sup>t</sup>. Density affects the power by 10%<sup>t</sup>. Other effects are changes of the blade surface roughness from ageing of the coating, wind shear, rain and ice sedimentation. For those, we estimate 20%<sup>t</sup> uncertainty. Blade contamination can differ from a few percent to 45%<sup>t</sup>. Differences between the blades produced and the airfoils tested in the wind tunnel also give about 20% uncertainty. Rotational effects add 10% uncertainty. The root-mean square effect on the power level is about 35% due to systematic deviations. Due to time-dependent deviations (superscript t) we estimate deviations of 20% if we neglect the yaw error, terrain concentration and contamination problems and we estimate a deviation of up to 60% when these effects are included.

### Stall Flag Visualisation Technique

Let us return to the main subject of this thesis. We developed a flow visualisation technique that has many advantages over the use of tufts. Stall is a highly dynamic process, which only can be studied with a technique that has a fast response and the possibility of evaluating the output signals automatically. Both characteristics are met by the stall flag technique. In particular on rotating objects, tufts are severely influenced by the centrifugal force and therefore display erroneous signals, while disturbing the flow. Stall flags are hardly affected by the centrifugal force (and in their most favourable positions, not at all), so that systematic errors and flow disturbances are avoided. The pressure driven stall flag will in most cases, introduce much less drag than the frictional-drag driven tufts. Disturbance is also caused by the self-excited flapping motion displayed by tufts, even in attached flow. The first stall flags had the same problem, but the later ones, with higher stiffness, remained stable and so the disturbance was avoided. Finally, stall flag signals can benefit from motion blur, while tuft signals become useless. Thanks to this property, we can visualise the flow on rapidly moving objects. In particular we can visualise the separation behaviour of full-scale wind turbines in detail. A summary of the stall flag characteristics compared to tufts is given in table 6.1.

### Correcting Systematic Deviations

If the actual power level of a stall-controlled turbine does not correlate with the designed value, the reason can be found by observing stall flags on that turbine. Stall flags which we developed and learned to use, are a unique tool for this purpose, and possibly also for other purposes. Once the cause of the deviation is known, adaptations are possible. Stall areas where the wind is below the rated value can be provided with vortex generators, and areas where the flow is still attached although the rated power has been surpassed can be provided with stall strips; in the latter case a small blade pitch adjustment is also possible.

With these adaptations, we can shift the power level up and down by about a factor of 2. From the stall flag signals we can determine the stall delay of vortex generators as a function of their chord-wise and radial position. So we have sufficient possibilities of correcting the error in the power level but we cannot correct for influence on the power caused by time-dependent blade contamination, by fluctuations in the air density, by terrain concentration or by vertical yaw. In short, we can avoid the systematic error of about 35%, but the time-variant error of 20-60% remains.

### Changing Ambient Conditions

Can the stall behaviour be made independent of changes in the environment? No. Stall is the consequence of frictional drag in the boundary layer and roughness such as caused by insects immediately influences this frictional drag. One can search for airfoils that are relatively insensitive to roughness. This dependency is often measured in the tunnel by pasting a zigzag tape at 5%*c*. A better impression of this effect will be obtained by using zigzag tape where the roughness is located in practice: at about 0%*c*. One may further try to avoid contamination by using special coatings, and by regular cleaning, but that will not solve the problem. A severe impact of insects can halve the power level, as we have seen, but a small number of impacts will bring the power down by many percentage points already.

The variation of the air density with time may even be more cumbersome. Separation is not much dependent on the density, but the power produced is affected in a linear sense. So the power control based on stall is passively shifting up and down with the air density. Besides these two, we have time-dependent effects on the power by yaw errors, of which the vertical components cannot be avoided, and by concentration of the wind by the terrain.

### Blade and Turbine Requirements

A good stall design requires precision in the yaw mechanism and especially in the blades. The turbine should always be in line with the wind. The shape of the blades should be well defined and be manufactured with very small tolerances. Even when systematic deviations in the actual stall power are corrected with the stall flag method, the inaccuracies in the manufacturing should be small. Otherwise one would need a stall flag experiment per turbine. So stall control sets high production standards, which will rise the price and could take away one of the main arguments for stall control.

### Predicting Stall Behaviour

One cannot yet produce, cost-effective, blades precise enough to meet a designed stall behaviour. We should add that there are no models to predict that behaviour, and even with such models, we can not make an accurate stall regulation. With the stall flags systematic deviations can be corrected, but the time-dependent effects remain a source of trouble. Taking all these things together, we conclude that power control by passive stall cannot be more accurate than +/-20% (the remaining time-dependent variation). We estimate that the production loss is about 13% in the case of a 20% surplus power (turbine stops 10% above rated) and 6% less for a 20% lower power level. We assumed that the level changed permanently, so this is an estimate for the production losses (10% average) when the systematic errors are not corrected. For the time-dependent effects, we roughly estimate that they act 50% of the time so the losses become on average 5% (the average of the half of 13% and of 6%). Active stall control can remove this uncertainty but will add complexity, thereby removing a major argument for stall control. We conclude that the effects on the energy production are not so large if we correct for systematic errors. Pitch-controlled wind turbines may also stall around rated wind speed. If we assume an average power loss due to separation of 5% from 12 to 16 m/s, it affects the production by 2.5%.

### Inherent Heat Generation

A final point should be made. We showed that when the flow outside the stream tube through the actuator is included in the analysis, the energy conversion process has an inherent dissipation of kinetic energy in heat. The heat produced in the flow is about half the energy extracted.

no.	property	stall flag	tufts
1.	purpose	1. detection of separated area 2. detection of separation height	detection of separated area
2.	visibility: -signal -resolution -motion blur	≈1000 times tuft visibility binary, clear detection 4×4 pixels advantage	tuft visibility continuous, not easy to detect 20×20 pixels fatal
3.	response speed	$7h/v$ , with $h$ = flap height	unknown, but comparable
4.	flow disturbance	1. cause transition 2. drag increase in laminar flow	1. cause transition 2. drag increase in all flow types 3. act as vortex generators and delay stall 4. self-excitation gives drag
5.	centrifugal force dependence	zero for hinge angle zero, which is the most useful angle.	large, comparable to aerodynamic force on rotors
6.	Kelvin-Helmholtz instability	avoided	not avoided (except with flow cones, but these have problems with aspects 2, 4, 5, 8 and 9)
7.	operating principle	pressure forces only during flip-over	always frictional drag
8.	data-acquisition	automated by image processing	manual
9.	applicability	objects up to 100m·100m	objects up to 10m·10m
10.	construction	hinge, flap, support, reflector	thread, support, (reflector)

**table 6.1** Comparison of stall flag and tuft.



# References

- 1 Abbott, H. and von Doenhoff, A.E., 'Theory of Wing Sections', Dover Publications, New York, 1959.
- 2 Adrian; R.J., 'Scattering Particle Characteristics and their effect on Pulsed Laser Measurements of Fluid Flow: speckle velocimetry vs. particle image velocimetry', Applied Optics 24 (1985), pages 44-52.
- 3 Bak, C.; Madsen, H.A.; Fuglsang, P.; Rasmussen, F., 'Double Stall', Risoe-R-1043(EN), June 1998.
- 4 Bak, C., Madsen, H.A., Fuglsang, P., Rasmussen, F., 'Observations and Hypothesis of Double Stall', Wind Energy, Wiley, Vol 2, No 4 Oct-Dec 1999.
- 5 Banks, W.H.H., Gadd, G.E.; 'Delaying Effect of Rotation on Laminar Separation', AIAA J., Volume 1, No 4, April 1963, pp.941-942.
- 6 Batchelor, G.K., An Introduction to Fluid Dynamics', Cambridge University Press, ISBN 0 521 098173, 1967.
- 7 Betz, A., 'Das Maximum der Theoretisch Möglichen Ausnützung des Windes durch Windmotoren', Zeitschrift für das gesamte Turbinewesen, Sept. 20th 1920, page 307-209.
- 8 Betz, A. 'Applied Airfoil Theory' Volume IV, Division J in Durand, W.F. 'Aerodynamic Theory, A General Review of Progress', 1935.
- 9 Brand, A.J.; Dekker, J.W.M.;Groot, de C.M.; Späth, M., 'Field Rotor Aerodynamics: the Rotating Case'.
- 10 Bunnes, P. and Fiddes, S., Laser Doppler Results Contributed to 'Dynamic Stall and Three Dimensional Effects', Joule II contractors meeting 8-10 feb 1995, NEL, Glasgow, U.K.
- 11 Corten, G. P., 'Parameterising Particle Image Velocimetry, The Feasibility Study to Visualise the Flow Around the 28 [m] Wind Turbine at ECN.', IW-95091R, Aug. '95.
- 12 Corten, G.P., 'The Stagnation Flap, an Instrument to Visualise and Locate Stagnation', November 1996, IW-96107R
- 13 Corten, G.P., 'The Stall Flag, Prior Development and First Results', Delft Faculty of Aerospace Engineering, Memorandum M774, Delft, February 1997.
- 14 Corten, G.P., 'Technical Development of the Stall Flag Method', ECN-CX--97-036, August 1997.

- 15 Corten, G.P., 'The Stall Flag Method: Proof of Concept', ECN-RX—98-001, Joint ASME, AIAA Wind Energy Symposium, Reno, USA, January 12-15, 1998.
- 16 Corten, G.P. & Vronsky, T, 'Stall Regulated Wood Epoxy Blades', IEA Symposium on the Aerodynamic of Wind Turbines, Lyngby Denmark, 3-4 December 1998.
- 17 Corten, G.P., 'The Tip Commands', ECN-RX--99-029, September 1999, presented at the BWEA 21, 1-3 September 1999, Cambridge, UK.
- 18 Corten, G.P., 'Technical Development of the Stall Flag Method, Prototypes 14-19, second report', ECN-CX--99-114, October 1999.
- 19 Corten, G.P., 'Insects Cause Double Stall', 13th IEA symposion Nov. 29-30 1999, Stockholm.
- 20 Corten, G.P., 'Optimisation of Vortex Generator Locations', 13th IEA symposion Nov. 29-30 1999, Stockholm.
- 21 Corten, G.P., 'Inviscid Stall Model', 13th IEA symposion Nov. 29-30 1999, Stockholm
- 22 Corten, G.P., 'Insects Cause Double Stall', ECN-CX—00-018, February 2000.
- 23 Crowder, J.P., 'Tufts', Chapter 9 of Handbook of Flow Visualisation, edited by Yang, W.Y., Hemisphere Publishing Corporation, 1989.
- 24 Crowder, J.P., 'Flow Direction and State Indicator', United States Patent 4,567,760, Febr. 4 1986.
- 25 Driscroll, W.G.; Vaughan, W., 'Handbook op Optics' Optical Society of America ISBN: 0-07 -047710-8, 1978.
- 26 Du, A.; Selig, M.S., 'A 3D Stall Delay Model for Horizontal Axis Wind turbine Performance Prediction', in 'A collection of the 1998 ASME Wind Energy Symposium', AIAA-98-0021, 36th AIAA Aerospace Meeting and Exhibit, Reno, January 1998.
- 27 Dyrmoose, S.Z., Hansen, P., 'The Double Stall Phenomenon and how to Avoid it', IEA Joint Action Aerodynamics of Wind Turbines, Lyngby, December 3-4 1998.
- 28 Edmund Scientific Catalog, Industrial Optics, Barrington USA.
- 29 Eggleston, D.M. and Starcher, K., 'Comparative Study of Aerodynamics of Several Wind Turbines Using Flow Visualisation', 8th ASME Wind energy Symposium, New York, 1989.
- 30 Fogarty, L.E., 'The Laminar Boundary Layer on a Rotating Blade', Journal of Aeronautical Sciences, April, 1951.
- 31 Freris, L.L., 'Wind energy Conversion Systems', ISBN 0-13-960527-4 Prentice Hall International UK, 1990.
- 32 Froude, R.E., Transactions, Institute of naval Architects, Vol 30, p.390, 1889.
- 33 Froude, W., Transactions, Institute of Naval Architects, Vol. 19, p.47, 1878.
- 34 Glauert, H. 'Airplane Propellors' Volume IV, Division L in Durand, W.F. 'Aerodynamic Theory, A General Review of Progress', 1934.
- 35 Grabau, P., 'Double Stall', LM Glasfiber A/S, February 1996.
- 36 Haslam, Flt., 'Wool Tufts: a Direct Method of Visually Discriminating between Steady and Turbulent Flow over the Wing Surfaces of Aircraft in Flight', Rep. Mem. Aeronaut. Res. Council 1209, 1928.
- 37 Herzke, U., Peinelt, I., 'Visualisation of the Stagnation Point: First Results of a New Method', IW-94079 R, August '94.
- 38 Hoerner, S.F. and Borst, H.V., 'Fluid Dynamic Liff', Published by Mrs. Hoerner, L.A., Hoerner Fluid Dynamics, Vancouver, WA , USA, 1985.

- 39 Hoerner, S.F., 'Fluid Dynamic Drag', Hoerner Fluid Dynamics, P.O. Box 65283, Vancouver, WA 98665, USA, 1965.
- 40 Holm, R and Gustavsson, J., 'A PIV Study of Separated Flow around a 2D Airfoil at High Angles of Attack in a Low Speed Wind Tunnel', in proceedings of IEA Annex XI, 'Aerodynamics of Wind Turbines', 13th symposium, November 1999, Stockholm.
- 41 Holten, van Th., 'On the Validity of Lifting line Concepts in Rotor Analysis', *Vertica*, Vol. 1 pp. 239-254, 1976.
- 41 Holten, van Th., 'Concentrator Systems for Wind energy, with Emphasis on Tip Vanes', *Wind Engineering*, Vol 5, no.1, p.29, 1981.
- 42 Hunt, V.D., 'Windpower', ISBN 0-442-27389-4, Litton Educational Publishing Inc., New York, 1981.
- 43 Johnson, W., 'Helicopter Theory', Princeton University Press, Princeton, New Jersey, USA, 1980.
- 44 Karman, Th. von; and Burgers, J.M., 'General Aerodynamic Theory Perfect Fluids', Volume II, Division E in Durand, W.F. 'Aerodynamic Theory, A General Review of Progress', 1934.
- 45 Kuik, G.A.M. van, 'On the Limitations of Froude's Actuator Disk Concept', ph.d. thesis 1991.
- 46 Lanchester, F.W., 'A Contribution to the Theory of Propulsion and the Screw Propeller', *Trans. Institution of Naval Architects*, Vol. XXX p. 330, March 25th, 1915.
- 47 Madsen, H.A., 'Aerodynamics of a Horizontal Axis Wind Turbine in Natural Conditions', *Riso M 2903* 1991.
- 48 Mönch, E., 'Technische Mechanik', ISBN 3-486-38766-9, 1986.
- 49 Schepers, J.G. en Snel, H., 'Aerodynamisch herontwerp NedWind 40 rotor' ECN-C--95-108, November '95, blz 9 3.1 'Beschikbare profielen'.
- 50 Schepers, J.G., Brand, A.J. e.a., 'Final Report of IEA Annex XIV: Field Rotor Aerodynamics', June 1997, ECN-C--97-027
- 51 Schlichting, H., 'Boundary Layer Theory', McGraw Hill Book company, ISBN 0 07 055334-3, 1979.
- 52 Snel, H., 'Scaling Laws for the Boundary Layer Flow on Rotating Wind Turbine Blades', proceedings of th fourth IEA Symposion on the Aerodynamics of wind Turbines, Rome 20-21 November 1990, ETSU-N-118, January 1991, ETSU, Dept. of Energy, UK.
- 53 Snel, H., Houwink, R. and Piers, W.J.; 'Sectional Prediction of 3D Effects for Separated Flow on rotating blades', 18th European Rotorcraft Forum, Avignon France 15-18 September 1992.
- 54 Snel, H.; Corten, G.P.; Dekker, J.W.M.; Boer, J.de; Chaviaropoulos, P.K., Voutsinas, S., 'Progress in the Joule Project: Multiple Stall Levels', presented at the EUWEC conference, March 1999, Nice, France.
- 55 Simpson, R.L., 'Aspects of Turbulent Boundary Layer Separation', *Prog. Aerospace Sci.*, Vol. 32, pp. 457-521, 1996.
- 56 Sørensen, J.N., 'VISCWIND, Viscous Effects on Wind Turbine Blades', ET-AFM-9902, Department of Energy engineering, Technical University of Denmark, June 1999.
- 57 Spera, D.A., 'Wind Turbine Technology', ASME Press New York, 1994.
- 58 Tangler, J.L. and Somers, D.M. 'Status of the special purpose airfoil families', Proceedings IEA-symposion on the aerodynamics of Wind Turbines.

- 59 Timmer, W.A., 'Nieuwe profielen voor windturbines, een literatuurstudie', IW-92056R, TUDelft, 1992.
- 60 Vermeer, L.J., 'Measurements on the Properties of the Tip Vortex of a Rotor Model', proceedings of EWEC '94, volume 1, page 805-808, 10-14 Oct. '94.
- 61 Vermeer, L.J. and Timmer, W.A., 'Identification of Operational Aerofoil State by means of Velocity Measurements', EWEC 1-5 March 1999, Nice, France.
- 62 Viterna, L.A. and Corrigan, R.D., 'Fixed Pitch Rotor Performance of Large Horizontal Axis Wind Turbines', presented at DOE/NASA workshop on Large HAWT's, Cleveland, Ohio, 1981.
- 63 Vries, O. de 'Fluid Dynamic Aspects of Wind Energy Conversion' AGARD -AG-243, ISBN 92-835-1326-6, July 1979.
- 64 White, F.M., 'Viscous Fluid Flow', McGraw-Hill, ISBN 0-07-100995-7, International Edition, 1991.
- 65 Wilson, R.E., Lissaman, P.B.S., Walker, S.N., 'Aerodynamic Performance of Wind Turbines', Oregon State University, June 1976

# Appendix A: The Aerpac 43m Rotor

The Dutch blade manufacturer Aerpac requested the author in the beginning of 1999 to improve the stall behaviour of their APX43 rotor. Figure A.1 shows several power curves of the rotor. If we look at the intended curve ‘design’ and measured curve ‘initial’, then we see the discrepancy at the start of the project. The turbine of 600 kW rated power could maximally produce 660kW, but, above 16 m/s, when the rotor captures even more than 700 kW, the turbine will be halted.

This is needed to prevent the turbine from overloading or overheating, but the penalty is of course a production loss. We also see that the rotor produces less than predicted below rated and in particular at approximately 10 m/s. This again represents production losses. Both deviations caused a loss of approximately 10% relative to the design. We will try to change the passive power control by adaptation of the stall behaviour, which we base on stall flag diagnostics. Two series of stall flag measurements were carried out, one in July 1999 and one in March 2000.

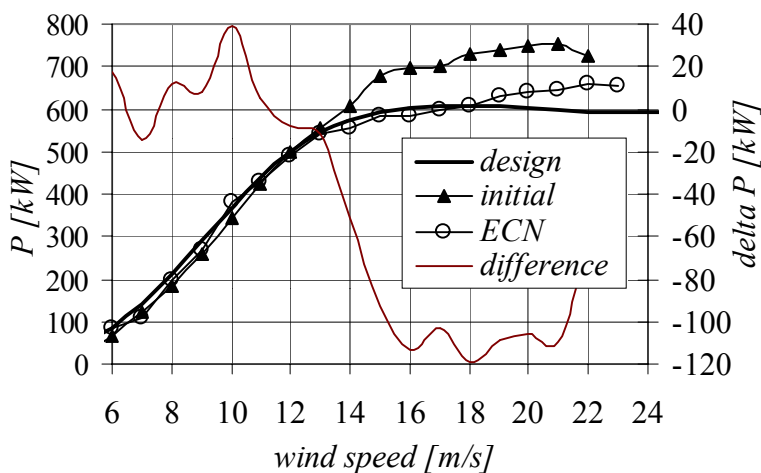


**figure A.1** The predicted power curve of the APX43 ‘design’ (1.86 GWh), the measured curve before the project started ‘initial’ (1.65 GWh), and the measured curve after the first stall flag measurement ‘ECN’ (1.79 GWh). The scale on the right-hand side refers to the difference between the two measured curves.

## A.1 First Stall Flag Measurement

During the first measurement for Aerpac we had periods of low wind and periods of rain, causing the flaps to stick to the blade surface. Only one measurement could be made. We present the most valuable result, namely for the APX43 blade in standard layout with some

adaptations. Delft University of Technology, who had an important input in the aerodynamic design of the APX43, proposed to install stall strips at approximately  $0.85R$  to avoid overpower, and to extend the line of vortex generators from  $0.52R$  to  $0.58R$  to increase the power below rated. The power curve ‘initial’ refers to this layout. The pattern of stall flags and vortex generators during the first measurement is shown in figure A.2.

After installation of the stall flags, we started the turbine several times, while recording the stall flags signals responding to the increasing rotation speed, and thus the increasing tip speed ratio  $\lambda$ . The video frames were analysed by the image-processing program. The frames were binned on tip

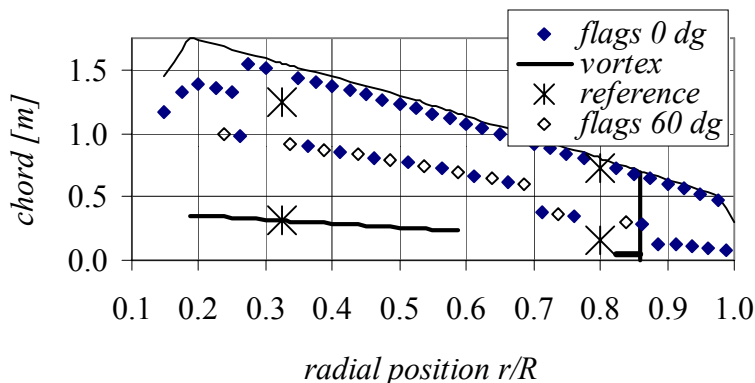


**figure A.2** The pattern during the first measurement. The vertical line at  $0.86R$  is the tip division and the stall strip is located just to the left of it at the leading edge.

speed ratios and we obtained table A.1 as output. The table displays the average signals of each pair of adjacent trailing edge stall flags. The second row shows the radial positions from the tip to the root of the blade. The first column shows the value for  $\lambda$  for each bin and the second column shows the number of video frames in each bin. Therefore, the first row of data shows that 57 video frames were analysed for the  $\lambda=2.0$  bin, and the first two stall flags on the tip were open during a fraction 0.3 of the 57 frames. The column with the heading ‘strip’ shows the signal of the pair of stall flags behind the stall strip. We see that this strip causes

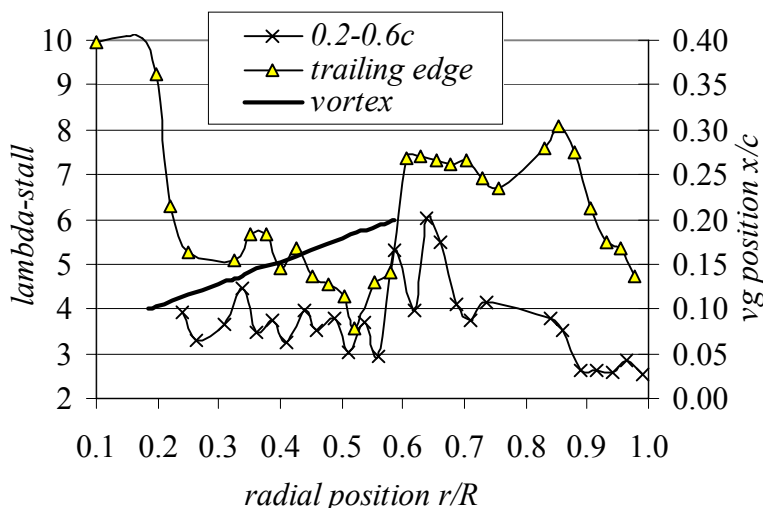


**figure A.3** Trailing edge  $\lambda$ -stall values for the first measurement. The turbine reaches rated power for  $\lambda \approx 4.5$ , so the blade surface near the stall strip stalls much too soon and the surface between  $0.45R$  and  $0.55R$  is too late.

stall for  $\lambda < 7.5$ . The tip speed of this rotor is  $61.5 \text{ m/s}$ , so stall occurred above  $8 \text{ m/s}$ , which is much too soon. The columns in the vortex generator area show that these generators effectively delay stall.

We see that the switching over of a stall flag is gradual. The  $\lambda$ -values in the table are obtained from  $\Omega R/U$ . For  $U$  we used the average of the anemometer signal, obtained at hub height from a mast upwind, for  $R$  the known rotor dimension and for the angular frequency  $\Omega$  the rather precise result of the image processing. Although the error in  $U$  makes  $\lambda$  somewhat uncertain, there is

also a systematic variation in  $U$  due to wind shear. The stall flags usually light up in the upper half and close down in the lower half, indicating that the wind speed in the lower half is less than that in the upper half. The switching of the stall flags will take place at distinct angles of attack, which in our methodology results in a range of  $\lambda$ -values. Using all data, we can however estimate the mean  $\lambda$  when each stall flag switches over. For the stall flags on the trailing edge those  $\lambda$ -values are given in figure A.3. In the area below the curves, the flow is separated, above the curve it is still attached. Such  $\lambda$ -stall graphs display how stall extends over the rotor and this helps us to see which areas stall too late or too soon. In the design the rotor reaches rated power at approximately  $\lambda=4.5$ , so stall should not occur above this value, and since we have overpower, stall is not sufficient above it. We see that up to approximately  $0.45R$  the behaviour is good. Moving outwards the vortex generators between  $0.45R$  and  $0.55R$  are too effective; the blade remains attached below  $\lambda=4.5$ . The additional row of vortex generators at approximately  $0.55R$  was meant to reduce the overpower, but appears to be responsible for overpower.

$\lambda \downarrow$	# frames $\downarrow$	strip							vortex generators								
		r/R $\rightarrow$	1	.9	.8	.8	.7	.7	.6	.6	.5	.5	.4	.4	.3	.2	.2
2.0	57	.3	.6	1	1	1	1	1	1	.5	.8	.9	.8	.7	.6	.7	.4
2.3	109	.8	.9	.9	1	1	1	1	1	.7	.9	.8	.9	.8	.9	.8	.3
2.6	69	.6	.8	1	1	1	1	1	1	.5	.9	.9	.8	.8	.9	.9	.4
2.9	48	.9	.9	1	1	1	1	1	1	.7	1	.9	1	.8	.8	.9	.3
3.2	54	.8	1	1	1	1	1	1	1	.6	1	1	1	1	.9	.9	.3
3.5	38	.5	.8	1	1	1	1	.9	.9	.5	1	1	1	.8	.8	1	.8
3.9	25	.4	.9	1	1	1	1	1	.9	.5	.7	1	.9	.8	.7	1	.5
4.2	29	.6	1	1	1	1	1	1	.9	.2	.9	1	.9	.9	.9	1	.4
4.5	28	.7	1	1	1	1	1	1	.5	.1	.4	.7	.6	.7	.7	1	.5
4.8	23	.5	1	1	1	1	1	1	.0			.1	.2	.3	.4	1	.5
5.1	17	.3	1	1	1	1	1	1				.0	.2	.1	.1	1	.4
5.4	21	.1	.4	1	.5	1	1	1				.2	.3	.2	.1	1	.7
5.8	21	.0	.6	1	1	1	1	1				.0		.3	.1	1	.6
6.1	21	.4	1	.9	1	1	1	1							.0	1	.8
6.4	14	.0	1	.6	.4	.4									.1	1	.8
6.7	19	.2	1	.1	.1	.2										1	.8
7.0	19	.3	1	.2	.6	.9	.9					.0		.1		1	.6
7.3	20	.0	.6	.0	.0	.0										1	.7
7.7	14		.2													1	.8
8.0	22		.1													1	.8
8.3	22		.0													1	.7
8.6	13															1	.8
8.9	11															1	.9
9.2	186															1	.8
9.5	151															1	.9

**table A.1** The rough signals of the stall flags, each time a pair of stall flags is averaged. We see the advance of stall caused by the stall strip already causing losses for  $\lambda=8$ , the vortex generators delay stall from  $\lambda \approx 8$  to  $\lambda \approx 4.5$ .

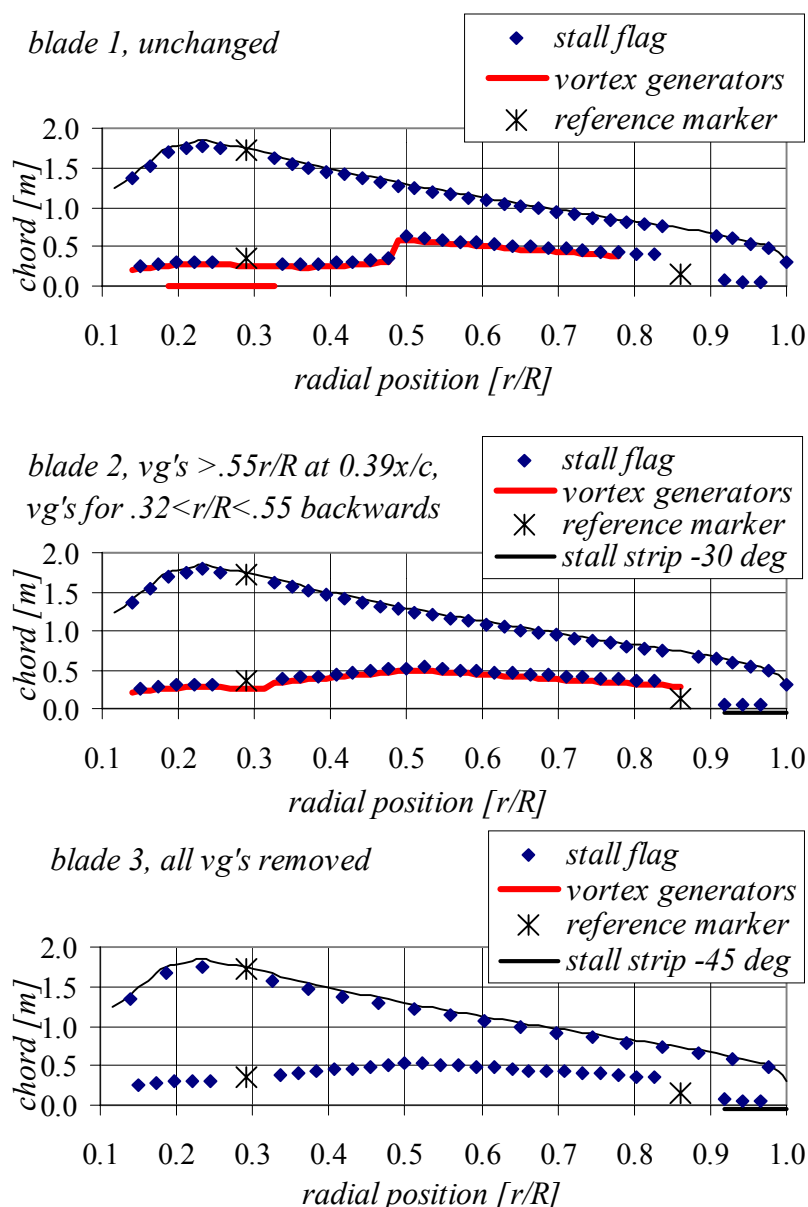


**figure A.4** The pattern of the second measurement. Blade 1 has the pattern according to the first advice of ECN. Blade 2 has a second new pattern. The vortex generators of blade 3 were removed, while the blade has the same stall flag pattern as blade 2, except of the smaller number on the trailing edge.

most importantly, what had to be done: Remove the stall strips, since the blade stalls too soon in this range even without them. Install vortex generators up to much larger radial positions, say 0.8R. Reduce the effectiveness of the vortex generators between 0.45R and 0.6R by moving them to a larger chord-wise position, and maybe, make the tip stall sooner. So we designed a new vortex generator pattern (see figure A.7). The power curve was measured again with this pattern and figure A.1 shows the result. We see that the overpower problem has disappeared. While the turbine had to be halted above 15m/s in the initial situation, it could now operate up in its full design range. The difference of the two power curves (also

The stall flags placed under a hinge angle of 60° correspond to the lower values of the zigzag line labelled '0.2-0.6c' in figure A.3, so they close sooner during a start. This indicates that, with decreasing angle of attack, the separated flow over the blade changes direction from the reversed to the radial direction. This is as expected, since at large angles of attack (at low tip speed ratios) rotation has little effect on a reversed flow, which then behaves as a 2-dimensional separated flow.

Between 0.6R and 0.9R the blade stalls much too soon, especially in the stall strip area. This clearly is the reason for the losses below rated. Another observation is that the stall strip has only effect on the stall flags behind it, so its influence is restricted to its physical dimensions. Finally, we see that the tip is a bit late in stalling.

We come to the remarkable conclusion that both measures proposed to correct the stall behaviour made the problems worse! Using stall flags, we could clear up what really happened, why the corrections didn't help, and



shown in the figure) clarifies that the power below rated has improved, especially around 10 m/s where the rotor captures much energy. Due to both effects the production increased by 8%.

A.2 Second Stall Flag Measurement

We were not satisfied with the above improvement below rated and decided to carry out a further measurement. When we returned to the turbine, we found 7 metres of vortex generators under the turbine. These rows had come loose and thus the power curve ‘ECN advice 1’ of figure A.1 does not correspond precisely to the intended configuration.

The most interesting configuration during the second measurement is shown in figure A.4. We see the pattern according to our first advice on blade 1, a new configuration on blade 2 and the same stall flag pattern on blade 3, but here without vortex generators; blades 2 and 3 also had stall strips on the tips. We analysed the data of two starts and averaged the signals to obtain more accuracy. Figure A.5 shows the trailing edge signals of the three blades. We immediately see the large difference between blade 3 (without vortex generators) and the two other blades. Figure A.6 shows the results for the stall flags behind the vortex generators near the leading edge. As above, we used these signals to design the vortex generator pattern indicated with ‘ECN advice 3’ in figure A.7. This advice is been protected by patent application 1012949. At this moment (September 2000),

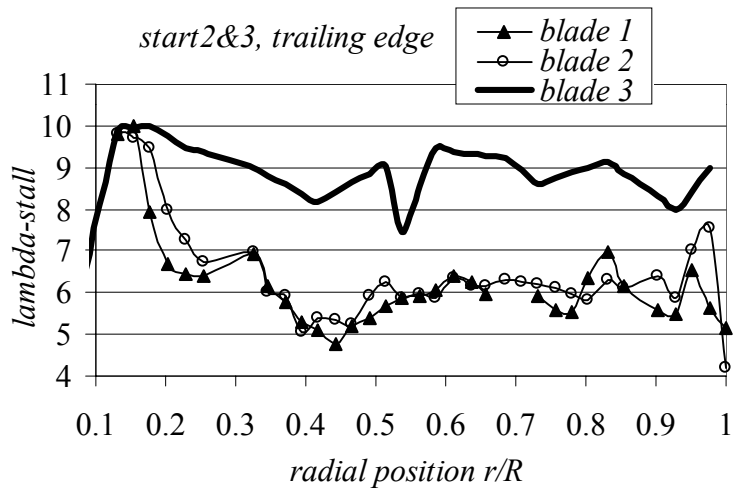


**figure A.5** Trailing edge  $\lambda$ -stall graphs for the second measurement. Blades 1 and 2 show small differences, while blade 3 without vortex generators attaches much later.

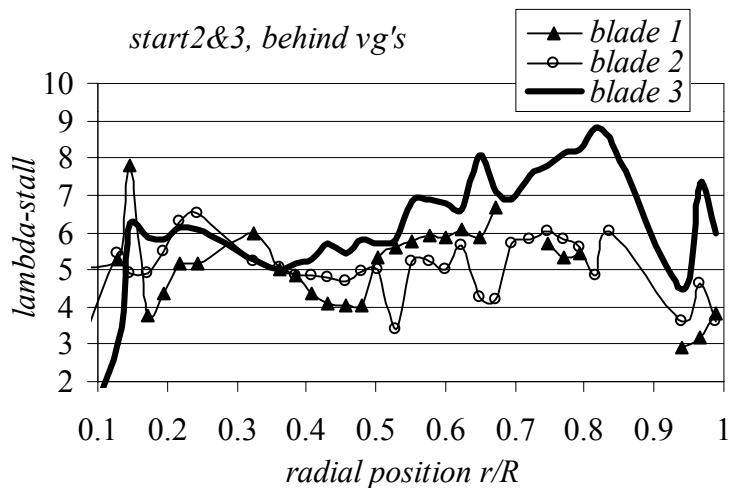


**figure A.6** Leading edge  $\lambda$ -stall graphs. The differences at the tip are due to stall strips between 0.92R and R on blades 2 and 3.

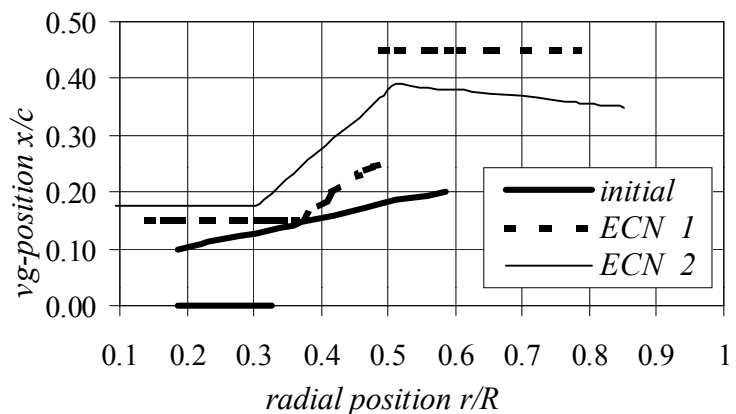


**figure A.7** The vortex generator patterns.

the vortex generator pattern has just been installed, but the power curve is not yet known. This did not prevent us to apply a comparable pattern already to a larger Aerpac rotor, the APX45. In this case we could certify (see figure A.8) that the power rises well up to rated value and that the final level is flat, although we do not have data above 18 m/s. This power curve is excellent for a stall turbine.

### A.3 Vortex Generator Modelling

Vortex generators are a powerful tool to correct even large deviations in the stall behaviour, but we do not know how their efficiency depends on the radial and chord-wise position. Let us derive their effect from the stall flag observations. We start with expressing the stall behaviour in terms of stall-angles instead of stall tip speed ratios. Remember that the induction has to be built up and that it thus will be too low during a start (see section 5.1.3). Blade – element - momentum theory is based on a steady wake or on steady induction, so the estimated angles will be systematically too low during a start. By calculating the angles of attack with and without induction, we find a maximum and a minimum value for the angles. This error interval is not precisely the same for the three blades, since they stall at different instants, but the values are almost equal. Therefore we determined this average error and included it in figure A.9 with stall-angles for the three blades calculated without induction. The absolute error due to induction is

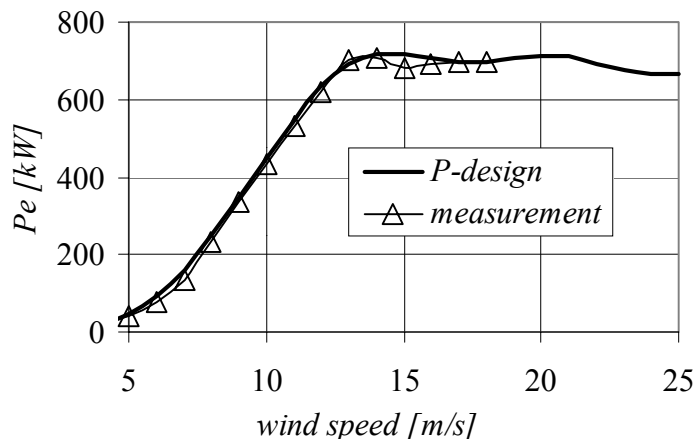


figure A.8 APX48 power curve, measured and predicted for a vortex generator pattern based on the APX43 experience.

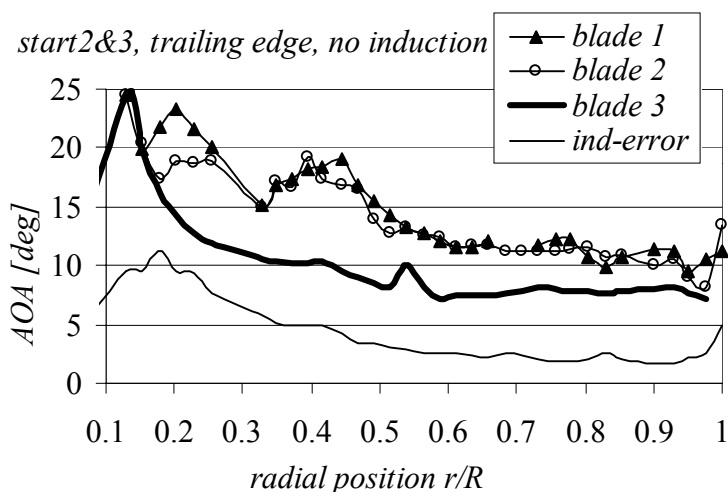


figure A.9 The stall angles at the trailing edge. The maximum induction error is included.

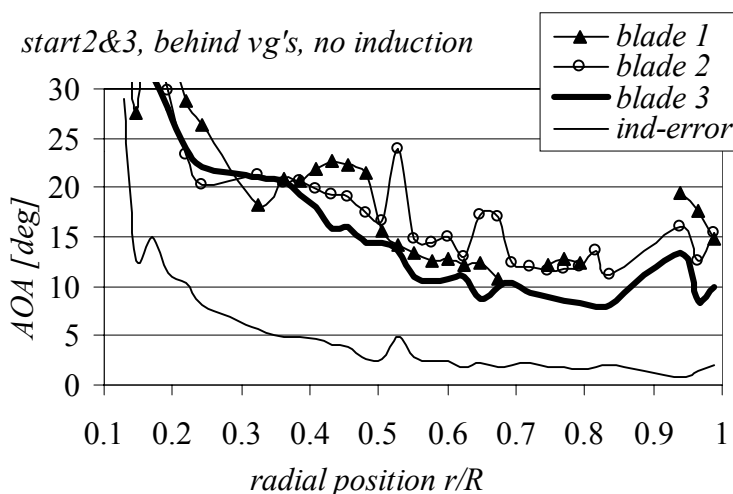
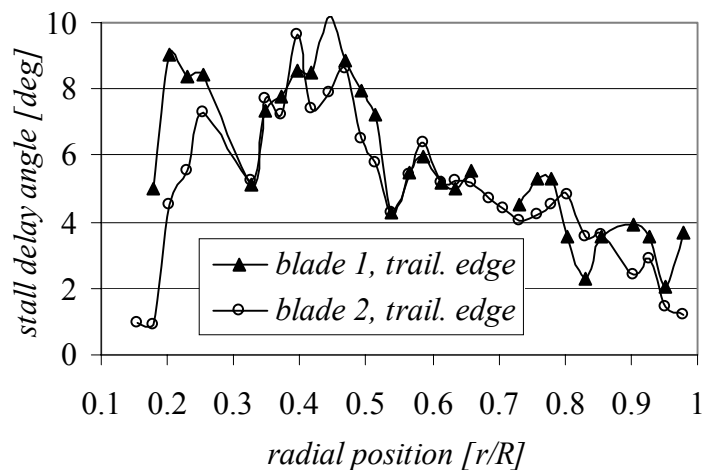


figure A.10 The stall flag angles at the leading edge.

approximately half the induction error in the figure, so it is approximately  $\pm 1^\circ$  at the tip, increasing to  $\pm 3^\circ$  at  $0.4R$  and  $\pm 6^\circ$  at  $0.2R$ . If we record stall patterns during steady turbine operation, the induction is also steady and the error vanishes. By comparing the stall patterns obtained during steady operation with those during a start, we can estimate the induction error and correct for it. Even without the steady measurements, we can compare different blades with different configurations. The differences will depend much less on the induction, since the error is approximately equal for all blades. We calculated the stall delay angles due to the vortex generators for blades 1 and 2 relative to blade 3 and plotted the results in figure A.11. The scatter in the points is representing the statistical error of approximately  $\pm 0.5^\circ$ , being increased by the subtraction. The figure shows how effective vortex generators are in terms of degrees of stall delay. So stall flags allow us to measure the stall delay and effective range of vortex generators as a function of their radial and chord-wise positions, with approximately  $\pm 0.5^\circ$  accuracy.

Arguments for ECN Advice 3

This time blade 1 remains attached up to  $\lambda \approx 4$  between  $0.4R$  and  $0.5R$  while blade 2 switches to the stalled state around  $\lambda \approx 5$ . The turbine reaches nominal power for  $\lambda \approx 4.5$ , and attached flow below this value may cause overpower. If the blade without vortex generators would also have the same pattern, the induction will be more and the angles of attack thus smaller. Therefore, the position of the vg's on blade 2 is acceptable. The stall flags at  $0.7R$  and  $0.73R$  on blade 1 were out of order, therefore the line is not continued. However, we can see that blade 1 stalls for  $\lambda \approx 5$  between  $0.55R$  and  $0.65R$  and at  $\lambda \approx 6$  for blade 2. So, the position on blade 2 ( $0.39c$ ) is fine again. Moving outboards to  $0.8R$  the stall tip speed ratio become slightly higher (from about 5 at  $0.6R$  to about 6 at  $0.8R$ ), indicating that the vortex generator can be moved a bit towards the leading edge. We finally see that the tips stall rather late. This might be a reason of overpower, so we may need stall strips on the tips.



**figure A.11** Stall delay of blades 1 and 2 with vortex generators relative to blade 3 without.



# Appendix B: Propeller Experiment

In this appendix we will demonstrate the applicability of stall flags on a small propeller.

## Set-up:

A two bladed propeller of 65 cm diameter was equipped with 14 stall flags on the trailing edge of one blade between  $0.30R$  and  $0.95R$ , see figure B.1. Special stall flags with a flap width of 1.5cm and a height of 1.0cm were used. At the right handed side a second small propeller of 21cm diameter was installed. This propeller rotated at about 10.000 rpm and blows a jet of air through the larger one, which rotated at 200 rpm. When the blades of the large propeller passed through the slipstream of the small one, the flow separated. On each blade tip a small retro reflector was attached to mark the swept areas. The stall flags were placed under a hinge angle of  $0^\circ$ , so their behaviour was centrifugal force independent. In a

second experiment we used even smaller stall flags of 0.5 cm height and 0.9 cm width. These stall flags were installed in turns under a hinge angle of  $0^\circ$  and  $30^\circ$  (for the definition we refer to figure 3.10), so that those under  $30^\circ$  would switch-over in pure radial flow. On the second blade we installed tufts between  $0.4R$  and  $0.9R$ , each  $0.1R$  apart. These tufts were 0.5mm thick, 2 cm long and of a thread of only 0.14g/m. This time the large propeller was operated at about 600 rpm while the smaller one was at standstill.

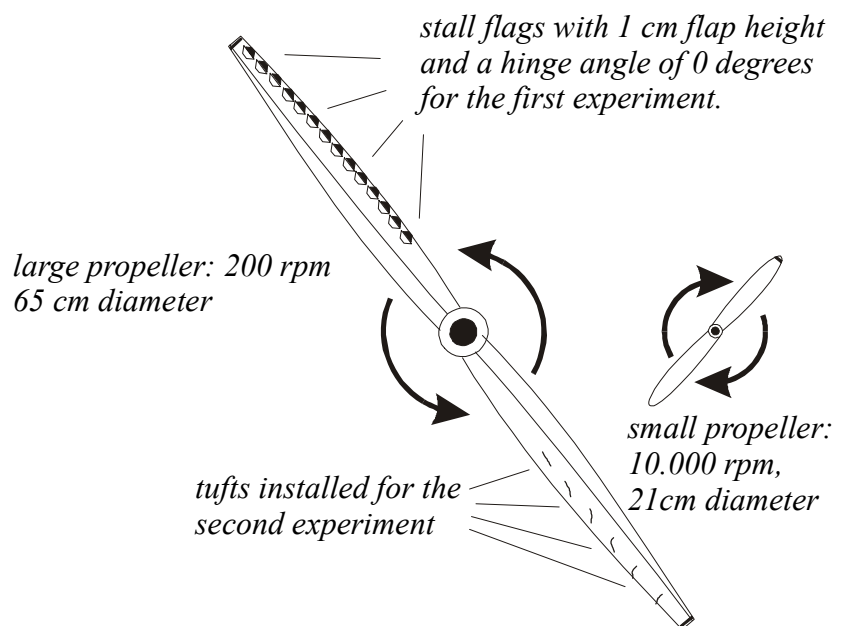


**figure B.1** Schematic set-up of the propeller experiment. We look on the suction side of the large propeller and on the pressure side of the smaller one.

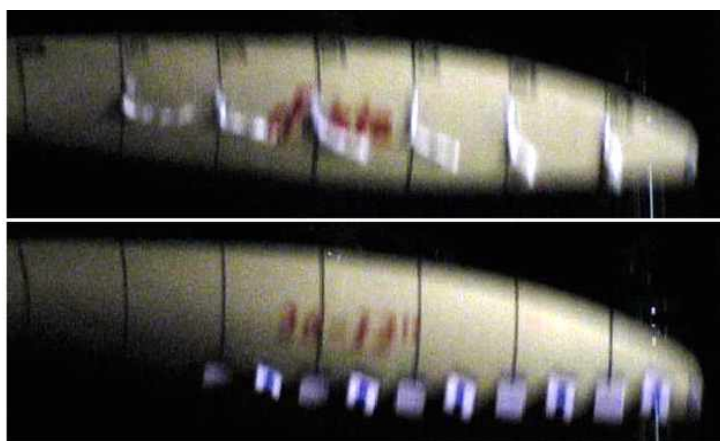
Results:

Figure B.2 shows a long shutter time recording of the both propellers in operation during the first experiment. It can be seen that the indicated area of reversed flow corresponds to the location of the jet of the smaller propeller, although there is a delay. This is caused by the response time of the stall flags and by the aerodynamic hysteresis. The hysteresis is in the order of 1 to 2 chords of the large propeller and the tracks of the stall flags are about 4-6 chord lengths. The stall flags switch of state in less than 1 chord length which equals to about 5 times the flap length which agreed sufficiently with the theoretical estimate of 7 (see section 3.2.4). This experiment also showed that the stall flag technique can profit from motion blur. The larger propeller rotated over about 1 third of a revolution during the shutter time, so that we could record the entire azimuthal stall distribution on a single picture. The same effect can be obtained on full scale turbines as can be seen in figure 3.1 and on the cover. Tufts signals would have become invisible even with much less motion blur.

Figure B.3 shows a short shutter time recording of two successive blade passages during the second experiment. We see that the tufts up to  $0.7R$  indicate pure radial flow, while the ones at  $0.8R$  and  $0.9R$  are directed towards the trailing edge with a radial deviation. All stall flags remain closed, while the centrifugal force tends to open those flags under  $30^\circ$ , so the flow direction must deviate more than  $30^\circ$  from the radial direction. The tuft is in general located in the lower part of the boundary layer, so it experiences low aerodynamic forces and therefore the centrifugal force determines its direction dominantly, even in attached flow. Or, in other words, tuft observations under rotating conditions can be very misleading. Crowder came to the same conclusion during his experiment on the 100m diameter MOD wind turbine (section 3.4).



**figure B.2** Experiment with two propellers, which swept areas are marked by the tracks of tip reflectors. The small propeller forces a stream through the swept area of the larger one, which has stall flags installed every  $0.05R$  at its trailing edge. It can be seen that the flow separates and rapidly reattaches.



**figure B.3** Two pictures half a revolution apart at a  $1/2000s$  exposure time. The tufts ( $0.14 \text{ g/m}$  and  $0.5\text{mm}$  thick) on the upper blade suggest radial flow but, in fact are deviated by the centrifugal force. The  $0.5 \text{ cm}$  high flags on the lower blade indicate that the flow is still attached. The flags are in turns placed at hinge angles of  $0^\circ$  and  $30^\circ$  degrees.

## Appendix C: Stall Flag Patent

At ECN the stall flag was regarded to be a valuable new instrument and therefore it was decided to apply for a patent. The procedure started with a Dutch patent no. OA 1003153 Ned., which was applied May 17, 1996 and granted November 11, 1997. It was also decided to extend the application to Europe and the Unites States of America. The application in Europe is still running, while that in the USA has just been granted. The latter is included here.





The  
United  
States  
of  
America



**The Director of the United States  
Patent and Trademark Office**

*Has received an application for a patent for a new and useful invention. The title and description of the invention are enclosed. The requirements of law have been complied with, and it has been determined that a patent on the invention shall be granted under the law.*

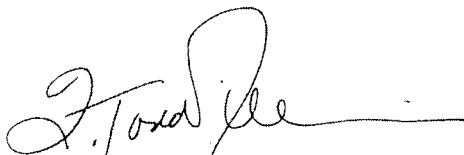
*Therefore, this*

**United States Patent**

*Grants to the person(s) having title to this patent the right to exclude others from making, using, offering for sale, or selling the invention throughout the United States of America or importing the invention into the United States of America for the term set forth below, subject to the payment of maintenance fees as provided by law.*

*If this application was filed prior to June 8, 1995, the term of this patent is the longer of seventeen years from the date of grant of this patent or twenty years from the earliest effective U.S. filing date of the application, subject to any statutory extension.*

*If this application was filed on or after June 8, 1995, the term of this patent is twenty years from the U.S. filing date, subject to any statutory extension. If the application contains a specific reference to an earlier filed application or applications under 35 U.S.C. 120, 121 or 365(c), the term of the patent is twenty years from the date on which the earliest application was filed, subject to any statutory extensions.*



Director of the United States Patent and Trademark Office

  
Attest



US006065334A

**United States Patent** [19]

**Corten**

[11] **Patent Number:** **6,065,334**

[45] **Date of Patent:** **May 23, 2000**

[54] **DEVICE FOR RENDERING VISIBLE THE FLUID FLOW OVER A SURFACE**

4,730,488 3/1988 David ..... 73/189

[75] Inventor: **Gustave Paul Corten**, Alkmaar, Netherlands

**FOREIGN PATENT DOCUMENTS**

702 289 1/1954 United Kingdom .

[73] Assignee: **Stichting Energieonderzoek Centrum Nederland**, Petten, Netherlands

**OTHER PUBLICATIONS**

U. Herzke et al., "Visualisation of the Stagnation Point: First Results of a New Method", 7 pages, TU Delft, Institute for Wind Energy, Aug. 1994.

[21] Appl. No.: **09/180,858**

*Primary Examiner*—William Oen  
*Attorney, Agent, or Firm*—Young & Thompson

[22] PCT Filed: **May 16, 1997**

[86] PCT No.: **PCT/NL97/00276**

§ 371 Date: **Jan. 26, 1999**

§ 102(e) Date: **Jan. 26, 1999**

[87] PCT Pub. No.: **WO97/44674**

PCT Pub. Date: **Nov. 27, 1997**

[57] **ABSTRACT**

In order to determine the flow status of a surface moving through the fluid, it is proposed to mount flaps on that surface. Such flaps hinge from the one to the other position depending on the flow conditions. The position of such flaps can be rendered particularly readily visible if the one side of the flap has an appearance which differs from that of the other side of the flap and/or if the surface which is covered by the flap has an appearance in the one end position which differs from the appearance of the surface which is covered by the flap in the other end position. A different appearance can, for example, be realized by providing a differently colored, reflective or retroreflective surface or existing differences in transmission, fluorescence or phosphorescence or even coverage of an illuminated surface.

[30] **Foreign Application Priority Data**

May 17, 1996 [NL] Netherlands ..... 1003153

[51] **Int. Cl.<sup>7</sup>** ..... **A63B 53/00; G01P 13/00; G01W 1/00**

[52] **U.S. Cl.** ..... **73/170.02**

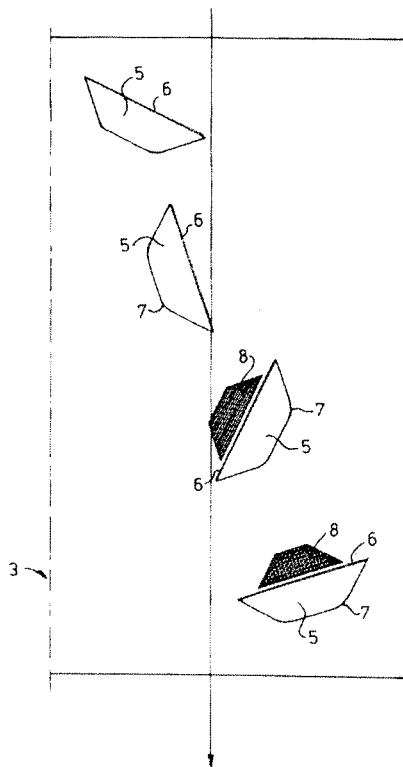
[58] **Field of Search** ..... **73/170.01, 170.02, 73/170.05, 170.06**

[56] **References Cited**

**U.S. PATENT DOCUMENTS**

4,567,760 2/1986 Crowder .

**22 Claims, 3 Drawing Sheets**



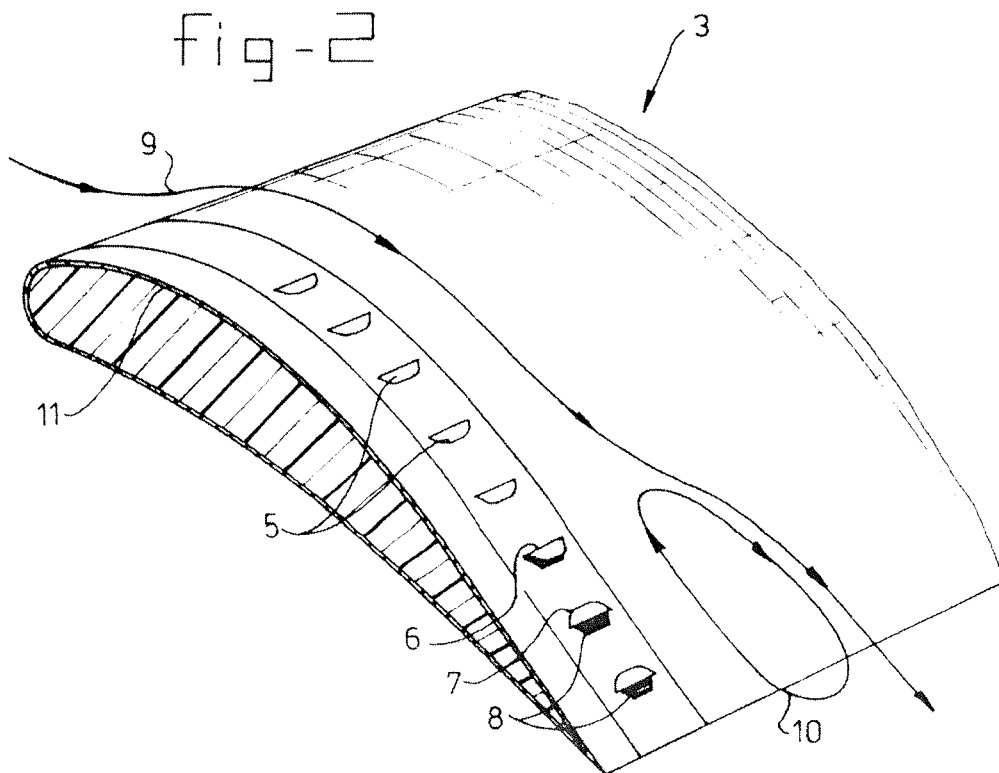
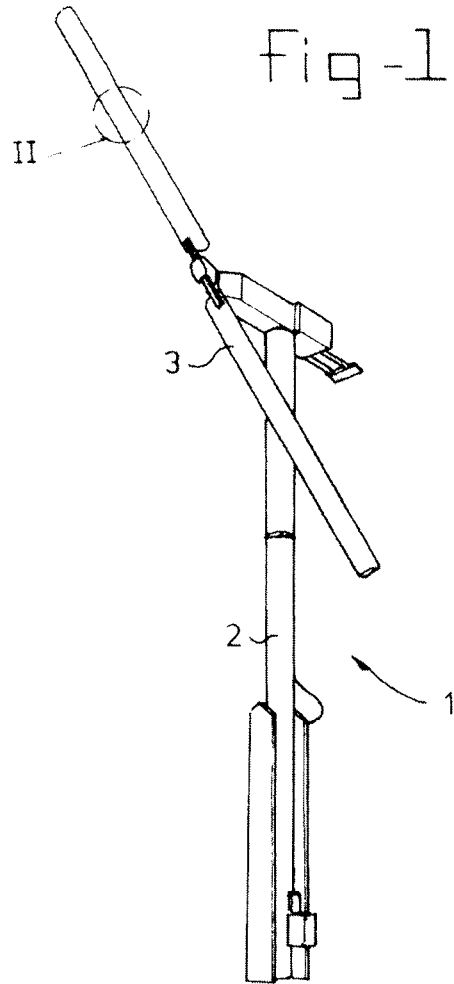


fig-3

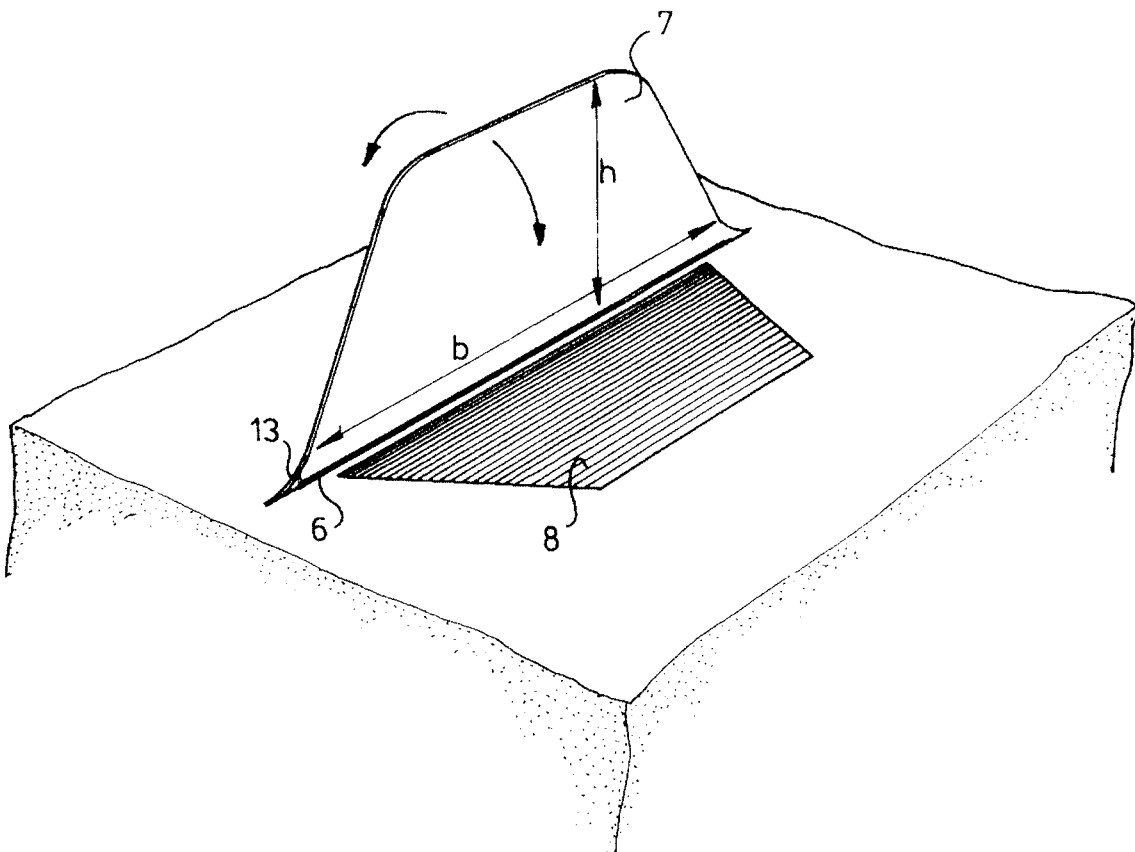
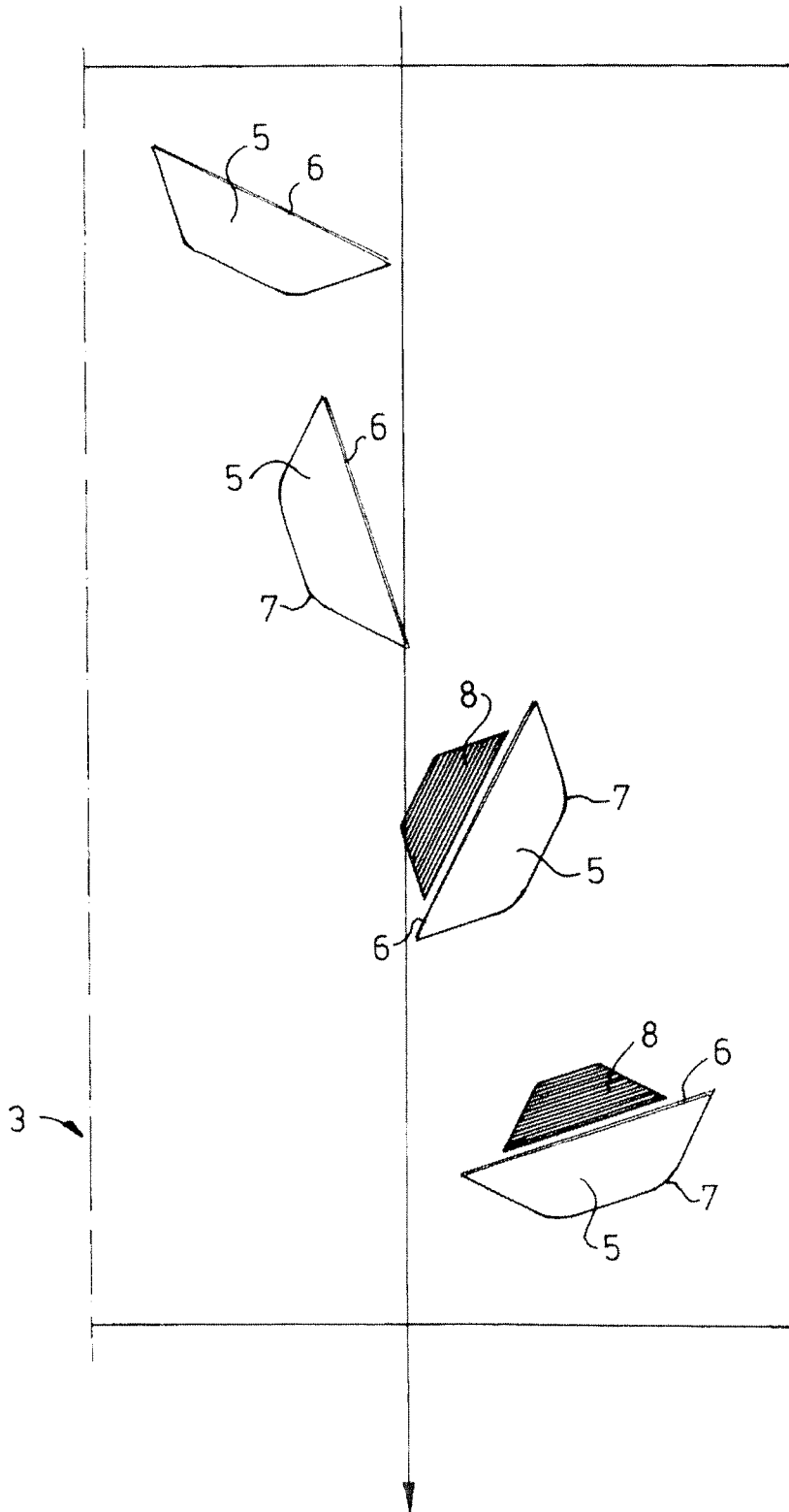


fig - 4



## DEVICE FOR RENDERING VISIBLE THE FLUID FLOW OVER A SURFACE

The present invention relates to an device according to the preamble of claim 1.

A device of this type is disclosed in report IW-94079-R of August 1994 by the Institute for Wind Energy, the Technical University of Delft, entitled: 'Visualisation of the Stagnation Point: First Results of a new Method'.

In this report it is proposed to fit one or more flaps, each having a width of approximately 1 metre, at the front, that is to say the zone close to the stagnation line (that is to say the stagnation point where flow ceases), of a wing-like surface. Such flap or flaps is/are fitted at an angle with respect to the so-called stagnation line and is/are of a width such that the stagnation line remains between the ends of each flap for all positions to be expected and certain conclusions relating to the flow are drawn from the shift in the turn-over point along the flap surface.

A construction of this type replaces constructions known in the prior art consisting of a number of preferably woollen threads, or jetting smoke or the like in the vicinity of the surface. Such a change has been made in particular because, especially when woollen threads are used on relatively large surfaces, the visibility of the position of the threads constitutes a problem.

If, for example, it is desired to obtain a general impression of the flow distribution in the case of wind turbines, it is not uncommon to take photographs thereof from a distance of 75 metres away from the vanes thereof. Small woollen threads are not visible on these photographs. Visibility remains poor even if use is made of technically sophisticated aids, such as stroboscopes. Large threads are influenced to a greater extent by the centrifugal force and give more flow disruption. Under certain flow conditions, the threads make rapid fluttering movements. As a consequence of this, blurring due to movement can become so severe that the position of the threads becomes invisible.

For these reasons electrical devices for rendering the flow direction visible by electrical means have been proposed in the prior art. However, these devices require vulnerable electrical connections for the power supply or signals. Moreover, these can affect the flow. An appreciable installation space in the object to be studied is also required. Consequently a long preparation time is necessary and the construction of the object can be weakened and a method of this type cannot be used in all locations.

This still takes no account of problems such as lightning strikes. Finally, woollen threads tend to be influenced by centrifugal force, that is to say to move outward.

The flap according to the abovementioned report solves these problems due to the effect of centrifugal force and the electrically complex construction.

However, visibility remains a problem at greater distances. After all, with a flap height of, for example, 5 mm it will be not be simple to detect (partial) turning over from a distance of a few tens of metres. The position at which the flap points towards the observer is visualised and, as a result, this position is dependent on the direction from which the observer views the flaps. This gives rise to systematic errors. The flap surface is stretched relatively severely close to the turn-over point for each flap. This is a disadvantage because permanent deformation can occur and because rapid response of the flap to a different flow condition is hindered by the hysteresis of the flap material. Moreover, the region close to the turn-over point is virtually perpendicular to the profile and, as a result, can easily give rise to flow disruption.

This problem is exacerbated when stalling is found. After all, the transition from one state to another then takes place gradually over a larger region.

The aim of the present invention is to avoid this disadvantage and to provide an improved device for detecting and rendering visible the fluid over a surface.

This aim is achieved with a device as described above having the characterising features of claim 1 or 2.

'Optically covered' is always understood as that condition which deviates essentially from the condition in which the relevant surface of said object is not covered. That is to say, even if the flap relating to the part of the surface does not completely cover but is (a few) tens of degrees removed therefrom, in certain circumstances there can still be said to be optical covering. Optical is understood not only as visible light but also as infrared or ultraviolet radiation and even other electromagnetic wave phenomena.

The invention is based on the insight that a different appearance is produced after the flap flips over. This can be caused because the flap itself is provided with different optical characteristics on the two sides, because the flap has optical characteristics which differ from those of the surface or because the part covered by the flap in a rest position has optical characteristics which differ from the rest of the surface. In all cases there will be a very clear visible change in appearance when the flap turns over. That is to say, different optical characteristics are produced in different positions of the flap with respect to the surface.

This change in appearance can be a difference in colour.

However, it is also possible that the reflective characteristics change because one or more of the surfaces is retro-reflective.

It is also possible to improve visibility by using fluorescence or phosphorescence. These and other possibilities for improvement are generally known to those skilled in the art.

In addition to the abovementioned possibilities, techniques such as polarisation, refraction and diffraction will occur to those skilled in the art.

The construction according to the Technical University of Delft report described above has the disadvantage that the flap has to be more or less elastic over the entire height thereof in order to be able to achieve the turning over. Consequently, the requirements in respect of the materials used are particularly stringent. The height of the flaps used in the said construction is at most 5 mm, as a result of which the visibility and sensitivity are limited.

The difference in appearance becomes particularly clear if the different sides of the flaps have a different colour. Another possibility is to provide that region of the surface for which the flow characteristics have to be determined, and on which the flap lies in the first position, with an appearance which differs from that of the region on which the flap lies in the second position.

In order to avoid this disadvantage, it is proposed according to the invention to fit a number of smaller flaps on the surface. Such flaps can then move independently of one another and, thus, the prevailing flow conditions can be accurately determined in any position. In contrast to the construction described above, the surface of the flap is always oriented in the same direction and no torsion takes place over the width of the flap. Moreover, the position of change can be accurately localised. This is in contrast to methods in which smoke is used.

Although the width of the flaps can have any value known in the prior art, preference is given, however, to making said flaps 1-20 cm and more particularly 8 cm wide. Using the same arguments, this gives 0.1-4 cm and more

particularly approximately 2.5 cm for the height. On the one hand the width is such that a substantial portion of the flow is covered and, on the other hand, a surface of 8 cm×2.5 cm is readily visible from a relatively large distance with the aid of the measures described above.

The flaps can have any shape known in the prior art. Preferably, however, the flaps are of trapezium-shaped construction, the corners of the free ends of the trapezium being rounded. In addition, the join to the blades etc. is also rounded. It has been found that it is possible to obtain an appreciably longer life by means of, in particular, this latter rounding.

The flap can be joined to the surface by any method known from the prior art. Preferably, the flap consists of a relatively rigid body section and a relatively flexible hinge section. The hinge section can, for example, be a film hinge, in which case a rubber sheet material is used.

The invention will be explained in more detail below, inter alia with reference to an illustrative embodiment shown in the drawings. In the drawings:

FIG. 1 shows, diagrammatically, a wind turbine;

FIG. 2 shows part of the vane profile of the wind turbine;

FIG. 3 shows a detail of a flap shown in FIG. 2 and

FIG. 4 shows the direction detector with four flaps.

The invention will be explained below with reference to one profile of a vane of a wind turbine. However, it must be understood that the device according to the invention can be used with equal success for any other profile for which the flow characteristics have to be determined. In this context consideration can be given to aircraft, sails, chimneys and the like.

This relates to gas flows. However, the invention is also applicable to fluid flows. In this context, consideration can be given to the study of the flow characteristics over ships' hulls, screws and the like in water.

The wind turbine 1 shown in FIG. 1 consists of an upright 2 with two blades or vanes 3, located opposite one another, mounted thereon. Detail II in FIG. 1 is shown in FIG. 2. Arrow 9 indicates the flow direction, whilst 10 indicates a section with backflow. This backflow is closely linked to the reduction in the load-bearing capacity of the profile with increasing angle of incidence of the flow, which is also termed "stalling" of the profile. In the case of the vanes of some wind turbines the occurrence of such stalling at large angles of incidence is important because it is possible by correct dimensioning of the vane to achieve a situation where above a certain wind force the vane disrupts the flow to such an extent that no further power is taken up by the mill.

That is to say, at low wind force the profile is utilised to the optimum to convert all incident wind as far as possible into useful energy, whilst at high wind force there is a deliberate aim not to use this energy to the full.

That is why it is important to know the flow characteristics over a profile accurately. It is clear that it is also particularly desirable to investigate what the flow characteristics of, for example, the wing profiles of aircraft are, albeit that the considerations are different in that case.

Detail II is shown in FIG. 2 and it can be seen from this that a number of small flaps 5 are also mounted on the suction side of the vane profile.

A single flap is shown in FIG. 3. This flap can be made of any material known in the prior art, such as polycarbonate. The flap width is indicated by *b* and the height by *h*. The width can be 8 cm and the height 2 cm. It is also indicated in FIG. 3 that the region 8 of the surface above which the flow characteristics have to be determined optically differs

in appearance from the region on the other side of this which is mirrored with respect to the hinge. This can be achieved by the region being retroreflective, fluorescent, etc. Fixing to the top section 11 of the profile can be via a strip or direct (see FIG. 2). In the embodiment shown in FIG. 2, the hinge edge 6 of the flap is the front edge and the free end the back edge. With this arrangement the hinge is made so flexible, for example in the form of a rubber hinge, that even a small component of the flow direction 9 or 10 from the back edge to the front edge is sufficient to cause the flap to turn over.

It can be seen from FIGS. 2 and 3 that the flap is of trapezium-shaped construction. It has been found that if the free corners of the flap are rounded (indicated by 7), the load on the hinge is less and, as a result, in particular the life of the hinge is appreciably extended or the hinge can be of much lighter construction. However, this can be promoted to a much more appreciable extent by making the fixing to the surface for which the flow characteristics have to be determined of rounded construction, which is indicated by 13.

As can be seen from FIG. 2, there is backflow, indicated by arrow 10, at the rear of the profile. As a result flaps 6, 7 and 8 turn (partially) over. As a result the retroreflective surface applied to the profile is exposed. It is, of course, possible to use a colour difference instead of a retroreflective region. Furthermore, it is possible to apply this colour difference not to the profile but to the flap.

It has been found that when retroreflective material is used it is particularly simple to detect when the flaps turn over and/or whether the flaps have been turned over. If a light source is arranged close to the observer, the latter is also able clearly to detect the turning over of the flaps from a great distance. Turning over can, moreover, be recorded photographically or on video.

It is clear that the thickness of the flap must be relatively small so as not to influence the flow. It is proposed to use a value of less than 0.3 mm.

It is obvious that the functioning of the flaps is no longer guaranteed if the profile is damp or even cools substantially in damp conditions (until it freezes solid). However, it has been found that once such adverse weather conditions no longer prevail the flaps are fully functional again.

FIG. 4 shows a direction detector with four flaps. Depending on the flow direction, the detector can lift in eight different ways. Every 45 degree change in the flow direction will always cause one flap to turn over.

If it is important to fit the device rapidly, the latter can be made in the form of a sticker. In the construction shown in FIG. 2, the adhesive part can be applied as a strip to the vane profile concerned and the non-adhesive flaps 5-7 can extend therefrom. It is also possible to fit each detector individually in the form of a sticker. Of course, here too all corners must as far as possible be rounded in order to prevent detachment.

It has been found that under certain conditions it is possible for water to penetrate beneath the flaps and for the latter to stick as a result. In such a case it can be important either to make the various parts water-repellent or to construct them such that said moisture can be removed in a suitable manner.

With the construction described above it is possible to work with colour differences. In principle, there is no limit to the number of different colours.

If stickers are not used, the flaps can be fixed by any other means known from the prior art, such as by double-sided adhesive tape.

It has been found that, especially when a retroreflective surface and a sufficiently powerful light source are used, it is also possible to investigate rapidly moving profiles. It is

5

true that blurring due to movement results, but if the various situations are recorded photographically it will be found that a light trace is or is not produced, depending on the position of the flap.

Although the invention has been described here with reference to a some preferred embodiments, it must be understood that numerous modifications can be made thereto without going beyond the scope of the present application, as defined in the appended claims. For instance, it is possible to use the device described above for testing all other profiles known in the prior art, such as the streamlined shape of aircraft. The device can also be used for advertising purposes or other applications which are not strictly functional.

What is claimed is:

1. Device for rendering visible the direction of a fluid flow over a surface of an object, comprising a flap-like member which is joined in a hinged manner to said surface and which is located closer to or further away from said surface depending on said flow, wherein the surface of at least one side of said flap and that part of the surface of said object which is located on one side of the hinge line are constructed such that when said part of the surface is optically covered by said flap an optical appearance is obtained differing from the optical appearance in case when said part of the surface is not optically covered, wherein said flap-like member comprises a number of stall flaps, each being arranged to move entirely from one position to another without torsion taking place over the width of the flap.

2. Device according to claim 2, wherein the optical characteristics of the other part of the surface of said object which is on the other side of the hinge line differ from the optical characteristics of the one part of the surface of said object which is on the one side of the hinge line.

3. Device according to claim 2, wherein the difference in optical characteristics is a color difference.

4. Device according to claim 2, wherein the difference in optical characteristics is a difference in reflective characteristics.

5. Device according to claim 2, wherein one of the sides of the flap or that surface of said object which is covered by the flap is a retroreflective surface.

6. Device according to claim 2, wherein the width (b) of the flap is approximately 8 cm.

7. Device according to claim 2, wherein the flap has a trapezium-shaped shape.

8. Device according to claim 7, wherein the free corners of the trapezium which are remote from the hinge line are rounded.

9. Device according to claim 7, wherein the transition between the flap and the surface is made rounded (13).

10. Device according to claim 2, wherein the flap comprises a relatively rigid body section and a relatively flexible hinge section.

6

11. Device according to claim 7, wherein the hinge section is made of rubber sheet material.

12. Device for rendering visible the direction of a fluid flow over a surface of an object, comprising a flap-like member which is joined in a hinged manner to said surface and which is located closer to or further away from said surface depending on said flow, wherein the surfaces of the sides of said flap which are located opposite one another are constructed such that a different appearance is obtained when observing one side of said flap differing from the optical appearance when observing the other side of said flap, wherein said flap-like member comprises a number of flaps, each being arranged to move entirely from one position to another without torsion taking place over the width of the flap.

13. Device according to claim 12, wherein the difference in optical characteristics is a color difference.

14. Device according to claim 12, wherein the difference in optical characteristics is a difference in reflective characteristics.

15. Device according to claim 12, wherein one of the sides of the flap or that surface of said object which is covered by the flap is a retroreflective surface.

16. Device according to claim 12, wherein the width (b) of the flap is approximately 8 cm.

17. Device according to claim 12, wherein the flap has a trapezium-shaped shape.

18. Device according to claim 12, wherein the free corners of the trapezium which are remote from the hinge line are rounded.

19. Device according to claim 18, wherein the transition between the flap and the surface is made rounded.

20. Device according to claim 18, wherein the flap comprises a relatively rigid body section and a relatively flexible hinge section.

21. Device according to claim 12, wherein the hinge section is made of rubber sheet material.

22. Device for rendering visible the direction of a fluid flow over a surface of an object according to claim 18, comprising a flap-like member which is joined in a hinged manner to said surface and which is located closer to or further away from said surface depending on said flow, wherein the surfaces of the sides of said flap which are located opposite one another are constructed such that a different appearance is obtained when observing one side of said flap differing from the optical appearance when observing the other side of said flap, wherein said flap-like member comprises a number of flaps, each being arranged to move entirely from one position to another without torsion taking place over the width of the flap.

\* \* \* \* \*



# Samenvatting

Op dit moment is wereldwijd 15GW aan windvermogen opgesteld en daarmee wordt per jaar ongeveer 100PJ elektriciteit opgewekt. Dit is slechts 0.2% van de wereldelektriciteitsproductie, maar zowel het opgestelde vermogen als de opgewekte energie nemen met circa 30% per jaar toe. Er zou nog 9% meer energie kunnen worden opgewekt als het fenomeen van stromingsloslating (overtrek) goed beheersbaar zou zijn.

## Vermogensregeling

Om schade aan windturbines te voorkomen, worden ze gewoonlijk boven windkracht 10 (25m/s) stilgezet. Het vermogen in de wind is dan ongeveer 8 keer hoger dan de turbine kan verwerken. Om te zorgen dat het turbinemaximum niet overschreden wordt, is het noodzakelijk om het opgenomen vermogen te kunnen regelen. Het is niet zinvol om de turbine zo te ontwerpen dat ook uit deze harde wind zo veel mogelijk energie kan worden gewonnen, omdat de zeer hoge windsnelheden zelden voorkomen. Een goed regelsysteem is wel zinvol en verhoogt dus de kosteneffectiviteit van de turbine. Globaal zijn er twee typen regelingen: actieve bladhoekverstelling (hierbij worden de bladen om hun as naar vaanstand gedraaid als het maximale vermogen overschreden wordt) en passieve overtrekregeling (waarbij de rotor op constant toerental draait en het opgenomen vermogen passief bepaald wordt door de rotor geometrie).

### Overtrekregeling

Overtrek is het verschijnsel dat de luchtstroming die van de voorrand naar de achterrاند over de bladen stroomt, boven een bepaalde kritische invalshoek voortijdig loslaat van het vleugeloppervlak (flow separation). Na het loslaatpunt stroomt de lucht zelfs terug, dat wil zeggen van de achterrاند van de vleugel naar de voorrand. De energieopname van het deel van de vleugel dat overtrekt neemt sterk af.

De kunst van het ontwerpen van een overtrekgerregelde turbine is de rotor geometrie zo te kiezen dat naarmate de windkracht toeneemt, het gebied van overtrek op de bladen, zodanig toeneemt, dat het opgenomen vermogen constant blijft. Dit moet gelden in het bereik van ongeveer windkracht 6 of 12.5 m/s (als het maximum vermogen net bereikt wordt), tot ongeveer windkracht 10 (als de turbine stopt). Het voordeel van deze regeling is dat het passief werkt, dus niet kwetsbaar is voor mankementen en goedkoop is in uitvoering.

## **Probleemstelling**

In de praktijk blijkt de overtrekregeling echter slecht beheersbaar en voldoen veel turbines niet aan de specificaties. Afwijkingen van het ontwerpvermogen tot tientallen procenten te veel of te weinig zijn niet ongevoel.

In de jaren '90 spitste het aërodynamische onderzoek zich toe op drie hoofdonderwerpen, te weten profielonderzoek in de windtunnel, de theorie van rotatie-effecten en drukmetingen op testturbines. Actuele problemen met het overtrekgedrag van commerciële windturbines konden daarmee echter niet voldoende onderzocht en begrepen worden.

Wij hebben daarom in deze dissertatie als kernvraag gekozen:

*'Verloopt de stromingsloslating over de bladen met de windsnelheid wel zoals wij denken?'*

Om dit vast te stellen is een meetmethode nodig die op grote commerciële turbines toepasbaar is, die het dynamische karakter van overtrek kan registreren, die ongevoelig is voor de sterke centrifugale kracht, en die natuurlijk geen significante verstoring geeft. Een dergelijke methode bestond niet. Daarom hebben wij een nieuwe techniek ontwikkeld.

### **'Stall flag'-methode**

Bij deze methode worden op een gerichte wijze honderden detectoren, verspreid over de rotor, in de vorm van stickers aangebracht. De detectoren (stall flags), die door ECN zijn geoptimaliseerd, hebben een reflecterende laag die afhankelijk van de luchtstromingsrichting al dan niet zichtbaar wordt. Door een krachtige schijnwerper in het veld op te stellen, lichten alle zichtbare reflectoren op, en kunnen we het veranderlijke overtrekpatroon registreren met een digitale videocamera, zelfs op 500m afstand. De 'stall flag'-signalen worden automatisch, met door ons ontwikkelde beeldbewerkingprogrammatuur opgemeten. De video camera registreert naast het stallpatroon de bladazimuthoeken en het rotortoerental en uit de optische signalen van andere sensoren ook nog de actuele windsnelheid en de windrichting. Uit de vele duizenden beelden karakteriseren we zo het stochastische overtrekgedrag.

#### Eigenschappen van de stall flag

De nieuwe detectortjes worden met de klassieke woldraadjes (tufts) vergeleken. Ze blijken minder weerstand te geven doordat ze werken op dynamische druk en niet, zoals tufts, op wrijvingsweerstand. Tufts vertonen een zelfgeëxciteerde klappergedrag (door de Kelvin-Helmholtzinstabiliteit) dat wij met een zorgvuldig ontwerp van de stall flag kunnen voorkomen. In de meest voorkomende opstelling zijn de stall flags bovendien ongevoelig voor de centrifugale kracht. Een experiment met een 65cm diameter propeller bewijst dat de stall flags onder draaiende omstandigheden blijven werken, terwijl tufts door de centrifugale kracht naar buiten slingeren, ook bij aanliggende stroming. Verder blijkt hieruit de zeer snelle respons van de stall flag.

Na het modelleren van het optisch gedrag, hebben wij het meetsysteem zodanig kunnen optimaliseren dat het toepasbaar is op turbines van alle voorkomende diameters. Vergeleken met tufts constateren we naast de eerder genoemde voordelen een minstens 1000 keer hoger contrast en 25 keer lagere resolutie-eisen aan de camera. Verder kunnen we van bewegingsonscherpte profiteren terwijl die voor tuftsignalen fataal is.

## Belangrijkste resultaten

In het kader van de fundamentele theorie over windturbines ontwikkelen wij twee nieuwe theoretische inzichten die betrekking hebben op het overtrekgedrag. Aansluitend analyseren we twee praktijkproblemen met de nieuwe meetmethode. Deze vier onderdelen worden hieronder kort besproken.

### 1. Inherente warmteontwikkeling

Als bij de energie-extractie door een windturbine ook de stroming om de rotor wordt meegenomen, blijkt dat er een inherente warmteontwikkeling in het zog ver achter de turbine optreedt. Bij optimaal turbinebedrijf is dat maar liefst de helft van het opgewekte vermogen. Hierdoor en door een argument met betrekking tot geïnduceerde weerstand zien wij geen aanleiding om de fundamentele theorie over energie-extractie aan te passen met de door Van Kuik (1991) voorgestelde 'edge-forces'. Wel bevelen wij aan om het door Lanchester (1915) ontwikkelde gedachtegoed over deze theorie verder uit te werken. Binnen de fundamentele theorie analyseren we het begrip inductie en vinden we dat de impulsstheorie, slankheidscorrecties en geïnduceerde weerstand alle drie hetzelfde fysische effect in rekening brengen. Onbekendheid hiermee kan leiden tot dubbele correcties (Viterna & Corrigan, 1981).

### 2. De invloed van rotatie op het overtrekgedrag

Bij het ontwerp van windturbines baseert men zich op aërodynamische karakteristieken, bepaald voor vast opgestelde profielsecties in een windtunnel. Om deze te vertalen naar het praktijkgedrag van draaiende rotorbladen zijn correctiemethoden ontwikkeld (Snel, 1990-1999). De daarbij gehanteerde aanname, dat de grenslaagtheorie geldig is in en nabij het losgelaten-stromingsgebied, onderschrijven wij niet.

In plaats daarvan gaan wij uit van de Navier-Stokesvergelijkingen, die we reduceren op basis van fysische argumenten. We verwaarlozen viscositeit, met het argument dat de losgelaten laag dik is. Uit de condities van loslating, leiden wij af dat de drukgradiënt en de Corioliskracht elkaar balanceren in koorderichting. Dan volgt dat de lucht in het losgelaten gebied door de radiale drukgradiënt en de centrifugale kracht naar de tip versnelt. Zo ontstaat een analytisch oplosbaar stelsel, waarin de convectieve term  $v_r \partial v_r / \partial r$  in de vergelijking voor de radiale richting (verwaarloosd in andere modellen) dominant is.

### 3. Meervoudige Vermogensniveaus

Bij verschillende grote commerciële windmolens worden af en toe vermogensdalingen tot 45% waargenomen bij schijnbaar gelijkblijvende omstandigheden. Eerder onderzoek naar mogelijke oorzaken, zoals technische gebreken, aërodynamische instabiliteiten en vervuiling had geen afdoende verklaring opgeleverd.

Wij formuleren drie hypothetische oorzaken. Door middel van 'stall flag'-metingen en twee andere cruciale experimenten kregen wij bevestiging voor één van de drie: de insectenhypothese. Insecten vliegen alleen bij lage windsnelheden en slaan in op specifieke plekken op de rotorbladen. Gebleken is, dat dit nu juist de plekken zijn die het vermogen bij hoge windsnelheden, als insecten niet vliegen, sterk beïnvloeden.

De andere, verworpen hypothesen, geven wel twee nieuwe inzichten. Ten eerste verwachten we meerdere vermogensniveaus indien de vorm van het terrein de wind concentreert. De niveaus worden dan bepaald door de windrichting en zullen optreden op alle typen windturbines, ook de bladhoekgeredelden. Ten tweede stellen we met de stall flags vast dat

het overtrokken deel van het blad zich op een continue wijze aanpast aan de aanstroming. Het sterke bi-stabiele hysterese gedrag van een overtrokken bladsectie in de windtunnel gaat in het veld dus verloren.

#### 4. Afwijkingen van Ontwerpspecificaties

Het vermogen van overtrekgergelde turbines vertoont in de praktijk vaak forse systematische afwijkingen van het ontwerp. Wij onderzochten met de stall flags een geval waarbij het vermogen 30% te hoog was (en de turbine overbelast werd). De gebieden op de rotor met een afwijkend gedrag werden onmiddellijk zichtbaar en het gedrag aldaar kon aangepast worden met grenslaagmanipulatoren zoals vortexgeneratoren. Zo ontstond een vermogenscurve, die aanzienlijk dichter bij de ontwerpspecificaties lag en realiseerden wij een opbrengstverbetering van 8%.

# Curriculum Vitae

Gustave Paul Corten werd geboren in Rotterdam op 8 september 1968. Hij doorliep het Merletcollege te Cuijk, waar hij op 4 juni 1986 het diploma Atheneum behaalde. Daarna studeerde hij aan de Technische Universiteit Delft aan de faculteit Technische Natuurkunde. In 1990 verkoos hij af te studeren op het onderwerp ‘tweefase stroming in een kokend-water reactor’ bij de vakgroep kernreactorkunde. Het doctoraal examen werd afgelegd op 24 november 1992.

Tijdens het afstuderen verschoof zijn interesse in de richting van duurzame energie. Daarom begon hij een promotieonderzoek bij het Instituut voor Windenergie aan dezelfde universiteit. Deze promotieplaats werd gefinancierd door het Energieonderzoek Centrum Nederland, waar hij op 1 mei 1997 een baan kreeg aangeboden. Tot op heden bekleedt hij daar een onderzoeksfunctie binnen de Unit Windenergie.

Al vanaf zijn tiende jaar was fotografie één van de voornaamste hobby's. Zo blies hij in zijn studententijd nieuw leven in de fotoclub van DSV St-Jansbrug. Vervolgens speelde de fotografie een belangrijke rol in zowel zijn afstudeerwerk als in het daarop volgende promotieonderzoek. Een andere voorname hobby is watersport in de vorm van roeien, kanoën en zeilen, waarbij nauwe relaties bestaan tussen de optimalisatie van de catamaran en die van de windturbine.

In 1998 ging hij samenwonen met Lies de Jong en op 21 April 2000 ontstond hun nieuwe hobby: hun kindje Veerle.



# Dankwoord

Het is af! Zeven jaar werk was nodig om te komen van de eerste ideeën over het zichtbaar maken van overtrek op windturbines tot een effectieve methodiek die inmiddels standaard is geworden. Het onderzoek heeft de eerste 3 jaar in Delft plaatsgevonden bij het Instituut voor Windenergie, daarna heb ik het bij het ECN voortgezet. Dit werk, de meettechniek en de nieuwe theorie zouden niet tot stand hebben kunnen komen zonder de steun en medewerking van een groot aantal mensen die ik hier bedanken wil.

Dank gaat uit naar Jan Dragt en Theo van Holten voor hun inzet en bijdragen als promotoren in de eerste fase van dit promotieonderzoek. Verder naar Arno Brand en Herman Snel, als naaste collega's. Arno voor de zorgvuldige wijze waarmee hij de contacten vanuit ECN onderhield en omdat hij de nieuwe methode het voordeel van de twijfel gaf. Herman, die - als een van eerste theoretici - het belang van 'stall flag'-methode onderschreef en zo moreel steunde. De vele discussies met hem over stromingsloslating en andere theoretische onderwerpen waren af en toe heftig, maar altijd verhelderend. Speciaal wil ik Otto de Vries bedanken, zowel voor de controles van delen van dit werk als voor zijn waardevolle Agardograph publicatie uit 1979. Dan Toon de Vries, voor het uren samenwerken in weer en wind in de werkbak van een hoogwerker, om honderden stall flags op windturbinebladen te plakken. Hij dacht als geen ander mee over het ontwerp van de stall flag, dat pas na jaren onderzoek voldoende bestand bleek tegen de omstandigheden op een windturbineblad. Ook Cees de Groot wil ik bedanken voor het bedienen van de 25mHAT tijdens diverse nachtelijke experimenten.

Bijzonder veel dank gaat uit naar Kees Andriessse. Pas in oktober 1999 heb ik hem benaderd met dit onderzoek. Hij was onmiddellijk gecharmeerd van de kracht van de eenvoud van de stall flag. Ik was zeer verheugd dat hij na zorgvuldige bestudering van mijn werk bereid was als promotor op te treden. Hij bracht het gestagneerde promotieonderzoek in een stroomversnelling. Ingestuurde hoofdstukken kwamen binnen een week terug voorzien van zorgvuldig commentaar en schaduwberekeningen. Onder zijn leiding konden de nieuwe theorieën over warmteontwikkeling en rotatie-effecten ontstaan. Kortom: dit proefschrift had zonder zijn enorme inzet en zijn wetenschappelijke toewijding niet kunnen ontstaan.

Dank gaat ook uit naar de mensen die dit onderzoek financieel mogelijk hebben gemaakt. Jos Beurskens en Harry van Grol hebben alles geïnitieerd door mijn promotieonderzoek, ook de periode in Delft, te financieren. In de fase dat de mogelijkheden van de methode nog onzeker waren, was Frits Verheij van NOVEM bereid om een groot project over de 'stall flag'-methode voor 80% mee te financieren. Door dit project werd de methode enorm verbeterd. We kunnen nu meten op elke commerciële turbine, ook als de diameter 80m is. Daardoor volgden opdrachten vanuit de industrie. Jaap de Boer en Henk Heerkes van Aerpac bedank ik voor hun opdracht om een Aerpac rotor met de stall flags te optimaliseren. Dick Veldkamp voor de opdracht van NEG Micon om het stallgedrag van turbines met meervoudige vermogensniveaus te onderzoeken. Ook wil ik hem bedanken voor de samenwerking binnen dit project in de VS. Then I thank Thomas Vronsky and Mark Hancock for including the method in a Joule-project to diagnose the stall behaviour of a 64m diameter Aerolaminates rotor installed in Denmark. Binnen het Joule-project 'MUST', waarbinnen eveneens de meervoudige vermogensniveaus onderzocht werden, zijn ook een aantal 'stall flag'-metingen opgenomen. Deze financieringen, althans het deel voor het 'stall flag'-werk, hadden samen een omvang van ongeveer 700kEuro. Mijn dank gaat ook uit naar ECN voor het vergoeden van de drukkosten van dit proefschrift.

Al zeg ik het zelf, er is best wat bereikt. En dat is allemaal niet bepaald zonder slag of stoot tot stand gekomen. Ik heb dan ook veel morele steun nodig gehad. Er was voor mijn gevoel een onuitputtelijk doorzettingsvermogen nodig om de techniek te krijgen waar hij is. De stall flag was *onbegrijpelijk* simpel. Het was in de eerste fase in Delft onmogelijk om uit te leggen wat ermee kon. Dat ik dat toentertijd gered heb is te danken aan een groot aantal vrienden, vriendinnen en gezinsleden. Een aantal mensen wil ik hiervoor speciaal bedanken: Carien Kuperus, Roosmarijn Sweers, Ella van Buuren, Camiel en Sigrun Heffels, Hans de Nivelte, en de paranimfen Guido van Geelen en Iegte de Jong. Zij voerden met mij veel relativerende en opbeurende gesprekken.

De meeste dank ben ik echter verschuldigd aan mijn partner Lies de Jong. Voor haar morele steun én voor haar tolerantie. Promoveren is namelijk asociaal: 's avonds en in het weekend was ik vaak aan het schrijven, vakanties werden meestal opgeofferd. Ook de woonkamer moest het ontgelden. Hier werden experimenten met kleine windturbines uitgevoerd. Soms assisteerde Lies daarbij met gevaar voor eigen leven. De plank op het achterwiel van de Suzuki waarop stall flags getest werden, vond ze aanvankelijk eng en later overigens best leuk. Veelre bedank ik voor haar voorbeeldfunctie: ze was altijd alleen met hoofdzaken bezig.

Tot slot wil ik mijn familie bedanken. Mijn ouders hebben tot op de dag van vandaag een omgeving gecreëerd waarin diverse activiteiten met grote diepgang centraal stonden. Hun galerie voor moderne kunst en architectuur is zo'n activiteit, de medische (ethische) wetenschap, de omgang met de natuur, de humanistische kijk op de wereld. Deze omgeving van doorzetten en nadenken is waarschijnlijk de bron geweest voor dit werk. Zowel mijn vader, moeder en broers wil ik bovendien bedanken voor de morele steun die tijdens mijn onderzoek regelmatig nodig was en voor hun concrete bijdragen: Het ontwerp van de kaft komt van mijn ouders, de samenvatting is gebaseerd op een interview door broer Frans en mijn broer Paul heeft essentieel bijgedragen aan het ontwerp van de beeldbewerkingalgoritmen. Laat ik tenslotte Heer Ollie B. Bommel-3 niet vergeten. Tijdens het uitlaten toonden zijn zwarte vachtharen bij veel wind soms ineens zijn spierwitte vel. Dat was de inspiratie voor het heldere signaal van de hedendaagse stall flag.



Stellingen behorende bij het proefschrift

## Flow Separation on Wind Turbine Blades

Gustave Paul Corten

1. Een windturbine in bedrijf op de Lanchester-Betzlimiet haalt, in tegenstelling tot heersende opvattingen, 50% meer kinetische energie uit de stroming dan de nuttige arbeid die hij levert. Dit meerdere komt vrij als warmte (dit proefschrift).
2. Onbekendheid over het moment waarop en de gebieden waar de rotorbladen van windturbines overtrekken leidt tot grote economische schade. Met de in dit proefschrift ontwikkelde 'stall flag'-meetmethode kan de ontbrekende informatie voor elke turbine verkregen worden.
3. Indien een windturbine op de Lanchester-Betzlimiet met de windsnelheid tegen de wind in beweegt en het hiervoor benodigde vermogen in rekening wordt gebracht, dan verdubbelt zijn opbrengst.
4. De acceptatie van windturbines verbetert als ze 4 of 5 in plaats van 3 bladen hebben. Ze kunnen dan langzamer draaien bij gelijke opbrengst. Dit geeft minder onrust in het landschap, een sterke geluidsreductie en een bladsnelheid die vogels meer tijd geeft om uit te wijken.
5. Het vertuien van grote windturbinerotoren kan trillingen voorkomen, de rotormassa verminderen en de opbrengst verhogen.
6. De beste gebruikers van de aërodynamica snappen er het minste van: vogels.
7. De stall flag is onbegrijpelijk simpel (dit proefschrift).
8. Het verspreiden van kernafval boven een stad, bijvoorbeeld door een terrorist, kan tot grotere contaminatie leiden dan een kernexplosie. Dit afval dient daarom onder het non-proliferatieverdrag te vallen.
9. Alleen aan je *eigen* auto zitten overwegend voordelen.
10. Subsidiëren van onderzoek verlaagt de kans op kwaliteit.
11. Kernafval kan het beste in proefschriften worden opgeslagen: die verdwijnen meestal voor eeuwig in bureaulades.
12. Een proefschrift is als een kunstwerk: de tijd zal leren of het waardevol is.

